New Engineering Principles in Atrium Smoke Management

New Approach Flow and Spill Plume Model for Wide Openings

Guidelines on CFD Grid Quality Control and Buoyancy-driven Vent Flow Modeling

Morten Birk Sabroe Valkvist

PhD Thesis

NIRAS Safety
NIRAS A/S

Department of Civil Engineering
Technical University of Denmark

November 2007

New Engineering Principles in
Atrium Smoke Management
New Approach Flow and Spill Plume Model
for Wide Openings
Guidelines on CFD Grid Quality Control and
Buoyancy-driven Vent Flow Modeling
Copyright (c), Morten Birk Sabroe Valkvist, November 2007
Printed by Technical University of Denmark
NIRAS Safety, NIRAS A/S and
Department of Civil Engineering, Technical University of Denmark
ISBN: 978-87-7877-242-8
ISSN: 1601-2917
Report no.: R-168

Preface

This thesis is submitted as a partial fulfilment of the requirements for the Danish Industrial PhD degree.

All proposed methods, correlations and principles must only be applied within the assumptions and limitations provided. Any application of the aforementioned methods etc. in fire safety design, should be carried out by an informed user and with adequate conservatism. Any responsibility in connection with the application of the methods etc. rests solely with the user, i.e. the author can not be held liable by any means.

The author may be contacted by email at *mbm@niras.dk* (or private email at *morten@valkvist.dk*).

Acknowledgements

The author wishes to acknowledge the following people and institutions:

NIRAS A/S and the Danish Ministry of Science, Technology and Innovation for funding the Industrial PhD project.

National Research Council Canada (Fire Research Program) for funding and accommodating the small-scale experimental program on approach flows.

Supervisor Head of Department Mr Finn Buus Steffensen (NIRAS Safety, NIRAS A/S) for his continuing inspiration, encouragement, endless challenging questions and for giving me this opportunity.

The group of university supervisors Associate Professor Dr Lars Schioett Soerensen (Department of Civil Engineering, Technical University of Denmark), Professor Dr Per Grove Thomsen (Informatics and Mathematical Modeling, Technical University of Denmark) and Professor Dr Peter Vilhelm Nielsen (Department of Building Technology and Structural Engineering, Aalborg University Denmark) for inspiration, guidance and support.

My external supervisors Senior Research Officer Dr Gary Lougheed and Technical Officer Mr Cameron McCartney with the Fire Research Program at National Research Council Canada (NRCC) for their guidance and inspiration during and after my internship at NRCC in 2005, and for really opening my eyes to fire research.

My colleagues in NIRAS Safety for helping me keep up the spirit and in particular Mrs Anne Osbourne for assisting me with digital drawing.

Abstract

A typical atrium smoke management setup was divided into characteristic flow regions; axisymmetric plume, ceiling jet/approach flow, rotation region and spill plume. A grid convergence study was conducted on each of the flow regions in order to determine the non-dimensional grid resolution required to obtain a grid independent solution. Rules of thumb for grid resolutions are proposed.

An experimental program comprising seven tests of approach flows in wide openings was conducted in a $\sim 1/3$ scale model corresponding to a fire compartment 5 m high with a compartment openining of 40 m on the full-scale. The experiments were conducted at the National Research Council Canada test facility in Almonte, ON. CFD models of the test setup were implemented in the CFD fire model *Fire Dynamics Simulator ver. 4.06* and validated against experimental data.

CFD models were scaled to full-scale and new simulations conducted and validated against scaled experimental data to verify the applicability of the CFD model in modeling wide opening approach flows. A full-scale numerical program including 42 simulations were conducted to provide data for the development of a new method to calculate mass flow rates in wide opening approach flows. Opening widths up to 87 m were addressed. To provide supporting data, the full-scale CFD predictions were scaled 3/5 and 4/5 to provide additional data points to support the versatility of the new method. An iterative method for calculating approach flow mass flow rates was proposed. The method decouples the axisymmetric plume flow in the fire compartment from the approach flow, treating it as a source for the mass flow rate in the approach flow.

To supplement the new approach flow method, a modified method for calculating mass flow rates in wide spill plumes with a lateral extent up to 87 m and rising heights of up to 55 m was proposed. The method was derived from CFD predictions of mass flow rates computed in a full-scale numerical program including 14 simulations. The mass flow rate in the spill plume depends on the approach flow mass flow rate, thus a correlation based on the aforementioned simulations were proposed for the entrainment in the rotation region.

A full-scale numerical study of the outflow through buoyancy driven vents was carried out to address the lacking contraction of outflows in vents described by a simple passive boundary condition in CFD modeling. A correction coefficient for the geometrical passive vent area was proposed based on the Froude number. The coefficient was derived from 216 full-scale CFD simulations of horizontal and vertical orifice vents of sizes normal in fire safety design.

Resumé

Et typisk atrium setup blev inddelt i områder med samme karakteristiske flow; aksesymmetriske plume, loftsjet/tilløbsflow, rotationsregion og spildplume. Det blev undersøgt hvilke gridstørrelser der kræves for at opnå en griduafhængig løsning i de respektive strømningsområder. Resultatet er et sæt tommelfinger-regler for dimensionsløse gridstørrelser.

Syv skalatests af masseflowet i tilløbsflow under etagedæk blev udført i skala 1/3, hvilket i fuld skala modsvarer en rumhøjde på 5 m og en åbningsbredde på op til 87 m. CFD-simuleringer af den eksperimentelle forsøgsopstilling blev udført for at validere den anvendte CFD-model *Fire Dynamics Simulator ver. 4.06*.

De anvendte CFD-modeller blev skaleret til fuld skala og valideret mod de experimentelle data for at verificere CFD-modellens egnethed. En forsøgsserie på 42 fuldskala simuleringer blev udført med henblik på at tilvejebringe data for udviklingen af en ny metode til at beregne masseflowet i tilløbsflow. Den nye metode er iterativ og anvender en eksisterende anerkendt plumemodel til at beregne masseflowet i den aksesymmetriske plume, der fungerer som kilde til tilløbsflowet.

Som supplement til den nye metode for tilløbsflow under etagedæk blev der udviklet en modificeret spildplumemodel gældende for spildkantlængder op til 87 m og plumehøjder op til 55 m. Spildplumemodellen er baseret på data fit af masseflow beregnet i 14 fuldskala simuleringer. Masseflowet i spildplumen afhænger af tilløbsflowet, hvorfor en korrelation for røgproduktionen i rotations-området ligeledes blev udviklet.

I CFD-modellering af naturlige afkaståbninger ignores kontraktion af flowet ofte, idet der anvendes simple randbetingelser, som kun tager den indvendige del af beregningsområdet i betragtning. Anvendelsen af en numerisk kontraktionsko-efficient til at øge det beregnede areal, således at vena contracta tages i regning, foreslås baseret på Froude-tallet i åbningen. Den foreslåede koefficient er baseret på 216 simuleringer af fuldskala ventilationsåbninger med arealer typiske inden for brandventilation.

Table of Contents

List of Acronyms **1**

Nomenclature **3**

List of Figures **9**

List of Tables **15**

1 Introduction **17**
1.0.1 Atrium Smoke Management Design 17
1.0.2 Grid Quality Design 17
1.0.3 Smoke Flows Emanating From Wide Openings 18
1.1 Buoyancy Driven Vent Flows 20

2 Grid Quality Control in CFD Fire Modeling **21**
2.1 Introduction 21
2.2 Present Research 22
2.3 Errors in CFD Fire Modeling 23
2.4 Description of Applied CFD Model 25
2.4.1 Hydrodynamic Model 25
2.4.2 Turbulence Model 27
2.4.3 Combustion Model 27
2.4.4 Radiation Model 29
2.4.5 Surface Boundary Conditions 31
Energy BCs 31
Velocity BC 33
2.4.6 Fire/Heat Source BC 33
2.4.7 Flow Boundary Conditions 34
Passive Flow BC 34
Symmetry Flow BC 35
2.4.8 Numerical Model 35
Computational Grid 35
Temporal Discretization 36
Spatial Discretization 38
2.5 Characteristic Length Scales 41
2.6 Computing Flow Rates 42

2.7 Flow Regions . . . 44
2.8 Grid Convergence Study . . . 45
2.8.1 Discretization Error . . . 45
2.8.2 Modeling Parameters . . . 46
2.8.3 Simulations Breakdown . . . 46
2.8.4 Measurements . . . 46
2.9 CFD Model Setup . . . 48
2.9.1 Modeling Procedure . . . 48
2.9.2 Computational Grid and Boundary Conditions . . . 48
2.9.3 Measuring Positions . . . 48
2.9.4 CFD Model Inputs . . . 49
2.10 Results of Grid Convergence Study . . . 53
2.10.1 Axisymmetric Flow Region . . . 53
2.10.2 Approach Flow Region . . . 62
2.10.3 Rotation Region . . . 70
2.10.4 Spill Plume Region . . . 73
2.11 Conclusion . . . 85
2.12 Future Research . . . 86

3 Small-scale Modeling of Approach Flows in Wide Openings 87
3.1 Introduction . . . 87
3.2 Present Research . . . 89
3.3 Mass Flow Rates . . . 89
3.4 Depth of Smoke Layer . . . 91
3.5 Small-scale Approach Flow Studies . . . 92
3.5.1 Experimental Objective . . . 92
3.5.2 Experimental Parameters . . . 92
3.6 Experimental Program . . . 93
3.6.1 Test Breakdown . . . 93
3.6.2 Description of Experimental Test Facility . . . 93
Fire Compartment . . . 93
Fire Source . . . 97
Instrumentation . . . 98
Test Procedure . . . 100
Data Processing . . . 101
3.7 Modeling Program . . . 102
3.7.1 Simulations Breakdown . . . 102
3.7.2 Description of CFD model . . . 103
Modeling Procedure . . . 103
Computational Grid and Boundary Conditions . . . 103
Measuring Positions . . . 104
Data Processing . . . 104
CFD Model Inputs . . . 107
3.8 Assessing Sub-model Impacts . . . 109
3.9 Results . . . 112

3.9.1 Reynolds Number . . . 112
3.9.2 Conservation of Energy . . . 113
3.9.3 Temperature Profiles . . . 114
3.9.4 Velocity Profiles . . . 119
3.9.5 Symmetric Flow Properties . . . 123
3.9.6 Mass Flow Rates . . . 123
3.9.7 Smoke Layer Depth . . . 125
3.10 Conclusion . . . 126
3.11 Discussion . . . 127
3.12 Future research . . . 128

4 Physical Scale Modeling 129
4.1 Introduction . . . 129
4.2 Non-dimensional Groups . . . 129
4.3 Froude Modeling . . . 132
4.4 Froude Modeling Study . . . 133
4.4.1 Modeling Objective and Parameters . . . 133
4.4.2 Methodology . . . 133
4.4.3 Simulations Breakdown . . . 133
4.4.4 Description of CFD Model . . . 134
General Properties . . . 134
Geometry of CFD Model and Grid Design . . . 134
Data Processing . . . 134
4.5 Assessing Radiation Dependency . . . 137
4.6 Results . . . 137
4.6.1 Temperature Profiles . . . 137
4.6.2 Velocity Profiles . . . 138
4.6.3 Heat Flow Rates . . . 140
4.6.4 Mass Flow Rates . . . 140
4.7 Conclusion . . . 141

5 Full-scale Approach Flows in Wide Openings 143
5.1 Present Research . . . 143
5.2 Full-scale Model Studies . . . 143
5.2.1 Modeling Objective . . . 143
5.2.2 Modeling Parameters . . . 143
5.3 Modeling Program . . . 145
5.3.1 Simulations Breakdown . . . 145
5.3.2 Description of CFD Model . . . 145
Modeling Procedure . . . 145
Computational Grid and Boundary Conditions . . . 145
Measuring Positions . . . 146
Data Processing . . . 146
CFD Model Inputs . . . 146
5.4 Results . . . 151

5.4.1 Conservation of Energy . . . 151
5.4.2 Mass Flow Rates per Unit Length . . . 151
5.4.3 Location of Fire Base . . . 152
5.5 Development of New Approach Flow Method . . . 156
5.5.1 Methodology . . . 156
5.5.2 Assumptions and Limitations . . . 156
5.5.3 Approach Flow Method . . . 157
5.5.4 Testing the New Method for Mass Flow Rate . . . 161
5.6 Conclusions . . . 163
5.7 Future Research . . . 164

6 Wide Opening Spill Plumes 165
6.1 Introduction . . . 165
6.2 Present Research . . . 166
6.3 Full-scale Model Studies . . . 167
6.3.1 Modeling Objective . . . 167
6.3.2 Modeling Parameters . . . 167
6.4 Modeling Program . . . 168
6.4.1 Simulations Breakdown . . . 168
6.4.2 Description of CFD Model . . . 168
Modeling Procedure . . . 168
Computational Grid and Boundary Conditions . . . 170
Measuring Positions . . . 175
Data Processing . . . 175
CFD Model Inputs . . . 175
6.5 Results . . . 177
6.5.1 Conservation of Energy . . . 177
6.5.2 Lateral Temperature Distribution in Spill Plume . . . 177
6.5.3 Mass Flow Rates Per Unit Length in Spill Plume . . . 179
6.5.4 Spill Plume Collapse . . . 182
6.6 Development of Spill Plume Method for Wide Openings . . . 186
6.6.1 Functional Form . . . 186
6.6.2 Assumptions and Limitations . . . 187
6.6.3 Mass Flow Rate at the Spill Edge Elevation . . . 188
6.6.4 Entrainment in the Rotation Region . . . 189
6.6.5 Entrainment in the Wide Spill Plume . . . 192
6.6.6 Application of Spill Plume Method . . . 196
6.6.7 Testing Spill Plume Methods for Mass Flow Rate . . . 196
6.7 Conclusion . . . 201
6.8 Future Research . . . 202

7 Modeling Buoyancy Driven Vent Flows 205
7.1 Introduction . . . 205
7.2 Orifice Flow Formulas . . . 206
7.3 Froude Number . . . 209

7.4 Present Research . . . 210
7.5 Full-scale Model Studies . . . 210
7.5.1 Modeling Objective . . . 210
7.5.2 Modeling Parameters . . . 210
7.6 Modeling Program . . . 211
7.6.1 Simulations Breakdown . . . 211
7.6.2 Description of CFD Model . . . 214
Modeling Procedure . . . 214
Computational Grid and Boundary Conditions . . . 214
Measuring Positions . . . 218
Data Processing . . . 219
CFD Model Inputs . . . 220
7.7 Results . . . 222
7.7.1 Coefficients of Discharge . . . 222
7.7.2 Vent Exhaust Capacities . . . 222
7.8 Development of Method for Correcting Vent Area . . . 227
7.8.1 Methodology . . . 227
7.8.2 Assumptions and Limitations . . . 227
7.8.3 Mass Flux Corrections . . . 228
Horizontal vent . . . 228
Vertical vent . . . 229
7.8.4 Application of the Method . . . 233
7.9 Conclusions . . . 235
7.10 Future Research . . . 236

8 Conclusion **237**
8.1 General . . . 237
8.2 Grid Quality Design . . . 237
8.3 Small-scale Approach Flows . . . 238
8.4 Approach Flows in Wide Openings . . . 238
8.5 Wide Opening Spill Plumes . . . 239
8.6 Buoyancy Driven Exhaust Vents . . . 240

Bibliography **243**

A Multi-grid Modeling **247**

B Impact of Wall Velocity BC on Ceiling Jet **251**

C B4138-108 Small-scale Test Program: Assessing Sub-model Dependency **255**

D B4138-XXX Small-scale Test Program: Temperature Profiles **259**

E B4138-XXX Small-scale Test Program: Velocity Profiles **267**

F B4138 Scaling Laws: Temperature Profiles **275**

G B4138 Scaling Laws: Velocity Profiles **281**

H B4138-108 Full-scale Test Program: Assessing Sub-model Dependency **287**

I Scaling the Full-scale Approach Flow CFD-model **291**

J Lateral Temperature Distribution in WOSP **295**

K Lateral Temperature Distribution in WOSP **299**

L Cross-sectional Temperature Distribution in WOSP **303**

List of Acronyms

ASHRAE	:	American Heating, Refrigerating and Air-Conditioning Engineers
BC	:	Boundary Condition
BD	:	Backward Difference scheme
CD	:	Central Difference Scheme
CFD	:	Computational Fluid Dynamics
CFL	:	Courant, Friedrich, Levy condition
COM	:	Center-of-mass
CPU	:	Central Processing Unit (in a computer)
DD	:	Downwind Difference scheme
DNS	:	Direct Numerical Simulation (turbulence model)
FD	:	Forward Difference scheme
FDS	:	Fire Dynamics Simulator ver. 4.06
FVM	:	Finite Volume Method
HRR	:	Heat Release Rate
IMS	:	Industrial Methylated Spirits
LES	:	Large Eddy Scale (turbulence model)
NIST	:	National Institute of Standards and Technology
NRCC	:	National Research Council Canada
PDE	:	Partial Differential Equation
PECE	:	Predictor-corrector scheme
RANS	:	Reynolds-Averaged Navier-Stokes (turbulence model)
RTE	:	Radiative Transport Equation
SHEV	:	Smoke and Heat Exhaust Ventilator
SLCF	:	FDS SLiCe File
UD	:	Upwind Difference scheme

Nomenclature

Latin

A_a	:	Area of vena contracta (aerodynamic) $[m^2]$
A_f	:	Surface area of fire base $[m^2]$
A_v	:	Geometric area of vent $[m^2]$
A_w	:	Cross-sectional area of smoke layer in opening $[m^2]$
AR_l	:	Aspect ratio of spill plume $[m]$
AR_v	:	Aspect ratio of SHEV [1]
b^*	:	Grid resolution relative to b [1]
b	:	Flow profile width at $1/2 * T_{max}$ $[m]$
C_Z	:	Empirical constant in flame sheet correction [1]
C_a	:	Coefficient of contraction [1]
C_d	:	Coefficient of discharge [1]
$C_{i,fds}$	:	Correction coefficient applied with passive vents [1]
C_d^*	:	Simple coefficient of discharge [1]
C_s	:	Smagorinski constant (turbulence model) [1]
C_l	:	Empirical spill plume entrainment constant $[kg/(m * s)]$
C_v	:	Coefficient of contraction [1]
C_{wo}	:	Empirical convective heat transfer constant [1]
C_ϵ	:	Constant in discretization error
C_{mu}	:	Coefficient of viscosity [1]
c_p	:	Constant pressure specific heat capacity $[kJ/(kg * K)]$
c_s	:	Specific heat capacity of gas at fixed pressure $[kJ/(kg * K)]$
c_s	:	Specific heat capacity of solid $[kJ/(kg * K)]$
c_p	:	Constant volume specific heat capacity $[kJ/(kg * K)]$
D_p^*	:	Characteristic length scale of circular/rectangular fire source $[m]$
D_i^*	:	Generic characteristic length scale of fire source $[m]$
D_l^*	:	Characteristic length scale of fire line source $[m]$
D_{fb}	:	Distance from fire base to compartment opening $[m]$
D_{fc}	:	Depth of fire compartment $[m]$
D	:	Diffusion coefficient of gas mixture $[m^2/s]$
D	:	Diameter of fire base $[m]$
D_l	:	Diffusion coefficient of species l $[m^2/s]$
D_l	:	Cross-sectional extent of spill plume $[m]$
D_O	:	Diffusion coefficient of oxygen $[m^2/s]$

d_b	:	Depth of balcony $[m]$
d_d	:	Depth of downstand $[m]$
d_h	:	Hydraulic diameter $[m]$
d_i	:	Depth of the smoke layer base at position i $[m]$
d_s	:	Smoke layer depth $[m]$
d_w	:	Depth of smoke layer in compartment opening $[m]$
$\mathbf{f}$	:	External forces exerted on the subvolume (not gravity) $[N/m^3]$
Fr	:	Froude number [1]
g	:	Gravitational acceleration $[m/s^2]$
$\mathbf{g}$	:	Gravity vector $[m/s^2]$
ΔH_c	:	Heat of combustion $[kJ/kg]$
ΔH_O	:	Heat of combustion of oxygen $[kJ/kg]$
$\mathcal{H}$	:	Pressure head $[Pa * m^3/kg]$
H_c	:	Height to the ceiling $[m]$
H_{fb}	:	Height of fire base $[m]$
H_{fc}	:	Height of fire compartment $[m]$
H_o	:	Height of vertical opening $[m]$
H_v	:	Geometrical height of vent $[m]$
h	:	Enthalpy $[kJ]$
h_a	:	Height to vena contracta $[m]$
h_c	:	Convective heat transfer coefficient $[kW/(m^2 * K)]$
h_l	:	Enthalpy of species l $[kJ]$
$I(\mathbf{x}, \mathbf{s})$	:	Radiative intensity of the gaseous mixture $[kW/m^2]$
$I_b(\mathbf{x})$	:	Radiative source term $[kW/m^2]$
$I_n(\mathbf{x})$	:	Local incident radiative intensity $[kW/m^2]$
$I_\lambda(\mathbf{x}, \mathbf{s})$	:	Radiative intensity at wavelength λ $[kW/m^2]$
k	:	Thermal conductivity $[kW/(m * K)]$
k	:	Variable accounting for geometrical similarity in approach flows [1]
k_s	:	Thermal conductivity of solid $[kW/(m * K)]$
L	:	Characteristic length $[m]$
L_f	:	Mean flame height $[m]$
L_l	:	Length of line source $[m]$
l	:	Geometric length scale $[m]$
M_F	:	Fuel molecular weight $[kg/mol]$
M_l	:	Molecular weight of l'th species $[g/mol]$
M_O	:	Oxygen molecular weight $[kg/mol]$
M_w	:	Molecular weight $[g/mol]$
$\dot{m}$	:	Mass flow rate $[kg/s]$
$\dot{m}_{a,v}$	:	Mass flow rate through horizontal vent $[kg/s]$
$\dot{m}_{a,v}$	:	Mass flow rate through vertical vent $[kg/s]$
$\dot{m}_c$	:	Mass flow rate below ceiling $[kg/s]$
$\dot{m}_e$	:	Mass flow rate at elevation of spill edge $[kg/s]$

$\dot{m}_l$	:	Mass flow rate in spill plume $[kg/s]$
$\dot{m}_{l,net}$	:	Net mass flow rate in spill plume $[kg/s]$
$\dot{m}_p$	:	Mass flow rate in axisymmetric plume $[kg/s]$
$\dot{m}_w$	:	Mass flow rate compartment opening $[kg/s]$
$\dot{m}''_f$	:	Mass flux at fire base $[kg/(m^2 * s)]$
$\dot{m}'_l$	:	Mass flow rate per unit length in spill plume $[kg/(m * s)]$
$\dot{m}'''_l$	:	Mass production per unit volume of l'th species $[kg/(s * m^3)]$
$\dot{m}''_v$	:	Mass flux in the vent opening $[kg/(m^2 * s)]$
N_T	:	Total number of computational cells [1]
N_λ	:	Number of wave length bands [1]
$\mathbf{n}$	:	Normal unit vector
$\mathbf{n}_x$	:	Base vector in x direction
n^*	:	Grid resolution relative to D_i^* [1]
n_t	:	Number of grid cells in time space [1]
n_x	:	Number of grid cells in x direction [1]
n_y	:	Number of grid cells in y direction [1]
n_z	:	Number of grid cells in z direction [1]
Pr	:	Prandtl number [1]
p^*	:	Characteristic pressure defect $\rho_\infty U^2$ $[Pa]$
p'	:	$p - p_\infty$ $[Pa]$
p_∞	:	Ambient pressure $[Pa]$
p	:	Pressure $[Pa]$
p	:	Order of numerical scheme
p_0	:	Background pressure component $[Pa]$
p_d	:	Dynamic pressure component $[Pa]$
Δp_b	:	Pressure increase at bottom of vertical vent $[Pa]$
p_s	:	Static pressure component $[Pa]$
$\tilde{p}$	:	Pressure pertubation (away from p_0 and hydrostatic comp.) $[Pa]$
Q	:	Fire load $[kJ]$
$\dot{Q}_c$	:	Convective heat release rate $[kW]$
$\dot{Q}_w$	:	Convective heat release rate in compartment opening $[kW]$
$\dot{Q}_r$	:	Radiative heat release rate $[kW]$
$\dot{Q}_T$	:	Total heat release rate $[kW]$
$\dot{Q}''$	:	Specific heat release rate or heat flux $[kW/m^2]$
$\dot{Q}'''$	:	Heat release rate per unit volume $[kW/m^3]$
$\dot{Q}''_{c,pre}$	:	Prescribed convective heat release rate per unit area $[kW/m^2]$
$\dot{Q}''_{T,pre}$	:	Prescribed total heat release rate per unit area $[kW/m^2]$
$\mathbf{q}_r$	:	Radiative heat flux vector $[kW/(m^2)]$
$\dot{q}''$	:	Local heat release rate per unit area $[kW/(m^2)]$
$\dot{q}'''$	:	Local heat release rate per unit volume $[kW/(m^3)]$
$\dot{q}''_{c,f}$	:	Convective heat flux at heater base $[kW/(m^2)]$
$\dot{q}''_{c,in}$	:	Incicent convective heat flux $[kW/(m^2)]$
$\dot{q}''_{r,in}$	:	Incicent radiative heat flux $[kW/(m^2)]$

R	:	Gas constant $c_p - c_v$ $[kJ/(kg * K]$
Re	:	Reynolds number [1]
$\mathbf{s}$	:	Directional vector [1]
$\mathbf{s}_{bf}$	:	Directional vector pointing in the bulk flow direction [1]
ΔT	:	Wall boundary layer temperature difference $[K]$
ΔT	:	Core plume cut-off filter $[K]$
T	:	Absolute temperature $[K]$
T_0	:	Plume center line temperature $[K]$
T_{cw}	:	Absolute temperature below the ceiling $[K]$
T_g	:	Absolute gas temperature $[K]$
T_{ghost}	:	Ghost cell temperature $[K]$
T_{max}	:	Maximum temperature $[K]$
T_s	:	Temperature in solid $[K]$
T_w	:	Wall temperature $[K]$
T_∞	:	Ambient temperature $[K]$
Δt	:	Time step $[s]$
$\overline{t}$	:	Averaging time interval $[s]$
t	:	Time scale $[s]$
t_s	:	Thickness of solid $[m]$
U	:	Mean velocity component in x direction $[m/s]$
$\tilde{\mathbf{U}}$	:	Mean local control volume core velocity in flow section $[m/s]$
u	:	Velocity component in x direction $[m/s]$
$\mathbf{u}$	:	Velocity vector $\mathbf{u} \in \{u, v, w\}$ $[m/s]$
u_*	:	Velocity slip condition [1]
u_∞	:	Ambient velocity field $[m/s]$
u_τ	:	Tangential velocity component on solid wall $[m/s]$
V	:	Mean velocity component in y direction $[m/s]$
V	:	Volume $[m^3]$
v	:	Velocity component in y direction $[m/s]$
v_i	:	Horizontal smoke layer velocity at position i $[m/s]$
v_n	:	Normal velocity component on solid wall $[m/s]$
W	:	Mean velocity component in z direction $[m/s]$
W	:	Characteristic velocity $[m/s]$
W_b	:	Width of spill plume at the spill edge $[m]$
W_f	:	Width of outflow from exhaust vent $[m]$
W_{fc}	:	Width of fire compartment $[m]$
W_l	:	Lateral extent of spill plume $[m]$
W_v	:	Geometrical width of vent $[m]$
W_w	:	Width of fire compartment opening $[m]$
w	:	Velocity component in z direction $[m/s]$
Δx	:	Grid spacing $[m]$
$\Delta \mathbf{x}$	:	Vector of grid spacings $\{\Delta x, \Delta y, \Delta z\}$
$\mathbf{x}$	:	Position vector $\mathbf{x} \in \{x, y, z\}$ $[m]$
x	:	X position $[m]$

x_{fb}	:	Position of fire base $[m]$
x_i	:	X position at the discrete point i
Y	:	Mass fraction of gas mixture $[kg/kg]$
Y_F	:	Mass fraction of fuel $[kg/kg]$
Y_F^I	:	Mass fraction of fuel in the fuel stream $[kg/kg]$
Y_i	:	Mass fraction of i'th species $[kg/kg]$
Y_l	:	Mass fraction of l'th species $[kg/kg]$
Y_O	:	Mass fraction of oxygen $[kg/kg]$
y	:	Y position $[m]$
Z	:	Mixture fraction [1]
Z_f	:	Mixture fraction at the flame sheet [1]
z	:	Z position $[m]$
z	:	Rising height $[m]$
z_0	:	Distance from virtual origin to fire base $[m]$
z_e	:	Elevation of spill edge $[m]$
z_l	:	Rising height above spill edge $[m]$
z_{sl}	:	Location of lower boundary condition in fire compartment $[m]$

Subscripts

a	:	Property of the vena contracta
bf	:	Property of the bulk flow
cj	:	Position in ceiling jet
e	:	Spill edge position
f	:	Full-scale model
h	:	Grid spacing
h	:	Horizontal vent
I	:	Cell center index in x direction
i	:	Cell face or vertex index in x direction
i	:	Interior property (usually in fire compartment)
∞	:	Ambient property
J	:	Cell center index in y direction
j	:	Cell face or vertex index in y direction
K	:	Cell center index in z direction
k	:	Cell face or vertex index in z direction
l	:	Position in spill plume
m	:	Scale model
p	:	Position in axisymmetric plume
w	:	Position in compartment opening
v	:	Vertical vent

Superscripts

$\bar{\phi}$	:	Average value of ϕ
$\tilde{\phi}$	:	Filtered property ϕ
f	:	Full vent
n	:	Time index
p	:	Simple passive vent

Greek

χ_r	:	Radiative fraction [1]
Δ	:	Filter width $[m]$
δ	:	Thickness of surface material $[m]$
ϵ_{ih}	:	Discretization error for solution obtained with grid spacing ih
$\tilde{\epsilon}_{ih}$	:	Relative discretization error for solution using grid spacing h
ϵ_i	:	Local Courant number for $i \in \{u, v, w\}$ [1]
$\kappa(\mathbf{x}, \mathbf{s})$	:	Absorption coefficient [1]
κ_m	:	Profile correction factor applied in approach flows (κ_m=1.3)
λ	:	Wavelength $[m]$
μ	:	Viscosity of the gas mixture $[kg/(m * s)]$
μ_0	:	Viscosity in fluid at rest and ambient temp. $[kg/(m * s)]$
μ_{LES}	:	Modeled viscosity (LES model) $[kg/(m * s)]$
ν_F	:	Stoichiometric coefficient of fuel [1]
ν_O	:	Stoichiometric coefficient of oxygen [1]
Ω	:	Integration domain $[m^3]$
ω	:	Vorticity vector $\omega = [\omega_x, \omega_y, \omega_z]$ $[s^{-1}]$
ω	:	Solid angle
Φ	:	Exact solution to (system of) PDE(s)
$\phi(x)$	:	Continuous differentiable function
ϕ_h	:	Approximate solution to PDEs obtained with grid spacing h
ρ	:	Gas density $[kg/m^3]$
$\tilde{\rho}$	:	Local control volume core density $[kg/m^3]$
ρ_s	:	Density of solid $[kg/m^3]$
ρ_∞	:	Ambient gas density $[kg/m^3]$
$\bar{S}_ij$	:	Strain rate $[1/s]$
σ	:	Stefan Boltzmann's constant $[5.67 * 10^{-11} kW/(m^2 * K^4)]$
Θ	:	Temperature above ambient $[K]$
Θ_{so}	:	Smoke layer temperature above ambient in opening $[K]$
Θ_{cw}	:	Temperature above ambient below the ceiling $[K]$
τ	:	Viscous stress tensor $[N/m^2]$
τ	:	Characteristic time scale $[s]$

List of Figures

1.1 Axisymmetric plume in atrium. 19
1.2 Spill plume in atrium. 19

2.1 Interpretation of the energy boundary condition. 31
2.2 Interpretation of the velocity boundary condition. 33
2.3 Interpretation of the passive boundary condition. 35
2.4 Interpretation of the symmetry boundary condition. 36
2.5 Computational grid applied in FDS. 37
2.6 Typical smoke flow in atrium smoke management design. 44
2.7 Axisymmetric plume region: CFD model. 51
2.8 Other regions: CFD model. 52
2.9 Axisymmetric plume region. 53
2.10 Axisymmetric plume region: Temperature profiles. 54
2.11 Axisymmetric plume region: W velocity profiles. 55
2.12 Axisymmetric plume region: Convergence trends. 57
2.13 Axisymmetric plume region: Order of numerical method. 58
2.14 Axisymmetric plume region: Width of temperature profile b. . . . 60
2.15 Axisymmetric plume region: Validation with simple correlations for mass flow rates $\dot{m}_l$. 61
2.16 Approach flow region. 63
2.17 Approach flow region: Temperature profiles. 64
2.18 Approach flow region: W velocity profiles. 65
2.19 Approach flow region: Convergence trends. 66
2.20 Approach flow region: Order of numerical method. 67
2.21 Approach flow region: Order of numerical method. 69
2.22 Rotation region. 70
2.23 Rotation region: Convergence trends and order p of numerical method. 72
2.24 Spill plume region. 73
2.25 Spill plume region: Temperature profiles. 74
2.26 Spill plume region: W velocity profiles. 75
2.27 Spill plume region: Convergence trends. 77
2.28 Spill plume region: Width of core plume b. 78
2.29 Spill plume region: Grid size $\Delta\mathbf{x}$ as a function of rising height z_l. 79
2.30 Spill plume region: Order of numerical method. 80

2.31 Spill plume region: Validation with simple correlations for mass flow rates $\dot{m}_p$. 84

3.1 Basic smoke flow from a fire on a floor opening up to a tall large space (atrium). 88
3.2 Nomenclature in approach flows. 90
3.3 Fire compartment applied in the experimental small-scale approach flow program. 94
3.4 Configuration W: Geometry of small-scale experimental setup. All dimensions in m. 95
3.5 Configuration WO: Geometry of small-scale experimental setup. All dimensions in m. 96
3.6 Experimental burner setup. 97
3.7 Measuring positions designated THCP. All dimensions in m. . . . 99
3.8 CFD model: Configuration W. 105
3.9 CFD model: Configuration WO. 106
3.10 B4138-108 - Small-scale: Temperature profiles at THCP0 and THCP±3.110
3.11 B4138-108 - Small-scale: U velocity profiles at THCP0 and THCP±3.110
3.12 B4138-108: Assessing impact from including heat conduction and radiation in the CFD model. 111
3.13 Reynolds number in NRCC tests. 112
3.14 Conservation of energy in CFD model: Input convective heat release rate $\dot{Q}_c$ vs. $\dot{Q}_{c,w}$ in the compartment opening. 113
3.15 Conservation of energy: CFD model vs. experimental test, $\dot{Q}_{c,w}$ in the compartment opening. 114
3.16 Comparing modeling and experiment: Temperature profiles at location THCP0. 116
3.17 Symmetric flow properties in approach flows: Temperature profiles at THCP±3. 117
3.18 Comparing modeling and experiment: Temperature profiles at location THCP6. 118
3.19 Comparing modeling and experiment: Velocity profiles at location THCP0. 120
3.20 Symmetric flow properties in approach flows: Velocity profiles at THCP±3. 121
3.21 Comparing modeling and experiment: Velocity profiles at location THCP6. 122
3.22 B4138-XXX: Mass flow rates per unit length in compartment opening. 124
3.23 B4138-XXX: Total mass flow rates. 125
3.24 B4138-XXX: Smoke layer depth in the compartment opening. . . 126

4.1 Full-scale CFD model: Configuration W. 135
4.2 Full-scale CFD model: Configuration WO. 136

4.3 B4138-108: Assessing impact from including radiation in the full-scale CFD model. . . . 138
4.4 Comparing modeling and experiment: Temperature profiles at location THCP0. . . . 139
4.5 Comparing modeling and experiment: Velocity profiles at location THCP0. . . . 140
4.6 B4138-{105-108}: Scaling of heat flow rate. . . . 141
4.7 B4138-{105-108}: Scaling of mass flow rate. . . . 142

5.1 CFD model: Full-scale approach flow setup. . . . 147
5.2 Conservation of energy in the CFD model: Convective heat release rate input $\dot{Q}_c$ vs. $\dot{Q}_{c,w}$ in the compartment opening. . . . 151
5.3 Downstand $d_d = 0$ m : Mass flow rates per unit length. . . . 153
5.4 Downstand $d_d = 1$ m: Mass flow rates per unit length. . . . 154
5.5 Mass flow rate dependency on location of fire base. . . . 155
5.6 Smoke layer depth dependency on location of fire base. . . . 155
5.7 Nomenclature adopted in deriving the mass flow rate in approach flows. . . . 157
5.8 Correlating mass flow rates in the compartment opening $\dot{m}_w$. . . . 159
5.9 Correlating smoke layer depths in the compartment opening d_w. . 160
5.10 Testing new approach flow correlations. . . . 161
5.11 Testing new approach flow correlations - close up. . . . 162
5.12 Evaluating mass flow rates predicted by the method in Eqn. (5.5.8). 163

6.1 CFD model: Full-scale spill plume setup, vertical section. . . . 173
6.2 CFD model: Full-scale spill plume setup, horizontal section. . . . 174
6.3 Conservation of energy in CFD model: Convective heat flow in the spill plume $\dot{Q}_c$. . . . 177
6.4 WOSP075-XXX-XX-BSP: Lateral mean temperature distributions. 178
6.5 Edge erosion in wide spill plumes. . . . 180
6.6 Lateral mass flow rate distributions as a function of temperature cut-off filter magnitude. . . . 181
6.7 Cross-sectional mass flow rates per unit length. . . . 182
6.8 WOSP075-XXX-ND-BSP: Lateral mean temperature distributions. 184
6.9 WOSP025-087-ND-BSP, $D_{fb} = 7.8$ m, $W_w = 87.2$ m, $d_d = 0$ m: Lateral mean temperature distributions. . . . 185
6.10 WOSP025-087-ND-BSP, $D_{fb} = 7.8$ m, $W_w = 87.2$ m, $d_d = 0$ m: Lateral mass flow rate per unit length distributions. . . . 185
6.11 Spill plume transformation: Aspect ratio D_l/W_l. . . . 186
6.12 Nomenclature adopted in deriving the spill plume mass flow rate. 187
6.13 Total mass flow rate in spill plume $\dot{m}_l$. . . . 189
6.14 Mass flow rate in lower spill plume $\dot{m}_l$ - close up. . . . 190
6.15 Fitted vs. predicted mass flow rates in the lower spill plume. . . . 190
6.16 Correlating mass flow rate at elevation of spill edge $\dot{m}_e$ to approach flow mass flow rate $\dot{m}_w$. . . . 192

6.17 Total mass flow rate in intermediate spill plume region $\dot{m}_l$. 193
6.18 Entrainment coefficients in the intermediate spill plume region $C_{l,int}$ using the simple spill plume method Eqn. (6.6.5). 194
6.19 Entrainment coefficients in the intermediate spill plume region $C_{l,int}$ using the modified spill plume method Eqn. (6.6.6). 195
6.20 Testing spill plume methods against predicted net mass flow rates $\dot{m}_{l,net}$. 198
6.21 Testing spill plume methods against predicted net mass flow rates $\dot{m}_{l,net}$. 199
6.22 Testing spill plume methods against predicted net mass flow rates $\dot{m}_{l,net}$. 200
6.23 Photo taken from the base of the ten-story atrium facility in Almonte (ON, Canada) by the author during an internship at NRCC, Fire Research Program in 2005. 203

7.1 Example of the formation of a vena contracta outside the buoyancy driven exhaust vent. 206
7.2 Nomenclature applied for the horizontal vent. 207
7.3 Nomenclature applied for the vertical vent. 209
7.4 CFD model: Horizontal vent, full outflow. 215
7.5 CFD model: Vertical vent, full outflow. 216
7.6 CFD model: Horizontal and vertical vents, simple passive boundary condition applied in modeling the vent. 217
7.7 Grid convergence study of horizontal vent flow. 218
7.8 Calculating the distance to the vena contracta h_a. 220
7.9 CFD model: Horizontal and vertical vents, simple passive boundary condition applied in modeling the vent. 223
7.10 Predicted distances to the vena contracta h_a for the horizontal vent. 224
7.11 Comparing coefficients of discharge, derived from the universal flow formula Eqn. (7.2.9a) or the simple formula Eqn. (7.2.10a) applied in EN 12101-2. 224
7.12 Mass fluxes in horizontal and vertical exhaust vents. 225
7.13 Horizontal vent: Full-vent. 226
7.14 Comparing the universal flow formula proposed by Emmons (1997) in Eqn. (7.2.6) with CFD predictions of mass flux through the horizontal vent. 227
7.15 Horizontal vent: Quality of correlations. 230
7.16 Horizontal vent. 231
7.17 Vertical vent: Quality of correlations. 232
7.18 Vertical vent. 234

A.1 Perpendicular grid interface: Absolute temperature T. 248
A.2 Parallel grid interface: Absolute temperature T. 248
A.3 Perpendicular grid interface: W velocity W. 249
A.4 Parallel grid interface: W velocity W. 249

B.1 Temperature predictions: Assessing impact of the wall velocity, u_τ, boundary condition on the ceiling jet flow. 252
B.2 Velocity predictions: Assessing impact of the wall velocity, u_τ, boundary condition on the ceiling jet flow. 252

C.1 B4138-108 - Small-scale: Temperature profiles. 256
C.2 B4138-108 - Small-scale: U velocity profiles. 257

D.1 B4138-105 - Small-scale: Temperature profiles. 260
D.2 B4138-106 - Small-scale: Temperature profiles. 261
D.3 B4138-107 - Small-scale: Temperature profiles. 262
D.4 B4138-108 - Small-scale: Temperature profiles. 263
D.5 B4138-109-100 - Small-scale: Temperature profiles. 264
D.6 B4138-109-150 - Small-scale: Temperature profiles. 265
D.7 B4138-109-200 - Small-scale: Temperature profiles. 266

E.1 B4138-105 - Small-scale: U velocity profiles. 268
E.2 B4138-106 - Small-scale: U velocity profiles. 269
E.3 B4138-107 - Small-scale: U velocity profiles. 270
E.4 B4138-108 - Small-scale: U velocity profiles. 271
E.5 B4138-109-100 - Small-scale: U velocity profiles. 272
E.6 B4138-109-150 - Small-scale: U velocity profiles. 273
E.7 B4138-109-200 - Small-scale: U velocity profiles. 274

F.1 B4138-105: Temperature profiles. 276
F.2 B4138-106: Temperature profiles. 277
F.3 B4138-107: Temperature profiles. 278
F.4 B4138-108: Temperature profiles. 279

G.1 B4138-105: U velocity profiles. 282
G.2 B4138-106: U velocity profiles. 283
G.3 B4138-107: U velocity profiles. 284
G.4 B4138-108: U velocity profiles. 285

H.1 B4138-108 - Full-scale: Temperature profiles. 288
H.2 B4138-108 - Full-scale: U velocity profiles. 289

J.1 WOSP075-XXX-XX-BSP: Lateral mean temperature distributions. 296
J.2 WOSP025-XXX-XX-BSP: Lateral mean temperature distributions. 297

K.1 WOSP075-XXX-XX-BSP: Lateral mass flow rate distributions. . . 300
K.2 WOSP025-XXX-XX-BSP: Lateral mass flow rate distributions. . . 301

L.1 WOSP075-XXX-XX-BSP: Cross-sectional mass flow rate distributions. 304
L.2 WOSP025-XXX-XX-BSP: Cross-sectional mass flow rate distributions. 305

List of Tables

2.1 Grid convergence study: List of simulations. 47
2.2 Boundary conditions according to designations in Figures 2.7 and 2.8. 49
2.3 Measured quantities and positions relative to the dimensions in Figure 2.7 and Figure 2.8. 49
2.4 Grid convergence study: Model input parameters. 50

3.1 Small-scale approach flows: List of tests conducted. 93
3.2 Temperature: Measuring positions. 98
3.3 Velocity: Measuring positions. 100
3.4 Movable north thermocouple tree position in seconds from start of test. 101
3.5 Small-scale approach flow modeling: List of simulations. 102
3.6 Characteristic length scales in the small-scale approach flow model. 103
3.7 Grid spacings according to designations in Figures 3.8 and 3.9. . . 104
3.8 Boundary conditions according to designations in Figures 3.8 and 3.9. 104
3.9 Measured quantities and positions applied in the small-scale approach flow CFD model relative to dimensions in Figure 3.8 and Figure 3.9. 104
3.10 Small-scale approach flow setup: Model input parameters. 108
3.11 Thermal properties of the modeled insulating ceramic fiber material lining walls and ceiling in the fire compartment. 109

4.1 Full-scale properties of CFD model scaled ∼1.55/5 134
4.2 Characteristic length scales in the full-scale approach flow model. 134
4.3 Grid spacings in the full-scale CFD-model according to designations in Figures 4.1 and 4.2. 137

5.1 Full-scale approach flow modeling: List of simulations. 148
5.2 Characteristic length scales in the full-scale approach flow model. 149
5.3 Grid spacings according to designations in Figure 5.1. 149
5.4 Boundary conditions according to designations in Figure 5.1. . . . 149
5.5 Measured quantities and positions applied in the full-scale approach flow CFD model relative to dimensions in Figure 5.1. . . . 149
5.6 Full-scale approach flow setup: Model input parameters. 150

6.1 Full-scale wide opening spill plume modeling: List of simulations. 169
6.2 Characteristic length scales in the full-scale approach flow model. 170
6.3 Grid spacings according to designations in Figures 6.1 and 6.2. . . 171
6.4 Boundary conditions according to designations in Figures 6.1 and 6.2. 173
6.5 Measured quantities and positions applied in the full-scale approach flow CFD model relative to dimensions in Figures 6.1 and 6.2. 175
6.6 Full-scale approach flow setup: Model input parameters. 176
6.7 Computed mass flow rates in approach flow $\dot{m}_w$ and at the elevation of the spill edge $\dot{m}_e$. 191

7.1 Full-scale vent flow modeling: List of simulations. 213
7.2 Boundary conditions according to designations in Figures 7.4 and 7.5. 214
7.3 Full-scale vent flow modeling: Grid convergence study. 218
7.4 Grid spacings according to designations in Figures 7.4 and 7.5. . . 219
7.5 Measured quantities and positions applied in the full-scale vent flow CFD models relative to dimensions in Figures 7.4 and 7.5. Here $\mathbf{x} = \{x, y, z\}$ represents a point position. 219
7.6 Full-scale vent flow setup: Model input parameters. 221

B.1 Simulations addressing impact of wall velocity boundary condition u_τ. Predictions are depicted in Figure B.1 and B.2. 251

I.1 List of simulations scaled 4/5. 292
I.2 List of simulations scaled 3/5. 293

Chapter 1

Introduction

1.0.1 Atrium Smoke Management Design

After the introduction of performance based fire codes in the Danish Building Code in 2004, the demand for fire safety design of large tall spaces such as atria, open plan offices and shopping malls is ever-increasing. These spaces are often referred to as simply an atrium with communicating floors opening up into the tall space. Because of the large undivided space and extremely long routes of egress, atria seldom conform to prescriptive building codes, thus requiring a fire safety design analysis to describe the fire safety measures that need to be installed in the building in order to achieve an adequate level of fire safety. The present study addresses the principles applied in the design of atrium smoke management systems with the objective of providing new and modified methods for engineering principles in fire safety consulting.

The research topics in the present thesis are the result of the author's experience with shortcomings in the existing engineering principles for smoke management design.

1.0.2 Grid Quality Design

CFD simulations are often adopted in atrium smoke management design because of it's superiority in predicting smoke and heat flows in multi zones as opposed to the two zone thermal models only considering the lower ambient and hot upper zone of a fire compartment. The grid design and resolution is paramount in achieving qualitatively and quantitatively good results.

Assessing the quality of the grid resolution in a typical atrium setup can be very time consuming, since it requires systematically refined grids to determine when the solution is grid independent. As each halving of the grid size requires on the order of 16 times longer computational time, the grid convergence study can be very time consuming and hence often subjected to reduced focus in fire safety engineering. The impact of a grid dependent solution can not be underestimated since it can lead to erroneous conclusions and non-conservative design. In the present study a simple method to assess adequate grid resolutions is presented, supplemented with rules of thumb.

Having assessed the quality of the grid resolutions, the model must be validated against experimental data. This is obviously almost impossible in fire safety design, since the building has still to be erected. Thus the modeler is encouraged to validate the applied CFD model against existing engineering relations within their range of application. Conducting this form of simple validation study has been difficult for approach flows and spill plumes emanating from wide openings, because the application range of the existing engineering relations were limited to compartment openings up to $W_w \leq 14$ m. The proposed correlations for wide opening approach flows and spill plumes in the present study are thought of as being applicable in simple validation studies of CFD models in fire safety design, thus obliging the shortcomings of the existing correlations. Before determining the exhaust capacities in the atrium, the modeler is encouraged to validate the applied CFD model against the proposed correlations by subdividing the entire flow domain into individual flow regions, where appropriate engineering relations can be applied, e.g. axisymmetric and spill plume regions.

1.0.3 Smoke Flows Emanating From Wide Openings

Atrium smoke management design comprises the determination of adequate exhaust capacity to maintain tenable conditions at least during the required time of egress, and additionally provide fire fighters with appropriate conditions for fighting the fire, e.g. prevent flashover (usually not a problem in large atria) and increase visibility. Exhaust capacities are determined from the amount of smoke that must be removed from the atrium to maintain tenable conditions. Smoke production is calculated from the entrainment into the smoke flowing from the fire and rising to the ceiling from where it is exhausted. A thorough introduction to different atrium fire safety designs are provided in Morgan, et al. (1999).

In the determination of adequate exhaust capacities usually at least two type of fire scenarios are addressed, a fire in the base of the atrium, see Figure 1.1, and a fire in a communicating space from where smoke migrates into the atrium space and rises to ceiling, see Figure 1.2. The production of smoke from a fire on the base of the atrium can be calculated from numerous engineering relations for mass flow rates in axisymmetric thermal plumes, see e.g. Morgan et al. (1999) or Klote & Milke (2002).

The fire scenario in the communicating space is depicted in Figure 1.2. The flow is described as an initial axisymmetric buoyant plume entraining air as it rises to the bottom of the smoke layer, a ceiling jet/approach flow under the ceiling toward the compartment opening where entrainment is minimal since there is no rising height, a rotation region where the horizontal approach flow is rotated to a vertical position during which air is entrained, a thermal spill plume extending to the bottom of the smoke layer under the ceiling and subjected to severe entrainment because of it's large perimeter, and finally the formation of a smoke layer under the ceiling. Engineering relations exist for calculating the mass flow rates in approach flows and spill plumes from openings up to $W_w \leq 14$ m, beyond which no validation data of the existing correlations exist.

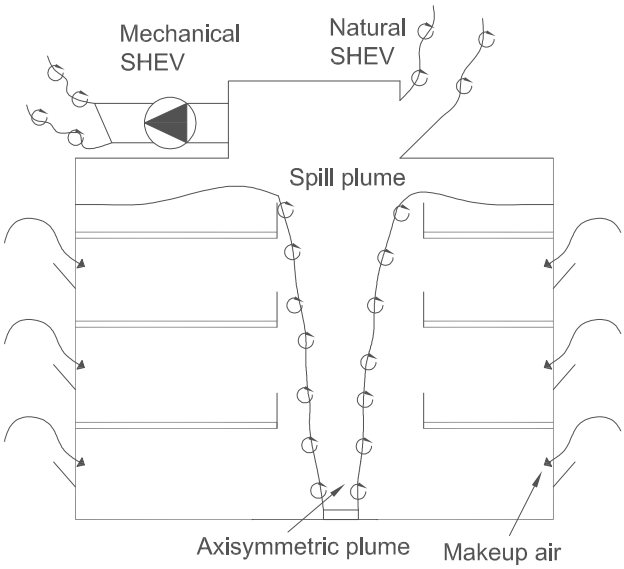

Figure 1.1 *Axisymmetric plume in atrium.*

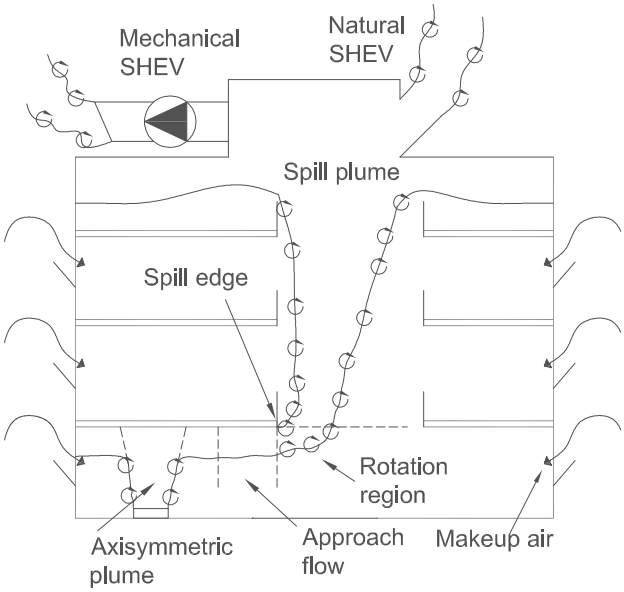

Figure 1.2 *Spill plume in atrium.*

Outside the application range of the existing engineering relations, CFD modeling is usually applied, substantially increasing computation time and hence the cost of design. To reduce design costs and provide simple validation data for CFD modeling, the present research aims at developing new engineering relations for mass flow rates in approach flows and spill plumes from wide compartment openings $W_w > 14$ m. This would considerably reduce the costs associated with calculating simple estimates for exhaust rates to be used in tender material or final design.

1.1 Buoyancy Driven Vent Flows

Exhausting smoke from the smoke layer in an atrium can be done by mechanical or buoyancy driven vents, see Figure 1.2, designated smoke and heat exhaust ventilators (SHEVs). In the calculation of adequate mechanical exhaust capacities, the mass flow rate through the vent is simply balanced with the smoke production in the upstream flow. For buoyancy driven flows this is a little more complicated because the flow through the vent is driven by buoyancy and pressure differences across the vent. Smoke being exhausted through a buoyancy driven vent is subjected to a vena contracta in the outflow, reducing the capacity of the vent. In engineering relations and hence also two zone fire models, the mass flow rate out of the vent is reduced by a coefficient of discharge to account for contraction effects.

In CFD modeling computational costs are of great importance, thus the computational domains are reduced to only model the most important characteristics of the smoke flow. This often means that any flow outside the building envelope is disregarded including wind effects and the vena contracta in buoyancy driven vents. Instead simple boundary conditions of e.g. constant pressure and ambient temperature are applied. This type of boundary condition does not take the formation of a vena contracta into consideration, i.e. over predicting the exhaust capacity of the vent leading to a non-conservative fire safety design. The present research proposes a coefficient of correction for the geometrical vent area of the passive vent when applying simple passive boundary conditions for buoyancy driven vents.

Chapter 2

Grid Quality Control in CFD Fire Modeling

2.1 Introduction

With the introduction of performance-based fire codes, building designs have become more complex with respect to fire safety, and fire modeling is usually the only way to asses the fire safety level of the building. In this context fire modeling is considered the modeling of fire behavior; physical full-scale/small-scale testing, mathematical modeling applying engineering relations and mathematical modeling applying numerical techniques. Physical full-scale testing is usually not practicable due to great expenses and lack of test facilities that can accommodate e.g. a full size atrium mock-up. Small-scale testing adopting the principles of Froude modeling can be a good alternative to full-scale testing as long as the flow can be considered fully turbulent, see e.g. Quintiere (1989). Numerous researchers have developed engineering relations for a number of common modeling problems in fire safety engineering, e.g. models for the axisymmetric plume (e.g. Heskestad (1986)), the spill plume (e.g. Morgan et al. (1999)), the ceiling jet (e.g. Alpert (1972)) etc.

In recent years increased computer speed at a lower cost has opened up for the use of computational fluid dynamics (hereafter designated CFD) in mathematical fire modeling. The complexity of most CFD models requires intensive attention to the model setup and hence should be performed by an informed modeler. A common misconception among non-informed users of CFD fire models is that a model can safely be adopted for a particular problem as long as the CFD model is widely acknowledged and widely validated. However this may not hold true. CFD models are verified and validated with a certain set of input parameters that are chosen specifically for that particular problem, i.e. changing the parameters and/or the grid design can greatly influence the results. Several publications address quality control of computational fluid dynamics within different engineering/research disciplines. Soerensen & Nielsen (2003) addresses quality control of computational fluid dynamics in indoor environments emphasizing on the influence of grid design and differencing schemes. In fire safety engineering Klote

(2002) attempts to outline an approach in reviewing CFD analyses stressing the importance of validating the numerical results with experimental data. One of the strong assets of CFD is the diverse scope of application, with general purpose codes being applied in modeling anything from aerodynamics over creeping flow, chemical reacting flows, meteorological flows and also fire dynamics. The diverse application of CFD can also be considered one of the pitfalls, as an aeronautical engineer does not necessarily posses the correct skills to review (nor model) a fire dynamical CFD analysis. CFD modeling in different engineering disciplines calls for different sub-models e.g. radiation, combustion, turbulence etc., hence it can be difficult to outline an exhaustive best-practice for CFD modeling. An attempt can be found in Casey & Wintergerste (2000).

Conducting CFD fire modeling in fire safety engineering can be quite a dilemma. On one hand the modeler is looking for results of high quality and on the other hand computational costs (i.e. CPU time) must be taken into consideration. Arriving at an acceptable solution can be a tedious job; identifying and describing boundary conditions (e.g. design fires, passive/active fire protection measures[1]), performing numerous sensitivity analyses on input parameters, studying the influence of grid design on the results and validating the numerical results with experiment. Hadjisophocleous & McCartney (2005) provides guidelines on CFD fire and smoke modeling addressing grid design, combustion/soot modeling and velocity boundary conditions.

A grid sensitivity study has been published by Ma & Quintiere (2003) addressing the effect of grid resolutions in axisymmetric plumes. In a publication by Bounagui, et al. (2003) it is proposed that > 14 control volumes across the characteristic diameter of the fire D_f is required to adequately resolve the axisymmetric plume. Attempts to provide guidelines for resolutions of other fire dynamical flows are sparse or non-existing.

2.2 Present Research

The present research intends to assess grid design in CFD fire modeling of smoke flows from an axisymmetric plume, approaching a wide opening and spilling into an atrium, a design fire scenario of great importance in the design of atrium smoke management systems. The research is conducted through a numerical study applying the CFD fire model *Fire Dynamics Simulator ver. 4.06* (FDS). The objectives of the research are:

Describe applied CFD model - This is important in identifying assumptions and approximations of relevance to designing a good grid in CFD fire modeling.

Define flow regions - Characteristics of flows from fires can to a large extent be divided into certain flow regions. Predictions downstream are

[1] E.g. smoke and heat exhaust ventilators (SHEVs), fire sprinklers and passive fire protection measures.

dependent on upstream grid quality, hence each flow region must be adequately resolved to provide reliable predictions downstream.

Study grid convergence - Requirements for grid convergence in each identified flow region are determined.

Simple validation of model - Predictions using a CFD model are compared to predictions by engineering relations to assess grid resolutions required to meet the accuracy associated with the simple engineering relations.

Propose improved guidelines for grid design - Guidelines for grid design in fire safety engineering are essential in obtaining reliable predictions and can save valuable time in designing CFD models.

2.3 Errors in CFD Fire Modeling

For validation purposes in applied fire safety engineering, as opposed to code development in fire research, errors in CFD fire models can be considered to originate from the following model components:

The mathematical model consists of partial differential equations (PDEs) describing the hydrodynamic model, combustion model and thermal radiation model (list is not exhaustive) and sets of boundary conditions. The quality of the mathematical model depends on how well understood the physical and chemical phenomena taking place in a fire are understood and to what extent they can be put into mathematical form.

The discretization method approximates the differential equations at discrete points in time and space. A typical differencing method in CFD fire modeling is to approximate the differential equations by a system of algebraic equations adopting the finite volume method (FVM). Discretizing the differential equations introduces a grid of discrete points in the model, a grid which the produced results are highly dependent on.

The solution method solves the system of algebraic equations marching the solution through time. Due to the strong nonlinear nature of the algebraic equations, the system of equations is solved using an iterative scheme, e.g. predictor/corrector scheme.

The convergence criteria in both steady and unsteady flows must ensure that the solution is converged, i.e. has reached a steady solution or converges at each time step respectively.

In assessing the quality of a CFD analysis each of the above mentioned model components should be validated. Usually the mathematical model can only be validated by verifying that a grid independent solution, i.e. a solution that is independent of a further grid refinement, approaches the experimental data. A sensitivity analysis on the input parameters and boundary conditions can usually

provide information used in judging if the mathematical model behaves accordingly. Considering the aforementioned it is important to have experimental data available for data validation, for instance discrete experimental data from full-scale/reduced-scale tests or validated engineering relations.

Before assessing the mathematical model the quality of the discretization must be addressed. Examining the spatial and temporal convergence of CFD simulations are straightforward and usually termed a grid convergence study[2]. Refining the grid (spatial and temporal) successively should force the discretization errors to asymptotically approach zero, computer round-off error excluded, provided that the solution is obtained in the asymptotically range, see Roache (1994). Doubling the spatial resolution usually leads to a analogous increase in the temporal resolution:

$$\begin{aligned} N_{T,n} &= n_x n_y n_z n_t \\ N_{T,2n} &= 2^4 n_x n_y n_z n_t \end{aligned}$$

where N_T [1] is the total number of computational grid cells and n_i [1] is the number of grid cells in each of the spatial directions $i \in \{x, y, z\}$ and in time t [s]. Hence it can be seen that halving the grid spacing in each of the four mathematical dimensions yield a 16-fold increase in the number of total computational grid cells, approximately increasing the computational time at the same rate.

For a CFD analysis of a normal size building, it is clear that even a few successively grid refinements lead to disproportionate computation times. Typical CFD fire models in applied fire safety engineering are setup with an expected run time of maximum a few days. Doubling the grid resolution (temporal and spatial) in the entire computational domain would lead to computation times ranging from weeks to months on the same processing unit. Running the model in parallel mode would obviously reduce run times, but also increase demand for data processing units (nodes). Doubling the resolution does not necessarily ensure that the model operates in the asymptotically range, i.e. where it is expected that the discretization error asymptotically approaches zero. It is difficult to judge convergence based on only two points, hence more than one grid refinement must be conducted. Acknowledging the difficulties in performing a grid refinement study on the entire computational domain, it is suggested, as will be shown later, that flow regions expected to carry most of the information in the flow, are subjected to a thorough grid convergence analysis, leading to these flow regions being adequately resolved, whereas flow regions remote from the fire or point of interest are only coarsely resolved.

The solution methods are usually based on acknowledged numerical solvers subjected to intense benchmarking and validation on simple numerical problems. The task of the modeler is to choose the right solver for the problem and supplying input parameters adequate to arrive at a converged solution, i.e. relaxation factors, initial time step, individual time steps (for fixed time step solvers) and convergence criteria (list is not exhaustive). Arriving at a converged solution,

[2]Also known as a *grid refinement study*.

this being an unsteady or steady solution, is paramount to the quality of a CFD analysis. The criteria for convergence should be chosen relative to the magnitude of the solution. For steady state simulation the modeler must make sure that progressing the temporal iteration/time stepping does not lead to a solution that does not meet the convergence criteria. In unsteady modeling the solution must evidently converge at each time step in order to arrive at the correct solution to the discretized PDEs. A list of widely acknowledged solution methods can be found in Ferziger & Perić (2002).

2.4 Description of Applied CFD Model

CFD fire modeling in this thesis is carried out using *Fire Dynamics Simulator ver. 4.06* (abbreviated FDS) developed by *National Institute of Standards and Technology*, USA, (abbreviated NIST) in cooperation with *VTT Building and Transport*, Finland. A comprehensive documentation for the CFD fire model, explaining assumptions and approximations behind the mathematical model and the numerical solution method can be found in McGrattan (2005a). A validation and verification study of the CFD model, including an extensive verification with experimental data, has been published in Salley & Kassawara (2007).

FDS is a special purpose CFD model for modeling fluid flows from building fire combustion processes. This section will provide a brief overview of the CFD model with emphasis on sub-models and boundary conditions relevant for this thesis.

2.4.1 Hydrodynamic Model

FDS solves the conservation equations for mass (Eqn. (2.4.1a)), species (Eqn. (2.4.1b)), momentum (Eqn. (2.4.1c)) and energy (Eqn. (2.4.1d)):

$$\frac{\partial \rho}{\partial t} + \nabla \cdot \rho \mathbf{u} = 0 \tag{2.4.1a}$$

$$\frac{\partial}{\partial t}(\rho Y_l) + \nabla \cdot \rho Y_l \mathbf{u} = \nabla \cdot \rho D_l \nabla Y_l + \dot{m}_l''' \tag{2.4.1b}$$

$$\rho \left(\frac{\partial \mathbf{u}}{\partial t} + (\mathbf{u} \cdot \nabla)\, \mathbf{u} \right) + \nabla p = \rho \mathbf{g} + \mathbf{f} + \nabla \cdot \tau \tag{2.4.1c}$$

$$\frac{\partial}{\partial t}(\rho h) + \nabla \cdot \rho h \mathbf{u} = \frac{\partial p}{\partial t} + \mathbf{u} \cdot \nabla p - \nabla \cdot \mathbf{q}_r + \nabla \cdot k \nabla T \ldots + \sum_l \nabla \cdot h_l \rho D_l \nabla Y_l \tag{2.4.1d}$$

Here t is time $[s]$, $\{x, y, z\}$ is the coordinate positions $[m]$, ρ is the gas density $[kg/m^3]$, $\mathbf{u}$ is the velocity vector $[m/s]$, Y_l is the mass fraction of species l $[kg/kg]$, D_l is the diffusion coefficient of species l $[m^2/s]$, $\dot{m}_l'''$ is the mass production per unit volume of l'th species $[kg/(s * m^3)]$, h_l is the enthalpy of species l $[kJ]$, p is the pressure $[Pa]$, $\mathbf{g}$ gravity vector $[m/s^2]$, $\mathbf{f}$ is the external forces exerted on the subvolume (not gravity) $[N/m^3]$, τ is the viscous stress tensor $[N/m^2]$, h is

the enthalpy $[kJ]$, h_l is the enthalpy of species l $[kJ]$, T is the temperature $[K]$, $\mathbf{q}_r$ is the radiative heat flux vector $[kW/(m^2)]$ and k is the thermal conductivity $[kW/(m*K)]$.

The pressure p is decomposed into a background component p_0 $[Pa]$, a hydrostatic component and a flow-induced component:

$$p = p_0 - \rho_\infty g z + \tilde{p} \tag{2.4.2}$$

where z is the elevation above a reference level $[m]$, ρ_∞ is the ambient density $[kg/m^3]$, and $\tilde{p}$ is the perturbed pressure $[Pa]$ away from the background and hydrostatic component. The background pressure p_0 can usually be considered constant (the case in this thesis), and the latter two components are small compared to p_0. Hence it is possible to replace the pressure in the equation of state, Eqn. (2.4.3), and in the energy equation, Eqn. (2.4.1d), by the background pressure:

$$p_0 = \rho T R \sum \left(\frac{Y_i}{M_i} \right) = \frac{\rho T R}{M} \tag{2.4.3}$$

where R is the universal gas constant $[8.314\ kJ/(K*mol)]$, M and M_i is the total molecular weight of the gas mixture and i'th species respectively $[kg/mol]$, and Y and Y_i are the mass fractions of the gas mixture and i'th species respectively $[kg/kg]$. Decomposing the pressure means for low-Mach number flows that the density and temperature can be considered inversely proportional, and that acoustic waves are filtered out, bounding the time step size in the solver by the flow speed only.

Adopting the approach outlined in McGrattan (2005a) the momentum equation can be rewritten in the form:

$$\begin{aligned} \frac{\partial \mathbf{u}}{\partial t} - \mathbf{u} \times \omega + \nabla \mathcal{H} + \left(\frac{1}{\rho} - \frac{1}{\rho_\infty} \right) \nabla \tilde{p} = & \frac{1}{\rho} \left((\rho - \rho_\infty) \mathbf{g} \right. \\ & \left. + \mathbf{f} + \nabla \cdot \tau \right) \end{aligned} \tag{2.4.4}$$

where $\omega = [\omega_x, \omega_y, \omega_z]$ is the vorticity vector $[s^{-1}]$ introduced in the vector identity:

$$(\mathbf{u} \cdot \nabla) \mathbf{u} = \frac{\nabla |\mathbf{u}|^2}{2} - \mathbf{u} \times \omega$$

and the head pressure $\mathcal{H}$ $[Pa * m^3/kg]$:

$$\mathcal{H} = \frac{|\mathbf{u}|^2}{2} + \frac{\tilde{p}}{\rho_\infty} \tag{2.4.5}$$

Taking the divergence of the momentum equation Eqn. (2.4.4) and collecting terms:

$$\nabla^2 \mathcal{H} = -\frac{\partial (\nabla \cdot \mathbf{u})}{\partial t} - \nabla \cdot \mathbf{F} \tag{2.4.6}$$

gives the pressure equation, where:

$$\mathbf{F} = -\mathbf{u} \times \omega + \left(\frac{1}{\rho} - \frac{1}{\rho_\infty} \right) \nabla \tilde{p} - \frac{1}{\rho} \left((\rho - \rho_\infty) \mathbf{g} + \mathbf{f} + \nabla \cdot \tau \right) \tag{2.4.7}$$

2.4.2 Turbulence Model

FDS provides two turbulence models; *Direct Numerical Simulation* (DNS) and the *Large Eddy Scale* (LES) model, of which only the LES model is applied in this study. Turbulence in the CFD model is treated as an artifical viscosity μ_{LES} introduced by the turbulence model:

$$\mu = \mu_0 + \mu_{LES} \tag{2.4.8}$$

where μ is the viscosity of the gas mixture $[kg/(m*s)]$, μ_0 is the viscosity in the fluid at rest and at ambient temperature $[kg/(m*s)]$, and μ_{LES} is the LES model viscosity $[kg/(m*s)]$ proposed by Smagorinsky (1963):

$$\mu_{LES} = \rho \left(C_s \Delta\right)^2 \left|\bar{S}\right| \tag{2.4.9}$$

where C_s is an empirical constant (often $C_s = 0.20$), Δ is the filter width $[m]$ on the order of the characteristic length of a subvolume in the model and $\left|\bar{S}\right| = \left(\bar{S}_{ij}\bar{S}_{ij}\right)^{1/2}$. $\bar{S}_ij$ is the strain rate $[1/s]$ of the resolved flow field, i.e. flow on the grid scale[3], see Ferziger & Perić (2002).

Changing the temporal grid spacing affects the eddy viscosity μ_{LES} not only through the filter width Δ, but also through the strain rate of the computed flow field $\bar{S}_ij$. Hence it is evident that the computed flow field and the derived production of smoke are highly dependent on the grid spacing. Basically LES turbulence modeling resolves eddies larger than the filter width Δ (i.e. the characteristic grid spacing), whereas eddies smaller than the filter width are modeled. The bulk flow in CFD fire modeling is considered dominated by the large energy carrying eddies resolved at the grid level, hence the accuracy of the computed flow is considered to be insignificantly affected by the small eddies modeled at the sub-grid scale, but highly affected by the resolution of the large eddies.

As opposed to Reynolds-average Navier-Stokes (RANS) turbulence modeling, LES turbulence modeling does not apply any temporal or spatial averaging, and the accuracy of the prediction of flow quantities increases with reduced filter width, Δ (i.e. reduced grid spacing).

2.4.3 Combustion Model

In this study FDS is set up with a mixture fraction combustion model. The mixture fraction Z is a conserved quantity [1], see Eqn. (2.4.10), carrying information about the quantity of material at any point in the gas mixture that originates from the fuel stream:

$$\rho \left(\frac{\partial Z}{\partial t} + \mathbf{u} \cdot \nabla Z\right) = \nabla \cdot \rho D \nabla Z \tag{2.4.10}$$

Here D is the diffusion coefficient of the gas mixture $[m^2/s]$. The mixture fraction is constructed such that $Z = 1$ in the fuel stream, where the mass fraction of fuel

[3] As opposed to the sub-grid scale.

$Y_F^I = 1kg/kg$, and $Z = 0$ where no fuel exists, i.e. the mass fraction of oxygen takes on it's ambient value, Y_O^∞ $[kg/kg]$:

$$Z = \frac{sY_F - (Y_O - Y_0^\infty)}{sY_F^I + Y_O^\infty} \tag{2.4.11}$$

where Y_F and Y_0 are the mass fractions of fuel and oxygen respectively [1] and:

$$s = \frac{\nu_O M_O}{\nu_F M_F} \tag{2.4.12}$$

where ν_F and ν_O are the stoichiometric coefficients [1] and M_F and M_O molecular weights $[kg/mol]$ of fuel and oxygen respectively.

It is assumed that combustion is mixing-controlled, i.e. controlled by the turbulence, and that oxidation progresses infinitely fast. This assumption leads to the consequence that oxygen and fuel can not co-exist. Rewriting Eqn. (2.4.11):

$$Z_f = \frac{Y_0^\infty}{sY_F^I + Y_O^\infty} \tag{2.4.13}$$

which defines the *flame sheet* Z_f as the two-dimensional surface embedded in three-dimensional space where the combustion process takes place. The flame sheet is the boundary between the flame zone ($Z > Z_f$) and outside the flame zone ($Z < Z_f$). Based on the oxygen consumption rate $\dot{m}_O'''$ $[kg/(s * m^3)]$ at the flame sheet, the local heat release rate $\dot{q}'''$ can be computed following the basis of oxygen calorimetry proposed by Huggett (1980):

$$\dot{q}''' = \Delta H_O \dot{m}_O''' \tag{2.4.14}$$

with ΔH_O being the heat of combustion of oxygen $[kJ/kg]$.

The derivative of the oxygen consumption rate $Y_O(Z)$ is discontinuous at the flame sheet $Z = Z_f$ due to the infinitely fast reaction assumption. This is very challenging to implement numerically, thus the local heat release rate, $\dot{q}''$, is expressed per area of flame sheet through the conservation equation of oxygen mass fraction, see McGrattan (2005a), where the mass low of oxygen $\dot{m}_O''$ is:

$$-\dot{m}_O'' = \left.\frac{dY_O}{dZ}\right|_{Z<Z_f} \rho D_O \nabla Z \cdot \mathbf{n} \tag{2.4.15}$$

Here D_O is the diffusion coefficient of oxygen $[m^2/s]$ and ρ is the density of the gaseous mixture $[kg/m^3]$. The numerical computation methodology for the heat release rate is to first locate the flame sheet (Z_f), then compute the local heat release rate $\dot{q}''$ $[kW/m^2]$:

$$\dot{q}'' = \Delta H_O \dot{m}_O'' \tag{2.4.16}$$

Finally this local heat release rate is distributed to the grid cells cut by the flame sheet.

The combustion model also incorporates a simple model for combustion criteria, based on the findings by Quintiere (1984) and Beyler (2002), used to decide

if combustion conditions are met in the proximity of the flame sheet. The criteria for combustion is based on local temperature and oxygen concentration.

Mass fractions for each of the species comprising the gaseous mixture can be derived from state relations, see McGrattan (2005a).

In coarsely gridded computations, the fire can not be resolved adequately. Large control volumes tend to smear out temperatures and concentrations of fuel and combustion products through enhanced numerical diffusion, underestimating mean flame height and heat release rate (because the combustion criteria are not met), see Ma & Quintiere (2003). Underestimating the height and extent of the flame sheet affects the heat release rate per unit area of flame sheet, $\dot{q}''$, and hence the distribution of energy in the vicinity of the fire. The location of the flame sheet can be changed by modifying the mixture fraction defining the flame sheet Z_f, i.e. introducing an effective mixture fraction at the flame sheet $Z_{f,eff}$ that scales with the resolution of the grid:

$$Z_{f,eff} = \min\left(1, C_Z \frac{D_p^*}{\Delta x}\right) Z_f \tag{2.4.17}$$

here D_p^* is a characteristic length scale of the fire $[m]$, see Section 2.5, Eqn. (2.5.4b), C_Z=0.6 is an empirical constant [1] and Δx is the local grid size $[m]$.

In contrast to some of the other CFD models applied in fire safety engineering, FDS models the fire as a source of combustion reactants from which the local heat release rate is computed. Another widely adopted approach in CFD fire modeling[4] is to model the fire as a source of heat and combustion products, i.e. neglecting the combustion process.

2.4.4 Radiation Model

For the modeling in this study radiative heat transfer is not considered of great importance, because the modeling relates to the convective transport of smoke in plumes and ceiling jets. Applying adiabatic walls yields a conservative estimate for the smoke transport, because no energy is lost by heat conduction through the fire compartment enclosure. However a simple sensitivity analysis to asses influence of radiative heat transfer has been conducted. FDS provides a radiation model based on the *Radiative Transport Equation* (RTE) for an absorbing/emitting and non-scattering medium:

$$\mathbf{s} \cdot \nabla I_\lambda(\mathbf{x}, \mathbf{s}) = \kappa(\mathbf{x}, \lambda)\left[I_b(\mathbf{x}) - I_\lambda(\mathbf{x}, \mathbf{s})\right] \tag{2.4.18}$$

$I_\lambda(\mathbf{x}, \mathbf{s})$ is the radiative intensity $[kW/m^2]$ at wavelength λ $[m]$, $I(\mathbf{x}, \mathbf{s})$ is the radiative intensity of the gaseous mixture $[kW/m^2]$, $\mathbf{s}$ is the direction vector of the intensity, $\kappa(\mathbf{x}, \mathbf{s})$ is the local absorption coefficient and $I_b(\mathbf{x})$ is the radiative source term $[kW/m^2]$. For practical reasons FDS only solves the RTE for a limited number of bands N_λ of wave lengths λ deriving separate RTEs for each band,

[4]Usually adopted in fire modeling with multi-purpose CFD codes.

hence:

$$I(\mathbf{x},\mathbf{s}) = \sum_{n=1}^{N_\lambda} I_n(\mathbf{x},\mathbf{s}) \tag{2.4.19}$$

For most building fires thermal radiation from the fire and smoke layer is controlled by the properties of the soot. From *Kirchoff's Law* the spectral absorptivity κ_λ and emissivity ϵ_λ are equal when subjected to the same temperature:

$$\kappa_\lambda(\lambda,T) = \epsilon_\lambda(\lambda,T) \tag{2.4.20}$$

Soot can be assumed to have a continuous radiation spectrum, thus rewriting Eqn. (2.4.20):

$$\kappa(T) = \epsilon(T) \tag{2.4.21}$$

This is the gray gas assumption applied by default in FDS. Prior to any simulation FDS tabulates the absorption coefficient $\kappa(Z,T)$ as a function of mixture fraction Z and gas temperature T. Local absorption coefficients are thus found by simple table-lookup.

The radiative source term is treated differently inside the flame zone as opposed to outside the flame zone, see Eqn. (2.4.23). The radiative source term depends on the temperature:

$$I_b(\mathbf{x}) \propto T^4 \tag{2.4.22}$$

This means that even small uncertainties in the computed temperature have enormous effects on the radiative source term because of the fourth power scaling. To address this problem the source term is modeled according to:

$$\kappa I_b = \begin{cases} \frac{\kappa\sigma T^4}{\pi} & Z < Z_f \\ \max\left(\frac{\chi_r \dot{q}'''}{4\pi}, \frac{\kappa\sigma T^4}{\pi}\right) & Z > Z_f \end{cases} \tag{2.4.23}$$

where χ_r is the radiative fraction [1]. Despite χ_r depends on both flame temperature and concentration of combustion products, FDS models combustion and radiative transport with a constant radiative fraction for fuels.

The radiative fraction χ_r also controls the convective heat release rate $\dot{Q}_c$ $[kW]$:

$$\dot{Q}_c = (1-\chi_r)\,\dot{Q}_T \tag{2.4.24}$$

where the total heat release rate $\dot{Q}_T$ $[kW]$ is:

$$\dot{Q}_T = \int_{V_{domain}} \dot{q}''' dV \tag{2.4.25}$$

Here $\dot{q}'''$ is the local heat release rate, see Eqn. (2.4.14). From Eqn. (2.4.24) it is clear that the radiative fraction χ_r is a single parameter that can heavily influence both the convective heat transport $\dot{Q}_c$, i.e. the production of smoke and temperature in the smoke layer, and the radiative intensity transported to building components.

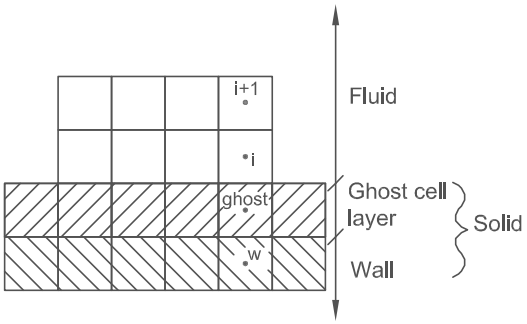

Figure 2.1 *Interpretation of the energy boundary condition.*

The radiative heat loss term in the energy equation Eqn. (2.4.1d) is interpreted as the net energy gained by the control volume, i.e. the difference by incident radiative energy and that emitted:

$$-\nabla \cdot \mathbf{q}_r(\mathbf{x}) = \kappa(\mathbf{x})\left[I_{in}(\mathbf{x}) - 4\pi I_b(\mathbf{x})\right] \tag{2.4.26}$$

where $I_{in}(\mathbf{x})$ is the local incident radiative heat flux $[kW/m^2]$ in the control volume:

$$I_{in}(\mathbf{x}) = \int_{4\pi} I(\mathbf{x}, \mathbf{s})\, d\Omega \tag{2.4.27}$$

2.4.5 Surface Boundary Conditions

This section briefly describes the boundary conditions of interest to this particular study.

Energy BCs

Energy transfer from the gas phase to the solid material is exchanged in a layer of *ghost cells* constituting the first layer in the solid, see Figure 2.1. The ghost cells do not represent a physical fact but are simply a numerical construct to handle the transformation of the incident heat flux to heat conduction in the solid material.

Adiabatic BC The adiabatic wall boundary condition is interpreted as a zero heat flux condition, i.e. no temperature gradient across the boundary at $x = 0$:

$$\frac{\partial T(0)}{\partial \mathbf{n}} = 0 \tag{2.4.28}$$

hence the temperature in the first solid grid cell (the ghost cell) T_{ghost} $[K]$ is equal to the gas temperature T_i $[K]$ in the first gas cell layer, see Figure 2.1:

$$T_{ghost} = T_i \tag{2.4.29}$$

Thermally Thick BC For a thermally thick material the one dimensional heat conduction equation is solved for the temperature in the solid T_s $[K]$:

$$\rho_s c_s \frac{\partial T_s}{\partial t} = \frac{\partial}{\partial x}\left(k_s \frac{\partial T_s}{\partial x}\right) \tag{2.4.30}$$

Here ρ_s is the density $[kg/m^3]$, c_s is the specific heat capacity $[kJ/kg]$, k_s is the thermal conductivity $[kW/(m\ K)]$ and T_s in $[K]$ is the temperature in the solid respectively.

The boundary condition at $x = 0$ for a thermally thick non-burning material is written:

$$-k_s \frac{\partial T_s}{\partial x}(0,t) = \dot{q}''_{c,in} + \frac{\dot{q}''_{r,in}}{\epsilon} - \underbrace{\sigma T_w^4}_{\text{emit. flux}} \tag{2.4.31}$$

where T_w is the wall temperature $[K]$, σ is Stefan Boltzmann's constant, $\dot{q}''_{r,in}$ is the incident radiative heat flux $[kW/m^2]$ from the RTE, see Eqn. (2.4.18) , and $\dot{q}''_{c,in}$ $[kW/m^2]$ is the incident convective heat flux:

$$\dot{q}''_{c,in} = h_c \Delta T \tag{2.4.32}$$

with the boundary layer temperature ΔT $[K]$:

$$\Delta T = T_i - T_{ghost} \tag{2.4.33}$$

and the convective heat transfer coefficient h_c $[kW/(m^2 * K)]$ for a LES computation:

$$h_c = \max\left[C_{wo}\left|\Delta T\right|^{1/3}, \frac{k}{L^*}0.037\mathrm{Re}^{4/5}\mathrm{Pr}^{1/3},\right] \tag{2.4.34}$$

Here C_{wo} is an empirical constant for convective heat transfer on vertical and horizontal surfaces[5], see Holman (1989), k is the thermal conductivity $[kW/(m * K)]$ and L^* a characteristic length along the wall.

Thermally Thin BC For a thermally thin material the temperature distribution across the material thickness δ can be assumed uniform, and by conservation of energy we get the temperature in the material T_s $[K]$:

$$\frac{\partial T_s}{\partial t} = \frac{1}{\rho_s c_s \delta}\left(\dot{q}''_{c,in} + \frac{\dot{q}''_{r,in}}{\epsilon} - \sigma T_w^4\right) \tag{2.4.35}$$

where δ is the thickness of the material $[m]$.

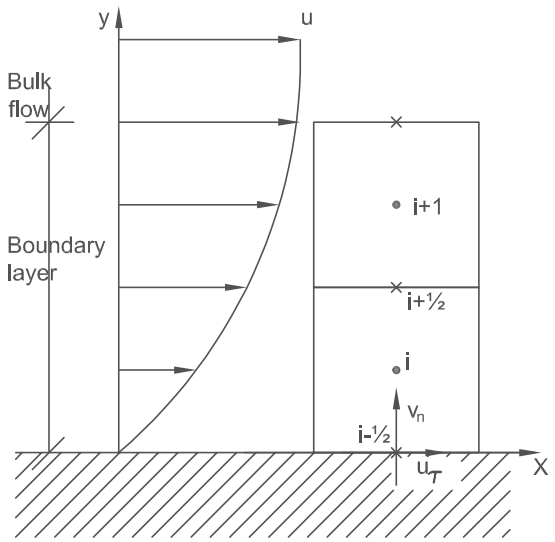

Figure 2.2 *Interpretation of the velocity boundary condition.*

Velocity BC

Velocity boundary conditions determines the tangential u_τ and normal velocities v_n on the surface of the wall, see Figure 2.2. The normal velocity component v_n is obviously zero since no momentum flux is allowed for a solid wall:

$$v_n = 0 \tag{2.4.36}$$

Physically the tangential velocity $u_\tau = 0$ on the wall, *no-slip* condition, increasing rapidly through the boundary layer following a logarithmic increase, see Davidson (2003). For most highly turbulent flows, e.g. fire induced flows, the boundary layer is very thin and can not be resolved adequately, hence a simple boundary condition is invoked for the tangential velocity component u_τ on the surface of a wall:

$$u_\tau = \frac{1}{2}\left(1 + u^*\right) u_i \tag{2.4.37}$$

where u^* is the velocity slip condition [1] and u_i is the velocity $[m/s]$ in the first gas phase cell abutting the solid wall. For $u^* = -1$ the condition is no-slip, for $u^* = 1$ the condition is *free-slip* and for $-1 < u^* < 1$ the condition is *partial slip*.

2.4.6 Fire/Heat Source BC

This study only addresses fires with prescribed heat release rates. The fire source is described through an inhomogeneous *Dirichlet* boundary condition for the mass

[5]Horizontal; $C = 1.52$, vertical; $C = 1.31$.

flux of fuel at the fire base, $\dot{m}''_f$ $[kg/(m^2\ s)]$:

$$\dot{m}''_f = \frac{\dot{Q}''_{T,pre}}{\Delta H_c} \tag{2.4.38}$$

where $\dot{Q}''_{T,pre}$ is the prescribed total heat release rate per unit area $[kW/(m^2)]$ and ΔH_c is the heat of combustion. The mass flow rate of fuel follows the prescribed heat release rate but the actual heat release rate in the computational domain depends on the combustion criteria, i.e. if the oxygen consumption in the combustion process is higher than the oxygen supply, the heat release rate decreases leaving unburnt gases to flow out of the combustion region - allowing for ignition in an oxygen rich and high temperature environment, e.g. window flames out of a fire compartment.

FDS also provides a convective heat source as a boundary condition. The heat source is prescribed through an inhomogeneous *Dirichlet* boundary condition for the convective heat flux at the base of the heat source, $\dot{q}''_{c,f}$ $[kW/(m^2)]$:

$$\dot{q}''_{c,f} = \dot{Q}''_{c,pre} \tag{2.4.39}$$

where $\dot{Q}''_{c,pre}$ is the prescribed convective heat release rate per unit area of heater $[kW/m^2]$.

2.4.7 Flow Boundary Conditions

Passive Flow BC

Passive flow boundaries are used where flow enters or leaves the computational domain, e.g. vents to ambient surroundings. In FDS the passive flow boundary condition is designated an *OPEN* vent. The temperature boundary condition for the passive vent is, according to nomenclature in Figure 2.3:

$$T_i = T_\infty \tag{2.4.40}$$

where T_∞ is the ambient temperature $[K]$. This means that flow entering the computational domain has ambient temperature. The temperature boundary condition is expected to have a minor effect on the velocity of a buoyant flow leaving the computational domain, because the temperature above ambient is the driving force in a buoyant flow.

The velocity boundary conditions for the passive vent are of homogeneous *Neumann* type for flow leaving the computational domain:

$$\left(\frac{\partial u}{\partial x}\right)_{i-1/2} = 0 \ \forall(\mathbf{u}\cdot\mathbf{n} > 0) \tag{2.4.41a}$$

$$u_{i+1/2} = u_{i-1/2} \ \forall(\mathbf{u}\cdot\mathbf{n} > 0) \tag{2.4.41b}$$

and of inhomogeneous *Dirichlet* type for flow entering the computational domain:

$$u_{i+1/2} = u_\infty \ \forall(\mathbf{u}\cdot\mathbf{n} < 0) \tag{2.4.42}$$

where $\mathbf{n}$ is the outward pointing normal vector and u_∞ is the ambient fluid velocity field (usually considered at rest, i.e. $u_\infty = 0$. Please refer to Figure 2.3 for nomenclature.

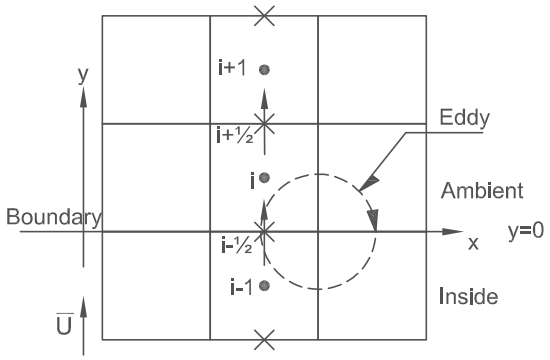

Figure 2.3 *Interpretation of the passive boundary condition.*

Symmetry Flow BC

Symmetry flow boundaries are used where the flow can be considered symmetric, i.e. the flow properties on each side of the boundary condition are considered identical, and zero mass and energy flux across the boundary. In FDS the symmetry flow boundary condition is designated a *MIRROR* vent. The temperature boundary condition for the symmetry vent is of zero gradient *Neumann* type:

$$\left(\frac{\partial T}{\partial x}\right)_i = 0 \tag{2.4.43a}$$

$$T_i = T_{i-1} \tag{2.4.43b}$$

The velocity boundary condition is of inhomogeneous *Dirichlet* type:

$$u_{i+1/2} = -u_{i-1/2} \tag{2.4.44}$$

Hence it can be seen that the velocity field is reversed. In Figure 2.4 the flow field induced by an eddy leaving the computational domain with the symmetry boundary condition is outlined with a dashed line. As it can be seen the eddy induced flow is "canceled" introducing an error in the local turbulence field along the entire boundary employing the symmetry boundary condition. Depending on the extent and the flow direction this can cause severe mixing errors yielding an increased smoke production. This is especially true for flow fields parallel to the symmetry boundary condition, where the error is amplified by the successive application of the boundary condition as the flow propagates along the boundary.

2.4.8 Numerical Model

Computational Grid

FDS solves the conservation equations, radiative transport equations and submodels on a rectilinear grid of control volumes. Curvilinear geometries can be

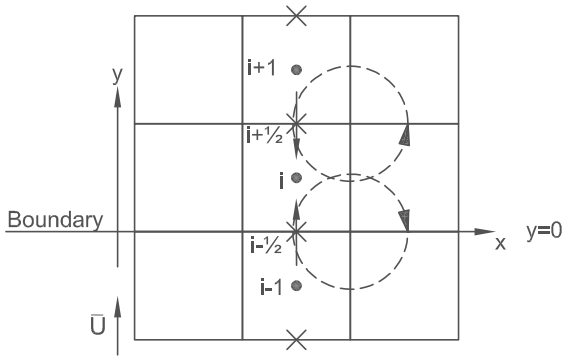

Figure 2.4 *Interpretation of the symmetry boundary condition.*

approximated by *stair-stepping* the non-rectangular boundaries and suppressing the vortex production on sharp *artificial edges* of the non-rectangular boundary, a feature provided in FDS through the parameter *SAWTOOTH*. Scalar quantities (e.g. temperature, density and mass fractions) are defined at control volume centers $\{i, j, k\}$, see ($\bullet$) in Figure 2.5, and vector quantities (e.g. velocities and radiative intensities) are defined at control volume faces $\{i+1/2, j+1/2, k+1/2\}$, see ($\times$) in Figure 2.5.

The grid can be stretched in two of the three directions ($\mathbf{x} \in \{x, y, z\}$) using a piecewise or polynomial mapping of the axis coordinates, see McGrattan (2005b).

A multi-grid feature is provided with FDS, making it possible to use multiple grids to resolve the computational domain. Information about the flow field is exchanged at grid boundaries, i.e. not at interior grid points, at the end of every time step through an interpolation scheme. Obviously this introduces a numerical interpolation error and a relatively smaller round-off error that one must be aware of when designing the grid.

Temporal Discretization

FDS solves the system of partial differential equations applying an implicit predictor-corrector scheme (PECE). In this section superscripts n describes quantities at the previous time step, $(n+1)_p$ predicted variables at the next time step and $(n+1)$ is the corrected quantities at the next time step. The predictor for a generic thermodynamic variable ϕ[6] is written:

$$\phi^{(n+1)_p} = \phi^n - \Delta t \left(\mathbf{u}^n \cdot \nabla \phi^n + \phi^n \nabla \cdot \mathbf{u}^n \right) \tag{2.4.45}$$

[6]This can be ρ, Y_i and p_0.

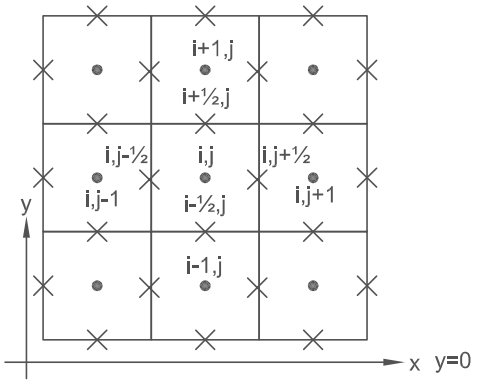

Figure 2.5 *Computational grid applied in FDS.*

from which the divergence $(\nabla \cdot \mathbf{u})^{(n+1)_p}$ can be derived. Deriving the pressure head $\mathcal{H}$ from the predicted divergence yields:

$$\nabla^2 \mathcal{H}^n = -\frac{(\nabla \cdot \mathbf{u})^{(n+1)_p} - (\nabla \cdot \mathbf{u})^n}{\Delta t} - \nabla \cdot \mathbf{F}^n \tag{2.4.46}$$

and predicting the velocity at the next time step $(n+1)_p$:

$$\mathbf{u}^{(n+1)_p} = \mathbf{u}^n - \Delta t \left(\mathbf{F}^n + \nabla \mathcal{H}^n\right) \tag{2.4.47}$$

Invoking the corrector step on all predicted quantities yields for the generic thermodynamic quantities ϕ:

$$\phi^{(n+1)} = \frac{1}{2}\left(\phi^n + \phi^{(n+1)_p} - \Delta t \left(\mathbf{u}^{(n+1)_p} \cdot \phi^{(n+1)_p} + \phi^{(n+1)_p} \nabla \cdot \mathbf{u}^{(n+1)_p}\right)\right) \tag{2.4.48}$$

Updating the pressure head $\mathcal{H}$ based on the divergence $(\nabla \cdot \mathbf{u})^{(n+1)}$ from Eqn. (2.4.48):

$$\nabla^2 \mathcal{H}^{(n+1)_p} = -\frac{2\,(\nabla \cdot \mathbf{u})^{(n+1)}\,(\nabla \cdot \mathbf{u})^{(n+1)_p} - (\nabla \cdot \mathbf{u})^n}{\Delta t} - \nabla \cdot \mathbf{F}^{(n+1)_p} \tag{2.4.49}$$

and inserting in the corrector for the velocity $\mathbf{u}^{(n+1)}$:

$$\mathbf{u}^{(n+1)} = \frac{1}{2}\left(\mathbf{u}^n + \mathbf{u}^{(n+1)_p} - \Delta t \left(\mathbf{F}^{(n+1)_p} + \nabla \mathcal{H}^{(n+1)_p}\right)\right) \tag{2.4.50}$$

All quantities are now advanced to the next time step $n+1$. A thorough description of the solution methodology can be found in McGrattan (2005a).

FDS employs a simple dynamical time step algorithm for LES computations based on the *Courant, Friedrich, Levy condition* (CFL) for stability in the solution of parabolic PDEs:

$$\Delta t < \min\left(\frac{\Delta x}{|u_{ijk}|}, \frac{\Delta y}{|v_{ijk}|}, \frac{\Delta z}{|w_{ijk}|}\right) \tag{2.4.51}$$

where u_{ijk}, v_{ijk} and w_{ijk} are local cell velocities $[m/s]$ in the x, y, z directions respectively and Δx, Δy and Δz are grid spacings $[m]$. This constrains the time step by the convective and diffusive transport speeds, i.e. a fluid particle is constrained from flowing through more than one grid cell/control volume during a time step.

Spatial Discretization

The conservation equations outlined in the previous sections are approximated by second order accurate finite differences on a rectilinear grid. Assuming any solution to the conservation equations can be described by a continuous differentiable function $\phi(x)$ in the vicinity of the position x_i, the *Taylor approximation* is:

$$\begin{aligned}\phi(x) =& \phi(x_i) + (x - x_i)\left(\frac{\partial \phi}{\partial x}\right)_i + \frac{(x - x_i)^2}{2!}\left(\frac{\partial^2 \phi}{\partial x^2}\right)_i \cdots \\ &+ \frac{(x - x_i)^n}{n!}\left(\frac{\partial^n \phi}{\partial x^n}\right)_i + O\left((x - x_i)^{n+1}\right)\end{aligned} \tag{2.4.52}$$

Expanding the continous function $\phi(x_{i+1})$ in the vicinity of i and rewriting for the first derivative at x_i:

$$\begin{aligned}\left(\frac{\partial \phi}{\partial x}\right)_i =& \frac{\phi_{i+1} - \phi_i}{x_{i+1} - x_i} - \frac{x_{i+1} - x_i}{2}\left(\frac{\partial^2 \phi}{\partial x^2}\right)_i \cdots \\ &- \frac{(x_{i+1} - x_i)^{n-1}}{n!}\left(\frac{\partial^n \phi}{\partial x^n}\right)_i + O\left((x - x_i)^n\right)\end{aligned} \tag{2.4.53}$$

Truncating terms of order $n \geq 2$ in Eqn. (2.4.52) results in the forward finite difference approximation (FD scheme) of the first derivative written on an equidistant grid with spacing Δx:

$$\left(\frac{\partial \phi}{\partial x}\right)_i = \frac{\phi_{i+1} - \phi_i}{\Delta x} + O(\Delta x) \tag{2.4.54}$$

Hence it has been shown that the FD scheme is of first order accuracy, i.e. the truncation error[7] is of first order and reduced by a factor of two by halving the grid spacing. At this point it should be evident that large grid spaces affect the finite difference approximations to the conservation equations and hence the mathematical model.

[7]The numerical error introduced by neglecting terms of order $n \geq 2$.

The central difference scheme (CD scheme) is derived by expanding the continous function $\phi(x)$, according to Eqn. (2.4.52), in the vicinity of x_{i+1} and x_{i-1}, truncating terms of order $n \geq 3$, collecting terms and rewriting for the first derivative yield:

$$\begin{aligned}\left(\frac{\partial\phi}{\partial x}\right)_i =& \frac{\phi_{i+1}-\phi_{i-1}}{x_{i+1}-x_{i-1}} - \frac{1}{2}\left[\frac{(x_{i+1}-x_i)^2-(x_{i-1}-x_i)^2}{x_{i+1}-x_{i-1}}\right]\left(\frac{\partial^2\phi}{\partial x^2}\right)_i \cdots \\ & - O\left(\frac{(x_{i+1}-x_i)^3}{x_{i+1}-x_{i-1}}\right) + O\left(\frac{(x_{i-1}-x_i)^3}{x_{i+1}-x_{i-1}}\right)\end{aligned} \tag{2.4.55}$$

which on an equidistant grid with spacing Δx reduces to:

$$\left(\frac{\partial\phi}{\partial x}\right)_i = \frac{\phi_{i+1}-\phi_{i-1}}{\Delta x} + O\left(\Delta x^2\right) \tag{2.4.56}$$

where terms of order $n \geq 3$ are truncated. This is a second order accurate approximation to the first derivative at x_i using quantities at neighboring grid points x_{i+1} and x_{i-1}.

In deriving the upwind difference scheme (UD scheme), the continuous function $\phi(x_i)$, Eqn. (2.4.52), is approximated in the vicinity of x_{i-1} and terms of order $n \geq 1$ are truncated:

$$\phi(x_i) = \phi_{i-1} + O(\Delta x) \; \forall \left(\mathbf{u}\cdot\mathbf{n}_x > 0\right)_i \tag{2.4.57}$$

Here $\mathbf{n}_x$ is the x axis base vector. This means that the quantity at grid point $i+1$ is based solely on the quantity in grid point i. From Eqn. (2.4.57) and Eqn. (2.4.52) it is clear that the UD scheme is only first order accurate. Clearly a downwind finite difference scheme (DD scheme) also exists:

$$\phi(x_i) = \phi_{i+1} + O(\Delta x) \; \forall \left(\mathbf{u}\cdot\mathbf{n}_x < 0\right)_i \tag{2.4.58}$$

Here again $\mathbf{n}_x$ is the x axis base vector. Taking a look at the terms truncated when deriving Eqn. (2.4.57) and Eqn. (2.4.58) for equidistant grid spacing Δx $[m]$:

$$\epsilon_h = O((\Delta x)) = \Delta x \underbrace{\left(\frac{\partial\phi}{\partial x}\right)_i}_{\text{diff. flux}} + \frac{\Delta x}{2}\left(\frac{\partial^2\phi}{\partial x^2}\right)_i + \ldots \tag{2.4.59}$$

it is clear that the leading term in the truncation error ϵ_h has the nature of a diffusive flux, which is the source of false diffusion in CFD fire modeling and requires very fine grids to produce accurate results.

Approximations to the second derivative can be computed by combining derivatives of first order halfway between neighboring grid points, e.g. at $x_{i+1/2}$ located halfway between grid points x_i and x_{i+1}:

$$\left(\frac{\partial^2\phi}{\partial x^2}\right)_i = \frac{\left(\frac{\partial\phi}{\partial x}\right)_{i+1/2} - \left(\frac{\partial\phi}{\partial x}\right)_{i-1/2}}{x_{i+1}-x_i} + O\left(\Delta x^2\right) \tag{2.4.60a}$$

$$= \frac{\phi_{i+1}-2\phi_i+\phi_{i-1}}{(\Delta x)^2} + O\left(\Delta x^2\right) \tag{2.4.60b}$$

where the CD scheme, see Eqn. (2.4.56), for equidistant grid spacing Δx has been applied and the second order accuracy preserved.

In analogy with normal practice for the approximation of convective terms in the conservation equations, FDS uses an upwind biased FD scheme based on the local *Courant* numbers ϵ_i [1]:

$$\epsilon_u = u\frac{\Delta t}{\Delta x} \tag{2.4.61a}$$

$$\epsilon_v = v\frac{\Delta t}{\Delta y} \tag{2.4.61b}$$

$$\epsilon_w = w\frac{\Delta t}{\Delta z} \tag{2.4.61c}$$

where Δx etc. represents the local grid spacing $[m]$ and Δt the time step $[s]$. The upwind biased scheme for a generic quantity ϕ in one dimension is written:

$$u\left(\frac{\partial\phi}{\partial x}\right)_i = \frac{1\mp\epsilon_u}{2}u_i\frac{\phi_{i+1}-\phi_i}{\Delta x} + \frac{1\pm\epsilon_u}{2}u_{i-1}\frac{\phi_i-\phi_{i-1}}{\Delta x} \tag{2.4.62}$$

For reasons of stability FDS applies an upwind biased difference scheme in the predictor, and corrects with a downwind biased scheme. In Eqn. (2.4.62) $\mp$ means minus in the predictor and plus in the corrector and vice versa for $\pm$. For the complete approximation of Eqn. (2.4.62) in three dimensional space please refer to McGrattan (2005a). For a Courant number ϵ_i close to unity, the fluid particle travels almost entirely through one grid cell during the applied time step, and it can be seen that the difference scheme is biased towards an entirely upwind scheme in the predictor:

$$u\left(\frac{\partial\phi}{\partial x}\right)_i = u_{i-1}\frac{\phi_i-\phi_{i-1}}{\Delta x} \tag{2.4.63}$$

For a weak flow (particle only travels a fraction of the cell size during a time step) the Courant number $\epsilon_i \to 0$ and the convective difference scheme approaches that of the CD scheme:

$$u\left(\frac{\partial\phi}{\partial x}\right)_i = \frac{1}{2}u_i\frac{\phi_{i+1}-\phi_i}{\Delta x} + \frac{1}{2}u_{i-1}\frac{\phi_i-\phi_{i-1}}{\Delta x} \tag{2.4.64}$$

Conduction terms are approximated according to the scheme for the derivatives of second order, see Eqn. (2.4.60a), here written for the generic quantity ϕ in one dimension:

$$(\nabla\cdot k\nabla\phi)_i = \frac{1}{\Delta x}\left(k_{i+1/2}\frac{\phi_{i+1}-\phi_i}{\Delta x} - k_{i-1/2}\frac{\phi_i-\phi_{i-1}}{\Delta x}\right) \tag{2.4.65}$$

For the complete finite difference scheme in three dimensional space, please refer to McGrattan (2005a).

It is important to realize that due to the combination of first and second order accurate finite difference schemes in the FDS solver, the reduction of the

truncation error can not be expected to follow that of a second order scheme, rather something in between. Eventually the sub-grid scale turbulence model is also expected to reduce the order, hence a first order reduction is probably the highest order attainable in a highly turbulent flow (e.g. thermal plumes). A faster rate of reduction is expected in low turbulent flow regions, e.g. ceiling jet.

2.5 Characteristic Length Scales

Characteristic length scales D_i^* $[m]$ are important in assessing grid resolutions, making it possible to assess adequate grid resolutions relative to the characteristic length scale, i.e. putting the grid resolutions on non-dimensional form. Writing the *simple* equation for conservation of energy:

$$\rho c_p \left(\frac{\partial T}{\partial t} + \mathbf{u} \cdot \nabla T \right) = \underbrace{\dot{q}'''}_{\text{Heat source}} + \nabla \cdot k \nabla T \tag{2.5.1}$$

and inserting the scaling groups, see Chapter 4:

$$\mathbf{x}^* = \frac{\mathbf{x}}{D_p^*} \tag{2.5.2a}$$

$$\mathbf{u}^* = \frac{\mathbf{u}}{\sqrt{D_p^* g}} \tag{2.5.2b}$$

$$t^* = \frac{t}{\sqrt{\frac{D_p^*}{g}}} \tag{2.5.2c}$$

$$\rho^* = \frac{\rho}{\rho_\infty} \tag{2.5.2d}$$

$$T^* = \frac{T}{T_\infty} \tag{2.5.2e}$$

$$k^* = \frac{k}{\rho_\infty c_p \sqrt{g} D_p^{*3/2}} \tag{2.5.2f}$$

Rewriting gives:

$$\rho^* \frac{\partial T^*}{\partial t^*} + \mathbf{u}^* \cdot \nabla T^* = \underbrace{\frac{\sqrt{D_p^*}}{\rho_\infty T_\infty c_p \sqrt{g}} \dot{q}'''}_{\text{Heat source}} + \nabla \cdot k^* \nabla T^* \tag{2.5.3}$$

Integrating the heat source term in Eqn. (2.5.3) over the entire domain Ω, where $dV = dx\, dy\, dz$ with the non-dimensional form $dV^* = D_p^{*3}\, dx^*\, dy^*\, dz^*$:

$$\int_\Omega \dot{q}'''^* \, dV^* = \frac{1}{\rho_\infty T_\infty c_p \sqrt{g} D_p^{*\frac{5}{2}}} \int_\Omega \dot{q}''' \, dV = 1 \tag{2.5.4a}$$

$$D_p^* = \left(\frac{\dot{Q}_c}{\rho_\infty T_\infty c_p \sqrt{g}} \right)^{2/5} \tag{2.5.4b}$$

D_p^* is the characteristic length scale of a fire source (axisymmetric or rectangular). Here $\dot{Q}_c$ is the convective heat release rate $[kW]$.

Zukoski (1995) showed that Eqn. (2.5.4b) can be modified to describe the characteristic length of a line source D_l^*:

$$D_l^* = \left(\frac{\frac{\dot{Q}_c}{L_l}}{\rho_\infty T_\infty c_p \sqrt{g}} \right)^{2/5} \tag{2.5.5}$$

where D_l^* is the characteristic length of the line source $[m]$ and L_l is the length of the line source (here the width of the opening at the spill edge W_w, see Figure 2.6).

According to Klote & Milke (2002) the depth of an unconfined ceiling jet is about 10% of the height from fire base to compartment ceiling, irrespective of the convective heat release rate $\dot{Q}_c$. Thus the depth of the unconfined ceiling jet is proposed as the characteristic length scale applicable for all ceiling jets D_{cj}^*:

$$D_{cj}^* = 0.1 \left(H_{fc} - H_{fb} \right) \tag{2.5.6}$$

where H_{fc} is the fire compartment height to ceiling $[m]$ and H_{fb} is the height of the fire base $[m]$.

2.6 Computing Flow Rates

Evaluating flow rates and extents of flow sections require a definition of the core flow. Throughout this study, cores of the flow section (e.g. axisymmetric plumes, ceiling jets, approach flows, spill plumes etc.) are defined based on the core density $\tilde{\rho}$ and mean core velocity $\tilde{\mathbf{U}}$ in the direction of the bulk flow. Core quantities must be evaluated in each control volume cut by the flow section. Core densities in the present study are defined where the temperature above ambient is $\geq$1 K:

$$\tilde{\rho}_i = \begin{cases} \rho_i & \forall\ \Delta T_i \geq 1\ K \\ 0 & \forall\ \Delta T_i < 1\ K \end{cases} \tag{2.6.1}$$

with i designating the local control volume index (obviously expanding in two or three dimensions).

Core velocities are defined as velocities in the direction of the bulk flow only (i.e. horizontally for ceiling jets and approach flows, and vertical for buoyant plumes):

$$\tilde{W}_i = \begin{cases} W_i & \forall\ \mathbf{U} \cdot \mathbf{s}_z > 0 \\ 0 & \forall\ \mathbf{U} \cdot \mathbf{s}_z \leq 0 \end{cases} \tag{2.6.2}$$

with the directional vector $\mathbf{s}$ pointing in the direction of the bulk flow. Of illustrative reasons the directional vector $\mathbf{s}_z$ in Eqn. (2.6.2) points in the upward direction z typical of buoyant plumes, i.e. only the positive part of the W component of the velocity vector is preserved.

Mass and heat flow correlations usually refer to gross flow rates in the two-dimensional plane cutting the plume, i.e. the total mass flow rate of smoke

"pumped" into the smoke layer. FDS provides a built-in tool for computing the net flow rate only. For this reason all flow rates are computed using external data processing resources.

Flow rates are based on control volume face quantities obtained as simple averages of the vertex quantities, i.e. for the generic flow quantity ϕ:

$$\phi_{i,j} = \frac{1}{4}\left(\phi_{i-1/2,j-1/2} + \phi_{i-1/2,j+1/2} + \phi_{i+1/2,j-1/2} + \phi_{i+1/2,j+1/2}\right) \tag{2.6.3}$$

For an illustration of the computational grid in two dimensions see Figure 2.5.

Mass flow rates $\dot{m}$ $[kg/s]$ are computed numerically based on the flow definitions outlined above:

$$\dot{m} = \int_{A_{flow}} \left(\tilde{\rho}\tilde{\mathbf{U}}\right) \cdot \mathbf{s}_{bf}\, dA \tag{2.6.4a}$$

$$= \sum_{i=1}^{n_x}\sum_{j=1}^{n_y} \tilde{\rho}_{i,j}\tilde{\mathbf{U}}_{i,j}\, \Delta x_{i,j}\, \Delta y_{i,j} \tag{2.6.4b}$$

here $\tilde{\mathbf{U}} = \{U, V, W\}$ are the mean core velocities $[m/s]$ in each of the axis directions respectively, n_x and n_y are the number of control volumes in the two axis directions spanning the flow section. The direction vector $\mathbf{s}_{bf}$ points in the direction of the bulk flow (abbreviated bf).

For the trivial mass flow rate per unit length $\dot{m}'_i$ $[kg/(s * m)]$ we get:

$$\dot{m}'_i = \int_{H_{flow}} \left(\tilde{\rho}\tilde{\mathbf{U}}\right) \cdot \mathbf{s}_{bf}\, dS \tag{2.6.5a}$$

$$= \sum_{j=1}^{n_y} \tilde{\rho}_{i,j}\tilde{\mathbf{U}}_{i,j}\, \Delta y_{i,j} \tag{2.6.5b}$$

Convective heat flow rates $\dot{Q}_c$ $[kW]$ are computed analogously:

$$\dot{Q}_c = \int_{A_{flow}} \left(\tilde{\rho}\tilde{\mathbf{U}} c_p \Delta T\right) \cdot \mathbf{s}_{bf}\, dA \tag{2.6.6a}$$

$$= \sum_{i=1}^{n_x}\sum_{j=1}^{n_y} \tilde{\rho}_{i,j}\tilde{\mathbf{U}}_{i,j} c_p \Delta T_{i,j}\, \Delta x_{i,j}\, \Delta y_{i,j} \tag{2.6.6b}$$

where ΔT are the temperature above ambient $[K]$.

Rewriting Eqn. (2.6.6) to arrive at the convective heat flow rate per unit length $\dot{Q}'_{c,i}$ yield:

$$\dot{Q}_{c,i} = \int_{H_{flow}} \left(\tilde{\rho}\tilde{\mathbf{U}} c_p \Delta T\right) \cdot \mathbf{s}_{bf}\, dS \tag{2.6.7a}$$

$$= \sum_{j=1}^{n_y} \tilde{\rho}_{i,j}\tilde{\mathbf{U}}_{i,j} c_p \Delta T_{i,j}\, \Delta y_{i,j} \tag{2.6.7b}$$

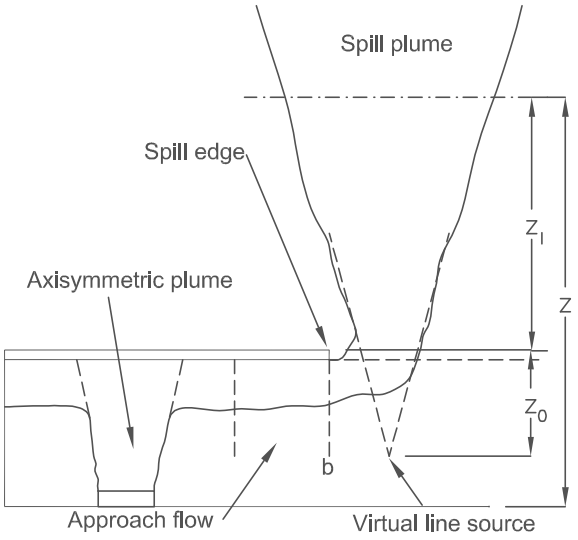

Figure 2.6 *Typical smoke flow in atrium smoke management design.*

2.7 Flow Regions

In CFD fire modeling the length scales range from $< 10^{-3}$ for the combustion processes to building sizes of the order 10^2 m, hence requiring resolutions of 10^5 in each of the three space dimensions yielding grid sizes of the order $(10^5)^3$, which is simply impossible to solve with any present computer architecture. To address the problem CFD fire models adopt models for turbulence and combustion, accepting that only the large energy carrying eddies of the bulk flow can be resolved accurately. Since the turbulent length scales change with the chemical and physical processes in fire dynamics, it is widely adopted to model different *flow regions* using different resolutions. A typical fire scenario in atrium smoke management can be found in Figure 2.6. The fire induced flow in Figure 2.6 can be divided into four flow type regions:

Axisymmetric plume region - see Section 2.10.1.

Approach flow region - see Section 2.10.2.

Rotation region - see Section 2.10.3.

Spill plume region - see Section 2.10.4

Each flow region mentioned above represents a distinct region that must be adequately resolved to produce accurate predictions of flow properties downstream. For a flow region to be considered adequately resolved, the solution must be grid independent, i.e. further grid refinements yield the same solution, or at least

the discrepancy must be addressed through e.g. validation with acknowledged engineering relations or experimental data.

In the following sections each flow region is subjected to a simple grid convergence study according to Section 2.8, and a validation against simple engineering relations. The CFD model setup is explained in Section 2.9.

2.8 Grid Convergence Study

2.8.1 Discretization Error

A grid convergence study serves the purpose of assessing if the approximate solution obtained with the CFD fire model can be considered grid independent, alternatively what is the error, or how much must the grid be refined to approach a solution of adequate accuracy.

Elaborating on the Taylor series in Eqn. (2.4.52), the exact solution Φ to the partial differential equations, PDEs, (conservation laws) constituting the mathematical model, see Eqn. (2.4.1), can be written as an approximated solution ϕ_h obtained with grid spacing h and a discretization error, ϵ_h, emanating from solving the PDEs on a discrete grid:

$$\Phi = \phi_h + \epsilon_h \tag{2.8.1}$$

Roache (1994) has shown that the truncation error emanating from the truncation of higher order terms in the finite difference approximations, see Eqn. (2.4.53) and Eqn. (2.4.54), acts as a source of the discretization error ϵ_h:

$$\epsilon_h \propto C_\epsilon h^p + O(h^{p+1}) \tag{2.8.2}$$

where C_ϵ is a constant independent of grid spacing h, p is the order of the numerical scheme and h is the grid spacing. Since Φ is not known, one must use the solution ϕ_h from a finer mesh (e.g. grid spacing h) in approximating the order of the method p. From Eqn. (2.8.2) it can be seen that the discretization error ϵ_h is reduced proportional to the grid spacing raised to the p'th power, when the grid is refined. Hence the order p of the method can be found from monitoring the reduction of the discretization error as a function of grid spacing. Writing for the relative discretization error $\tilde{\epsilon}_{ih}$:

$$\tilde{\epsilon}_{ih} \propto \frac{\phi_{ih} - \phi_{2ih}}{\phi_{2ih}} \quad \forall i = 1 \ldots N-1 \tag{2.8.3a}$$

$$\propto C_\epsilon \, (ih)^p \tag{2.8.3b}$$

$$\ln\left(\frac{\phi_{ih} - \phi_{2ih}}{\phi_{2ih}}\right) \propto p \ln(ih) + \text{Const.} \quad \forall i = 1 \ldots N-1 \tag{2.8.3c}$$

where i is an index counter and N is the number of grid refinements. The order p of the method is found by plotting Eqn. (2.8.3c) in a log-log plot or simply solving for p.

2.8.2 Modeling Parameters

The grid convergence index study is designed to assess the requirements to grid resolutions in CFD fire modeling of wide opening spill plumes. Focus are on an axisymmetric plume supplying smoke to an approach flow (emerged ceiling jet), the rotation of the approach flow around the spill edge and into the emerging wide opening spill plume. The approach flow is not restricted by any reflecting compartment walls in order to create a weak line source for the wide opening spill plume, and to remove the impact of reflected flow from the compartment walls on the ceiling jet. Modeled parameters are:

Grid spacing - Simulations with five systematically refined grid spacings ranging from $\Delta x = \{0.80, 0.40, 0.20, 0.10, 0.05\}$ m for the axisymmetric plume, approach flow/ceiling jet and the rotation region, and $\Delta x = \{1.60, 0.80, 0.40, 0.20, 0.10\}$ m for the spill plume.

Fire compartment - The fire compartment properties where kept constant throughout the simulation series.

Fire size - All fire properties where kept constant throughout the simulation series including fire location, extents and heat release rate. The total heat release rate of the fire $\dot{Q}_T$ was fixed at 5,000 kW to address design fires within the range common in Denmark.

Combustion - Propane was chosen for the combustion process throughout the grid convergence study.

Grid resolution - The grid resolution is described relative to the characteristic length scale of that particular flow region, i.e. relative to the size of the fire source. This serves to address resolutions of comparable fire sizes and heat release rates in a similar setup.

2.8.3 Simulations Breakdown

Simulations carried out in the grid convergence study are listed in Table 2.1 with applied total heat release rate $\dot{Q}_T$ $[kW]$, grid spacing Δx $[m]$ and averaging time period $\bar{t}$ $[s]$.

2.8.4 Measurements

Mean velocities $\mathbf{U} \in \{U, V, W\}$ and temperatures T are predicted by the CFD fire model at parallel two-dimensional sections of the flow regions described in Section 2.7.

Mass flow rates $\dot{m}_p$ of plumes are heavily dependent on the temperature field due to the density (inversely proportional to the temperature) and evidently through the temperature induced buoyancy controlled velocity field. Hence the mass flow rate for a particular fire gives a good indication of how accurately the model predicts average core temperatures, velocities, entrainment and smoke

Simulation ID	$\dot{\mathbf{Q}}_{\mathbf{T}}$ **[kW]**	$\boldsymbol{\Delta}$**x [m]**	$\bar{\mathbf{t}}$ **[s]**
plume080	5000	0.80	30
plume040	5000	0.40	30
plume020	5000	0.20	30
plume010	5000	0.10	30
plume005	5000	0.05	30
ceiling080	5000	0.80	30
ceiling040	5000	0.40	30
ceiling020	5000	0.20	30
ceiling010	5000	0.10	30
ceiling005	5000	0.05	30
rotation080	5000	0.80	30
rotation040	5000	0.40	30
rotation020	5000	0.20	30
rotation010	5000	0.10	30
rotation005	5000	0.05	30
spill160	5000	1.60	30
spill080	5000	0.80	30
spill040	5000	0.40	30
spill020	5000	0.20	30
spill010	5000	0.10	30

Table 2.1 *Grid convergence study: List of simulations.*

production in the bulk flow. To limit data output, convergence trends are only addressing mass flow rates in flow regions defined in Section 2.7. Simple validations of predicted velocities and temperatures against engineering relations serve to assess the accuracy of the model in predicting basic flow properties.

To decouple the mass flow rate $\dot{m}$ (and profile width b) in each flow region from any upstream effects (grid spacing, interpolation effects at the multi-grid interface etc.), all mass flow measurements (and profile widths) are reported relative to the initial mass flow rate $\dot{m}(0)$ (or profile width $b(0)$) upon entering the flow region:

$$\Delta\dot{m} = \dot{m}_i - \dot{m}(0) \tag{2.8.4a}$$

$$\Delta b = b_i - \dot{b}(0) \tag{2.8.4b}$$

where i designates the position of the flow section measurement.

Positions are reported on non-dimensional form relative to the characteristic length scale, e.g. elevations above the fire base z is reported relative to the characteristic length scale, e.g. D_i^*, see Eqn. (2.5.4b):

$$z^* = \frac{z}{D_i^*} \tag{2.8.5}$$

Grid resolutions are reported as the ratio of the characteristic length scale D_i^* to the grid spacing Δx:

$$n^* = \frac{D_i^*}{\Delta x} \tag{2.8.6}$$

i.e. a measure of how many grid cells span the characteristic length scale D_i^*.

2.9 CFD Model Setup

2.9.1 Modeling Procedure

The CFD model *Fire Dynamics Simulator ver. 4.06*, described in Section 2.4, has been applied in the grid convergence study.

The flow regions mentioned in Section 2.7 are modeled individually including only upstream regions in the individual simulations. Upstream flow regions are modeled at a fixed grid spacing of Δx=0.2 m. Computations are run until at least 30 s of steady state convective heat flow rate $\dot{Q}_c$ out through the computational domain boundaries has been achieved. Flow properties are averaged over the steady state time period $\tilde{\tau}$ (at least 30 s) with the conversion program *fds2ascii*[8] and saved for external data processing.

To avoid any discontinuous behavior in the CFD model, the flame sheet correction has been switched off, see Section 2.4.3, in the grid convergence study.

2.9.2 Computational Grid and Boundary Conditions

To allow for an analysis of the grid convergence at high elevations, the study of the axisymmetric region is conducted in a separate grid setup from the approach, rotation and spill plume regions. The grid is rectilinear and equidistant throughout grid #1. The geometrical ranges in the axisymmetric setup are outlined in Figure 2.7(a) and Figure 2.7(b). Boundary conditions are shown on the former figures and designated in Table 2.2. Grid spacings are systematically refined ranging from $\Delta x = \{0.80, 0.40, 0.20, 0.10, 0.05\}$ m.

Sketches of the computational grid along with geometrical dimensions applied in the grid convergence study of the approach flow, rotation and spill plume regions are shown in Figure 2.8(a) and Figure 2.8(b). Boundary conditions are shown on the former figures and designated in Table 2.2. All grids are rectilinear and equidistant within flow regions, i.e. #1-#4 in Figure 2.8(a) and Figure 2.8(b). Grid spacings are systematically refined ranging from $\Delta x = \{0.80, 0.40, 0.20, 0.10, 0.05\}$ m for approach flow/ceiling jet and the rotation region, and $\Delta x = \{1.60, 0.80, 0.40, 0.20, 0.10\}$ for the spill plume.

2.9.3 Measuring Positions

Measurements are recorded using the *slice file* (SLCF) output option in FDS at positions listed in Table 2.3 along with recorded quantities.

[8]Distributed with the Fire Dynamics Simulator package.

Designation	**Line type**	**BC type**	**FDS type**
Outflow	Dashed	Passive vent	*OPEN*
Floor	Solid	Adiabatic/partial slip	*ADIABATIC*
Walls	Solid	Adiabatic/partial slip	*ADIABATIC*
Ceiling	Solid	Adiabatic/partial slip	*ADIABATIC*
Fire base	Solid	Steady HRR	*HRRPUA*

Table 2.2 *Boundary conditions according to designations in Figures 2.7 and 2.8.*

Region	**Quantity**	**Position**
Axisymmetric	T,u,v,w	$z \in \{0.8, 2.4, 4.8, 7.2, 9.6, 12.0, 14.4\}$ m
Approach flow	T,u,v,w	$x \in \{7.8, 9.4, 11.0, 12.6, 14.2\}$ m
Rotation	T,u,v,w	$z \in \{6.6\}$ m
Spill plume	T,u,v,w	$z \in \{12.0, 16.8, 21.6, 26.4, 31.2\}$ m

Table 2.3 *Measured quantities and positions relative to the dimensions in Figure 2.7 and Figure 2.8.*

2.9.4 CFD Model Inputs

In this grid convergence study CFD modeling is carried out with the full hydrodynamic model including LES turbulence model, propane combustion, radiation model and adiabatic surface boundary conditions. Primary and non-default input parameters are listed in Table 2.4.

Turbulence model		
Smagorinsky constant	C_s	0.2
Prandtl number	Pr	0.5
Schmidt number	Sc	0.5
Combustion model		
Material	Propane	Default FDS v. 4.06
Heat of combustion	ΔH_c	47,251 kJ/kg
Radiative fraction	χ_r	0.286
Molecular weight	M_w	44.00 g/mol
Soot yield	y_s	0.01 kg/kg
Fire source		
Fire base area	A_f	3.2^2 m^2
Specific HRR	$\dot{Q}''_T$	488 kW/m^2
Flame sheet correction	*AUTOMATIC_Z*	*FALSE*
Radiation model		
Radiative model		Gray gas/non-scat.
Update time steps	*TIME_STEP_INC.*	12
Angle increment at update	*ANGLE_INC.*	20
Surface BCs		
Thermal model		Adiabatic
Ghost cell temperature	T_{ghost}	T_g
Velocity model		Partial slip
Wall velocity	u_τ	$0.5u_i$
Flow BCs		
Flow model	Passive vent	*OPEN*
Ambient temperature	T_∞	293 K
Ambient velocity	$\mathbf{u}$	0 m/s
Ambient perturbed pressure	$\tilde{p}$	0 Pa
Ambient static pressure	p_0	1.013 10^5 Pa

Table 2.4 *Grid convergence study: Model input parameters.*

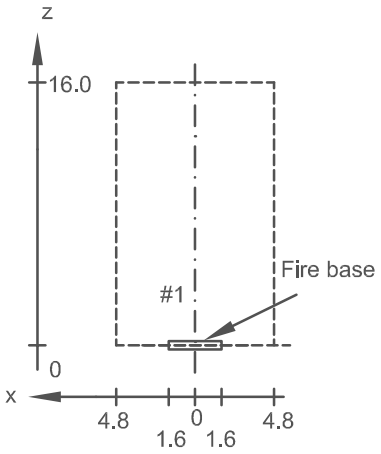

(a) Vertical section.

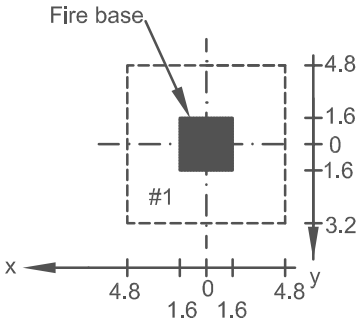

(b) Horizontal section.

Figure 2.7 *Axisymmetric plume region: CFD model.*

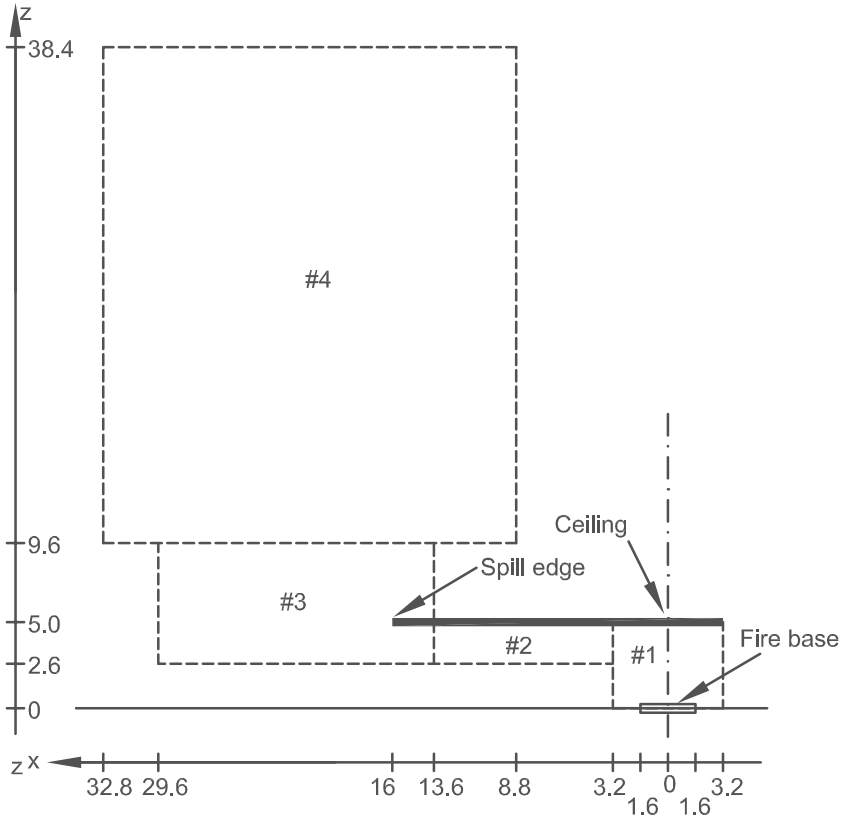

(a) Vertical section.

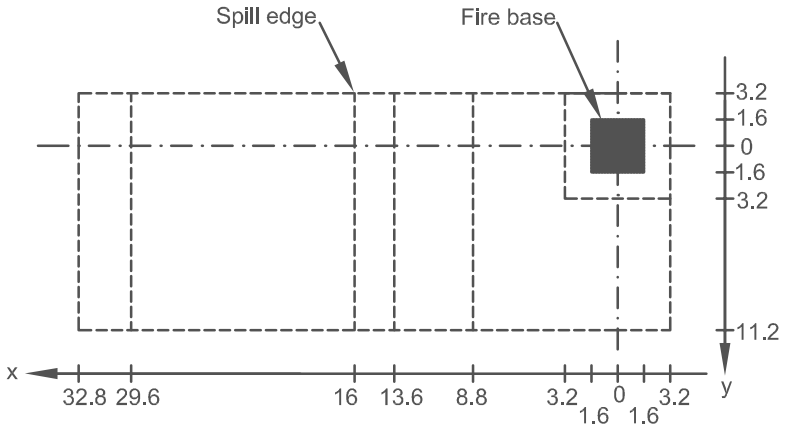

(b) Horizontal section.

Figure 2.8 *Other regions: CFD model.*

2.10 Results of Grid Convergence Study

2.10.1 Axisymmetric Flow Region

Characteristics of the axisymmetric plume region with respect to CFD fire modeling are:

Characteristic length scale - The characteristic fire diameter D_p^* from Eqn. (2.5.4b) is applied.

Entrainment - The flow is driven by buoyancy and the smoke production is highly dependent on the grid resolution because of the turbulence model.

Combustion processes - A high grid resolution is required to accurately predict the mean flame length L_f and temperature gradients in the plume region.

Center-of-mass - The flow profiles are symmetric about the plume center line and the position is independent of the grid resolution.

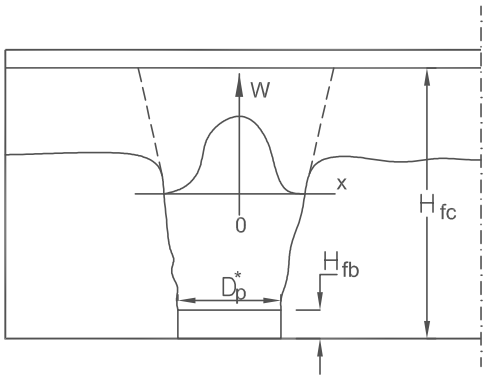

Figure 2.9 *Axisymmetric plume region.*

From profiles of temperature, Figure 2.10, and velocity, Figure 2.11, it is clear that FDS under predicts temperatures for low plume resolutions. Velocities in the plume are induced by buoyancy (i.e. temperature rise), and thus also prone to under prediction. Taking the non-dimensional mean flame height in the study $L_f^* = L_f/D^* = 2.1$ into consideration, there is no clear evidence that the predictions are more accurate above the mean flame height. It can be seen that the width of the plume increases with height above the fire base in agreement with the increasing turbulent length scale.

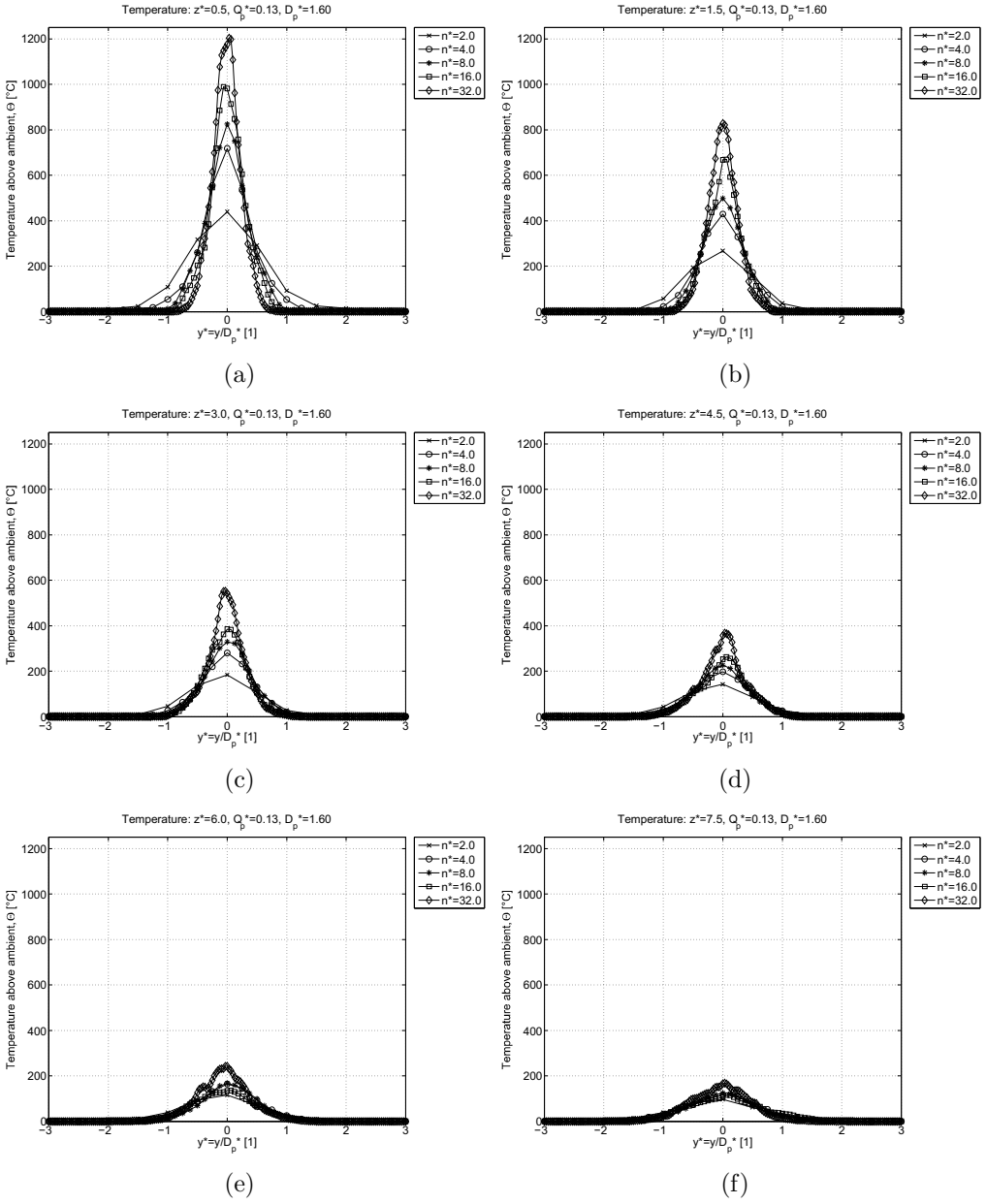

Figure 2.10 *Axisymmetric plume region: Temperature profiles.*

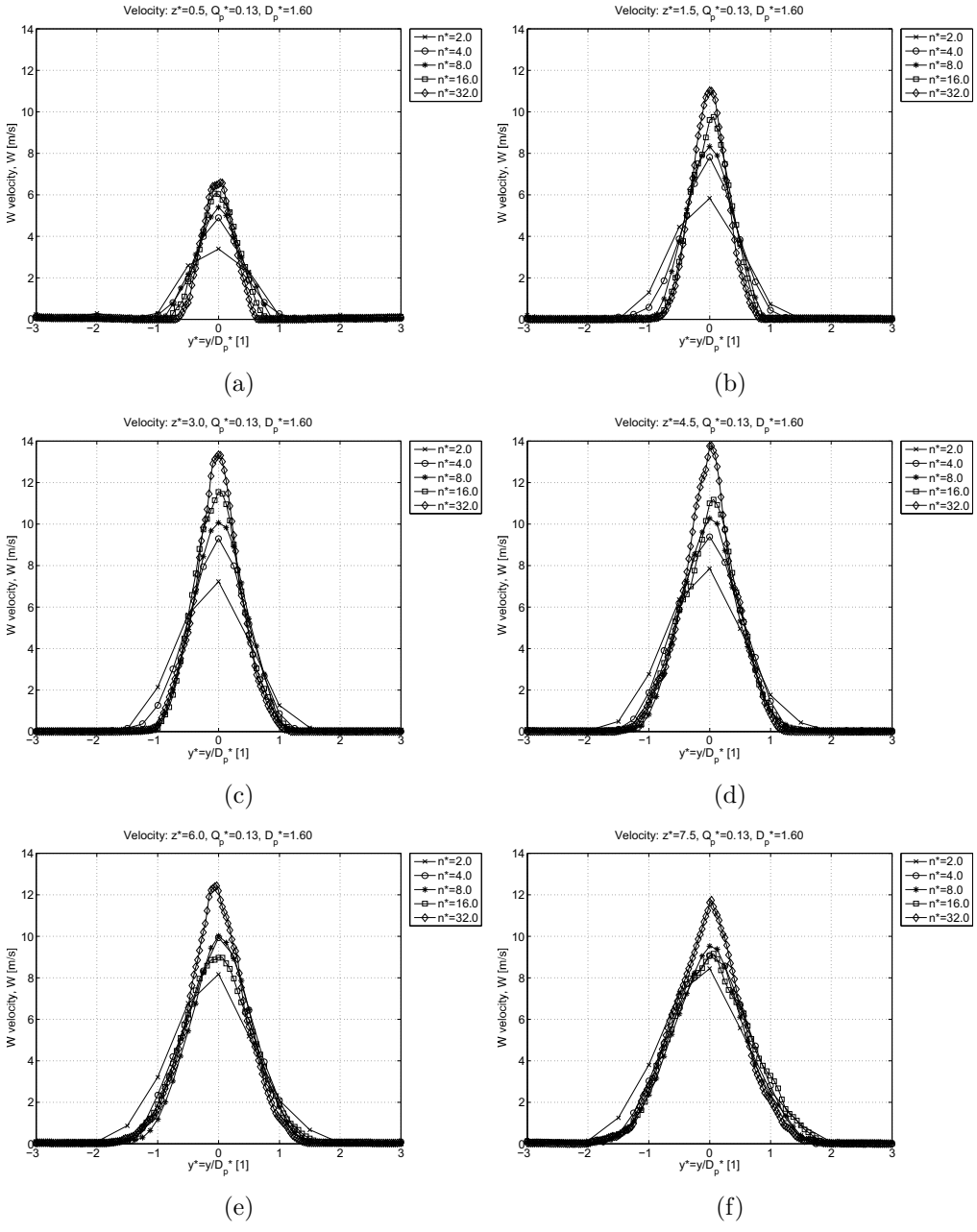

Figure 2.11 *Axisymmetric plume region: W velocity profiles.*

As a measure of the increasing turbulent length scale with rising height, the plume width b is computed following the approach suggested by Heskestad (1984):

$$b = w_p \,|_{T=0.5T_{max}} \tag{2.10.1}$$

where w_p is the width of the temperature profile (i.e. plume) at the point where the temperature has decreased to 50% of T_{max} $[K]$ in the profile (i.e. on the center line for an axisymmetric plume. Note that Heskestad (1984) used the nomenclature b for plume radius, whereas this study uses b for the entire width (i.e. diameter in an axisymmetric plume).

In recognition of the increasing turbulent length scale the resolution of the flow profiles in Figure 2.10 and Figure 2.11 increases with a fixed grid spacing Δx. Defining the resolution of the flow profile relative to the profile width b instead of the fixed characteristic length scale D_i^* yields a relative measure of resolution, b^* [1]:

$$b^* = \frac{b}{\Delta x} \tag{2.10.2}$$

i.e. a measure of how many grid cells span the profile width.

Convergence trends for the mass flow rates $\dot{m}_p$ of the axisymmetric plume are depicted in Figure 2.12. From Figure 2.12 it can be seen that for rising heights $z^* \leq 6$, i.e. six times the characteristic fire diameter D_p^*, the solution converges for resolutions close to $n^* \gtrsim 15$, which supports the findings in Bounagui et al. (2003). For elevations $z^* > 6$ the discrepancy between succeeding grid refinements increases, thus a clear convergence trend can not be identified. One might argue that the lack of convergence is influenced by the outflow boundary conditions at the top of the computational domain. At the highest elevation data is collected at least 2 to 32 (corresponding to $n^* \in [2 : 32]$) control volumes from the computational boundary. If the lack of convergence was (primarily) influenced by the boundary condition an increasing number of grid cells between the measuring elevation and the boundary should dampen out the effect of the boundary condition. This trend is not observed in Figure 2.12 since discrepancies between successive refinements increase even for the last two grid refinements. To handle the increasing number of control volumes, the simulation for $n^* = 32$ (> 20 mill. control volumes) was conducted on a parallel computer architecture with grid interfaces perpendicular to the bulk flow. As it is shown in Appendix A perpendicular multi-grid interfaces do not introduce any large errors in conserved bulk flow quantities, thus the lack of convergence is not attributed to the use of multi-grids in the simulation. This conclusion is also supported by the fact that the discrepancy increases for refinements from $n^* = 8 \rightarrow 16$, where single grids are adopted.

Looking at the computed order p of the numerical method, see Figure 2.13, it is evident that the order is not consistent with the theoretical order of $p \in [1 : 2]$ derived in Section 2.4.8. The order ranges from $\approx$0.1 to $\approx$2 and even a negative order can be observed at the second highest elevation, indicating that the discretization error increases with grid refinement. From Section 2.8.1 it can be seen that the order of the method only addresses systems of linear PDEs,

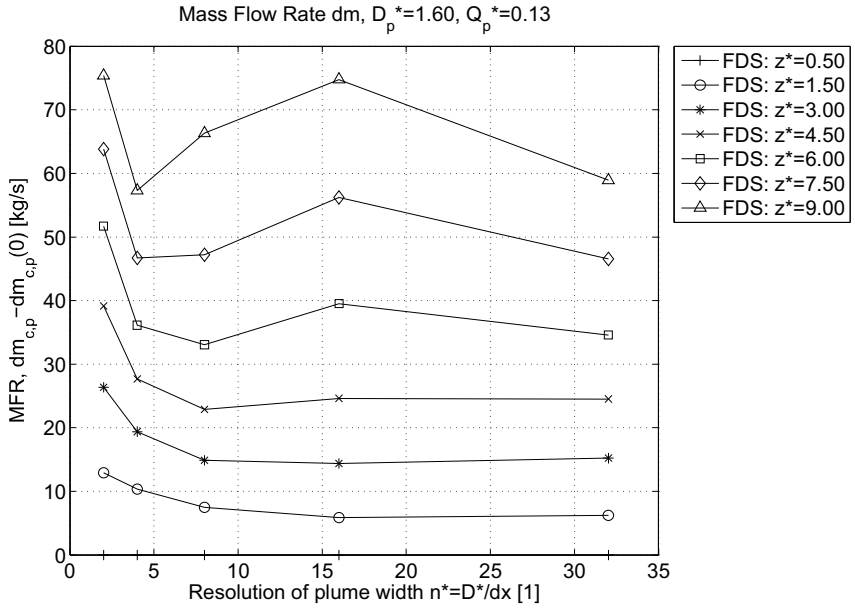

(a) Resolution relative to characteristic length scale D_p^*.

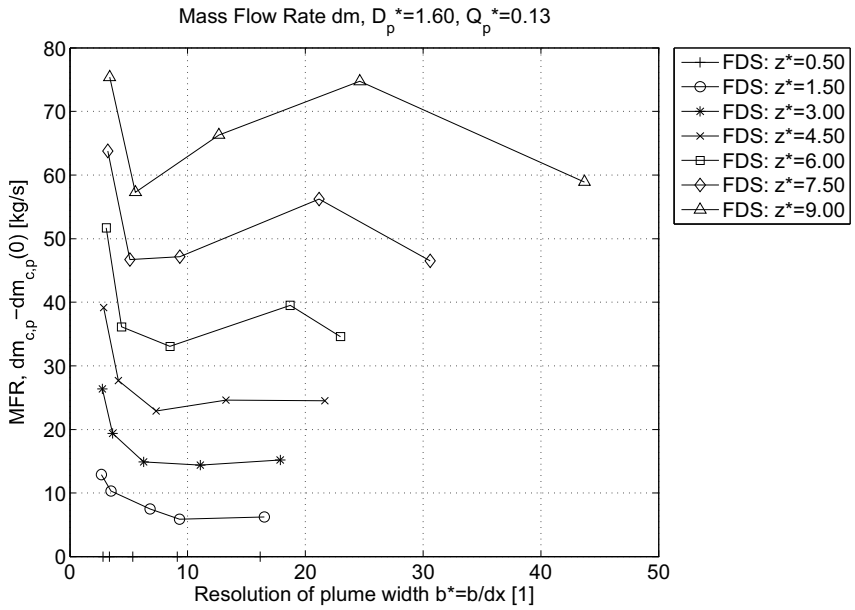

(b) Resolution relative to plume width b.

Figure 2.12 *Axisymmetric plume region: Convergence trends.*

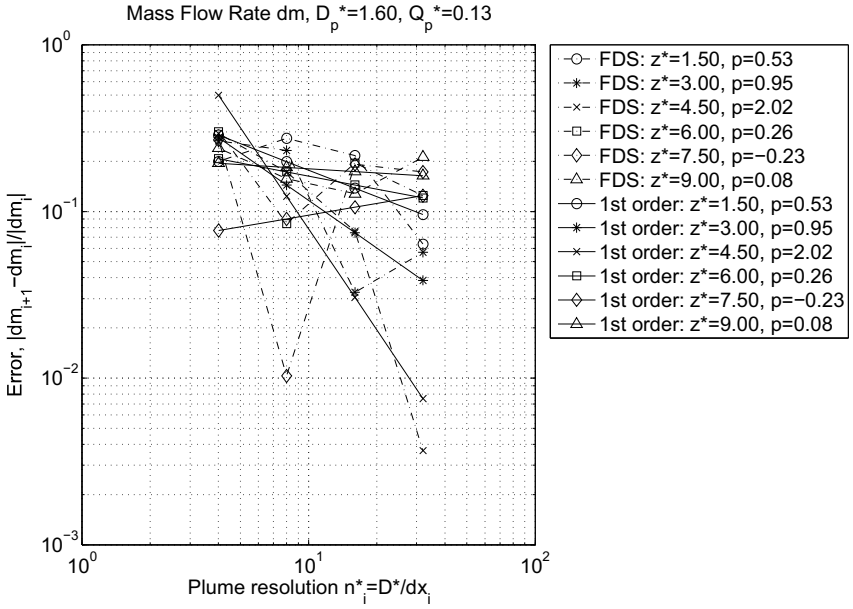

(a) Resolution relative to characteristic length scale D^*.

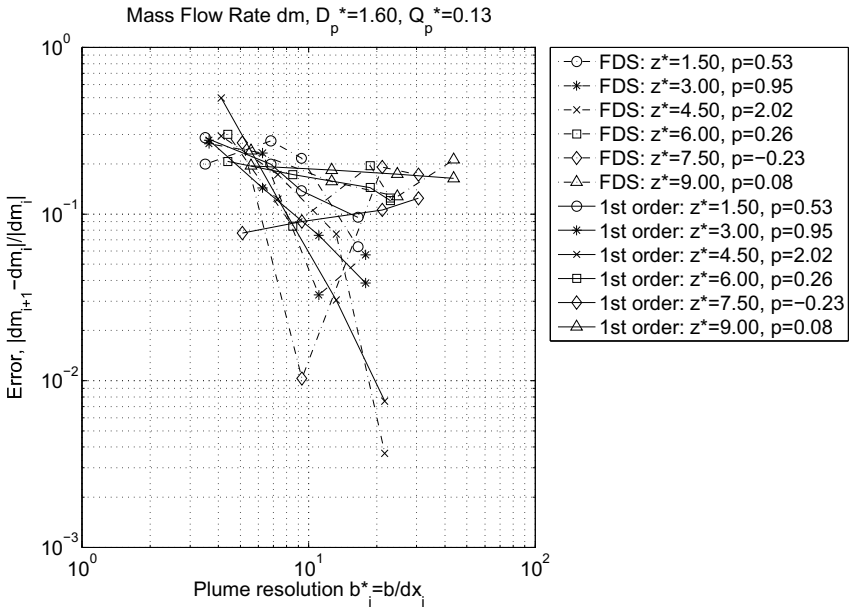

(b) Resolution relative to plume width b.

Figure 2.13 *Axisymmetric plume region: Order of numerical method.*

which is also noted in Ferziger & Perić (2002), and is also dependent on the order of the boundary conditions. Thus one can not expect to compute the theoretical order from the predicted bulk flow quantities, not only due to the lower order boundary conditions, but to a great extent also the highly buoyancy and turbulence dominated flow field exhibiting highly nonlinear behavior. It is worth noting that except for the data set with the negative order p, all other elevations exhibit decreasing magnitude of the discretization error as expected.

Figure 2.14 shows the increasing turbulent length scale by the increasing width of the core plume b, see Eqn. (2.10.1). Comparing this to the increasing resolution of the flow profiles with increasing rising height z, see Figure 2.12(b), it is proposed to allow for scaling of the grid spacing $\Delta\mathbf{x}$ by the plume width b:

$$\frac{\Delta\mathbf{x}(z_{i+1})}{b(z_{i+1})} = \frac{\Delta\mathbf{x}(z_i)}{b(z_i)} \tag{2.10.3}$$

Heskestad (1984) proposed a relation for the radius $b_{Heskestad}$ $[m]$ of the axisymmetric plume where the temperature has decreased to 50% of the temperature on the centerline T_0 $[K]$:

$$b = 2\, b_{Heskestad} = 2 \cdot 0.12 \left(\frac{T_0}{T_\infty}\right)^{1/2} (z - z_0) \tag{2.10.4}$$

The coefficient of two was introduced to relate the proposed radius $b_{Heskestad}$ to the width of the plume (i.e. diameter). The centerline temperature T_c can be determined from Heskestad (1984):

$$\Delta T_0 = 9.1 \left(\frac{T_\infty}{g\, c_p^2 \rho_\infty^2}\right)^{1/3} \dot{Q}_c^{2/3} (z - z_0)^{-5/3} \tag{2.10.5}$$

Determining the plume width ratio for a position z above the fire base $z = 0$ using Eqn. (2.10.4) yields:

$$\frac{b}{b(0)} = \frac{2 \cdot 0.12 \left(\frac{T_0}{T_\infty}\right)^{1/2} (z - z_0)}{2 \cdot 0.12 \left(\frac{T_0}{T_\infty}\right)^{1/2} (-z_0)} \tag{2.10.6a}$$

$$= 1 - \frac{z}{z_0} \qquad \forall\, z_0 < 0 \tag{2.10.6b}$$

Combining Eqn. (2.10.3) and Eqn. (2.10.6b) provides an initial guess for the scaling of the initial equidistant grid size $\Delta\mathbf{x}$ above the fire as a function of rising height z:

$$\frac{b}{b(0)} = 1 - \frac{z}{z_0} \qquad \forall\, z_0 < 0 \tag{2.10.7a}$$

$$\frac{\Delta\mathbf{x}\,(z)}{\Delta\mathbf{x}\,(0)} = 1 - \frac{z}{z_0} \qquad \forall\, z_0 < 0 \tag{2.10.7b}$$

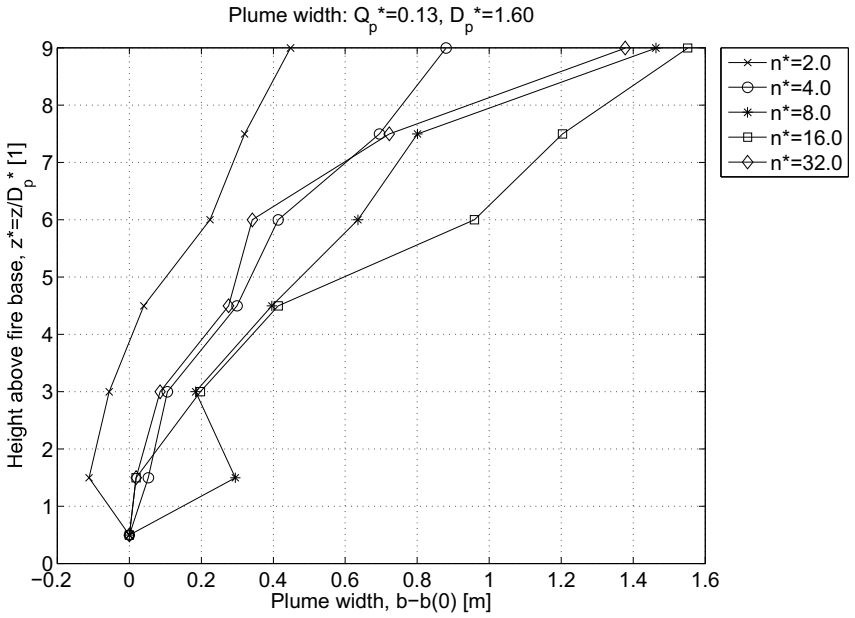

Figure 2.14 *Axisymmetric plume region: Width of temperature profile b.*

Mass flow rates in axisymmetric plumes have been studied extensively and selected correlations for mass flow rates $\dot{m}_p$ $[kg/s]$ are provided in Eqn. (2.10.8) for validation purposes of CFD fire simulations. Heskestad (1986) proposed that the mass flow rate below the mean flame height L_f $[m]$ was proportional to the height above the fire base z, see Eqn. (2.10.8a). Studies of the weak plume assumption for a heated point source were conducted by Yih (1952) leading to the mass flow rate in a weak plume Eqn. (2.10.8b). Heskestad (1986) proposed to extend the weak plume model to strong plumes, which by adopting data from Cetegen, et al. (1984) lead to Eqn. (2.10.8c).

$$\dot{m}_p = 0.0056\dot{Q}_c\frac{z}{L_f} \tag{2.10.8a}$$

$$\dot{m}_p = 0.153\left(\frac{g\rho_\infty^2}{c_pT_\infty}\right)^{1/3}\dot{Q}_c^{1/3}\left(z-z_0\right)^{5/3} \tag{2.10.8b}$$

$$\dot{m}_p = 0.196\left(\frac{g\rho_\infty^2}{c_pT_\infty}\right)^{1/3}\dot{Q}_c^{1/3}\left(z-z_0\right)^{5/3}\ldots \cdot\left(1+\frac{2.9\dot{Q}_c^{2/3}}{\left(g^{1/2}c_p\rho_\infty T_\infty\right)^{2/3}\left(z-z_0\right)^{5/3}}\right) \tag{2.10.8c}$$

where the distance to the virtual fire origin z_0 $[m]$ proposed by Heskestad (1983) is:

$$z_0 = 0.083\dot{Q}_T^{2/5} - 1.02D \tag{2.10.9}$$

Here D is the fire diameter $[m]$ and $\dot{Q}_T$ is the total heat release rate $[kW]$. Heskestad (1983) also proposes a correlation for the mean flame height L_f:

$$L_f = 0.235\dot{Q}^{2/5} - 1.02D \tag{2.10.10}$$

The engineering relations for mass flow rates in Eqn. (2.10.8) are plotted against computed mass flow rates from FDS in Figure 2.15. Cetegen et al. (1984) found

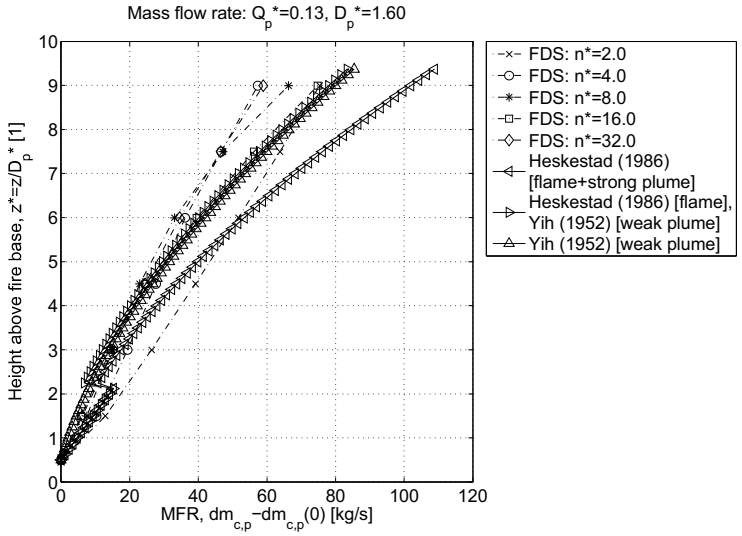

Figure 2.15 *Axisymmetric plume region: Validation with simple correlations for mass flow rates* $\dot{m}_l$.

that the correlation Eqn. (2.10.8b) over predicted the mass flow rate at high elevations which partly explains the increasing discrepancy between the FDS simulations and the depicted correlations in Figure 2.15. With respect to the resolution n^* it is not evident that resolutions $n^* \gtrsim 8$ yield more accurate predictions over the entire plume range (flame and thermal plume) when compared to engineering relations.

2.10.2 Approach Flow Region

Characteristics of the approach flow region with respect to CFD fire modeling are:

Approach flows - The velocity of a fire induced flow approaching a wide opening is to a large extent determined by the emerged ceiling jet. Thus for a simple assessment of the resolution of the approach flow, engineering relations for a ceiling jet can be applied. The actual approach flow is expected to be deeper (about 20% of the ceiling height for wide openings) but with a more homogeneous temperature profile for the bulk flow as opposed to the ceiling jet.

Characteristic length scale - According to Klote & Milke (2002) the depth of the ceiling jet is in the range 10% to 20% of the height from the fire base to the ceiling, the former attributed to an unconfined ceiling jet, the latter attributed to twice the depth because of flows reflected from the compartment walls. The present study is carried out for unconfined flows, i.e. the characteristic length scale of the approach flow should always be applied as:

$$D^*_{cj} = 0.1 H_{fc} \tag{2.10.11}$$

The constraints on the grid resolution derived in the present study should be applied to the entire depth of the approach flow, i.e. not only restricted to the top 10% of the fire compartment if the flow is reflected.

Entrainment - The ceiling jet is only induced by buoyancy but not subjected to a rising plume, hence entrainment in the ceiling jet is of little importance in fire safety engineering. In modeling velocities, temperatures and smoke concentrations in the ceiling jet, e.g. to determine detector activation times, an adequately resolved ceiling jet is crucial. Since the numerical method is mass conserving by nature, it is less important to adequately resolve the ceiling jet if it's modeling purpose is to serve as a line source for the spill plume.

The center-of-mass of the flow profiles - The flow profiles of the ceiling jet are not symmetric, i.e. the position of the center of mass of the profiles is of importance in assessing the resolution of the flow.

Theoretically the fluid is at rest at the wall, thus the velocity profile is forced to *"bend backward"* close to the wall and an adequately resolved flow profile must exhibit this behavior. Looking at the velocity profiles in Figure 2.18 it can be seen that only the two finest resolutions $n^* = \{5, 10\}$ meet this requirement. The temperature profiles in Figure 2.17 changes qualitatively for resolutions below $n^* < 2.5$, where the profile deepens considerably compared to the profiles with higher resolutions.

In comparing the profiles of the ceiling jet in Figure 2.17 and Figure 2.18 to the profiles of the axisymmetric plume in Figure 2.10 and 2.11, the lack of

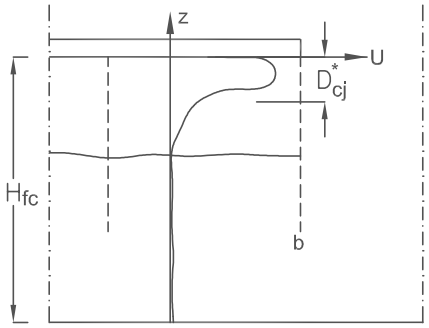

Figure 2.16 *Approach flow region.*

entrainment in the bulk flow is evident as the depths of the core flow profiles, see Eqn. (2.10.1), are roughly constant.

Convergence trends for the mass flow rates and center-of-mass (COM) of the heat flow profiles of the ceiling jet are depicted in Figure 2.19. The location of the COM is obviously dependent on the grid resolution, however discrepancy is only about 2% and thus only considered weakly dependent on the grid resolution. The mass flow rate converges for the first four grid resolutions, but changes rapidly with the finest grid resolution $n^* = 10$. Disregarding the finest resolution, convergence is achieved for $n^* \gtrsim 3$, however the velocity profile does not exhibit the expected behavior, thus $n^* \gtrsim 5$ is recommended an adequately resolved profile.

All measurements are recorded within the same computational grid, thus the behavior can not be attributed to interpolation errors in the interface between multi-grids. From the profiles in Figure 2.18 it is apparent that the velocity profile deepens considerably for the finest grid resolution compared to the other profiles. This should however not initiate an increased mass flow rate since buoyancy effects are negligible in the ceiling jet and mass flow is conserved.

The computed order of the numerical method is found to be roughly $p \approx 1$. A higher order is not considered plausible since the ceiling jet flow is dominated by the wall velocity boundary condition of first order, see Section 2.4.5.

The steady decreasing discretization error for the ceiling jet, see Figure 2.20, is attributed to the dominating wall velocity boundary condition, and less influenced by the dominating buoyancy and turbulence forces in the buoyant plume regions.

Maximum temperatures and velocities of the ceiling jet are validated against engineering relations to assess the scatter of the CFD data. Heskestad & Delichatsios (1973) carried out an extensive large number of scale studies proposing Eqn. (2.10.12a) and Eqn. (2.10.13a) for maximum temperature and velocity in a ceiling jet under an unconfined ceiling. Alpert (1972) also carried out a large number of scale studies including a number of full-scale experiments bounded by $r/H_{fc} < 2.2$ and proposed the correlations in Eqn. (2.10.12b) for temperature

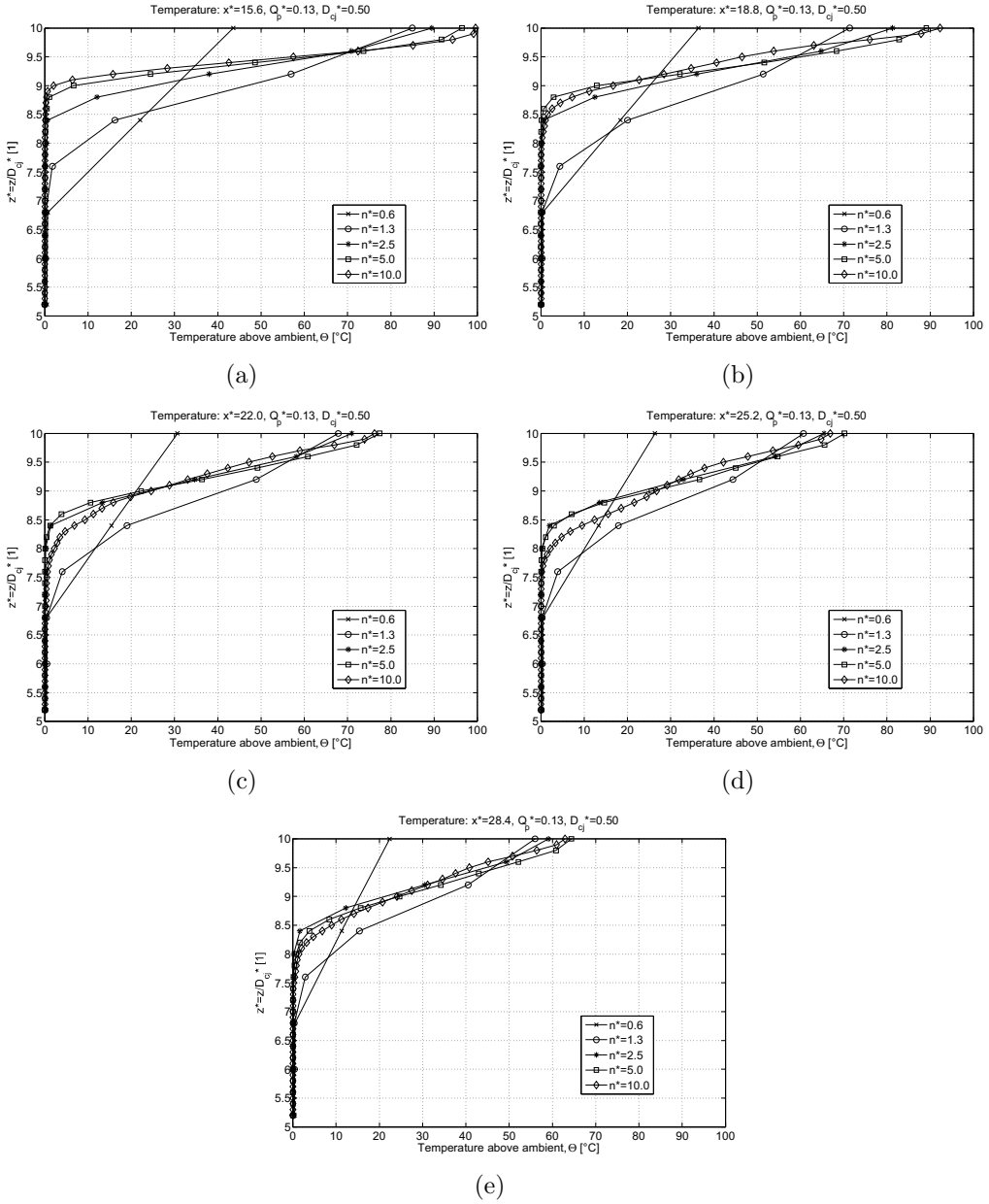

Figure 2.17 *Approach flow region: Temperature profiles.*

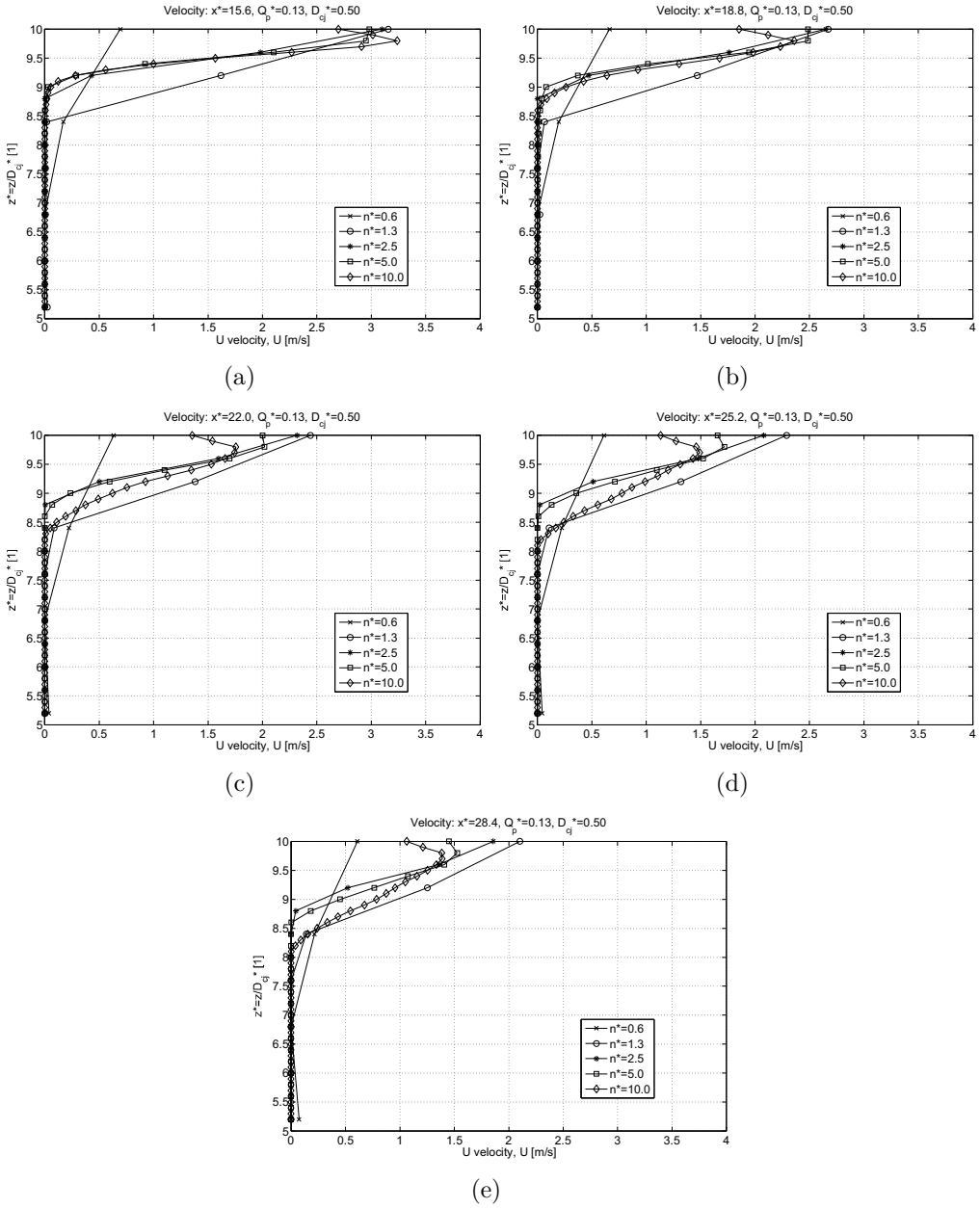

Figure 2.18 *Approach flow region: W velocity profiles.*

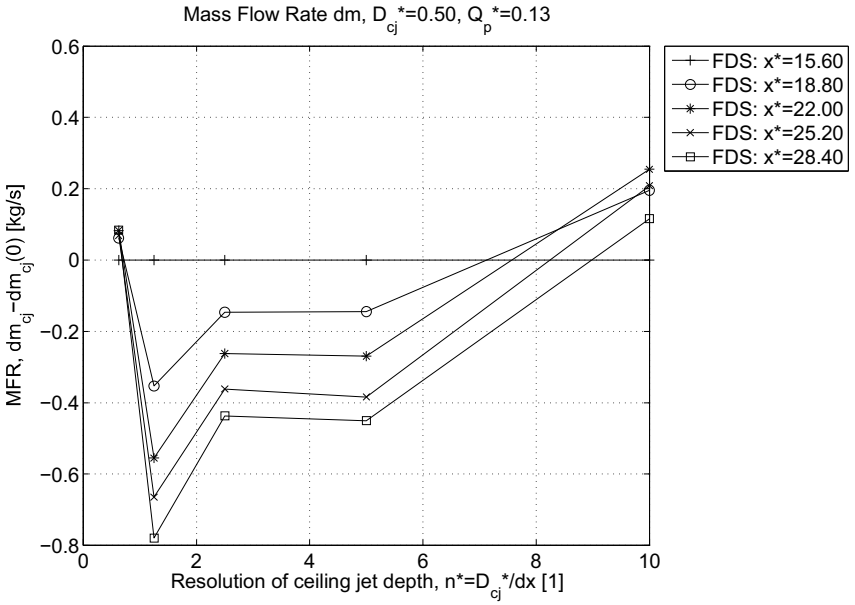

(a) Resolution relative to characteristic length scale D^*_{cj}.

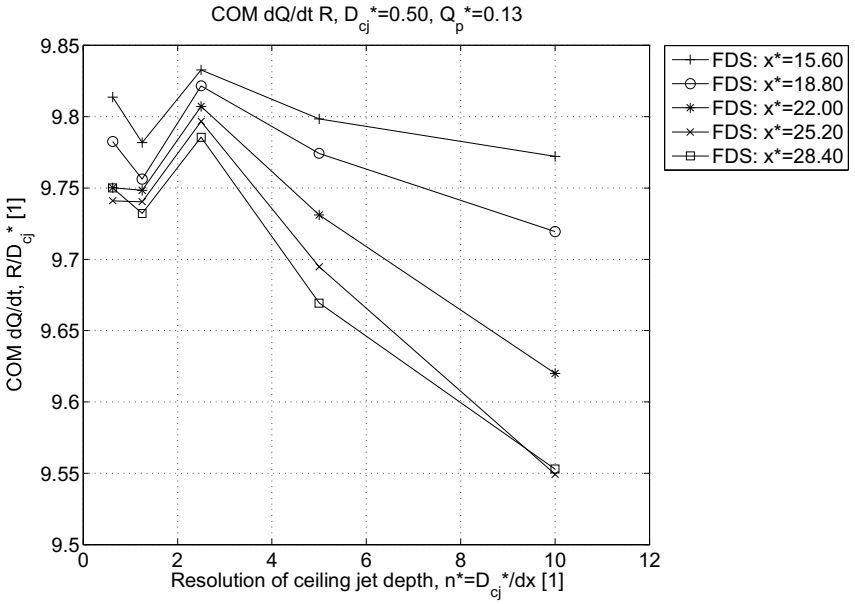

(b) Convergence trend relative to characteristic length scale D^*_{cj} of the center-of-mass of heat flow profile.

Figure 2.19 *Approach flow region: Convergence trends.*

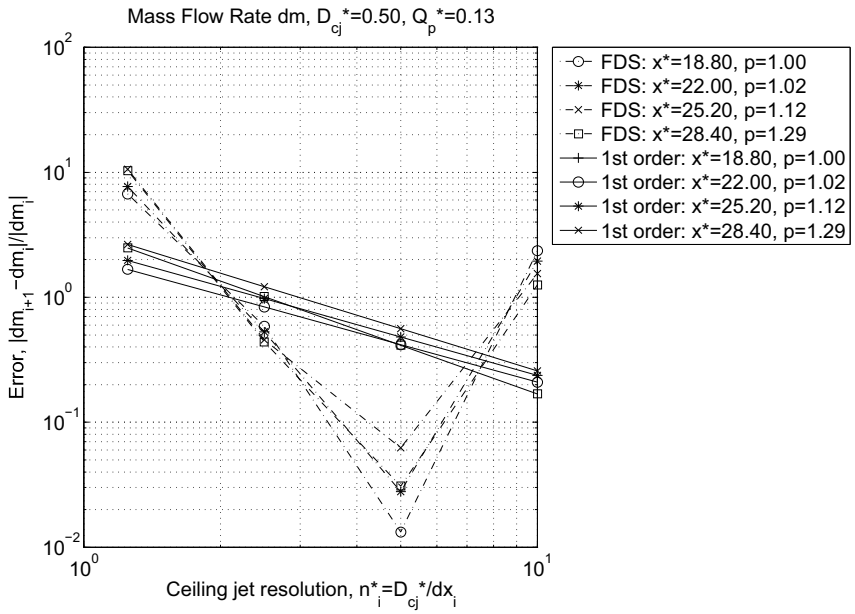

(a) Resolution relative to characteristic length scale D^*_{cj}.

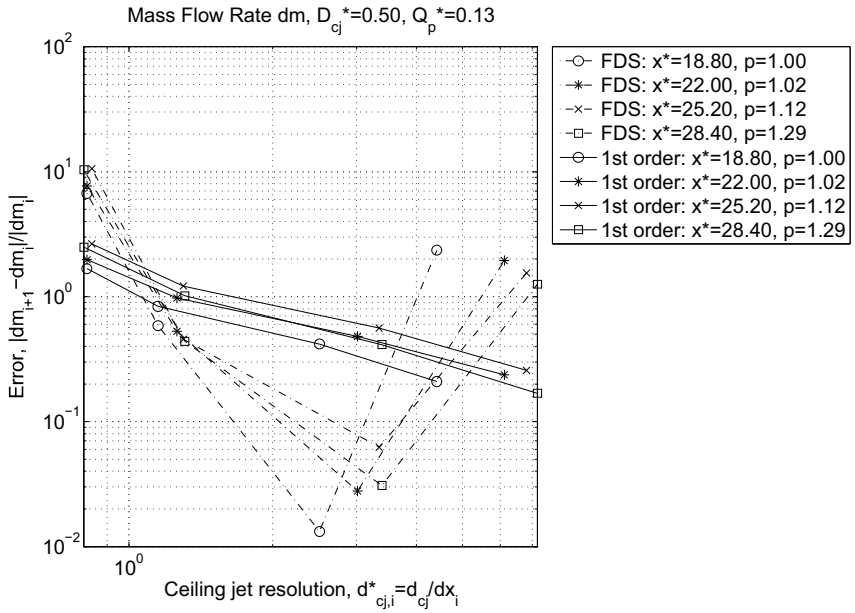

(b) Resolution relative to depth of ceiling jet d_{cj}.

Figure 2.20 *Approach flow region: Order of numerical method.*

and Eqn. (2.10.13b) for maximum velocities. Finally Cooper (1982) conducted a less comprehensive study than the former, arriving at the correlations for maximum temperature Eqn. (2.10.12c) and velocity Eqn. (2.10.13c):

$$\Delta T_{max} = 2.75 \left(0.188 + 0.313 \frac{r}{H_{fc}}\right)^{-4/3} \dot{Q}_T^{2/3} H_{fc}^{5/3} \quad \forall \ \frac{r}{H} \in [0.0; 8.0] \tag{2.10.12a}$$

$$\Delta T_{max} = 5.38 \left(\frac{r}{H_{fc}}\right)^{2/3} \dot{Q}_T^{2/3} H_{fc}^{5/3} \quad \forall \ \frac{r}{H} \geq 0.18 \tag{2.10.12b}$$

$$\Delta T_{max} = 5.77 \left(\frac{r}{H_{fc}}\right)^{-0.88} \dot{Q}_T^{2/3} H_{fc}^{5/3} \quad \forall \ \frac{r}{H} \geq 0.75 \tag{2.10.12c}$$

and velocity Eqn. (2.10.13c):

$$U_{max} = 0.179 \frac{\left(\frac{r}{H_{fc}}\right)^{-0.63}}{\left(0.188 + 0.313 \frac{r}{H_{fc}}\right)^{2/3}} \left(\frac{\dot{Q}_T}{H_{fc}}\right)^{1/3} \quad \forall \ \frac{r}{H} \in [0.4; 8.0] \tag{2.10.13a}$$

$$U_{max} = 0.197 \left(\frac{r}{H_{fc}}\right)^{-5/6} \left(\frac{\dot{Q}_T}{H_{fc}}\right)^{1/3} \quad \forall \ \frac{r}{H} \geq 0.18 \tag{2.10.13b}$$

$$U_{max} = 0.26 \left(\frac{r}{H_{fc}}\right)^{-1.1} \left(\frac{\dot{Q}_T}{H_{fc}}\right)^{1/3} \quad \forall \ \frac{r}{H} \geq 1.03 \tag{2.10.13c}$$

The validations of the predicted U velocities and temperatures with engineering relations are shown in Figure 2.21. The predictions of the temperature are in good agreement with the empirical correlations. However the maximum velocities are somewhat higher than computed with the engineering relations. Following the discussion in Appendix B the discrepancy is most likely attributed to the lack of information about the wall velocity boundary condition in the experimental setup. In Appendix B it was shown that by changing the wall velocity boundary condition, the maximum velocity in the profile can be reduced. Modeling boundary flows require detailed information about the wall boundary conditions which is not provided by the authors of the applied engineering relations. However all correlations refer to maximum quantities, hence thermal boundary conditions in the experimental setup must correspond to near adiabatic conditions in accordance with the model boundary condition.

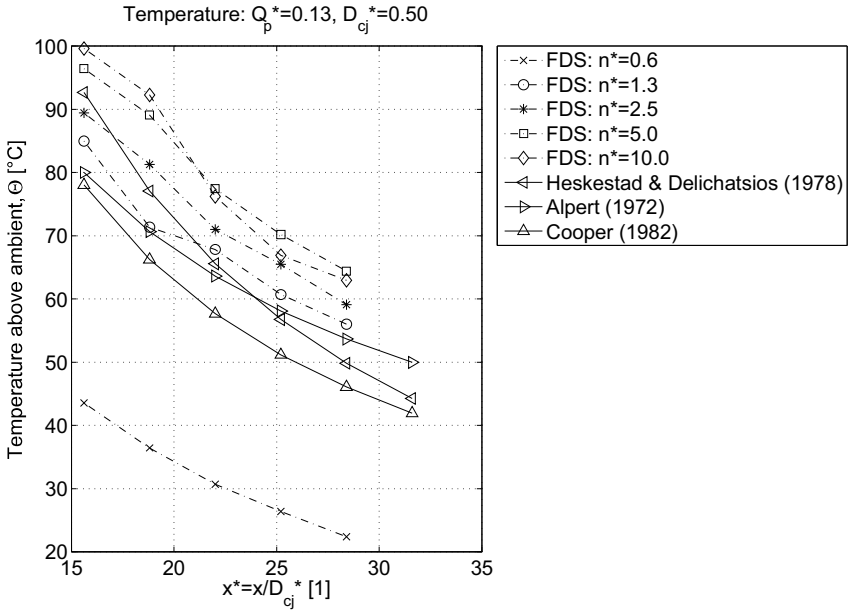

(a) Validation of temperature predictions.

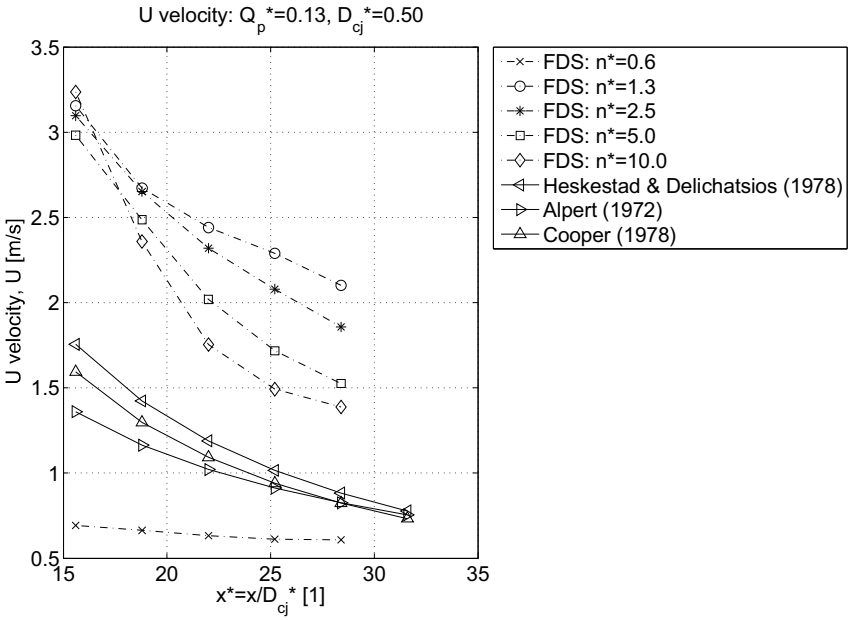

(b) Validation of velocity predictions.

Figure 2.21 *Approach flow region: Order of numerical method.*

2.10.3 Rotation Region

Characteristics of the rotation region with respect to CFD fire modeling are:

Characteristic length scale - The flow in the rotation region can be considered emanating from a line source, thus the characteristic fire length scale D_l^* from Eqn. (2.5.5), p. 42, can be applied [m].

Entrainment - As the flow rotates around the spill edge, see Figure 2.22, ambient air is entrained in the increasingly buoyant flow, thus the smoke production is highly dependent on the grid resolution because of the turbulence model.

The center-of-mass of the flow profiles - The horizontal position of the rotated flow profiles (i.e. where the bulk flow is dominated by the upward velocity component only) is important since this indirectly reflects the extent of the rotation region, and hence the distance over which entrainment takes place.

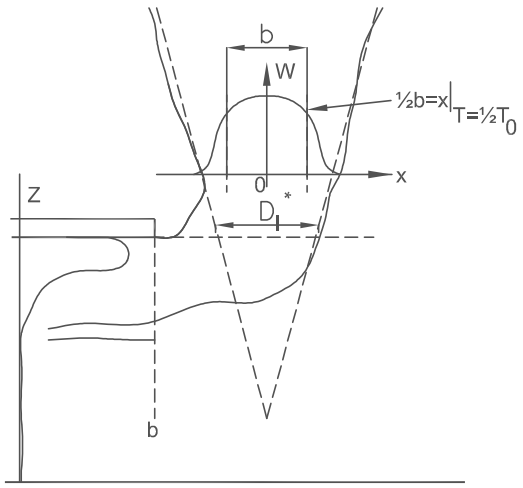

Figure 2.22 *Rotation region.*

The mass flow rate is evaluated roughly at $1/3H_{fc}$ above the spill edge, where the flow is considered dominated by the upward velocity component. The horizontal spill plume velocity is induced by the momentum in the ceiling jet, however the impact obviously decreases with rising height. This means that putting a downstand at the spill edge will generate an almost entirely vertical rising spill plume, i.e. a rotation region with very limited extents. The centerline of a spill plume emanating from an opening not obstructed by a downstand will *"drift"* away from the spill edge (until the bulk flow velocity is purely dominated by buoyant forces), i.e. the rotation region has a much greater extent without a downstand.

The mass flow rate is reported as the net mass flow rate between the opening $\dot{m}_w$ and at the elevated position $\dot{m}_l$, i.e. the net mass flow rate in the rotation region. From Figure 2.23(a) it is expected that the method will approach convergence for $n^* \gtrsim 3$. The order of the numerical method in the rotation region is $p = 0.14$, far from the theoretically derived $p \in [1:2]$, supporting the conclusion in Section 2.10.1 that the order of the numerical method decreases considerably in turbulence and buoyancy dominated flow regions.

As a final comment it is noted that the grid convergence study does not explicitly address rotating flows from openings obstructed by a downstand. The unobstructed flow is assumed to approximate the obstructed flow since the rotation region has a larger extent and thus a greater impact on the mass flow rate and location of the COM.

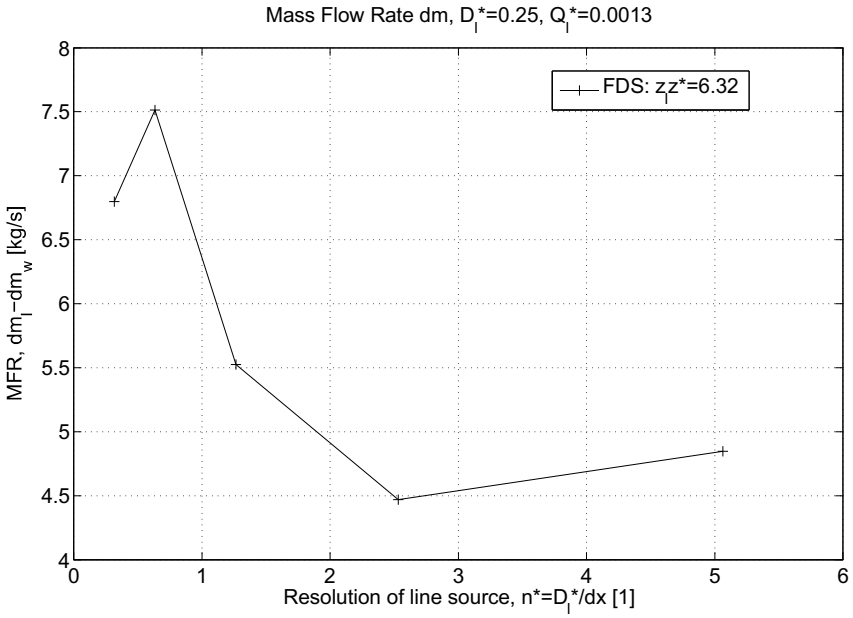

(a) Resolution relative to characteristic length scale D_l^*.

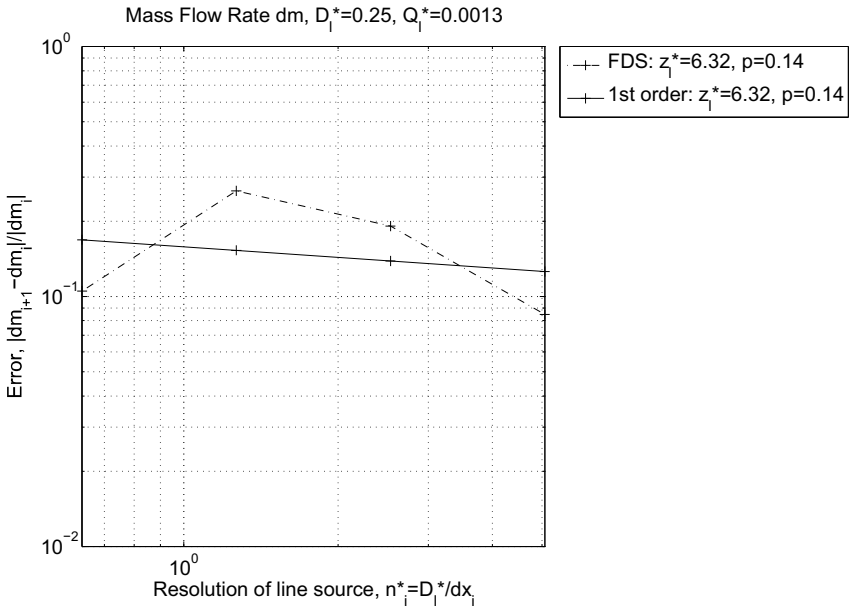

(b) Resolution relative to characteristic length scale D_l^*.

Figure 2.23 *Rotation region: Convergence trends and order p of numerical method.*

2.10.4 Spill Plume Region

Characteristics of the spill plume region with respect to CFD fire modeling are:

Characteristic length scale - The flow in the spill plume region is considered emanating from a virtual line source located below the spill edge. The characteristic length scale of the flow D_l^* $[m]$ is thus found from Eqn. (2.5.5), p. 42.

Entrainment - As the flow rotates around the spill edge, see Figure 2.24, ambient air is entrained in the increasingly buoyant flow. The bulk flow velocity in the spill plume region is dominated by the upward velocity component and driven by buoyancy. The turbulent nature of the rising spill plume entrains ambient air, thus an adequate resolution of the spill plume is crucial to the accuracy of the turbulence model and hence the production of smoke.

The center-of-mass of the flow profiles - The spill plume flow profiles are by nature roughly symmetric about the spill plume centerline independent of the grid resolution, see Figures 2.25 and 2.26.

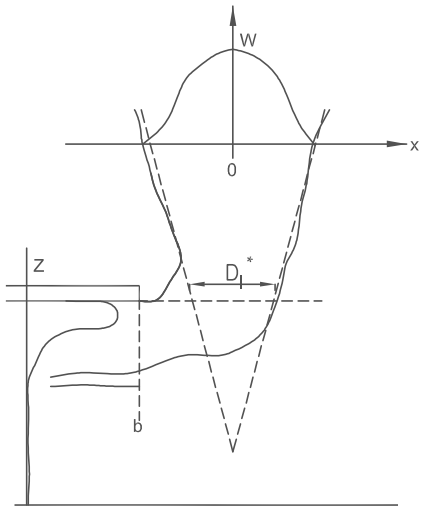

Figure 2.24 *Spill plume region.*

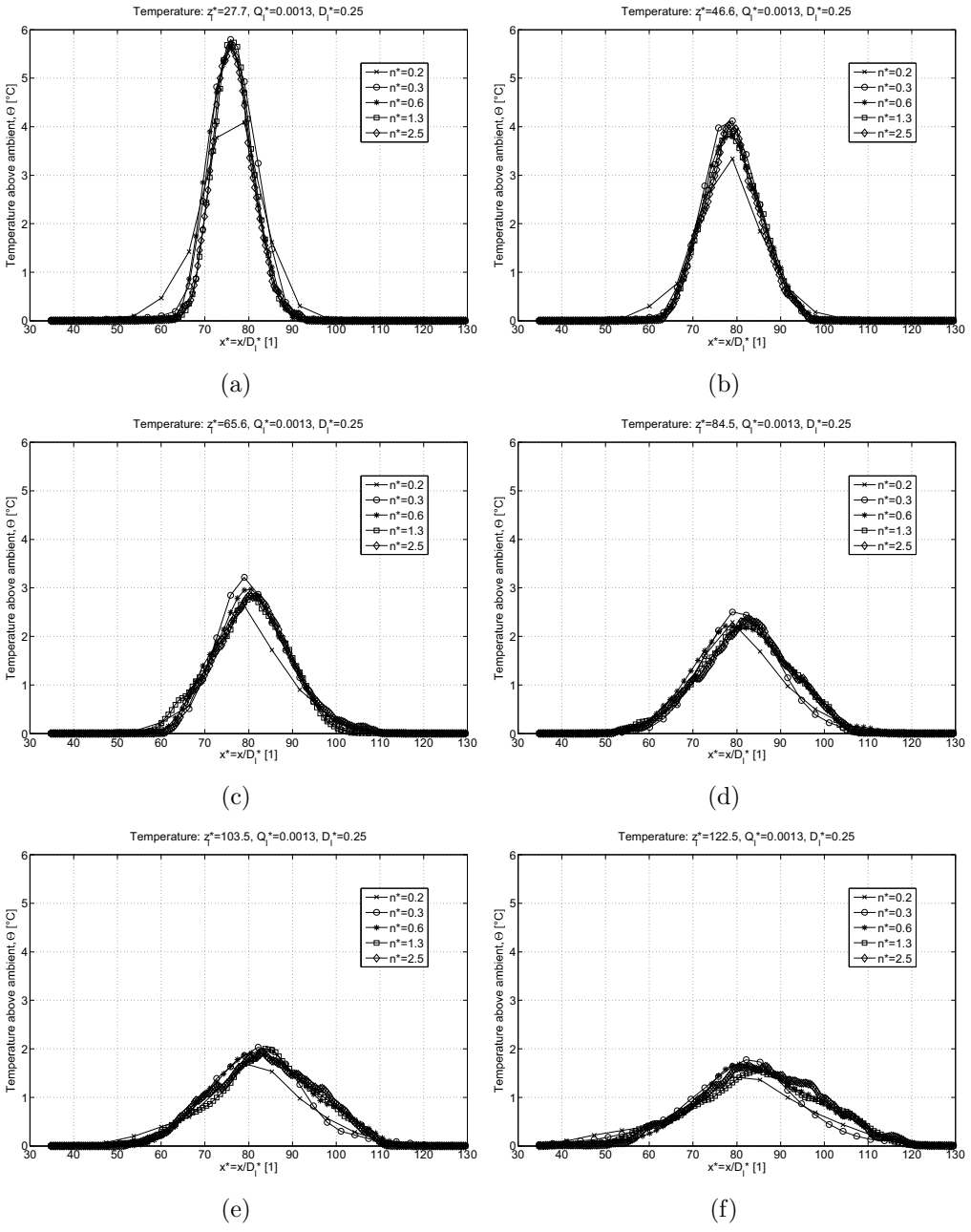

Figure 2.25 *Spill plume region: Temperature profiles.*

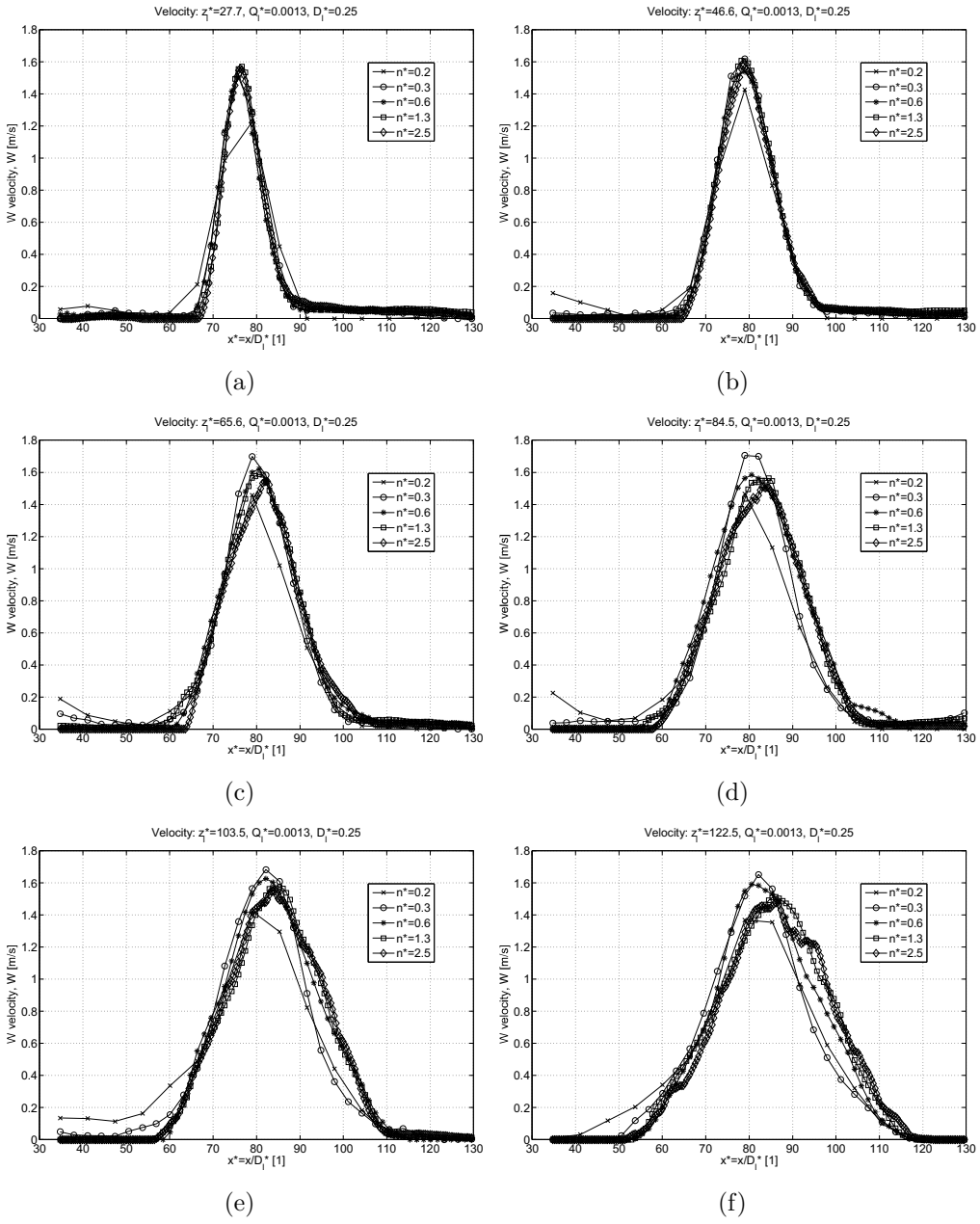

Figure 2.26 *Spill plume region: W velocity profiles.*

The comments on the predictions in the axisymmetric plume region, see Section 2.10.1, also holds for the spill plume region, obviously due to the two regions both being dominated by turbulence and buoyancy. From Figures 2.25 and 2.26 it can be seen that the CFD model is prone to under predict temperatures and hence velocities for low grid resolutions. By eye it is clear that the three lowest grid resolutions differ considerably from the solutions predicted by the CFD model. The two finest grid resolutions $n^* \in \{1.3, 2.5\}$ produce predictions that almost converges to the same solution throughout the computational domain. Looking at the mass flow rates in Figure 2.27(a) it is clear that the solution converges for $n^* \gtrsim 1$.

From the flow profiles in Figure 2.25 and Figure 2.26 it is evident that the spill plume widens with increasing rising height, thus the turbulent length scale increases.

Since FDS employs a LES turbulence model, see Section 2.4.2, anticipating the energy carrying eddies are resolved by the numerical grid, an increasing turbulent length scale means that the grid can be coarsened with increasing rising height without considerably impacting the accuracy of the model. Assuming geometrical similarity of the flow profiles, the grid size can be scaled with the relative turbulent length scale, see Eqn. (2.10.3), where increasing turbulent length scale is represented by the increasing core plume width b, see Figure 2.28.

Correlating the turbulent length scale to the rising height will provide a method to determine the increment of the grid size as a function of rising height. In Lee & Emmons (1961) the mass flow rate was shown to scale with the rising height z_l. The turbulent length scale is inherently correlated to the mass flow rate or entrainment rate, supporting the assumption that the turbulent length scale and hence core plume width b scale with the rising height. Correlating the plume width b from Figure 2.28 with the rising height z_l predicted by the highest resolution $n^* = 2.5$ yields:

$$\frac{b\,(z_l)}{b\,(0)} = C_m z_l + 1 \qquad \Big| \; C_m \;=\; 0.0805 \tag{2.10.14}$$

$$\frac{\Delta \mathbf{x}\,(z_l)}{\Delta \mathbf{x}\,(0)} = C_m z_l + 1 \qquad \Big| \; C_m \;=\; 0.0805 \tag{2.10.15}$$

where Eqn. (2.10.3) has been applied. The data were fitted with a correlation coefficient of $R^2 = 0.93$ and the result can be found in Figure 2.29(a) along with a plot of Eqn. (2.10.15) in Figure 2.29(b).

Defining the resolution of the flow profiles in Figure 2.25 and Figure 2.26 relative to the width of the core plume b, i.e. Eqn. (2.10.2), yield the convergence trends plotted in Figure 2.27(b). From this plot it can be seen that a resolution of about 20 control volumes are adequately to resolve the plume at all elevations z_l in the spill plume where the flow is dominated by the upward velocity component only, i.e. far from the rotation region.

The order of the numerical method is computed for the spill plume region and plotted in Figure 2.30. The order ranges from $p \in [0.9 : 2.4]$ with the highest order being computed at the highest elevation, higher than the theoretically derived

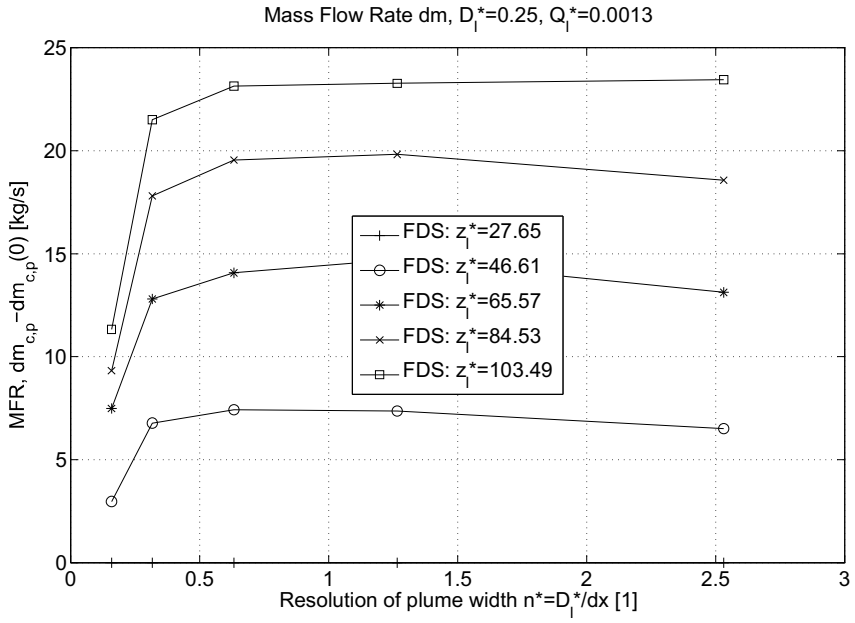

(a) Resolution relative to characteristic length scale D_l^*.

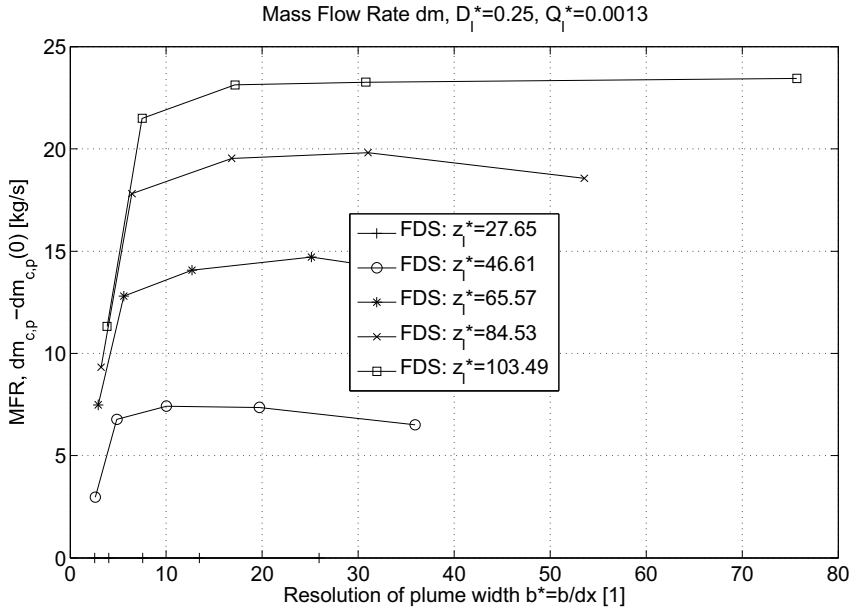

(b) Resolution relative to plume width b.

Figure 2.27 *Spill plume region: Convergence trends.*

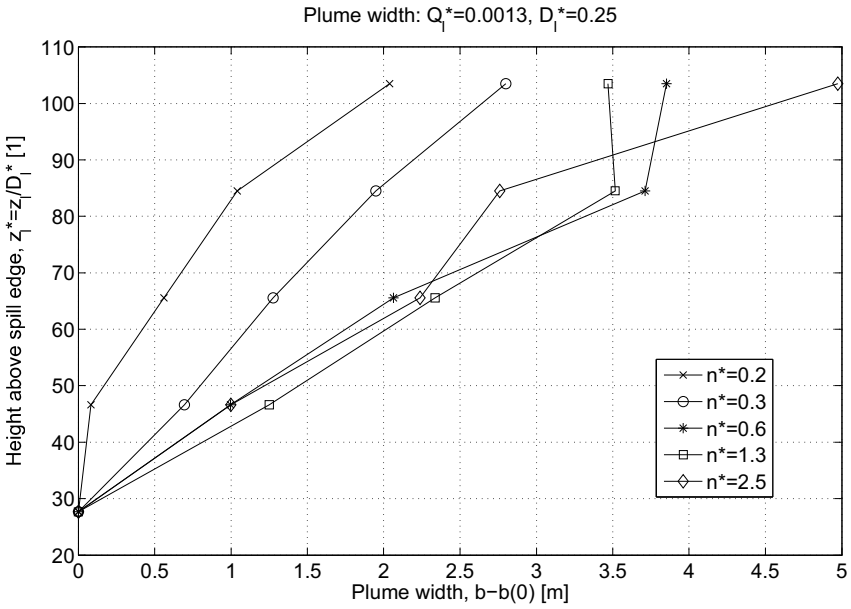

Figure 2.28 *Spill plume region: Width of core plume b.*

order of $p \in [1:2]$. At the highest elevation turbulence can be resolved on the grid scale, hence the nonlinear subgrid-scale turbulence model no longer dominates the turbulence predictions, and the reduction of the error is expected to follow the order of the numerical scheme. The flow is only very weakly influenced by the boundary conditions, consistent with the order being between the first order for the wall velocity boundary conditions and the second order for the free flow.

Engineering relations for this grid convergence study must be expressed in mass flow rate per unit length $\dot{m}_l'$ $[kg/(s\ m)]$ to address the infinite line source setup in the CFD model.

Mass flow rates in spill plumes have been studied over the past thirty years starting with the study of convective flow above a line source conducted by Lee & Emmons (1961). A series of experimental programs have provided data for mainly five simple spill plume models. All experiments were conducted at a 1/10 scale with different geometrical configurations. Morgan et al. (1999) proposed what is known as the BRE method[9], a comprehensive iterative multi-step model. The model involves numerous sub-calculations to arrive at the mass flow rate in the spill plume, and hence not considered a simple engineering relation within this study.

Key experimental data on spill plumes were provided by Morgan & Marshall (1975) and Morgan & Marshall (1979) based on 1/10 scale experiments of smoke flow from a shop unit. Heat was supplied by industrial methylated spirits (IMS)

[9]Short for Building Research Establishment.

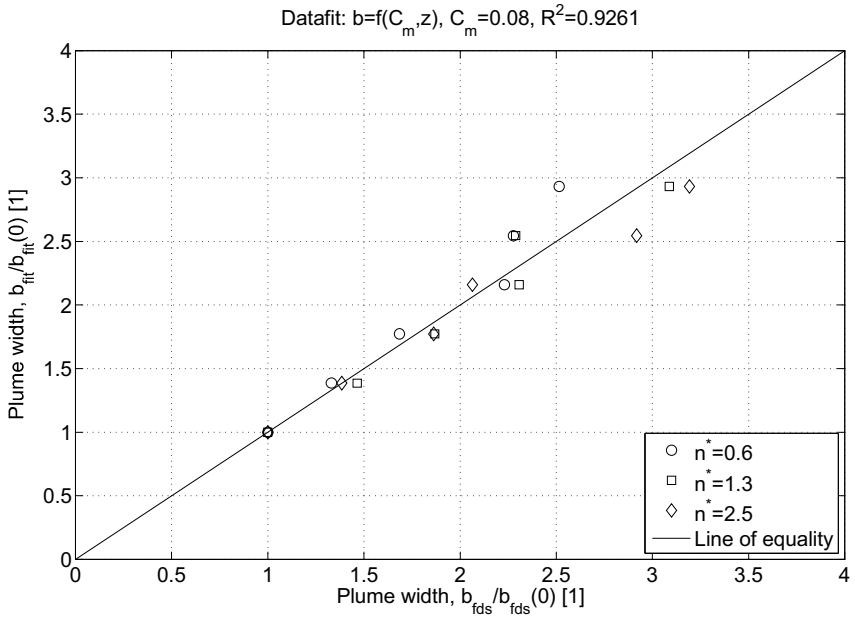

(a) Data fit of core plume width b as a function of rising height z_l.

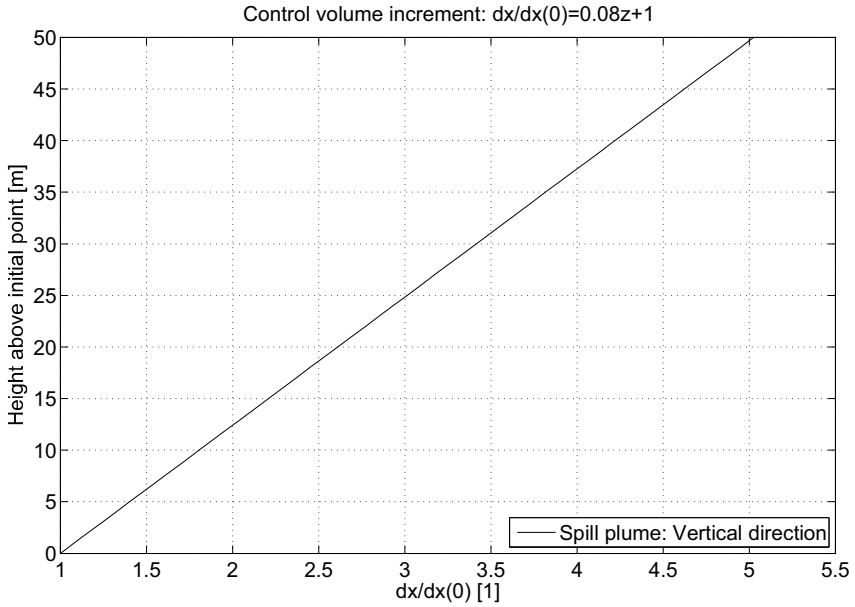

(b) Increment of grid size $\Delta\mathbf{x}/\Delta\mathbf{x}_0$ as a function of rising height z_l.

Figure 2.29 *Spill plume region: Grid size* $\Delta\mathbf{x}$ *as a function of rising height* z_l.

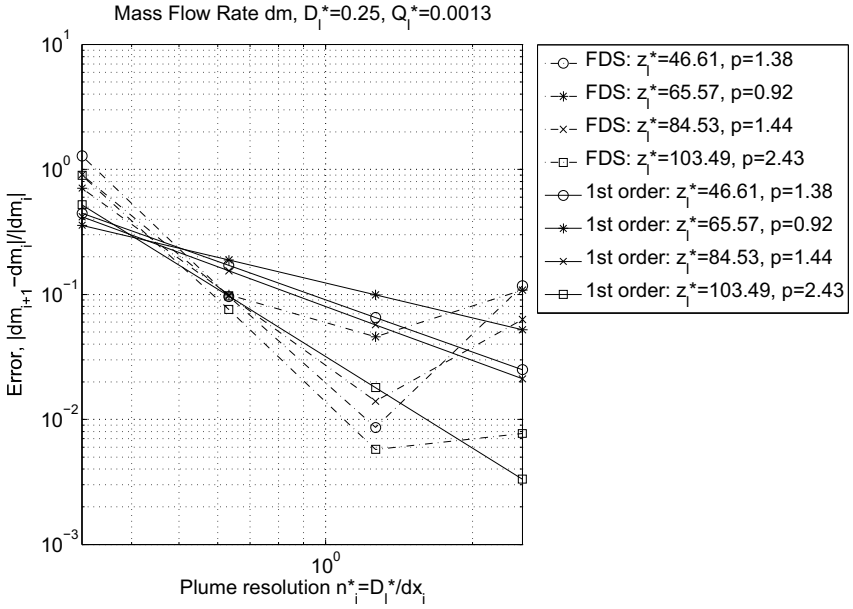

(a) Resolution relative to characteristic length scale D_l^*.

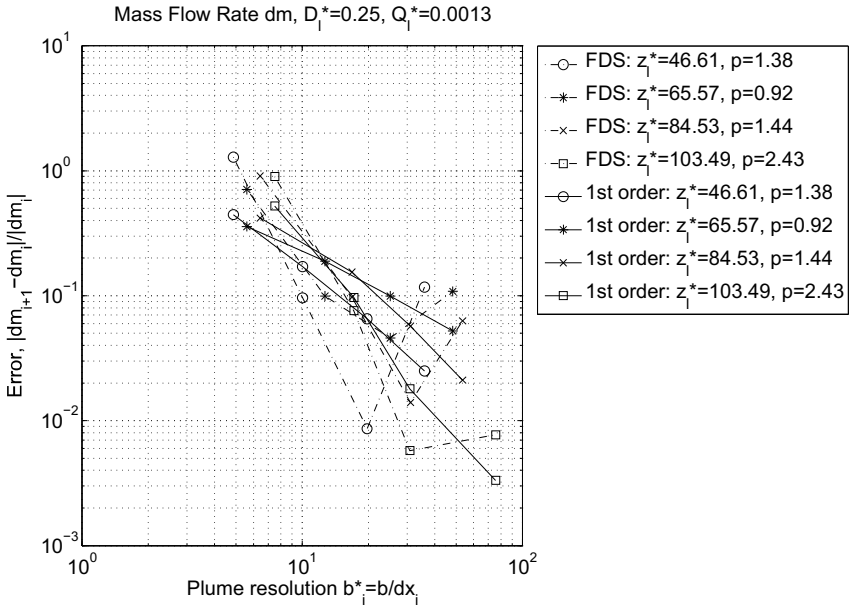

(b) Resolution relative to plume width b.

Figure 2.30 *Spill plume region: Order of numerical method.*

and electrical convective heaters respectively. Law (1986) applied the data by Morgan, et al. to derive the entrainment coefficient in the spill plume, and modeled the spill plume as emanating from a virtual line source below the balcony, see Figure 2.6, i.e. incorporating the entrainment in the rotation region in a single-step method for the entire spill plume, as opposed to Morgan et al. (1999) in which the rotation region was treated separately and added to the spill plume mass flow rate. Later Law (1995) proposed a new entrainment coefficient based on new experimental data provided by Hansell, et al. (1993) applying electrical convective heaters as a source of heat, yielding the correlation:

$$\dot{m}_l = 0.31 \dot{Q}_c^{1/3} W_b^{2/3} \left(z_l + 0.25 H_{fc}\right) \tag{2.10.16a}$$

$$\dot{m}'_l = 0.31 \left(\frac{\dot{Q}_c}{W_b}\right)^{1/3} \left(z_l + 0.25 H_{fc}\right) \tag{2.10.16b}$$

where $\dot{m}_l$ is the mass flow rate $[kg/s]$ in the spill plume above the spill edge, $\dot{Q}_c$ is the convective heat release rate $[kW]$, W_b is the width $[m]$ of the spill plume at the spill edge, z_l is the rising height above the spill edge $[m]$ and H_{fc} is the height $[m]$ from the fire base to the ceiling in the fire compartment.

Milke (2000) and CIBSE (2003) later adopted the approach and data by Law (1995) and derived the correlations Eqn. (2.10.17a) and Eqn. (2.10.18a) respectively using the total heat release rate $\dot{Q}_T$: as opposed to the convective heat release rate $\dot{Q}_c$:

$$\dot{m}_l = 0.41 \dot{Q}_T^{1/3} W_b^{2/3} \left(z_l + 0.25 H_{fc}\right) \tag{2.10.17a}$$

$$\dot{m}'_l = 0.41 \left(\frac{\dot{Q}_T}{W_b}\right)^{1/3} \left(z_l + 0.25 H_{fc}\right) \tag{2.10.17b}$$

$$\dot{m}_l = 0.36 \dot{Q}_T^{1/3} W_b^{2/3} \left(z_l + 0.25 H_{fc}\right) \tag{2.10.18a}$$

$$\dot{m}'_l = 0.36 \left(\frac{\dot{Q}_T}{W_b}\right)^{1/3} \left(z_l + 0.25 H_{fc}\right) \tag{2.10.18b}$$

It is clear that the two models only differ in the coefficients $C = 0.41$ and $C = 0.36$.

Using the entrainment coefficient proposed by Lee & Emmons (1961) and the virtual line source approach introduced by Law (1986), Thomas (1987) arrived at the correlation:

$$\dot{m}_l = 0.58 \rho \left(\frac{g}{\rho c_p T_\infty}\right)^{1/3} \dot{Q}_T^{1/3} W_b^{2/3} \left(z_l + d_b\right) + \dot{m}_b \tag{2.10.19a}$$

$$\dot{m}'_l = 0.58 \rho \left(\frac{g}{\rho c_p T_\infty}\right)^{1/3} \left(\frac{\dot{Q}_T}{W_b}\right)^{1/3} \left(z_l + d_b\right) + \frac{\dot{m}_b}{W_b} \tag{2.10.19b}$$

Thomas (1987) decoupled the approach flow mass flow rate at the spill edge $\dot{m}_b$ from the spill plume mass flow rate $\dot{m}_l$, hence introducing the approach flow mass flow rate at the spill edge $\dot{m}_b$ $[kg/s]$ and the depth of the smoke layer d_b $[m]$.

A new series of 1/10 scale tests published by Marshall & Harrison (1996) were adopted by Poreh, et al. (1998) to derive the entrainment coefficient and proposing the correlation:

$$\dot{m}_l = 0.16\dot{Q}_c^{1/3} W_b^{2/3} (z_l + d_b) + \dot{m}_b \tag{2.10.20a}$$

$$\dot{m}_l' = 0.16 \left(\frac{\dot{Q}_c}{W_b}\right)^{1/3} (z_l + d_b) + \frac{\dot{m}_b}{W_b} \tag{2.10.20b}$$

In Eqn. (2.10.20a) the approach flow mass flow rate at the spill edge is decoupled identical to the way Thomas (1987) addressed the source term in the spill plume model.

The experimental program by Marshall & Harrison (1996) did not include entrainment into the ends of the spill plume, i.e. end entrainment is not included in the work by Poreh et al. (1998). Thus Thomas, et al. (1998) proposed end entrainment be modeled as one half axisymmetric plume added to each end of the line plume emanating from the virtual line source. This approach was never verified by experiment. Thomas also rewrote the source term for the approach flow applying expressions for smoke layer depth d_b and approach mass flow rate $\dot{m}_b$ proposed by Morgan (1986). The resulting correlation is:

$$\dot{m}_l = 0.159\dot{Q}_c^{1/3} W_b^{2/3} z_l + 0.0027\dot{Q}_c + 0.09 \left(\frac{\dot{Q}_c}{W_b}\right)^{1/3} z_l + 1.2\dot{m}_b \tag{2.10.21a}$$

$$\dot{m}_l' = 0.159 \left(\frac{\dot{Q}_c}{W_b}\right)^{1/3} z_l + 0.0027 \left(\frac{\dot{Q}_c}{W_b}\right) + 0.09\dot{Q}_c^{1/3} W_b^{-4/3} z_l + 1.2\frac{\dot{m}_b}{W_b} \tag{2.10.21b}$$

Harrison (2004) carried out a number of new experiments on a 1/10 scale setup of smoke flow from a shop unit using methylated spirits as heat source, and proposing a unified update of the correlations by Poreh et al. (1998) and Thomas et al. (1998):

$$\dot{m}_l = 0.20\dot{Q}_T^{1/3} W_b^{2/3} z_l + 0.0017\dot{Q}_T + 1.5\dot{m}_b \tag{2.10.22a}$$

$$\dot{m}_l' = 0.20 \left(\frac{\dot{Q}_T}{W_b}\right)^{1/3} z_l + 0.0017\frac{\dot{Q}_T}{W_b} + 1.5\frac{\dot{m}_b}{W_b} \tag{2.10.22b}$$

The work by Harrison (2004) inherently included end entrainment as opposed to the work by Poreh et al. (1998) and Thomas et al. (1998), which explains the differences in the proposed correlations.

The first full-scale experimental series on spill plumes were conducted and published by McCartney (2006). The experimental program was part of a joint

National Research Council Canada (NRCC) and American Society of Heating, Refrigerating and Air-Conditioning Engineers (ASHRAE) research program on balcony spill plumes to investigate the large discrepancies in the various spill plume models. The experimental program addressed openings up to about 85% of the maximum full-scale opening widths applied in the experimental programs by Morgan & Marshall (1975) and Morgan & Marshall (1979). The size of the fire compartment and rising height of the spill plume were obviously limited by the extents of the test facility accommodating the test setup. Thus rising heights were limited to only 4 m above the spill edge as opposed to a maximum of 9 m in the previous 1/10 scale experiments. Heat was supplied using a propane burner system. McCartney (2006) proposed a correlation following the simple approach of a virtual line source proposed by Law (1986) and based on the data obtained in the full-scale experimental program:

$$\dot{m}_l = 0.52\dot{Q}_T^{1/3} W_b^{1/5} z_l + \dot{m}_b \tag{2.10.23a}$$

$$\dot{m}'_l = 0.52\dot{Q}_T^{1/3} W_b^{-4/5} z_l + \frac{\dot{m}_b}{W_b} \tag{2.10.23b}$$

The mass flow rates from the CFD model in the present study are validated against selected engineering relations for the net mass flow rate per unit length in the spill plume $\dot{m}'_{net,l}$:

$$\dot{m}'_{net,l} = \dot{m}'_l - \dot{m}'_l(0) \tag{2.10.24}$$

Hence all source terms cancel. The mass flow rates for the entire range of grid resolutions are shown in Figure 2.31 and it is clear that the predictions for $n^* \gtrsim 1.3$ converge to an almost identical solution.

From the mass flow rates shown in Figure 2.31, it is clear that the CFD model exhibits the expected linear dependence on the rising height z_l, consistent with the findings of Lee & Emmons (1961). The engineering relations plotted in Figure 2.31 shows considerable scatter in the data for the entrainment coefficient. Studies based on Law (1995) are prone to over predict the mass flow rates considerably compared to both experimental data and CFD predictions. The CFD model is setup to produce an infinite line source emanating from the fire compartment, i.e. end entrainment is not included in the predictions. This is supported by the fact that the Poreh et al. (1998) and Thomas et al. (1998) studies did not originally include end entrainment [10] and thus produce the lowest discrepancies between the engineering relations and the CFD predictions, see Figure 2.31.

[10] Thomas et al. (1998) proposed experimentally an unverified modification included in the correlation Eqn. (2.10.21a) applied in this study

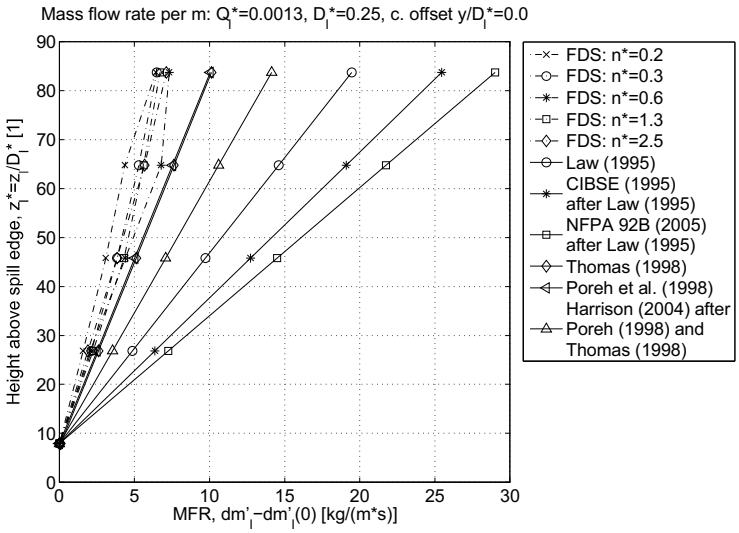

Figure 2.31 *Spill plume region: Validation with simple correlations for mass flow rates* $\dot{m}_p$.

2.11 Conclusion

This simple grid quality control study of a CFD model has presented a universal approach to assess the grid quality in CFD fire simulations. Four distinct flow regions have been proposed to represent the main flow regions in atrium smoke management. Adequate grid resolutions relative to the characteristic fire length scale D_i^* for each of the proposed flow regions are presented.

Axisymmetric plume region - The characteristic length scale of the fire is defined in Eqn. (2.11.1):

$$D_p^* = \left(\frac{\dot{Q}_c}{\rho_\infty T_\infty c_p \sqrt{g}} \right)^{2/5} \tag{2.11.1}$$

The axisymmetric plume can be considered adequately resolved for grid resolutions $n^* = D_p^*/\Delta x \gtrsim 15$. An initial guess for the grid size $\Delta \mathbf{x}(z)$ as a function of rising height z above the fire base is:

$$\frac{\Delta \mathbf{x}\,(z)}{\Delta \mathbf{x}\,(0)} = 1 - \frac{z}{z_0} \qquad \forall\, z_0 < 0 \tag{2.11.2}$$

Engineering relations should be applied in a validation of the predicted mass flow rates.

Approach flow region - An adequately resolved flow can be obtained with grid resolutions $n^* = D_{cj}^*/\Delta x \gtrsim 5$ with the characteristic length scale of the fire related to the depth of an unconfined ceiling jet D_{cj}^* corresponding to the present ceiling and fire base height, H_{fc} and H_{fb} respectively:

$$D_{cj}^* = 0.1\,(H_{fc} - H_{fb}) \tag{2.11.3}$$

The proposed grid resolution should be applied throughout the depth of the approach flow, i.e. d_b. Engineering relations are available for validating temperatures and velocities in the ceiling jet.

Rotation region - A grid resolution of $n^* = D_l^*/\Delta x \gtrsim 3$ is considered adequate. The characteristic length scale of the fire is defined in Eqn. (2.11.4):

$$D_l^* = \left(\frac{\frac{\dot{Q}_c}{L_l}}{\rho_\infty T_\infty c_p \sqrt{g}} \right)^{2/5} \tag{2.11.4}$$

Available engineering relations for net entrainment in the rotation region rely on numerous sub-calculations on approach flow mass flow rates and are a prerequisite in deriving spill plume mass flow rates. Thus the modeler is encouraged to validate entrainment in the rotation region by employing models for spill plume mass flow rates.

Spill plume region - Grid resolutions of $n^* = D_l^*/\Delta x \gtrsim 1.3$ can be considered adequate for most fire safety engineering applications. The characteristic length scale of the fire D_l^* is defined in Eqn. (2.11.4) above. Simple engineering relations are available and should be adopted in validating the CFD predictions. An approach to determine the grid size $\Delta \mathbf{x}\,(z_l)$ as a function of rising height z_l based on the core plume width b was presented and a simple correlation proposed:

$$\frac{\Delta \mathbf{x}\,(z_l)}{\Delta \mathbf{x}\,(0)} = C_m z_l + 1 \qquad \Big| \; C_m \;=\; 0.0805 \tag{2.11.5}$$

2.12 Future Research

More studies are needed for different heat release rates to verify that the non-dimensional approach to determine the grid resolution is valid, i.e. that $n^* = D_i^*/\Delta x$ are true for other heat release rates in accordance with the expected.

Validation data for spill plumes at high elevations are needed. A new joint National Research Council Canada and Carleton University (Ottawa, ON) 10-storey atrium test facility located in Almonte (ON), Canada, can accommodate large balcony spill plume test setups. However to obtain data for free spill plumes the experiments still have to be scaled down to avoid obstructing the spill plume flow by the walls of the test facility. The building was completed in the fall 2005. Spill plume experiments carried out at this facility are encouraged to provide validation data for CFD models of spill plumes at high elevations.

Chapter 3

Small-scale Modeling of Approach Flows in Wide Openings

3.1 Introduction

Fire safety engineering of modern buildings often encompasses the design of atrium smoke management systems to ensure tenable conditions during egress and fire fighting. The atrium setup with floors opening up to a tall large open space (designated the atrium) is one of the basic setups in designing smoke management systems. Usually at least two design fire scenarios are relevant in atrium smoke management design. These are fires on the floor within the atrium forming an axisymmetric plume rising to the top of the atrium, and fires in spaces opening up to the atrium e.g. open plan offices and shops in multi-level shopping malls. Various engineering relations for the mass flow rate in the former case have been proposed over the years, see e.g. Heskestad (1984) and Beyler (1986).

Morgan & Marshall (1975) proposed that the basic atrium smoke flow described in the latter case, see Figure 3.1, be divided into three flow regions; the approach flow, the rotation region and the spill plume. Evidently the initial axisymmetric smoke plume can be considered part of this conceptual approach. The initial axisymmetric plume eventually impinges on the ceiling and spreads under the ceiling, approaching the spill edge, where it is rotated into a vertically buoyancy-driven spill plume.

A series of experimental programs conducted in a 1/10 scale atrium model setup, see Morgan & Marshall (1975) and Morgan & Marshall (1979), at *Building Research Establishment* (BRE), UK, provided data for the multi-step BRE method. The mass flow rates in the approach flow (encompassing the entrainment in the axisymmetric plume), rotation and spill plume regions are calculated individually through a partial iterative approach. The experimental program addressed smoke spread from a shop unit in shopping malls of two or more stories with shop front openings limited to a full-scale width of 7 and 14 m. A comprehensive introduction to the BRE method can be found in Morgan et al. (1999).

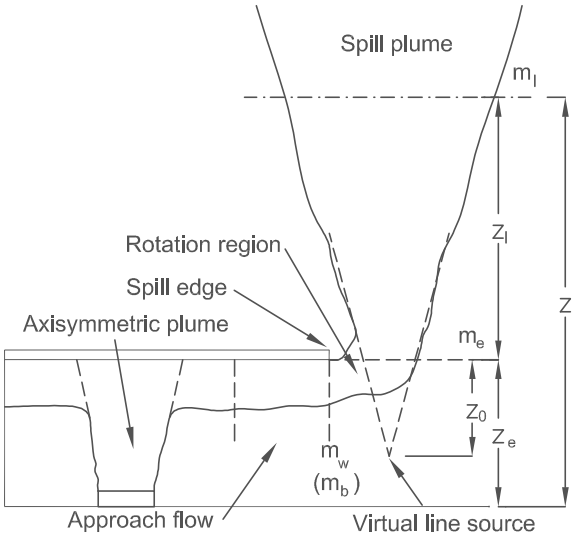

Figure 3.1 *Basic smoke flow from a fire on a floor opening up to a tall large space (atrium).*

In recognizing that the BRE method was a rather complicated method to apply in atrium smoke management design, Law (1986) proposed a single-step approach to calculate the mass flow rate in the spill plume by considering it emanating from a virtual line source located z_0 $[m]$ below the spill edge, see Figure 3.1. Law (1986) utilized the experimental data reported in Morgan & Marshall (1975) and Morgan & Marshall (1979). As opposed to the individual calculation of mass flow rate in the approach flow $\dot{m}_w$ (or $\dot{m}_b$) $[kg/s]$ and rotation regions $\dot{m}_r$ $[kg/s]$ in the BRE method, see Morgan & Marshall (1975), Law (1986) proposed to include them in a single-step method for the mass flow rate in the spill plume $\dot{m}_l$ $[kg/s]$. The approach flow $\dot{m}_w$ was expressed in terms of the fire compartment height H_{fc} $[m]$. A new experimental study by Hansell et al. (1993), also for a 1/10 scale atrium setup, provided data for an updated entrainment coefficient in the single-step method by Law (1986) leading to the updated method for spill plume mass flow rate published in Law (1995).

Prior to the experimental program by Morgan & Marshall (1975) and Morgan & Marshall (1979), Thomas, et al. (1963) conducted a series of experiments on the flow of hot gases in roof venting in a scaled down factory bay. The flow of hot gases under a roof screen was also investigated in this study and a correlation for the mass flow rate in the approach flow region $\dot{m}_w$ was proposed. Scaled to the full-scale ceiling heights of the experiments in Morgan & Marshall (1975) and Morgan & Marshall (1979), the width of the compartment opening in the study was ≈ 7 m.

Morgan (1986) questioned the use of a discharge coefficient C_d [1] in the correlation for the approach flow mass flow rate proposed by Thomas et al. (1963),

because it was not raised to the same power as the smoke layer depth d_s $[m]$ on which it was operating. Morgan (1986) noted that the application of a coefficient of discharge implied that a *vena contracta* existed outside the spill edge. Basically adopting the same approach as Thomas et al. (1963), Morgan (1986) revised the equation for conservation of energy along a stream line in the approach flow adopting a *"profile correction factor"* to account for the shape of the buoyancy profiles Θ/T being something between a step function and a triangular profile.

3.2 Present Research

The request for tall large open spaces in buildings is increasing of architectural and environmental reasons. Open plan offices and shopping malls with opening widths far beyond the validation limits of the above mentioned methods and engineering relations for the approach flow mass flow rates $\dot{m}_w$ (or $\dot{m}_b$), require a new experimental program to provide data for openings $W_b > 14$ m, which currently represents the upper limit of available experimental data.

The objective of the present research is:

Experimental program - To design a small-scale experimental program for approach flows in wide compartment openings and conduct tests to obtain data for the approach flow mass flow rate.

Validate CFD model - Validation data is provided from the small-scale experimental program and used to validate the applied CFD model.

3.3 Mass Flow Rates

Densely distributed thermocouples are used to measure temperatures in the fire compartment opening of the scale model. Using the approach outlined by Morgan (1986) the velocity field is computed from the temperature field, and computed velocities are verified against velocities obtained using an anemometer.

Morgan (1986) considered the approach flow in Figure 3.2(a) and assumed flow profiles at positions Λ and v to be similar. Hence conservation of mass and approach flow depth ratios respectively and ignoring upward acceleration at the spill edge yield:

$$v\left(x_v\right) = \frac{W_{fc} d_\Lambda}{W_w\, d_v} v\left(x_\Lambda\right) \tag{3.3.1a}$$

$$x_v = \frac{d_v}{d_\Lambda} x_\Lambda \tag{3.3.1b}$$

where x_i is the height above the smoke layer base $[m]$, v_i is the horizontal velocity $[m/s]$ and d_i is the depth of the smoke layer base $[m]$ all evaluated at positions $i \in \{v, \Lambda\}$. Widths of the fire compartment and fire compartment opening are designated W_{fc} and W_w $[m]$ respectively, see Figure 3.2(b).

At the bottom of the smoke layer base the temperature difference $\Theta = 0$ and the fluid is assumed at rest $v_v\left(0\right) = 0$. No work is done by the gases, thus writing

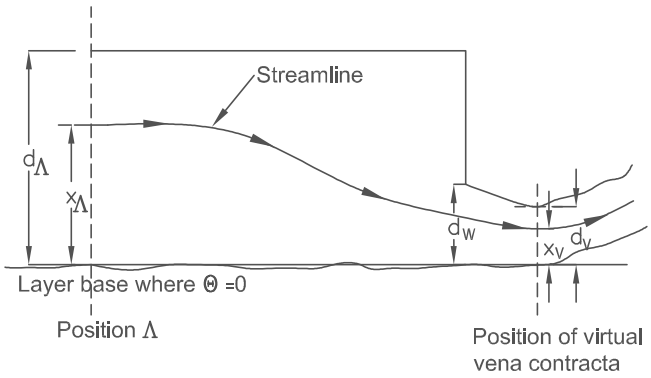

(a) Section showing the flow approaching a wide opening.

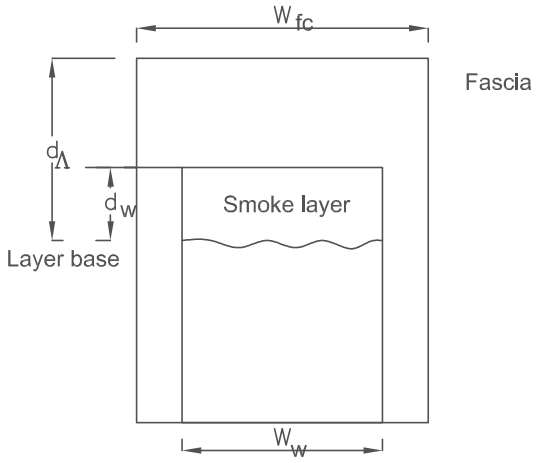

(b) Front view showing the flow emerging from the fire compartment.

Figure 3.2 *Nomenclature in approach flows.*

the steady-flow energy conservation equation for two streamlines at heights $x_v = 0$ and $x_v = x_v$ at the vena contracta:

$$p\left(0\right) = p\left(x_v\right) + \frac{\rho\left(x_v\right)}{2} v\left(x_v\right)^2 - \int_0^{x_v} \Delta\rho\left(x_v g\ dy\right) \tag{3.3.2}$$

Assuming no pressure difference across the smoke layer, i.e. $p\left(0\right) = p\left(x_v\right)$ and applying the assumption of geometrical similarity, Eqns. (3.3.1), the velocity v_Λ at position x_Λ can be written:

$$v\left(x_\Lambda\right) = \left(2g\frac{T\left(x_\Lambda\right)}{kT_\infty}\int_0^{x_\Lambda}\left(\frac{\Theta}{T}\right)\left(y_\Lambda\right)\ dy_\Lambda\right)^{1/2} \tag{3.3.3}$$

here k represents the assumption of geometrical similarity:

$$k = \frac{W_{fc}^2 d_\Lambda^3}{W_w^2 d_v^3} \tag{3.3.4}$$

In Thomas et al. (1963) the discharge coefficient C_d operates on the discharge area, whereas Morgan (1986) utilizes the fact that C_d operates on the smallest dimension of a discharge area with high aspect ratio, i.e. where $W_{fc} \gg d_\Lambda$ and $W_w \gg d_v$, and thus:

$$d_v = C_d d_w \tag{3.3.5}$$

and inserting in Eqn. (3.3.4):

$$k = \frac{W_{fc}^2 d_\Lambda^3}{W_w^2 C_d^3 d_w^3} \tag{3.3.6}$$

From the computed velocity field, Eqn. (3.3.3) the mass flow rate at the compartment opening $\dot{m}_w$ is found by a simple surface integral:

$$\dot{m}_w = \int_{A_w} \rho\left(x_w\right) v\left(x_w\right) dA \tag{3.3.7a}$$

$$\dot{m}_w = \int_0^{d_w}\int_0^{W_w} \rho\left(x_w\right) v\left(x_w\right) dx\ dy \tag{3.3.7b}$$

3.4 Depth of Smoke Layer

Experimental programs involving smoke layers, Morgan, et al. (1976), Morgan & Marshall (1979) and Marshall (1985), have shown that the depth of the smoke layer d_Λ correlates well with the buoyancy profiles Θ/T:

$$d_\Lambda\left(\frac{\Theta}{T}\right)_{max} = \int_0^{d_\Lambda}\left(\frac{\Theta}{T}\right)(x)\ dx \tag{3.4.1}$$

Throughout this study Eqn. (3.4.1) has been applied in determining the depth of the smoke layer in the approach flow, d_w.

3.5 Small-scale Approach Flow Studies

3.5.1 Experimental Objective

The experimental objective of the present physical small-scale experimental program is to measure temperature and velocity profiles in the fire compartment opening and use this data to validate similar profiles predicted by the CFD fire model. Mass flow rates are computed from the velocity profiles, and smoke layer depths from the buoyancy profiles. The experimental setup was located within the large burn hall at the National Research Council Canada test facility in Almonte, ON, Canada. The experimental test series were funded by National Research Council Canada to provide data and information about approach flow mass flow rate distributions in wide openings.

3.5.2 Experimental Parameters

Previous studies of approach flows in fire compartments are limited to openings of up to 14 m, see e.g. Thomas et al. (1963), Law (1995) and Harrison (2004), applying fixed distances from the fire base to the compartment opening. From the studies it is clear that the mass flow rate in the compartment opening depends strongly on the width of the opening and the heat release rate, but not how the flow is influenced by distance from the fire base to the spill edge. To allow for a versatile set of data to validate the CFD fire model, the present experimental program will study the approach flow mass flow rate as a function of the heat release rate and the distance to the fire base. The experimental parameters are:

Fire size $\dot{Q}_T$ - Total heat release rates of $\dot{Q}_T \in \{100, 150, 200, 250, 500\}$ kW are employed.

Distance to fire base D_{fb} - The distance from the fire base to the compartment opening are varied through $D_{fb} \in \{2.8, 7.0\}$ m.

For reasons of limited funding and time, not all parameters expected to impact the approach flow mass flow rate are varied in the present experimental program. Secondary parameters include:

Fire compartment size - The present study employs a fixed fire compartment size of 13.8×9.6×1.55 m with an entirely open floor base, hence the entrainment into the axisymmetric plume in the fire compartment is not influenced by the fire compartment geometry.

Fire compartment height H_{fc} - The height of the fire compartment clearly determines the rising height of the axisymmetric plume and hence the mass flow rate in the compartment opening. The present study employs a fixed compartment height of $H_{fc} = 1.55$ m.

Heat transfer in fire compartment - Heat transfer through compartment walls extracts energy from the approach flow, slowing down the flow and hence decreasing the mass flow rate in the opening. To protect the compartment

against the repetitive heat exposures, the fire compartment is lined with insulating material to minimize heat conduction. The experimental setup was fitted with an attached balcony, increasing the extents of the fire compartment, without insulating ceramic fiber, thus allowing for heat conduction through the ceiling.

Combustion - Propane was chosen for the small-scale approach flow program because of it's ease of application and straightforward calculation of heat release rate using a rotameter to measure the flow rate.

3.6 Experimental Program

3.6.1 Test Breakdown

Tests conducted in the small-scale experimental program on approach flow mass flow rates are listed in Table 3.1 with the experimental parameters total heat release rate $\dot{Q}_T$ $[kW]$, distance to fire base D_{fb} $[m]$, ambient temperatures T_∞ $[C^\circ]$, measured quantities and measuring methods for velocity (where *Thermo* and *Mecha.* designate thermal and mechanical anemometers respectively).

Test ID	$\dot{\mathbf{Q}}_\mathbf{T}$	$\mathbf{D_{fb}}$	**Geo.**	$\mathbf{T_\infty}$	**Temp.**	**Vel.**	**Velo.**
	[kW]	[m]	Conf.	[° C]	log	log	instr.
B4138-105	250	7.0	W	+2.23	YES	YES	Thermo
B4138-106	500	7.0	W	-5.88	YES	YES	Thermo
B4138-107	250	2.8	WO	+3.33	YES	YES	Mecha.
B4138-108	500	2.8	WO	+7.74	YES	YES	Mecha.
B4138-109-100	100	2.8	WO	-0.47	YES	NO	-
B4138-109-150	150	2.8	WO	-0.47	YES	NO	-
B4138-109-200	200	2.8	WO	-0.47	YES	NO	-

Table 3.1 *Small-scale approach flows: List of tests conducted.*

3.6.2 Description of Experimental Test Facility

Fire Compartment

Tests are conducted in a fire compartment scaled to roughly 1/3 of a full-scale setup with a 40 m wide and 5 m high compartment opening without any downstand. The test setup was modified from an earlier test setup applied in the joint National Research Council Canada (NRCC) and American Heating, Refrigerating and Air-Conditioning Engineers (ASHRAE, RP-1247), experimental program on balcony spill plumes, see e.g. McCartney (2006). A photography of the experimental setup before being stripped for the small-scale approach flow setup is provided in Figure 3.3.

Figure 3.3 *Fire compartment applied in the experimental small-scale approach flow program.*

The experimental program comprises two compartment depths to allow for a variation of the distance from the spill edge to the fire base D_{fb}. The two geometric configurations are designated W and WO (abbreviations for *with* and *without* balcony).

The small-scale fire compartment is 13.8 m wide by 5.4 m deep and 5.0 m high with an additional balcony 4.2 m deep supplied with draft curtains 2.9 m deep aligning with the fire compartment opening, i.e. 12 m apart. Smoke leaving the fire compartment is channeled between the draft curtains to the spill edge, resembling a 12 m wide extension to the fire compartment. The fire source is elevated 3.45 m above the fire compartment floor, i.e. 1.55 m below the ceiling. This creates a "virtual fire compartment" with a height from base to ceiling of $H_{fc} = 1.55$ m. With the draft curtains extending 2.9 m below the ceiling, the virtual fire compartment is enclosed by the fire compartment walls, ceiling, balcony and the draft curtains. The virtual fire compartment is hereafter designated only the fire compartment.

The geometry of the fire compartment for configuration W, $D_{fb} = 7.0$ m, with the balcony attached is shown in Figure 3.4 and configuration WO, $D_{fb} = 2.8$ m, with the balcony detached can be found in Figure 3.5.

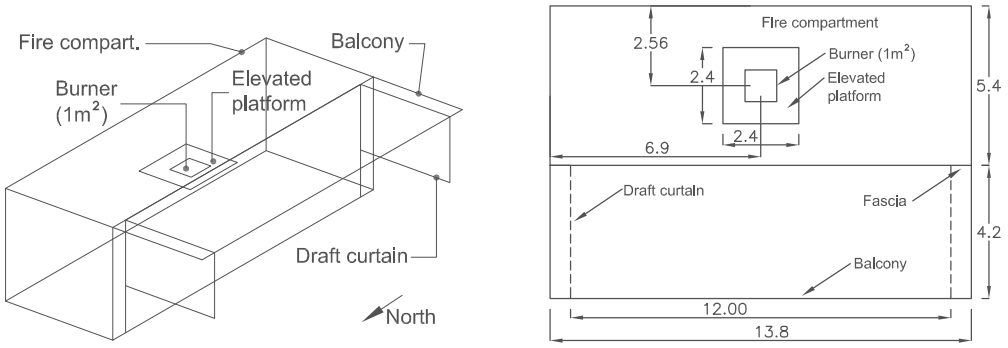

(a) Isometric view of fire compartment.

(b) Top view of fire compartment.

(c) South view of fire compartment.

(d) West view of fire compartment.

Figure 3.4 *Configuration W: Geometry of small-scale experimental setup. All dimensions in m.*

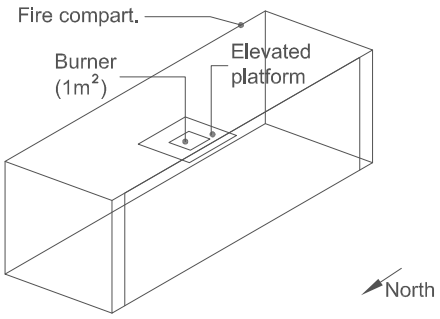

(a) Isometric view of fire compartment.

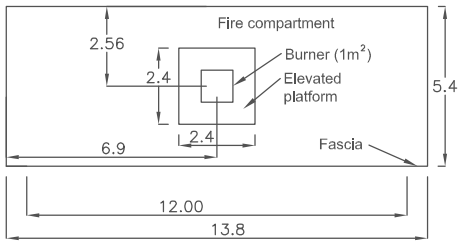

(b) Top view of fire compartment.

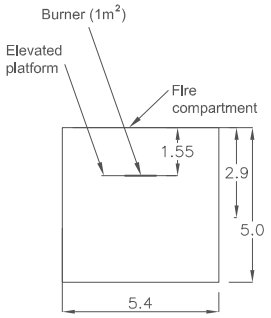

(c) South view of fire compartment.

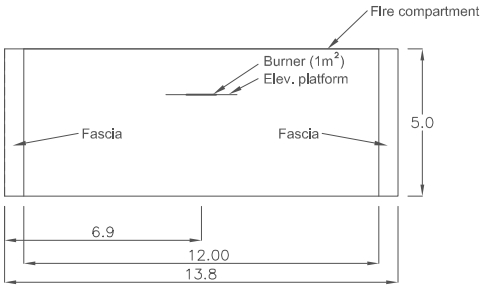

(d) West view of fire compartment.

Figure 3.5 *Configuration WO: Geometry of small-scale experimental setup. All dimensions in m.*

The entire fire compartment, ceiling and walls, is constructed of corrugated steel plate. Rear (east), side walls (north and south) and ceiling are lined with non-combustible ceramic fiber insulation to protect against fire exposure. Because of the insulating material heat conduction through the fire compartment enclosure is minimized, thus maximizing energy and momentum in the approach flow, yielding conservative estimates for the mass flow rate in the compartment opening. The fascia, balcony and draft curtains are not lined with ceramic fiber insulation, hence allowing for heat conduction.

The approach flow layer is allowed to flow unhindered into the burn hall and hence not influenced by the physical extents of the test facility.

Fire Source

The experimental fire source system consists of five propane pot burners aligned in a 1 m by 1 m array, see Figure 3.6. The center of the burner system is located on the compartment centerline 2.56 m from the rear wall (east). The burners are located on an elevated platform of cement board measuring 2.4 m by 2.4 m. The distance from the burners to the compartment ceiling is $H_{fc} = 1.55$ m.

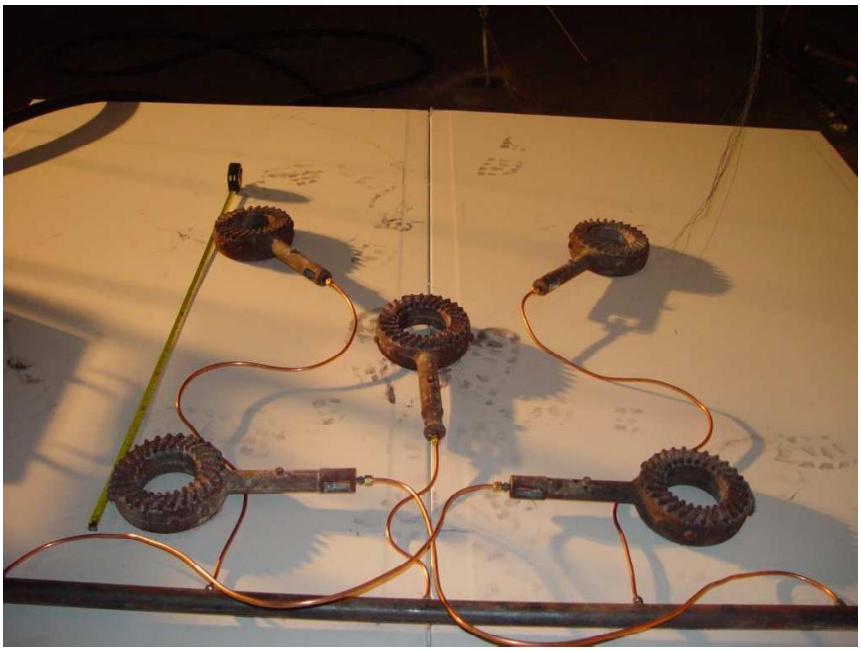

Figure 3.6 *Experimental burner setup.*

Propane flow rate was measured using a rotameter to determine the volumetric flow rate from which the total heat release rate was derived assuming complete combustion and using the heat of combustion for propane ΔH_c.

Since the platform supporting the burner system only extended 1.2 m out from the center of the fire base, air was allowed to flow "up through the base" of the fire

compartment, providing an evenly distributed entrainment into the axisymmetric plume. Hence effects from the entrainment air flow on the alignment of the plume axis can be ignored.

Instrumentation

To provide data for validation of the CFD fire model, the small-scale experimental test setup was instrumented to sample temperatures and velocities in the compartment opening. The setup was fitted with two fixed thermocouple trees on the centerline at the spill edge (THCP 0) and 3 m to the south (THCP -3) also at the spill edge. A movable thermocouple tree was used at north positions 1 m to 6 m from the compartment centerline along the spill edge (THCP 1-6). The fire source is located on the centerline and the fire compartment is symmetric about the centerline, thus the approach flow in the compartment opening is also expected to be symmetric about the centerline, which thermocouple tree THCP -3 was used to verify. All readings were taken at the spill edge, i.e. the thermocouple trees were repositioned when the balcony was detached and the setup changed from configuration W to WO. Measuring positions for both velocity and temperature (designated THCP) for configurations W and WO are shown in Figure 3.7.

The thermocouple trees consist of 20 thermocouples spaced at 25 mm for the initial 400 mm and additional thermocouples at positions 500, 750, 1000 and 1500 mm below the ceiling. The high resolution over the initial 400 mm was chosen to resolve the ceiling jet expected to have a thickness of about 20% of the compartment height, i.e. 300 mm, according to Klote & Milke (2002). Thermocouples at 1 m position below the ceiling were shielded from radiative influx. Thermocouple positions below the ceiling are listed in Table 3.2.

Position	**Test ID**		**Distance below ceiling [mm]**
THCP {-3,0-6}	B4138-{105-109}	$\Delta z \in$	$\{25, 50, 75, 100, 125, 150, 175, \ldots$ $200, 250, 275, 300, 325, 350, 375, \ldots$ $400, 500, 750, 1.000, 1500\}$ mm

Table 3.2 *Temperature: Measuring positions.*

Thermocouples applied in the experimental program were of type K (chromel-alumel) 0.5 mm diameter. According to Inc. (2004) the precision is assumed to be ±2.2 °C. Temperatures are logged every 2 seconds and averaged over a steady-state period of 60 s, removing any time dependency (turbulence or heat conduction in the thermocouple).

Velocities were measured using handheld devices at positions 25 mm below the ceiling and then spaced at 50 mm through to 325 mm with an additional reading at 425 mm. Readings were taken at all 8 positions for locations THCP 0, ±3 and 6, see Figure 3.7. To limit recordings velocity measurements at locations

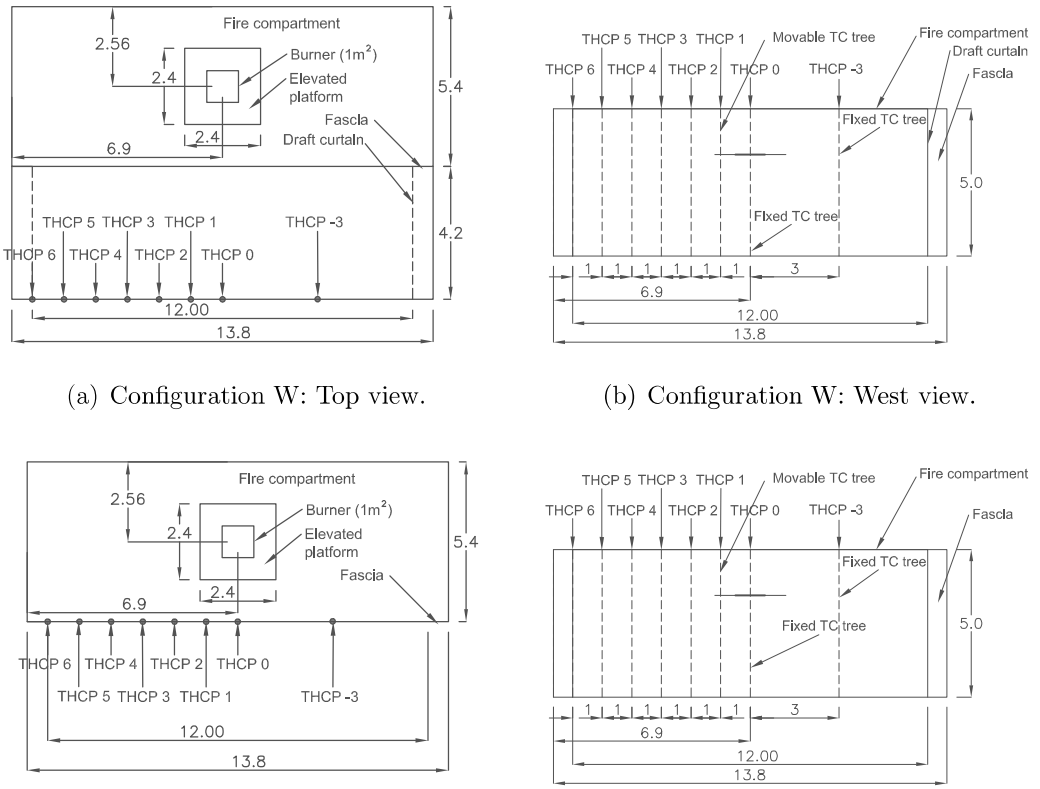

(a) Configuration W: Top view.

(b) Configuration W: West view.

(c) Configuration WO: Top view.

(d) Configuration WO: West view.

Figure 3.7 *Measuring positions designated THCP. All dimensions in m.*

THCP 1, 2, 4 and 5 were restricted to positions 75 mm and 225 mm below the ceiling. Measurement positions are listed in Table 3.3.

Measurements of the velocities in the first two experiments B4138-{105-106}, see Table 3.1, were carried out using a handheld thermal anemometer (hotwire). The anemometer was a TSI Model 8350 VELOCICALC (discontinued model) with a validated measuring range from [0.15:50] m/s. The resulting velocity profiles exhibited a strange shape and it was decided to use a mechanical vane anemometer for the remaining tests B4138-{107-109}. Measurements using the thermal anemometer were averaged over 1 s and 1-3 consecutive readings logged at each position. Velocities reported were based on the average of the consecutive readings. The short time constant used with the thermal anemometer is ideal for steady-state flows, but not suitable for turbulent flows, which is the reason for the use of 1-3 consecutive readings. The number of consecutive readings were determined from the fluctuations of the velocity, heavy fluctuations requiring more readings than nearly steady-state flow. Averaging turbulent velocities based on only 2-3 data entries with no information about the time lapse between readings

Position	Test ID		Distance below ceiling [mm]
ANEMOM {0,±3,6}	B4138-{105-108}	$\Delta z \in$	$\{25, 75, 125, 175, 225, 275, 325, \ldots 425\}$ mm
ANEMOM {1,2,4,5}	B4138-{105-108}	$\Delta z \in$	$\{75, 225\}$ mm

Table 3.3 *Velocity: Measuring positions.*

is not reliable, hence measurements using the mechanical vane are endorsed for validation purposes. Measurements using the mechanical vane anemometer were averaged over a steady-state time period of 30 s to even out turbulent fluctuations. The averaging method applied with the mechanical vane is considered more robust due to the continuous averaging.

The sensor element on the thermal anemometer probe is about 5 mm by 30 mm and fits easily within the dimensions of the measuring positions. The mechanical vane however is about 100 mm in diameter making it difficult to explicitly associate the measured velocity to the measuring position below the ceiling.

The uncertainties in the velocity measurements can not be ignored, and measurements should be compared to velocities obtained using other measuring techniques. In the present experimental program velocities obtained with the anemometers are compared to velocities derived from the temperature profiles in the compartment opening using the method described in Section 3.3, Eqn. (3.3.3).

Propane gas is supplied to the burner system through pressure regulators. The flow rate is measured using rotameters and applied in the derivation of the total heat release rate assuming complete combustion:

$$\dot{Q}_{T,test} = \Delta H_c^{C_3H_8} \rho^{C_3H_8} \dot{V}_{rot} \tag{3.6.1}$$

where $\dot{V}_{rot}$ is the measured flow rate from the rotameter $[m^3/s]$, $\Delta H_c^{C_3H_8}$ is the effective heat of combustion $[kJ/kg]$ of propane and $\rho^{C_3H_8}$ is the density of propane $[kg/m^3]$. Rotameters were checked regularly during the tests making sure propane was supplied at a steady rate. From the uncertainties in the visual reading of the rotameters and the properties of the propane gas, a typical error of ±10% on the total heat release rate $\dot{Q}_T$ is expected.

Test Procedure

A total of seven tests were conducted in the small-scale experimental setup. A complete list of the tests and experimental parameters can be found in Table 3.1.

Prior to igniting the burner system temperature recording was initiated, allowing for ambient temperatures to be determined from the first entries in the time series. The heat release rate was steadily increased to the prescribed test value and the rotameters checked throughout the test to make sure the heat flow

rate remained steady. The approach flow was allowed to settle for at least 1800 s before any measurements were recorded. Heat conduction within the fire compartment could be ignored because of the ceramic fiber insulation lining the walls and ceiling. The exposed corrugated steel plate used in the construction of the balcony and the fascia reached steady state heat conduction within the settling time because of the thin corrugated steel plate having almost no thermal inertia.

Temperatures from the two fixed thermocouple trees (THCP -3 and 0) are recorded continuously throughout the test at intervals of 2 s. The movable north thermocouple tree was installed at positions THCP 1-6 during the time intervals listed in Table 3.4 and temperatures also recorded at intervals of 2 s. Steady-state temperatures are computed as the average temperature over the last 60 s of the time interval the thermocouple tree is positioned at that particular location. The movable thermocouple tree is fixed on location for at least 300 s. For the fixed trees the temperature average is based on the last 60 s recorded.

Test ID	**THCP 1**	**THCP 2**	**THCP 3**	**THCP 4**	**THCP 5**	**THCP 6**
B4138-105	———	———	2790-3450	———	———	0000-2610
B4138-106	0000-3390	3510-3840	3990-4800	4920-5280	5490-5790	5880-7080
B4138-107	0000-3240	3450-3840	4020-4980	5160-5460	5640-6000	6180-7140
B4138-108	5280-5580	4860-5160	4020-4680	3540-3840	3120-3420	0000-2940
B4138-109-100	0480-0780	0860-1160	1260-1550	1650-1980	2070-2400	2520-2880
B4138-109-150	5100-5400	4710-5010	4320-4620	3930-4230	3550-3850	3120-3480
B4138-109-200	5490-5790	5880-6180	6270-6570	6660-6980	7050-7350	7410-7710

Table 3.4 *Movable north thermocouple tree position in seconds from start of test.*

After a settling time of at least 1800 s, velocity measurements are initiated. Velocities are measured at positions according to Table 3.3 by aligning the probe (thermal or mechanical) with the respective thermocouple in the thermocouple tree. Using the mechanical vane anemometer the readings are taken over a time period of 30 s yielding an average velocity at that position. Velocities measured with the thermal anemometer are averaged over a time period of 1 s, requiring consecutive readings to compute an average velocity. Based on the fluctuations of the velocity it was determined if more than one reading was required, heavy fluctuations requiring more readings than almost steady-state flows. Upon the successful completion of recording temperatures and velocities at one THCP location, the movable tree is repositioned to the next location and recordings initiated.

Tests B4138-{105-108} were conducted as isolated events, whereas tests B4138-109-{100-200} were conducted as three continuous events, i.e. the heat release rate was changed to the prescribed test values during the test and the flow allowed to settle before commencing new recordings.

Data Processing

Velocities are measured with anemometers and validated against velocities derived from the measured temperature fields.

Velocities derived from temperature readings provide a better resolution of the velocity field in the compartment opening because of the densely distributed measuring points, i.e. thermocouples, and thus more suitable for calculating flow rates in the opening. To provide intermediate data points between THCP locations, the measured temperature field is interpolated using a simple linear fit between THCP locations. The interpolated temperature field is applied in the derivation of the velocity field applying Eqn. (3.3.3), Section 3.3, p. 91.

Heat and mass flow rates are computed from the temperature derived velocity profiles and temperature profiles in the compartment opening using the numerical integration method outlined in Section 2.6, Eqns. (2.6.4) and (2.6.6), p. 43, and mass flow rates per unit length using Eqn. (2.6.5), p. 43. Smoke layer depths are computed from the buoyancy profiles applying the method described in Section 3.4, Eqn. (3.4.1), p. 91.

Quantities measured on one side of the compartment center line are mirrored to the opposite side, forcing symmetric flow properties. Readings taken at the quarter points (THCP±3) are compared to make sure that the approach flow is actually symmetric by nature.

3.7 Modeling Program

3.7.1 Simulations Breakdown

Simulations carried out in the small-scale approach flow modeling program are listed in Table 3.5 with applied total heat release rate $\dot{Q}_T$ $[kW]$, ambient temperature T_∞ $[°C]$, geometrical configuration (Conf.), sub-models (radiation (Rad.) and heat conduction (Heat.)) and averaging time interval $\bar{t}$ $[s]$.

				Sub-models		
Simulation ID	$\dot{\mathbf{Q}}_\mathbf{T}$	$\mathbf{T}_\infty$	**Conf.**	**Rad.**	**Heat.**	$\bar{\mathbf{t}}$
B4138-105	250	+2.23	W	NO	NO	30
B4138-106	500	-5.88	W	NO	NO	30
B4138-107	250	+3.33	WO	NO	NO	30
B4138-108	500	+7.74	WO	NO	NO	30
B4138-109-100	100	-0.47	WO	NO	NO	30
B4138-109-150	150	-0.47	WO	NO	NO	30
B4138-109-200	200	-0.47	WO	NO	NO	30
B4138-108-RAD	500	+7.74	WO	YES	NO	30
B4138-108-HC	500	+7.74	WO	NO	YES	30

Table 3.5 *Small-scale approach flow modeling: List of simulations.*

Config.	Plume D_p^*	Approach flow D_{cj}^*	Spill Plume D_l^*
B4138-105	0.48	0.16	0.18
B4138-106	0.64	0.16	0.24
B4138-107	0.48	0.16	0.18
B4138-108	0.64	0.16	0.24
B4138-109-100	0.34	0.16	0.12
B4138-109-150	0.40	0.16	0.15
B4138-109-200	0.45	0.16	0.16

Table 3.6 *Characteristic length scales in the small-scale approach flow model.*

3.7.2 Description of CFD model

Modeling Procedure

The CFD model *Fire Dynamics Simulator ver. 4.06*, described in Section 2.4, was applied in the modeling of the small-scale experimental approach flow tests.

Heat release rates are increased linearly to the prescribed test values according to Table 3.5 over a time period of 1 s. Computations are run until at least 60 s of steady state was achieved. Quantities of temperature and velocities are recorded at positions listed in Table 3.9. Measured quantities are averaged over the steady state time period $\bar{t}$ (at least 30 s) with the conversion program *fds2ascii* and saved for external data processing.

Computational Grid and Boundary Conditions

Sketches of the computational grids along with geometrical dimensions applied in the CFD model of the small-scale approach flow setups are shown in Figures 3.8 and 3.9 for geometrical configurations W and WO respectively. The fire source is elevated 0.05 m above the floor of the fire compartment. Discrepancies in the physical extents of the experimental setup and CFD model are caused by an updated measurement of the fire compartment that was not brought to the author's attention until after the majority of the CFD simulations were completed.

Grid spacings are determined from the characteristic length scales in the plume region D_p^* and the approach flow/ceiling jet D_{cj}^*, see Table 3.6, and recommendations provided in Chapter 2. All grids are rectilinear and grid spacings are provided in Table 3.7 applying the notation $\Delta\mathbf{x} = \{\Delta x, \Delta y, \Delta z\}$. A multiple of the largest grid size, i.e. $\Delta\mathbf{x} = 0.1$ m, is applied in the CFD model. Grids overlap by one or two grid cells depending on local grid spacings.

The lower thermal zone of a well-ventilated fire compartment can be assumed at rest and ambient temperature, hence boundary conditions of zero velocity and ambient temperature (passive vent) can be applied below (but not submerged in) the smoke layer, saving the computational cost of additional control volumes

	$\{\Delta x, \Delta y, \Delta z\}$ mm		
Config.	**Grid #1**	**Grid #2**	**Grid #3**
W	{25,25,25}	{100,50,25}	{25,50,25}
WO	{25,25,25}	{100,50,25}	{25,50,25}

Table 3.7 *Grid spacings according to designations in Figures 3.8 and 3.9.*

Designation	**Line type**	**BC type**	**FDS type**
Outflow	Dashed	Passive vent	*OPEN*
Smoker layer interface (z_{sl})	Dashed	Passive vent	*OPEN*
Floor	Dashed	Passive vent	*OPEN*
Walls	Solid	Adiabatic/partial slip	*ADIABATIC*
Ceiling	Solid	Adiabatic/partial slip	*ADIABATIC*
Balcony	Solid	Thermally thin/partial slip	*STEEL*
Draft curtain	Solid	Thermally thin/partial slip	*STEEL*
Fire base	Solid	Steady HRR	*HRRPUA*

Table 3.8 *Boundary conditions according to designations in Figures 3.8 and 3.9.*

in the lower thermal zone. To make sure the boundary conditions are not submerged in the smoke layer, conservation of heat is checked by recording the inflow of convective energy at the burner and the outflow of convective energy in the compartment opening. For an adiabatic fire compartment convective heat flow rates should be identical at the burner and the compartment opening.

Measuring Positions

Measurements are recorded using the slice file (SLCF) output option in FDS at positions listed in Table 3.9 along with recorded quantities.

Configuration	**Quantity**	**Location**	**Position**
W	T,u,v,w	Compartment opening	$x \in \{4.2\}$ m
WO	T,u,v,w	Compartment opening	$x \in \{0.0\}$ m

Table 3.9 *Measured quantities and positions applied in the small-scale approach flow CFD model relative to dimensions in Figure 3.8 and Figure 3.9.*

Data Processing

Convective heat $\dot{Q}_{c,w}$ and $\dot{m}_w$ mass flow rates are computed from the temperature and velocity profiles using the numerical integration method outlined in

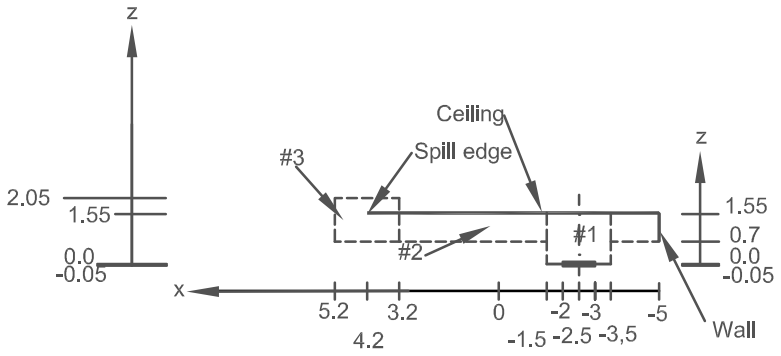

(a) Vertical section.

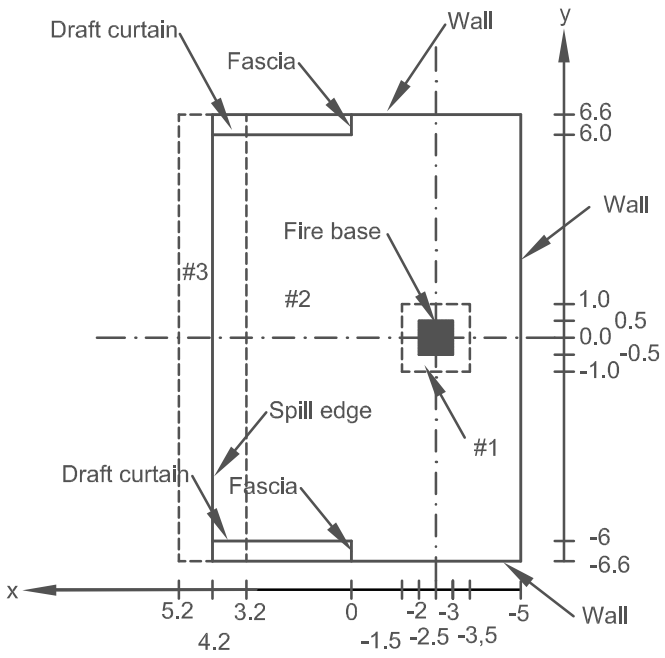

(b) Horizontal section.

Figure 3.8 *CFD model: Configuration W.*

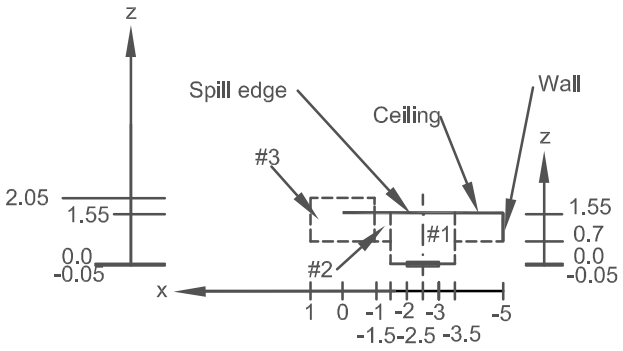

(a) Vertical section.

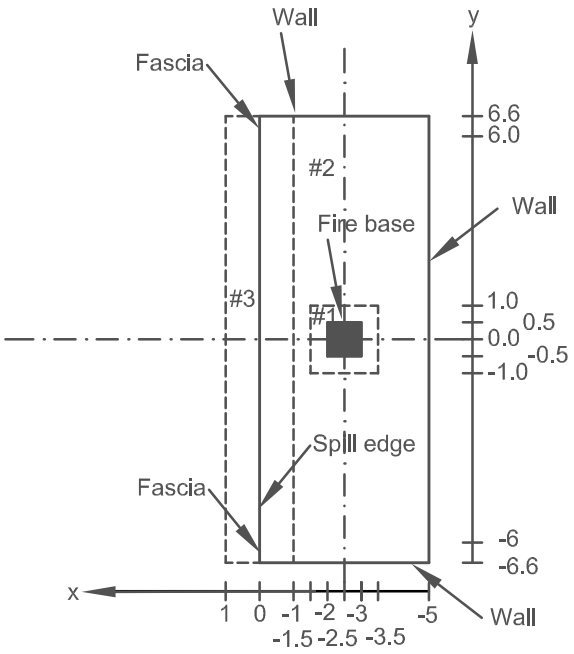

(b) Horizontal section.

Figure 3.9 *CFD model: Configuration WO.*

Section 2.6, Eqns. (2.6.4) and (2.6.6), p. 43. Mass flow rates per unit length $\dot{m}'_w$ are computed adopting the same approach, evidently only performing a one dimensional numerical integration according to Eqn. (2.6.5). Smoke layer depths d_w are computed from the buoyancy profiles applying the method in Section 3.4, Eqn. (3.4.1), p. 91.

CFD Model Inputs

The CFD modeling of the small-scale approach flow setups employ the full hydrodynamic model including LES turbulence model, propane combustion, no radiation model and adiabatic surface boundary conditions for all walls except the balcony and draft curtains where heat conduction through a 5 mm thick corrugated steel plate is applied, assuming a uniform temperature distribution through the thickness of the plate. The rather thick steel plate was chosen because of the sandwich construction applied in the balcony. Primary and non-default input parameters are listed in Table 3.10.

Turbulence model		
Smagorinsky constant	C_s	0.2
Prandtl number	Pr	0.5
Schmidt number	Sc	0.5
Combustion model		
Material	Propane	Default FDS v. 4.06
Heat of combustion	ΔH_c	47,251 kJ/kg
Radiative fraction	χ_r	0.286
Molecular weight	M_w	44.00 g/mol
Soot yield	y_s	0.01 kg/kg
Fire source		
Fire base area	A_f	1.0^2 m^2
Specific HRR	$\dot{Q}''_T$	see Table 3.5
Flame sheet correction	*AUTOMATIC_Z*	*TRUE*
Radiation model		
Radiative model		Gray gas/non-scat.
Update time steps	*TIME_STEP_INC.*	12
Angle increment at update	*ANGLE_INC.*	20
Surface BCs		
Thermal model	Thermally-Thick	*STEEL*
Specific heat	c_s	0.51 kJ/(kg)
Density	ρ_s	7850.0 kg/m^3
Thickness	t_s	0.005 m
Thermal model	All surfaces	Adiabatic
Ghost cell temperature	T_{ghost}	T_g
Velocity model		Partial slip
Wall velocity	u_τ	$0.5u_i$
Flow BCs		
Flow model	Passive vent	*OPEN*
Ambient temperature	T_∞	see Table 3.5
Ambient velocity	$\mathbf{u}$	0 m/s
Ambient perturbed pressure	$\tilde{p}$	0 Pa
Ambient static pressure	p_0	1.013 10^5 Pa

Table 3.10 *Small-scale approach flow setup: Model input parameters.*

3.8 Assessing Sub-model Impacts

Throughout the small-scale CFD modeling program walls and ceiling within the fire compartment are assumed to be adiabatic and heat conduction is only allowed through the balcony and draft curtains. To assess any error associated with neglecting heat conduction through the insulating ceramic fiber lining the walls and ceiling, a simulation of setup B4138-108 was conducted including heat conduction and designated B4138-108-HD. Thermal properties of the insulating ceramic fiber material applied in the CFD model can be found in Table 3.11. The approach flow mass flow rate $\dot{m}_w$ and the convective heat flow rate in the compartment opening $\dot{Q}_{c,w}$ are validated against predictions from the base model setup, i.e. no radiation and heat conduction (except in balcony and draft curtains), B4138-108, and are shown in Figure 3.12.

Surface BCs		
Thermal model	Thermally-Thick	*INSULATION*
Specific heat	c_s	1.0 kJ/(kg*K)
Density	ρ_s	100.0 kg/m^3
Heat conduction	k_s	0.2 W/(m*K)
Thickness	t_s	0.025 m

Table 3.11 *Thermal properties of the modeled insulating ceramic fiber material lining walls and ceiling in the fire compartment.*

A similar study was prepared with radiation included, B4138-108-RAD, and no heat conduction to allow for comparison with the base setup B4138-108. Setup B4138-108 was chosen because it represented the shortest distance from the fire base to the compartment opening, hence the highest temperatures in the compartment opening, and the highest heat release rate addressed in the study. The resulting approach flow mass flow rate $\dot{m}_w$ and the convective heat flow rate in the compartment opening $\dot{Q}_{c,w}$ are plotted in Figure 3.12.

Temperature and velocity profiles at center line and quarter point locations (THCP0 and THCP±3) from the two simple studies are provided in Figures 3.10 and 3.11. The complete series of temperature and velocity profiles are provided in Appendix C. From the temperature profiles it is clear that discrepancies between CFD predictions and experiment increases with distance to the center line along the compartment opening (and hence to the fire base). In B4138-108-HC heat conduction through the enclosure removes energy from the smoke layer, reducing the temperature below the ceiling. With increasing distance to the center line, the smoke layer is exposed to an increasing area of heat conducting surface, explaining why temperature agreement is better close to the center line. In B4138-108-RAD incident radiative energy from the flame region decreases with increasing distance to the center line. Far from the center line the smoke layer emits more energy than it receives explaining the decreasing temperatures. The base setup B4138-108 does not include radiation from the smoke layer, thus over predicting temperatures far from the center line by about 10-20%.

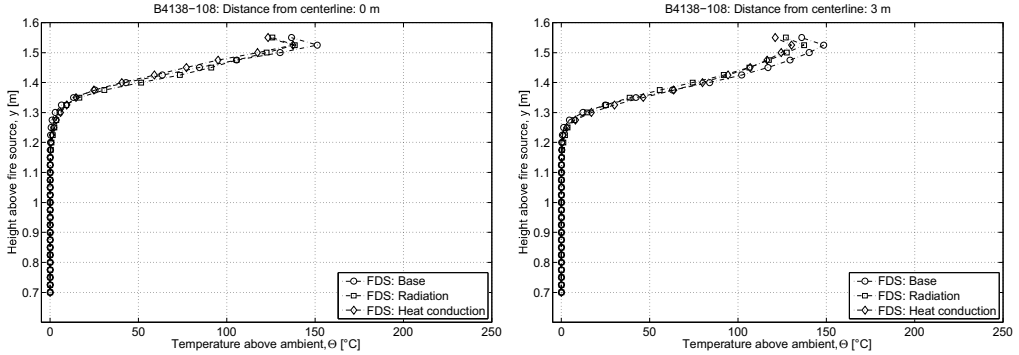

(a) Dist. from centerline: 0 m. (b) Dist. from centerline: 3 m.

Figure 3.10 *B4138-108 - Small-scale: Temperature profiles at THCP0 and THCP±3.*

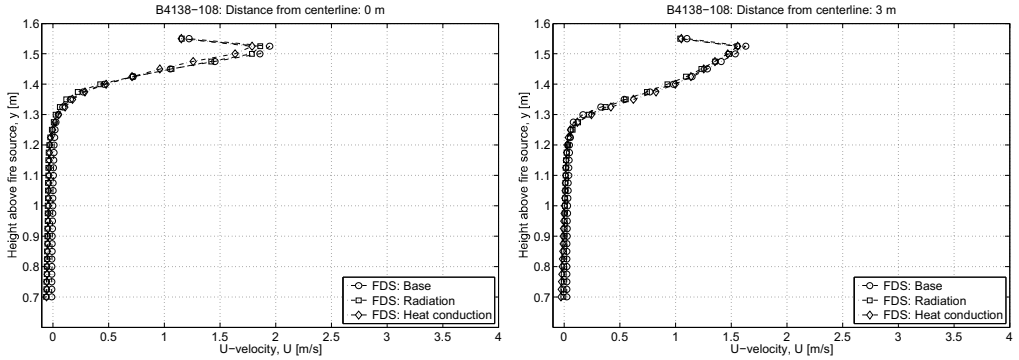

(a) Dist. from centerline: 0 m. (b) Dist. from centerline: 3 m.

Figure 3.11 *B4138-108 - Small-scale: U velocity profiles at THCP0 and THCP±3.*

Velocities predicted by the CFD model with radiation and heat conduction included respectively are in very good agreement with the base setup B4138-108, discrepancies are less than 5% throughout the compartment opening, hence the impact on the velocity profiles is considered insignificant.

A 10% over prediction of convective heat flow rate $\dot{Q}_{c,w}$ by the base setup B4138-108 can be identified in Figure 3.12(b). The approach flow mass flow rate $\dot{m}_w$ is over predicted by 5% relative to the base setup as seen on Figure 3.12(a). Figure 3.12(c) implies that the base setup B4138-108 under predicts smoke layer depths by 10%. Hence it can be deduced that the CFD modeling program is prone to slightly over predict mass flow rates and temperatures.

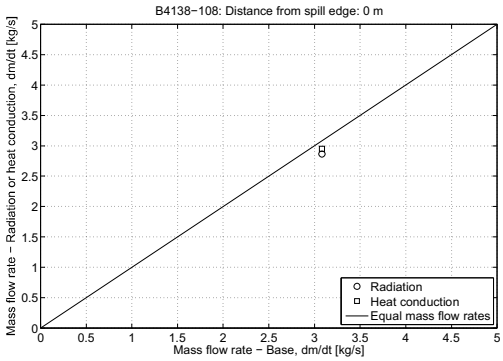

(a) B4138-108: Mass flow rates for base setup and applying radiation and heat conduction respectively.

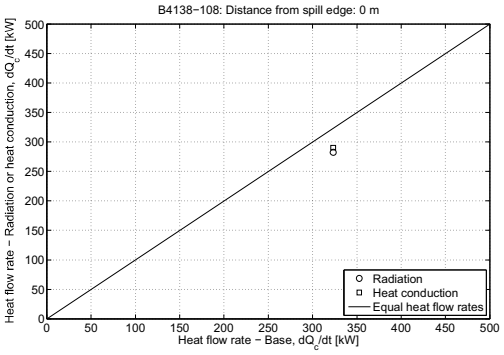

(b) B4138-108: Heat flow rates for base setup and applying radiation and heat conduction respectively.

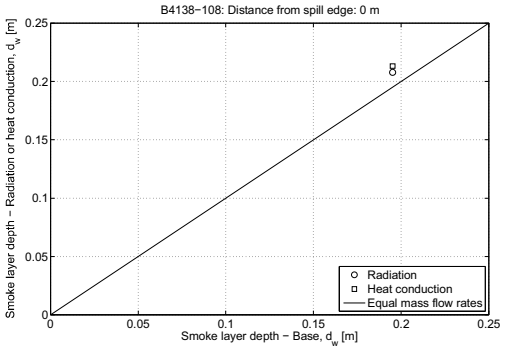

(c) B4138-108: Smoke layer depths for base setup and applying radiation and heat conduction respectively.

Figure 3.12 *B4138-108: Assessing impact from including heat conduction and radiation in the CFD model.*

3.9 Results

3.9.1 Reynolds Number

For the experimental setup to be applicable in any scaling studies, it must be ensured that viscous effects in the proximity of solid walls can be neglected. The Reynolds and Froude number can not both be preserved, thus making sure the flow is fully turbulent, only the Froude number needs to be preserved in the scaling process. An introduction to physical scale modeling and the applied scaling laws is provided in Chapter 4. For now we shall only make sure that the tests conducted in the small-scale experimental approach flow program are suitable for scaling purposes. To neglect any viscous effects close to solid walls, the flow must be fully turbulent, i.e. Reynolds number Re $>$ 4000, with the trivial definition of the Reynolds number:

$$\mathrm{Re} = \frac{U \rho_\infty l}{\mu} \tag{3.9.1}$$

Here U is the mean velocity $[m/s]$, ρ_∞ is the ambient density, μ is the temperature dependent viscosity of the gas mixture $[kg/(m*s)]$. The characteristic length scale l $[m]$ is in this case interpreted as the depth of the smoke layer in the compartment opening. From Figure 3.13 it is clear that the bulk flow in all tests conducted in the experimental program can be considered fully turbulent and hence suitable for Froude modeling.

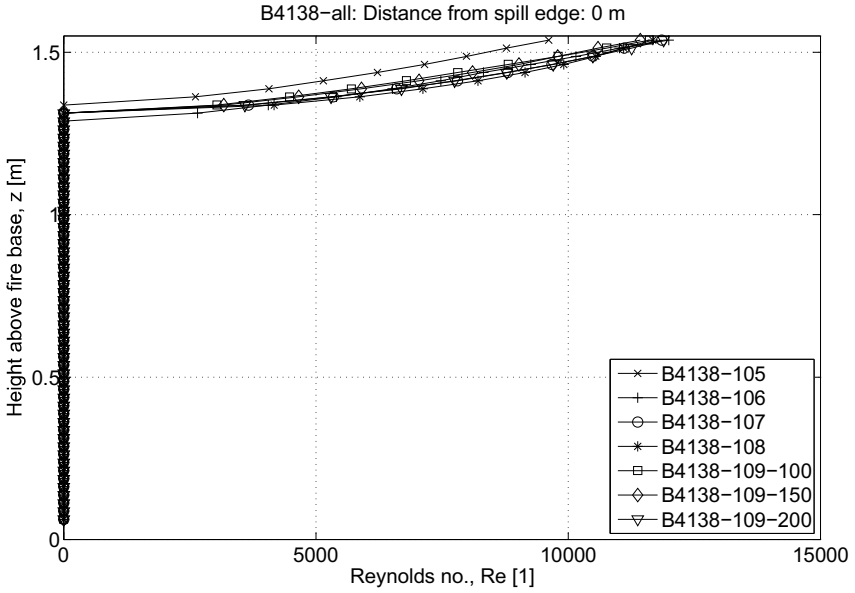

Figure 3.13 *Reynolds number in NRCC tests.*

3.9.2 Conservation of Energy

Conservation of heat is checked by computing the convective heat flow rate in the compartment opening $\dot{Q}_w$ and comparing this to the input convective heat flow rate $\dot{Q}_c$. Simulations B4138-{105-106} comprise heat conduction through the balcony and the draft curtains, hence convective heat flow input via the burner and heat flow rate out through the compartment opening are not expected to be equal. From Figure 3.14 it is clear that convective energy is not conserved for B4138-{105-106} but partly conducted through the balcony and draft curtains. Tests B4138-{107-109} all comprise an adiabatic enclosure conserving convective heat input, supported by the data points located almost completely on the line of equality in Figure 3.14. Conservation of energy also supports the application

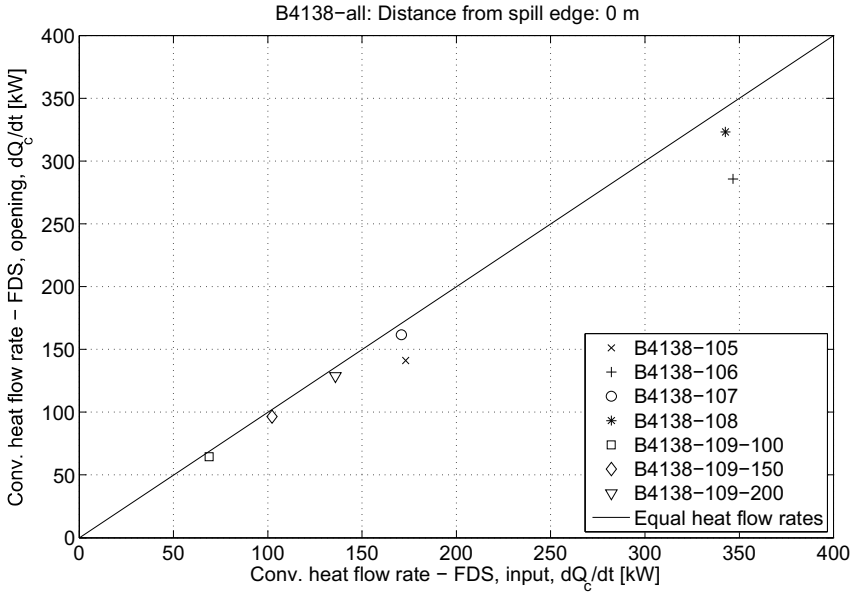

Figure 3.14 *Conservation of energy in CFD model: Input convective heat release rate $\dot{Q}_c$ vs. $\dot{Q}_{c,w}$ in the compartment opening.*

of the boundary conditions below the smoke layer interface z_{sl}, i.e. boundary conditions are not submerged in the smoke layer, hence conserving the approach flow mass flow rate.

Comparisons of the convective heat flow rate in the compartment opening $\dot{Q}_{c,w}$ from the CFD modeling program with the predictions from the experimental program can be found in Figure 3.15. Heat flow rates are generally in good agreement, supporting confidence in the applied CFD model. Heat flow rates in the CFD simulations including heat conduction, i.e. balcony and draft curtains (B4138-{105-106}), are prone to be slightly over predicted, suggesting that heat conduction through the balcony and draft curtains are actually higher than modeled, leading to conservative estimates for approach flow mass flow rates and temperatures.

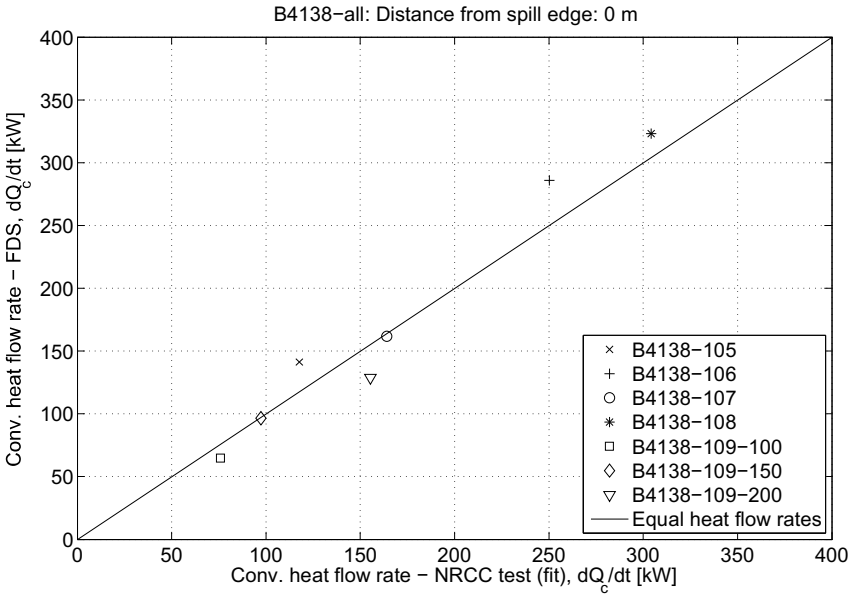

Figure 3.15 *Conservation of energy: CFD model vs. experimental test, $\dot{Q}_{c,w}$ in the compartment opening.*

3.9.3 Temperature Profiles

To reduce the number of plots in the main body of the present thesis, only temperature profiles on the center line, quater points and end points in the compartment opening are included in this section. Supporting plots can be found in Appendix D.

Looking at the figures provided in Figures 3.16-3.18 and Appendix D, a good agreement between CFD predictions and experiments can be observed. Temperatures are in general over predicted but within 20% of experiment with the lowest discrepancies close to the center line. In Section 3.8 it was learned that radiation from the smoke layer would cause a decreasing temperature in the compartment opening with increasing distance to the center line, yielding discrepancies of up to +20% for the CFD predictions in accordance with observations in Appendix D. Heat conduction was also shown to produce discrepancies of the same magnitude in Section 3.8, i.e. heat conduction could also explain discrepancies for increasing distance to the center line. Including both radiation and heat conduction correction would seriously under predict temperatures.

Invoking radiation or heat conduction corrections obviously decreases temperatures and thus increases density. From the discussion in Section 3.8 it was learned that velocity profiles were almost unaffected by invoking heat conduction or radiation correction. Increasing densities hence result in increased mass flow rates.

Looking at the temperature profiles in Appendix C for radiation and heat conduction correction, it is clear that only the maximum temperature, i.e. the

top most part of the profile, is reduced, but the lower part of the profile remains unchanged. From the temperature profiles in Appendix D it is observed that the CFD model under predicts the depth of the temperature profiles, see also Section 3.9.7. Thus invoking radiation correction or heat conduction will not provide better predictions of the lower part of the profile.

Poor agreement at compartment opening end points are attributed to CFD predictions being recorded at locations abutting the fascia edge, thus heavily impacted by the surface boundary conditions.

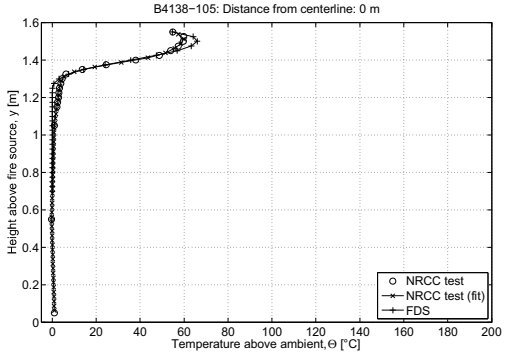

(a) B4138-105.

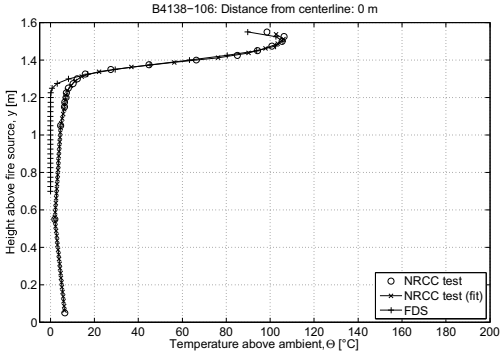

(b) B4138-106.

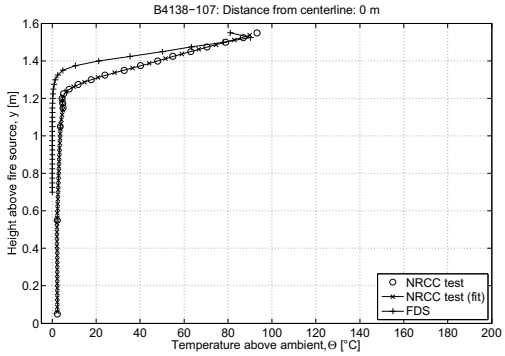

(c) B4138-107.

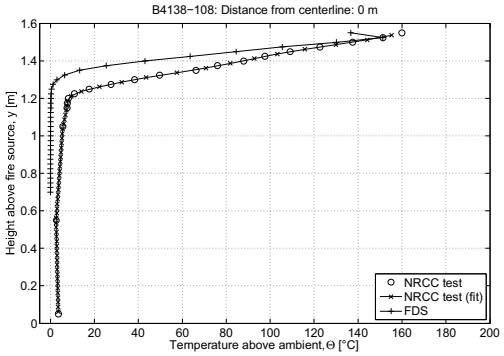

(d) B4138-108.

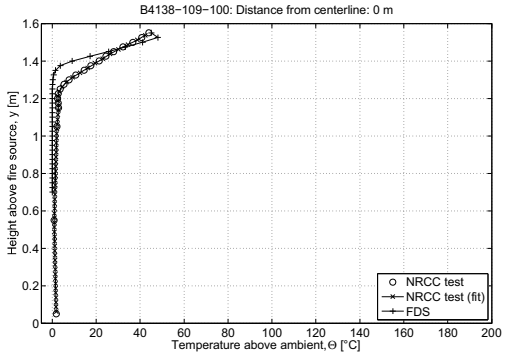

(e) B4138-109-100.

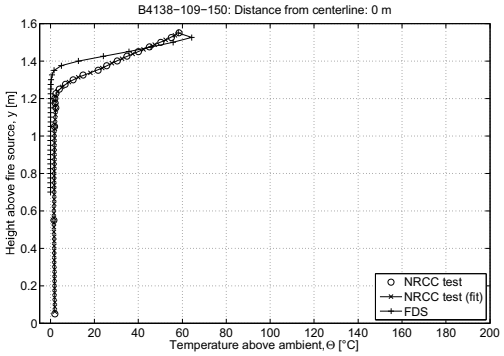

(f) B4138-109-150.

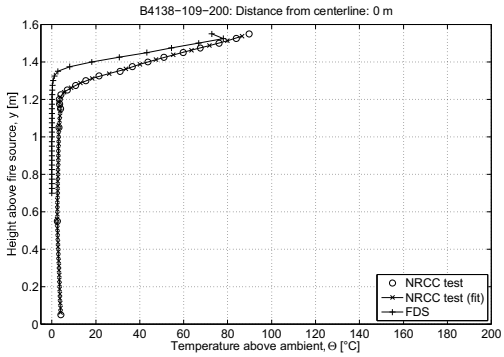

(g) B4138-109-200.

Figure 3.16 *Comparing modeling and experiment: Temperature profiles at location THCP0.*

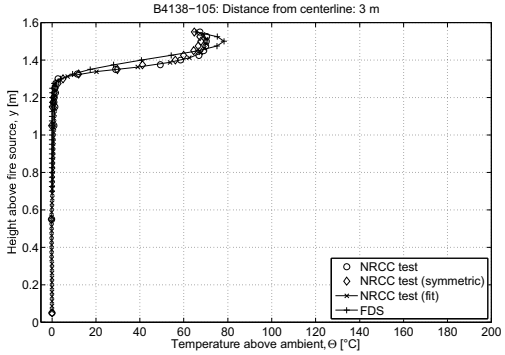

(a) B4138-105.

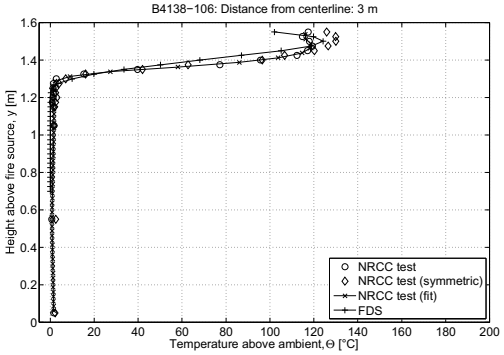

(b) B4138-106.

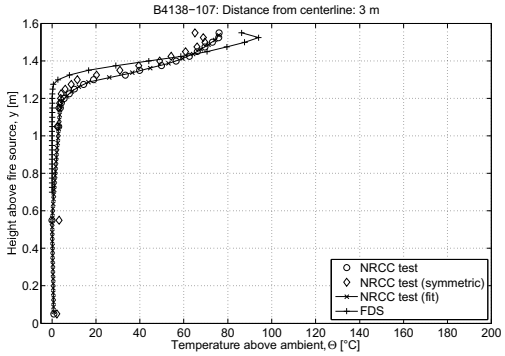

(c) B4138-107.

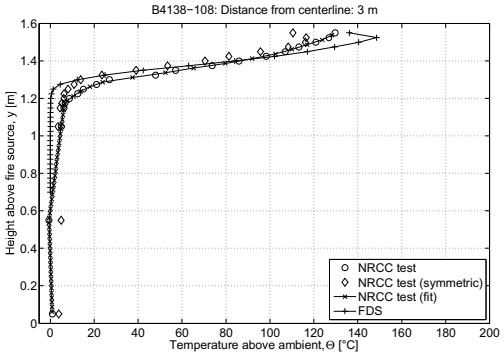

(d) B4138-108.

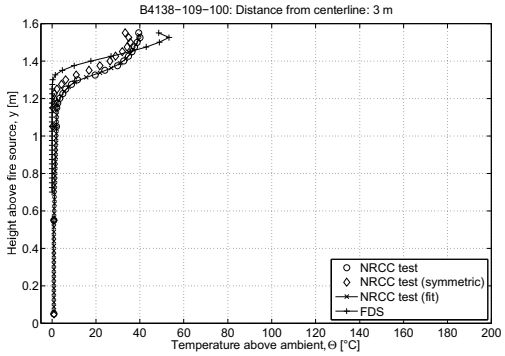

(e) B4138-109-100.

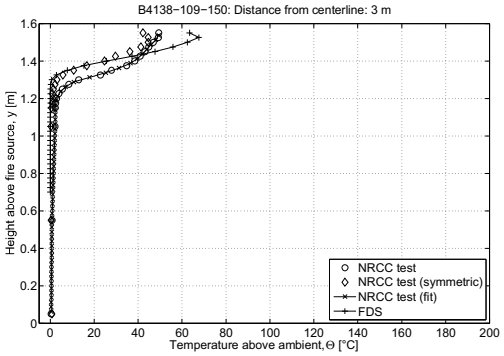

(f) B4138-109-150.

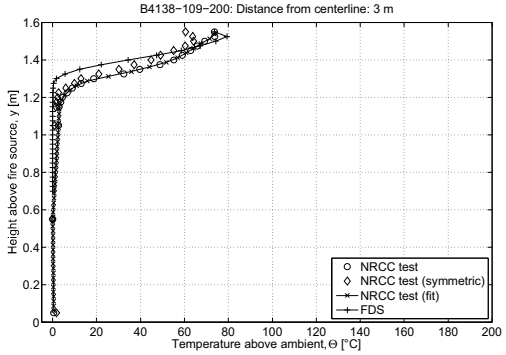

(g) B4138-109-200.

Figure 3.17 *Symmetric flow properties in approach flows: Temperature profiles at THCP±3.*

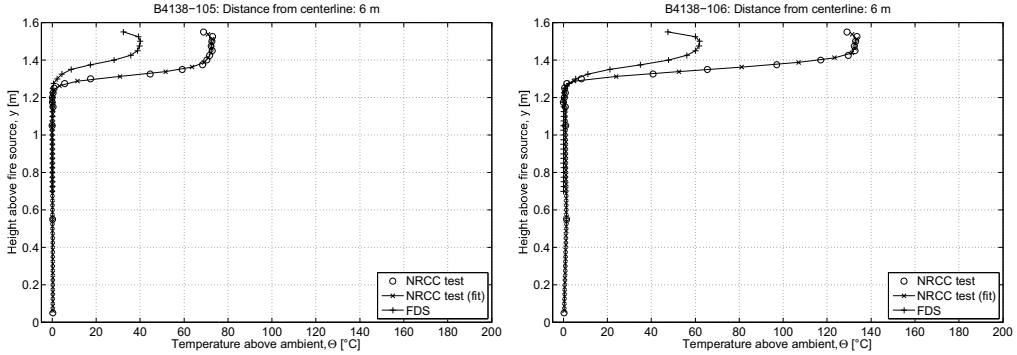

(a) B4138-105.

(b) B4138-106.

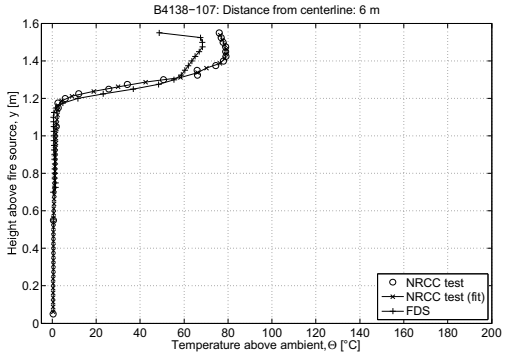

(c) B4138-107.

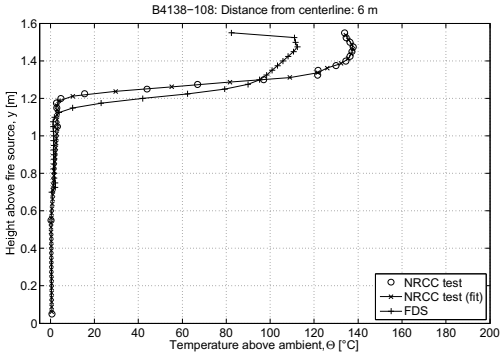

(d) B4138-108.

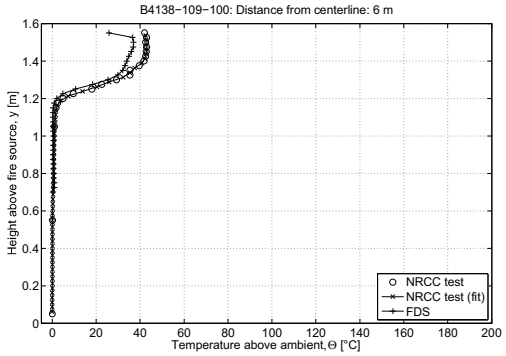

(e) B4138-109-100.

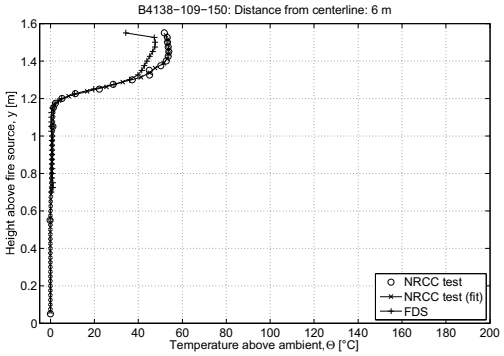

(f) B4138-109-150.

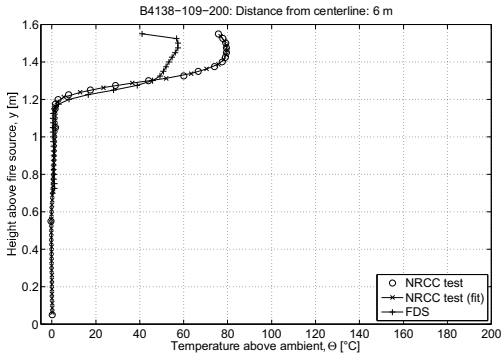

(g) B4138-109-200.

Figure 3.18 *Comparing modeling and experiment: Temperature profiles at location THCP6.*

3.9.4 Velocity Profiles

Plots of velocity profiles are limited in the main body of the thesis, supporting plots can be found in Appendix D.

Good agreement between predicted and measured velocities derived from the temperature field using the method proposed by Morgan (1986) can be identified in all tests, see Figure 3.19. Predictions are in general within 20% of the temperature derived velocities for all measuring locations (THCP0-THCP5) except right at the edges of the compartment opening THCP6. Regarding the discussion on radiation correction and heat conduction in Section 3.8, it should be noted that reducing the temperature rise above ambient inherently reduces velocities computed from the temperature field, hence decreasing discrepancies between CFD predictions and experiment at the top of the velocity profiles.

As mentioned previously the thermal anemometer applied in measuring velocities in tests B4138-{105-106} yielded strange looking velocity profiles, which can be observed in Figure 3.19 and Appendix D. Any clear explanation of the high discrepancies can not be provided, since measured velocities were within the validated measuring range for the instrument [0.15:50] m/s. By comparing the velocity profiles from the anemometer, see Figures 3.19(a) and 3.19(b) with the corresponding temperature profiles in Figures 3.16(a) and 3.16(b), it is clear that the velocity profiles do not behave accordingly.

A simple study of velocity boundary conditions were conducted in extension to the current validation study to see if it was possible to restore the shape of the velocity profiles measured by the thermal anemometer. Different slip conditions were invoked on the ceiling surface but the attempts were unsuccessful. The outcome is very briefly touched in Appendix B.

Based on the above discussion it was decided to disregard the velocity measurements obtained with the thermal anemometer, since no physical explanation can be found to explain the strange shape of the velocity profiles. Discrepancies are attributed to the instrument not being suited for the purpose, e.g. difficulties in aligning the probe in the direction of the flow or the averaging method, see Section 3.6.2.

Measurements using the mechanical vane anemometer in tests B4138-{107-108} exhibit very good agreement with the predicted velocities. Discrepancies are typically within 10-20% of experiment, with the highest discrepancies observed close to the smoke layer interface in the lower part of the velocity profile.

Very poor agreement between CFD predictions and experiments are observed for location THCP6, see Figure 3.21. This is largely attributed to measuring positions in the CFD model abutting the edge of the fascia, i.e. very high dependence on the numerical boundary conditions. In the experiments, measurements were conducted away from the fascia edge, i.e. physical boundary conditions can be neglected. The error committed in the CFD model greatly affects the mass flow rate per unit length $\dot{m}'_w$ at the ends of the fire compartment opening, due to velocities being under predicted. The impact is supported by the decreasing tail-ends observed on the mass flow rate per unit length profiles in Figure 3.22.

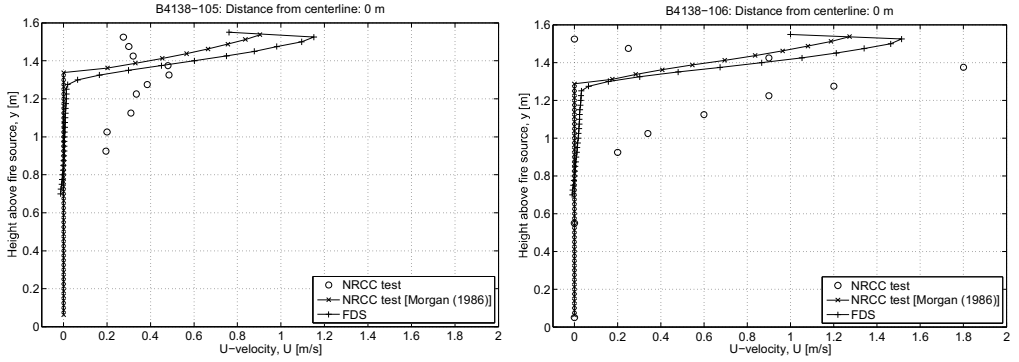

(a) B4138-105.

(b) B4138-106.

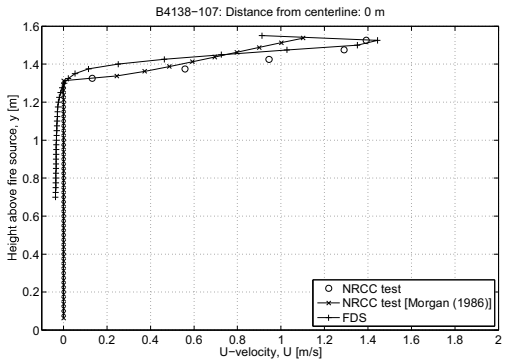

(c) B4138-107.

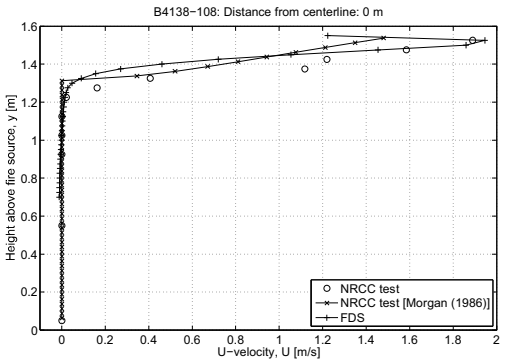

(d) B4138-108.

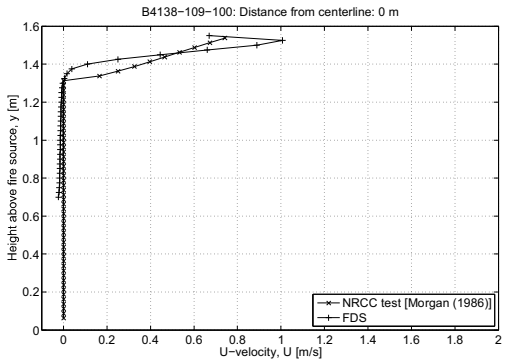

(e) B4138-109-100.

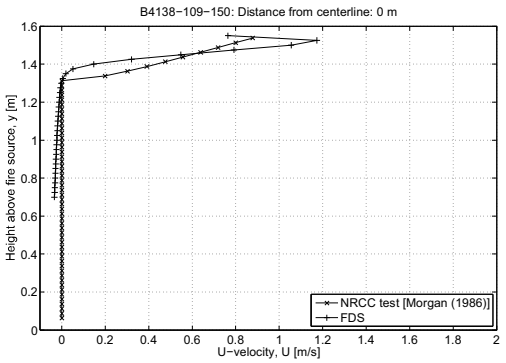

(f) B4138-109-150.

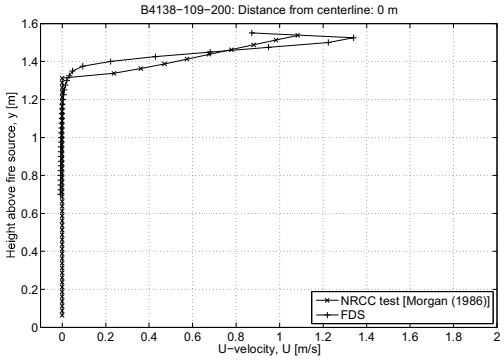

(g) B4138-109-200.

Figure 3.19 *Comparing modeling and experiment: Velocity profiles at location THCP0.*

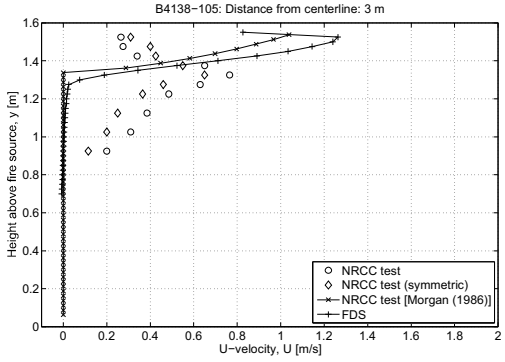

(a) B4138-105.

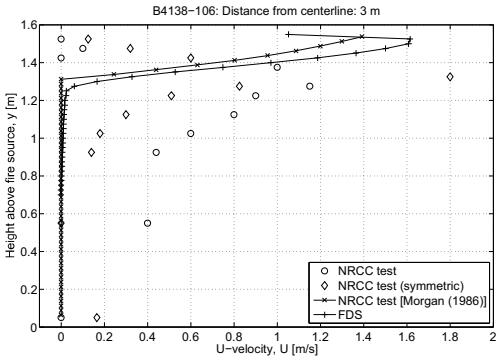

(b) B4138-106.

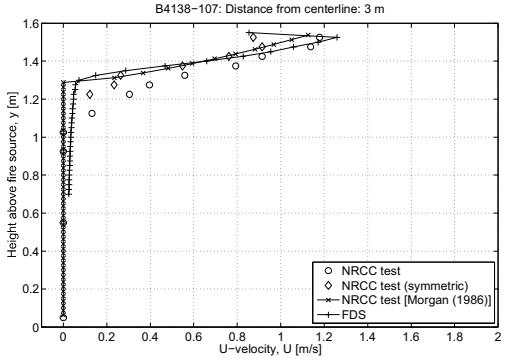

(c) B4138-107.

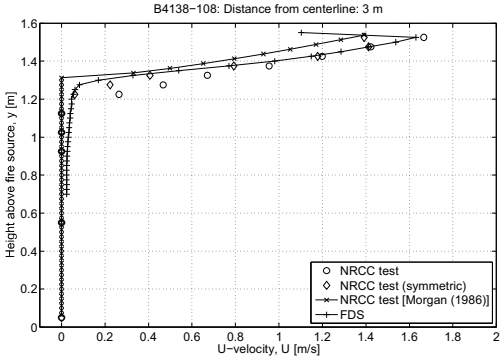

(d) B4138-108.

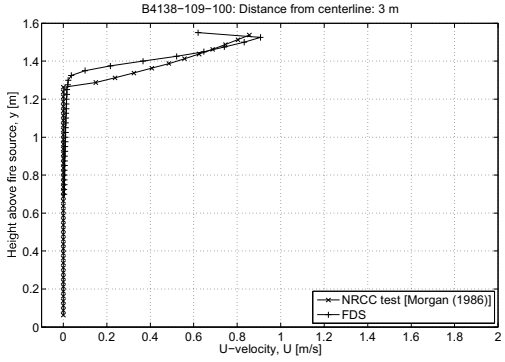

(e) B4138-109-100.

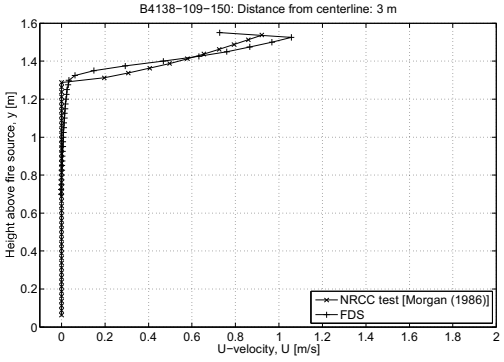

(f) B4138-109-150.

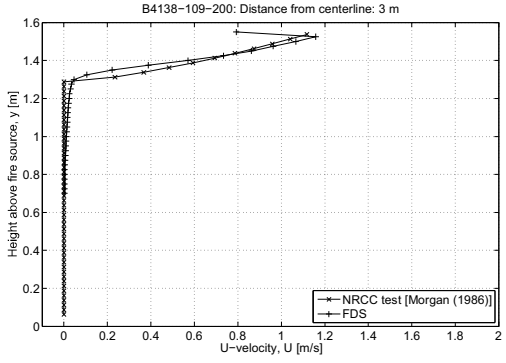

(g) B4138-109-200.

Figure 3.20 *Symmetric flow properties in approach flows: Velocity profiles at THCP±3.*

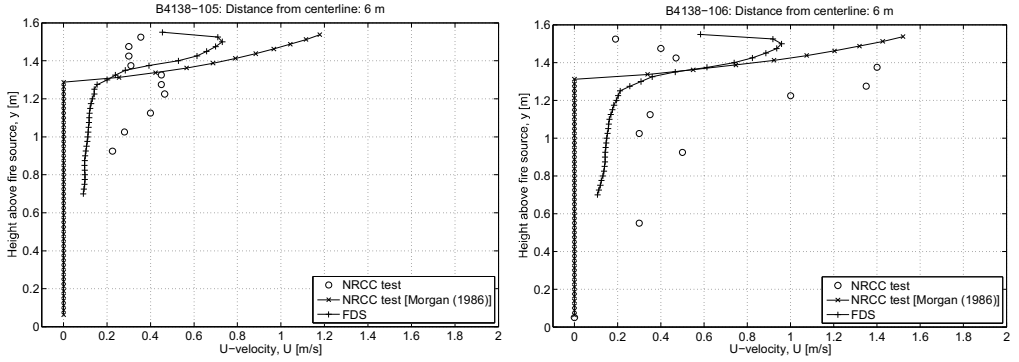

(a) B4138-105.

(b) B4138-106.

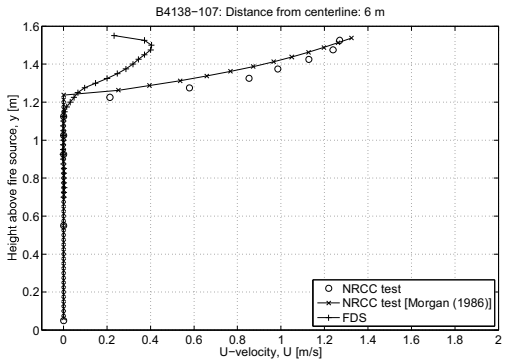

(c) B4138-107.

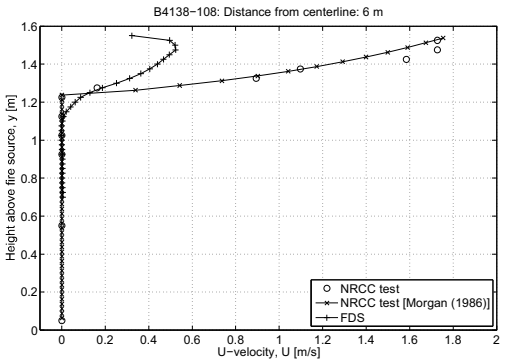

(d) B4138-108.

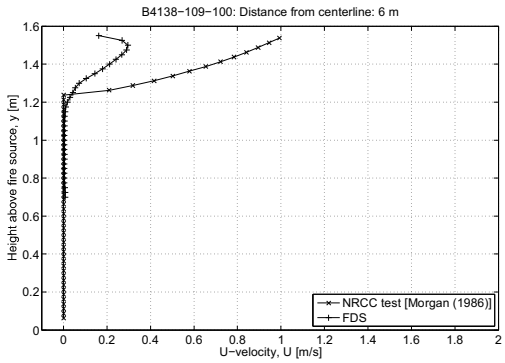

(e) B4138-109-100.

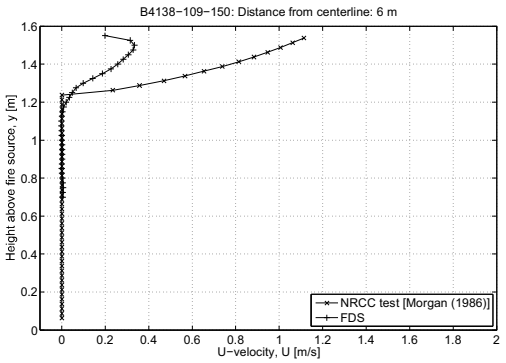

(f) B4138-109-150.

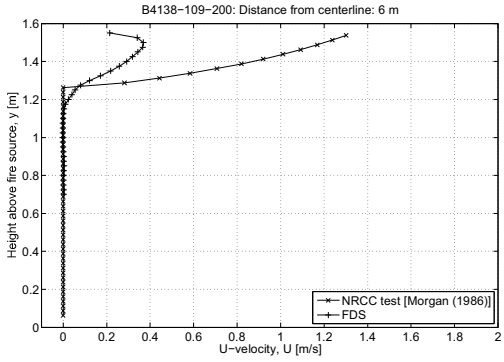

(g) B4138-109-200.

Figure 3.21 *Comparing modeling and experiment: Velocity profiles at location THCP6.*

3.9.5 Symmetric Flow Properties

The symmetric flow pattern expected in the approach flow is verified by comparing measurements at positions THCP±3, see Figure 3.7, p. 99. Temperatures and velocities agree within about 10% and can be found in Figures 3.20 and 3.17.

3.9.6 Mass Flow Rates

The mass flow rates per unit length in the compartment opening $\dot{m}_w$ are depicted in Figure 3.22. With respect to the profile shape, i.e. the distribution across the compartment opening, modeling predictions are in general in good agreement with experimental results. However it should be noted that poor quantitative agreement is identified for simulations B4138-{105-106}. The CFD model is prone to over predict mass flow rates for simulations where heat conduction is included, i.e. where the balcony and draft curtains are attached. Discrepancies are almost constant across the compartment opening. Quantitative agreement is very good in the tests involving only the adiabatic fire compartment (B4138-{107-109}), thus the partly slip velocity boundary condition invoked on all surfaces can be considered valid and applicable. Predictions are in general within 20% of experiment with improved agreement in tests B4138-{107-109} were all solid surfaces are assumed adiabatic. For tests B4138-109-{100-200} discrepancies are below 10% of experiment.

The thermal properties of the balcony and draft curtains are based on a material thickness of roughly 5 mm (all uncertainties taken into consideration). This may seem to be a fairly large thickness for a corrugated steel plate, but the value was chosen due to the thermal boundary condition. In FDS heat conduction (default mode) through a material is computed with a backing temperature equal to the ambient temperature. This means that heat is always conducted to a void at a fixed ambient temperature, no matter the heat influx. Two other boundary conditions are provided for the heat conduction equation; adiabatic (no heat loss to the void) and heat conduction to gas cells on the far side of the solid (identical to the boundary condition applied on the front side). The latter boundary condition would have been the most appropriate to apply in B4138-{105-106}, because energy is conducted through the balcony and draft curtains, heating the air on the far side. However because of the grid design and considering computational costs of adding extra control volumes, this was not considered an applicable boundary condition, since it requires gas phase control volumes on the far side of the solid transmitting the heat. The thickness of the corrugated steel plate applied in constructing the balcony and draft curtains in the physical model was about 3 mm. Applying steel plates with a thickness of 5 mm in the CFD model was considered a way to decrease heat conduction, and hence address the fact that the far side of the balcony and draft curtains were not kept at a fixed ambient temperature throughout the experimental tests, because of heat being convected and re-radiated away from the far side surface. The present approach is considered a good compromise, not reducing the applicability of the predictions and the confidence in the CFD model.

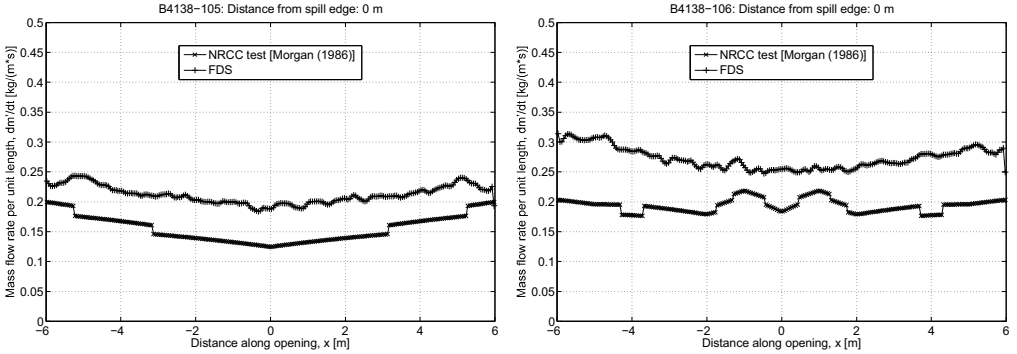

(a) B4138-105.

(b) B4138-106.

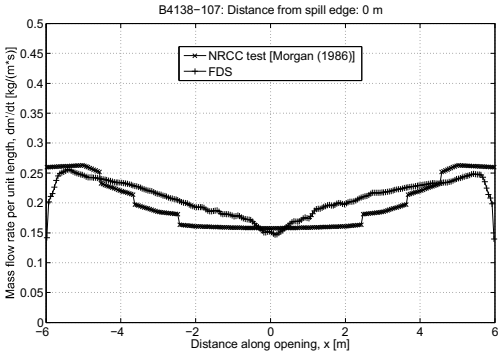

(c) B4138-107.

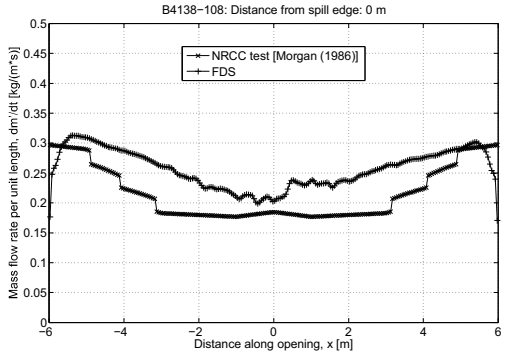

(d) B4138-108.

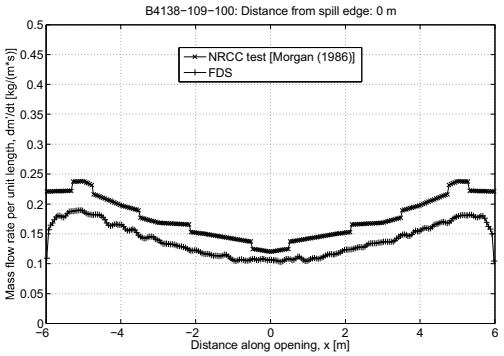

(e) B4138-109-100.

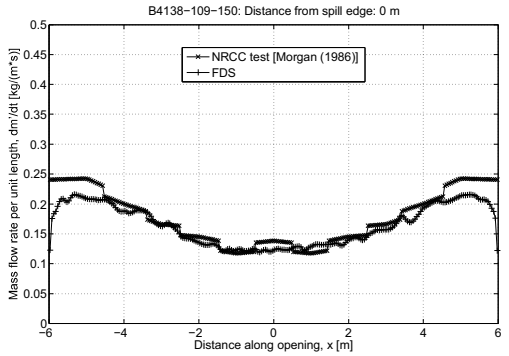

(f) B4138-109-150.

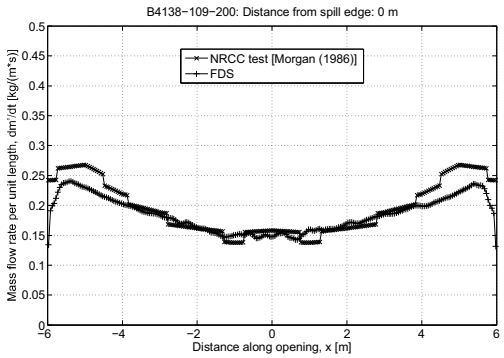

(g) B4138-109-200.

Figure 3.22 *B4138-XXX: Mass flow rates per unit length in compartment opening.*

The total mass flow rates in the compartment opening $\dot{m}_w$ supports the discussion above. Predictions in Figure 3.23 are generally within 20% of experiment. Larger discrepancies are however identified for experiments B4138-{105-106} (within 30% of experiment), attributed to the inadequately described and modeled thermal boundary condition for the balcony and draft curtains.

Discussions in Section 3.8 and Section 3.9.3 imply that invoking radiation correction or heat conduction will increase the total approach flow mass flow rate, because of increasing densities (temperatures are decreased) and almost conserved velocity profiles, see e.g. Figure 3.12(a). Looking at Figure 3.23 this will increase mass flow rates predicted by the CFD model, displacing points laterally, and thus deteriorate agreement by increasing discrepancies for tests B4138-{105-108}. If the 5% increment of mass flow rates observed in Figure 3.12(a) can be transfered to B4138-{109} this would improve agreement between mass flow rates predicted by CFD modeling and experiment.

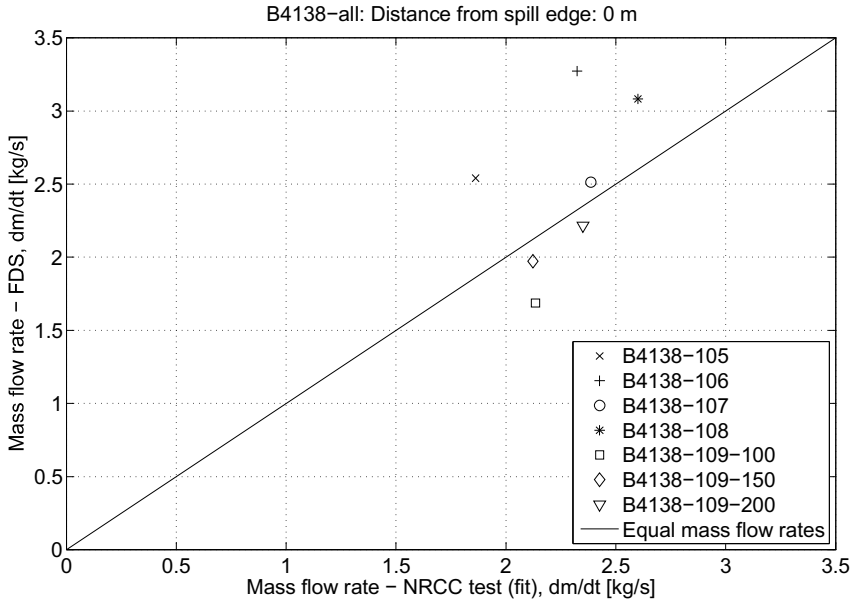

Figure 3.23 *B4138-XXX: Total mass flow rates.*

3.9.7 Smoke Layer Depth

Smoke layer depths d_w are computed from the buoyancy profiles, see Section 3.4. A poor agreement between modeled and measured smoke layer depths is the conclusion from Figure 3.24. The CFD model is prone to under predict the smoke layer depths, which was expected because of the deeper temperature profiles discussed in Section 3.9.3 inherently impacting the buoyancy profiles. The CFD model under predicts the smoke layer by about 30% compared to experiment.

Under predicting the smoke layer depth increases the rising height and hence the mass flow rate in the axisymmetric plume, over predicting the approach flow mass flow rate, which is supported by Figure 3.23.

However over predicting the mass flow rate from the axisymmetric plume inherently allows for more entrainment and hence a lower temperature in the smoke layer. This is not clearly supported by the temperature profiles found in Appendix D, where the CFD model is prone to slightly over predict the temperatures in the bulk flow compared to experiment. As discussed in Section 3.9.3 the over prediction of the temperature can partly be explained by the lack of radiation correction and/or heat conduction.

From the discussions in Section 3.8 it was learned that correcting for radiation and heat conduction would increase the average smoke layer depth. Transferring this conclusion to Figure 3.24 would displace points laterally, hence decreasing discrepancies between modeling and experiments. Smoke layer depths are however only expected to be increased by up to 10%, not significantly improving agreement in Figure 3.24.

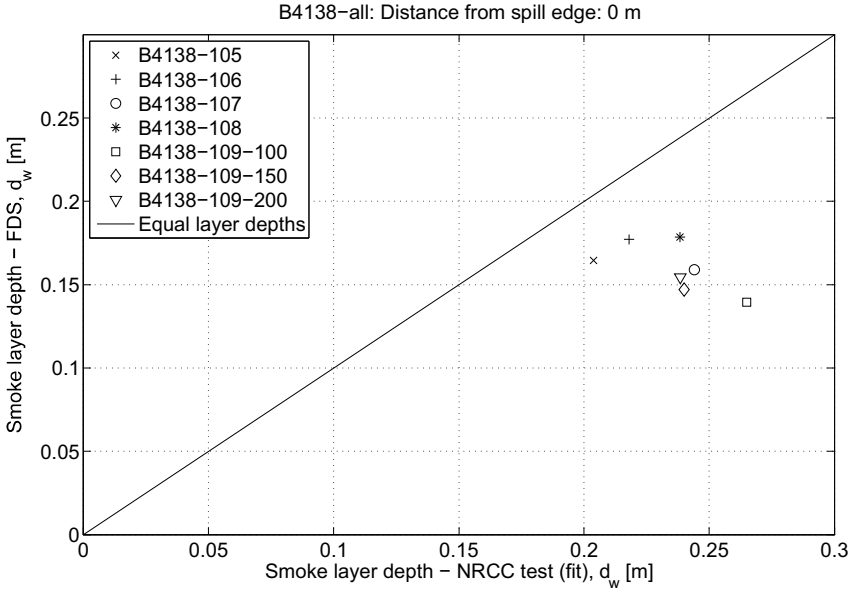

Figure 3.24 *B4138-XXX: Smoke layer depth in the compartment opening.*

3.10 Conclusion

The experimental small-scale approach flow program has provided validation data for approach flows emanating across a 12 m wide opening W_w with fire sizes $\dot{Q}_T$ ranging from 100 kW to 500 kW and distances from fire base to compartment opening D_{fb} ranging from 2.8 m to 7.0 m.

From considering the Reynolds numbers in the experimental program, it was shown that measurements were suitable for application in Froude modeling.

Results from the experimental program have been used in the validation of the CFD fire model *Fire Dynamics Simulator ver. 4.06*. From the validation study the following was learned about the present setup of the CFD model:

Good qualitative agreement - The predicted shape of mass flow rate profiles along with temperature and velocity profiles were in very good agreement with the results from the experimental program.

Temperatures are over predicted - Temperatures are predicted within 20% of experimental measurements with the lowest discrepancies ($\sim$5) close to the center line. Discrepancies are attributed to neglected radiation and heat conduction in the CFD model.

Velocities are in good agreement - Measurements from the thermal anemometer were discarded. Predictions compared to velocities measured with the mechanical vane anemometer were within 10-20% of the experimental measurements. CFD predictions were within 20% of velocities derived from temperatures using the method proposed by Morgan (1986).

Mass flow rates were over predicted - Mass flow rates in tests B4138-{105-106} were over predicted because of inadequately information and modeling of the heat conduction through the balcony and draft curtains. In general mass flow rates are predicted within 20% of experiment. Mass flow rates per unit length are predicted within 20% of experiment in the bulk flow.

Convective heat flow rates are in good agreement - CFD predictions are within 10% compared to measurements.

Smoke layer depths were under predicted - The CFD model under predicts the mean smoke layer depth in the fire compartment opening by up to 30% compared to experiment.

The validation study supported a high level of confidence in the applied CFD model, suggesting it can be applied in computing approach flow mass flow rates.

3.11 Discussion

The low soot yield in propane and the low heat release rates were the main reason for disregarding radiation in the modeling program. The low soot yield would produce low absorption coefficients κ, resulting in low net energy gain by a control volume submerged in the smoke layer, see Section 2.4.4. The above discussions do not provide a clear answer to whether overall agreement between CFD predictions and experiment would deteriorate or improve by including radiation. The present study aims at determining approach flow mass flow rates for which the impact by invoking radiation correction was shown to be almost

negligible. The computational costs of invoking the radiation model is about a 20% increase in CPU time, another reason for deciding to disregard radiation in the current modeling program.

3.12 Future research

Future research should incorporate radiation correction and heat conduction to clearly identify the impact on the approach flow mass flow rates. Additional simulations of different thermal boundary conditions for the draft curtains and balcony are expected to support the confidence in the applied CFD model, i.e. improving agreement between modeling and experiment. Focus should be on addressing the deeper temperature profiles obtained from experiment compared to profiles predicted by the CFD model. The present study does not support invoking radiation correction or heat conduction as means to improve the prediction of the temperature profile depths.

Chapter 4

Physical Scale Modeling

4.1 Introduction

The small-scale tests reported in Chapter 3 have shown that the CFD model *Fire Dynamics Simulator ver. 4.06* can be applied with confidence in modeling small-scale approach flows in wide openings. Validating the CFD model for full-scale flows requires that the scaling laws are verified for the present setup. A thorough introduction to the scaling principles are presented in Thomas et al. (1963) and Quintiere (1989), and is not repeated in it's entirety herein.

4.2 Non-dimensional Groups

The non-dimensional groups are derived to develop scaling relations for Froude modeling of the experimental setup in the present study. Defining the basic non-dimensional variables:

$$\hat{x} = \frac{x}{l} \tag{4.2.1a}$$

$$\hat{w} = \frac{w}{W} \tag{4.2.1b}$$

$$\hat{p} = \frac{p}{p^*} \tag{4.2.1c}$$

$$\hat{p}' = \frac{p'}{p^*} \tag{4.2.1d}$$

$$\hat{\rho} = \frac{\rho}{\rho_\infty} \tag{4.2.1e}$$

$$\hat{T} = \frac{T}{T_\infty} \tag{4.2.1f}$$

$$\hat{t} = \frac{t}{\tau} \tag{4.2.1g}$$

$$\hat{\dot{Q}} = \frac{\dot{Q}''' l}{\rho_\infty c_p T_\infty W} \tag{4.2.1h}$$

where l is a geometric length scale $[m]$, W is a characteristic velocity $[m/s]$, τ is a characteristic time scale $[s]$ and T_∞, p_∞, ρ_∞ are ambient temperature $[K]$,

pressure $[Pa]$ and density $[kg/m^3]$ respectively. p^* is termed the characteristic pressure defect $[Pa]$.

The scale and full-scale model of a test setup must evidently obey the conservation laws and the equation of state. Inserting the non-dimensional groups defined in Eqn. (4.2.1) in the conservation equations for mass Eqn. (4.2.2a), momentum Eqn. (4.2.3a), energy Eqn. (4.2.4a) and equation of state Eqn. (4.2.5a) yield the non-dimensional groups Π_i. Flows in fires are driven by buoyancy thus the scaling relations can be developed from looking at the vertical direction only. Conservation of mass:

$$\frac{\partial \rho}{\partial t} + \frac{\partial (\rho w)}{\partial z} = 0 \tag{4.2.2a}$$

$$\Pi_1 + \frac{\partial \hat{\rho}}{\partial \hat{t}} + \frac{\partial (\hat{\rho}\hat{w})}{\partial \hat{z}} = 0 \tag{4.2.2b}$$

where ρ is the density $[kg/m^3]$, w is the velocity $[m/s]$ in the vertical direction, t is the time scale $[s]$ and z is the position $[m]$.

Conservation of momentum in the vertical direction yields:

$$\rho\left(\frac{\partial w}{\partial t} + w\frac{\partial w}{\partial z}\right) = -\frac{\partial p'}{\partial z} + g\left(\rho_\infty - \rho\right) + \frac{4}{3}\mu\frac{\partial^2 w}{\partial z^2} \tag{4.2.3a}$$

$$\hat{\rho}\left(\Pi_1\frac{\partial \hat{w}}{\partial \hat{t}} + \hat{w}\frac{\partial \hat{w}}{\partial \hat{z}}\right) = -\Pi_2\frac{\hat{p}'}{\partial \hat{z}} + \frac{1}{\Pi_3}\left(1 - \hat{\rho}\right) + \frac{4}{3}\frac{1}{\Pi_4}\frac{\partial^2 \hat{w}}{\partial \hat{z}^2} \tag{4.2.3b}$$

where μ is the dynamic viscosity $[kg/(m * s)]$, g is the gravitational acceleration $[m/s^2]$, $p' = p - p_\infty$ with p and p_∞ being the absolute and ambient pressures respectively $[Pa]$.

Conservation of energy:

$$\rho c_p\left(\frac{\partial T}{\partial t} + w\frac{\partial T}{\partial z}\right) = k\frac{\partial T^2}{\partial z^2} - 4\kappa\sigma T^4 + \int_0^{4\pi}\kappa I d\omega + \dot{Q}'''\frac{\partial p}{\partial t} \tag{4.2.4a}$$

$$\hat{\rho}\left(\Pi_1\frac{\partial \hat{T}}{\partial \hat{t}} + \hat{w}\frac{\partial \hat{T}}{\partial \hat{z}}\right) = \frac{1}{\Pi_3\Pi_5}\frac{\partial^2 \hat{T}}{\partial \hat{z}^2} + \Pi_3\Pi_5\Pi_6\Pi_7\left(\int_0^{4\pi}\hat{I}d\omega - 4\hat{T}^4\right)\ldots$$
$$+ \hat{\dot{Q}} + \Pi_8\frac{\partial \hat{p}}{\partial \hat{t}} \tag{4.2.4b}$$

where c_p is the heat capacity at constant pressure $[kJ/(kg * K)]$, ω is the solid angle over which the radiant intensity is evaluated (the unit sphere), T is the gas temperature $[K]$, k is the thermal conductivity $[kW/(m * K)]$, I is the radiant intensity $[kW/m^2]$, κ is the absorption coefficient [1] and $\dot{Q}'''$ is the heat release rate per unit volume $[kW/m^3]$.

The equation of state:

$$p = \rho R T \tag{4.2.5a}$$

$$\hat{p} = \left(\frac{1}{\Pi_8} - \frac{1}{\Pi_8\Pi_9}\right)\hat{\rho}\hat{T} \tag{4.2.5b}$$

where the gas constant $R = c_p - c_v$ $[kJ/(kg * K]$.

The Π_1 group is constant for a characteristic time scale $\tau = l/W$:

$$\Pi_1 = \frac{l}{W\tau} = 1 \tag{4.2.6}$$

and thus preserved.

For a characteristic pressure defect $p^* = \rho_\infty W^2$ the Π_2 group is constant and thus preserved in scale modeling:

$$\Pi_2 = \frac{p^*}{\rho_\infty W^2} = 1 \tag{4.2.7}$$

The Froude number $\mathrm{Fr} = \Pi_3$ is the ratio of inertial to buoyancy forces:

$$\Pi_3 = \frac{W^2}{g\ l} = \mathrm{Fr}^2 \tag{4.2.8}$$

The Reynolds number $\mathrm{Re} = \Pi_4$ is the ratio of inertial to viscous forces:

$$\Pi_4 = \frac{lW\rho_\infty}{\mu} = \mathrm{Re} \tag{4.2.9}$$

The Prandtl number $\mathrm{Pr} = \Pi_5$ is the ratio of the viscous to the thermal diffusion rate:

$$\Pi_5 = \frac{\mu c_p}{k} = \mathrm{Pr} \tag{4.2.10}$$

For modeling purposes smoke is often considered to have the same properties as the ambient air, i.e. combustion products are dissolved in the hot air. The Prandtl number is roughly constant with respect to temperature, preserving Π_5 for modeling in hot air.

The three remaining Π groups for heat transfer are:

$$\Pi_6 = \kappa l \tag{4.2.11a}$$

$$\Pi_7 = \frac{\sigma T_\infty^3 l}{k} \tag{4.2.11b}$$

$$\Pi_8 = \frac{p^* l}{\rho_\infty c_p W T_\infty \tau} = \frac{W^2}{c_p T_\infty} \tag{4.2.11c}$$

where the pressure defect $p^* = \rho_\infty W^2$ has been inserted in Eqn. (4.2.11c).

Π_9 is the ratio of specific heats:

$$\Pi_9 = \frac{c_p}{c_v} \tag{4.2.12}$$

For air the ratio Π_9 is nearly constant, preserving Π_9 in hot air modeling.

4.3 Froude Modeling

Ideally all the Π groups developed in Section 4.2 must be preserved in physical modeling. However this is not practicable and good results can still be obtained under certain conditions where the important groups are preserved, and the remaining groups can be ignored.

Fire flows are dominated by buoyancy forces, hence the Froude number Π_3 (ratio of inertial to buoyancy forces) must be preserved in physical modeling - known as Froude modeling. In Froude modeling the temperatures are the same at identical positions in the full-scale and small-scale models.

In Section 4.2 it was shown that the non-dimensional groups Π_1, Π_2, Π_5 and Π_9 were preserved with the characteristic time scale $\tau = l/W$. Preserving the Froude number makes it impossible to also preserve the Reynolds number Π_4, since the velocities are changed. To neglect the Reynolds number, the viscous effects in the boundary layer close to solid surfaces must be negligible. This is the case for fully turbulent flows and is the major prerequisite in Froude modeling. The non-dimensional heat transfer groups, Π_6, Π_7 and Π_8 can not be preserved and Froude modeling is not applicable for modeling close to the flame region where the temperatures are high. At positions away from the fire, the temperatures in the smoke flow have decreased and the lacking preservation of the Π_i groups $i \in \{6, 7, 8\}$ in Eqn. (4.2.11) can be ignored.

The basic scaling of distances are:

$$x_m = \left(\frac{l_m}{l_f}\right) x_f \tag{4.3.1}$$

where l is the characteristic length, x the position and subscripts f and m designate full-scale and small-scale models respectively.

Temperatures are identical in Froude modeling:

$$T_m = T_f \tag{4.3.2}$$

Static pressures are also preserved, thus the scaling of densities are:

$$\rho_m = \rho_f \tag{4.3.3}$$

Preserving the Froude number yields the scaling relation for velocity W:

$$Fr = \frac{W_m^2}{l_m g} = \frac{W_f^2}{l_f g} \tag{4.3.4a}$$

$$W_m = \left(\frac{l_m}{l_f}\right)^{1/2} W_f \tag{4.3.4b}$$

The scaling relation for the mass flow rate $\dot{m}_m = \rho_m W_m x_m^2$ is derived by combining Eqns. (4.3.1), (4.3.3) and (4.3.4):

$$\dot{m}_m = \left(\frac{l_m}{l_f}\right)^{5/2} \dot{m}_f \tag{4.3.5}$$

Finally the scaling relation for the heat flow rate $\dot{Q}_m = c_p \dot{m}_m \Delta T_m$, where $\Delta T_m = \Delta T_f$, can be developed:

$$\dot{Q}_m = \left(\frac{l_m}{l_f}\right)^{5/2} \dot{Q}_f \tag{4.3.6}$$

4.4 Froude Modeling Study

4.4.1 Modeling Objective and Parameters

The intention of the Froude modeling study is to verify the applicability of the CFD model in predicting full-scale mass flow rates in wide opening approach flows. The experimental parameter is limited to the scaling of the model, which evidently changes all geometric extents of the models, heat release and mass flow rates.

4.4.2 Methodology

The predictions and measurements acquired in the small-scale experimental and numerical approach flow program, Chapter 3, are scaled by adopting the principles of Froude modeling, see Section 4.3. The intension in the small-scale program was to conduct tests for a 1.5/5 scale approach flow setup, corresponding to a compartment height of 5 m on the full-scale and 1.5 m on the small-scale. During the experimental program it was learned that the compartment height in the test setup was actually 1.55 m. The compartment height in the small-scale modeling program was adjusted accordingly. However the full-scale modeling setup remained scaled by 1.5/5 yielding a compartment height of 5 m corresponding to a 1.55/5 scaling. To adjust for the lower ceiling height in the full-scale model, the 1.55/5 scaling was applied for the scaling of the heat release rates.

Full-scale CFD models of tests B4138-{105-108} are prepared and simulations conducted to provide full-scale CFD predictions for comparison with scaled predictions and experimental data from the small-scale approach flow program in Chapter 3.

4.4.3 Simulations Breakdown

To limit the number of simulations and data processing, only tests B4138-{105-108} are included in the verification of the scaling laws. The experimental setups and the CFD models of tests B4138-{105-108} are scaled using the intentional 1.5/5 scale of the 1.5 m small-scale fire compartment to arrive at a full-scale fire compartment height of 5 m, representative of maximum ceiling heights in most retail shops and open plan office spaces. Heat release rates are scaled using the correct scaling of 1.55/5 to adjust for the reduced ceiling height in the full-scale compartment. The scaling laws derived in Section 4.3 are applied in computing full-scale properties of the CFD models applied in the small-scale experimental approach flow program, see Chapter 3. The scaled properties are listed in Table 4.1.

Sim. ID	Conf.	Scale	$\dot{Q}_T$	Scale	d_d	D_{fb}	W_w	D_{fc}	W_{fc}	H_{fc}
B4138-105	W	1.55/5	4700	1.5/5	0.0	22.4	40.0	31.0	44.0	5.0
B4138-106	W	1.55/5	9400	1.5/5	0.0	22.4	40.0	31.0	44.0	5.0
B4138-107	WO	1.55/5	4700	1.5/5	0.0	8.4	40.0	17.0	44.0	5.0
B4138-108	WO	1.55/5	9400	1.5/5	0.0	8.4	40.0	17.0	44.0	5.0

Table 4.1 *Full-scale properties of CFD model scaled ∼1.55/5*

	Plume	Approach flow	Spill Plume
Config.	D_p^*	D_{cj}^*	D_l^*
B4138-105	1.6	0.5	0.37
B4138-106	2.1	0.5	0.48
B4138-107	1.6	0.5	0.37
B4138-108	2.1	0.5	0.48

Table 4.2 *Characteristic length scales in the full-scale approach flow model.*

4.4.4 Description of CFD Model

General Properties

Properties are generally inherited from the small-scale program, e.g. CFD model inputs, methodology and procedures. Heat conduction through the balcony and draft curtains is included without any scaling, in agreement with Klote & Milke (2002) proposing that scaling of heat conduction properties can be ignored for flows far from the flame region.

Geometry of CFD Model and Grid Design

The full-scale geometry of the CFD models are shown in Figure 4.1 for tests B4138-{105-106} with the balcony attached and in Figure 4.2 for tests B4138-{107-108} with the balcony and draft curtains detached.

Grid spacings are determined from the characteristic length scales in the plume region D_p^* and the approach flow/ceiling jet D_{cj}^*, see Table 4.2, and recommendations provided in Chapter 2.

All grids are rectilinear and grid spacings are provided in Table 4.3 applying the notation $\Delta\mathbf{x} = \{\Delta x, \Delta y, \Delta z\}$.

Data Processing

Velocities $\mathbf{U}$, approach flow mass flow rates $\dot{m}_w$ and convective heat flow rates in the compartment opening $\dot{Q}_{c,w}$ are scaled using the 1.55/5 scaling applied for the fire heat release rate $\dot{Q}_T$.

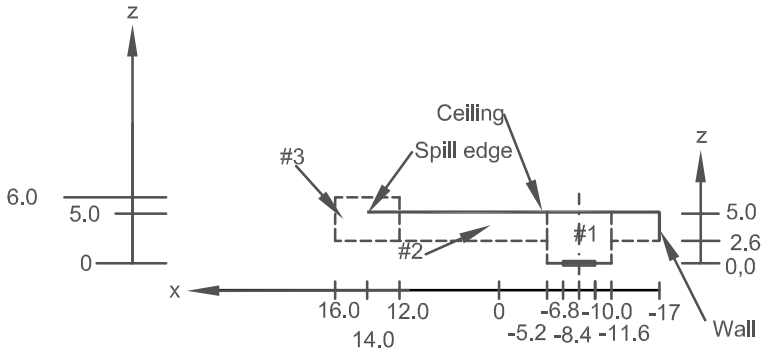

(a) Vertical section.

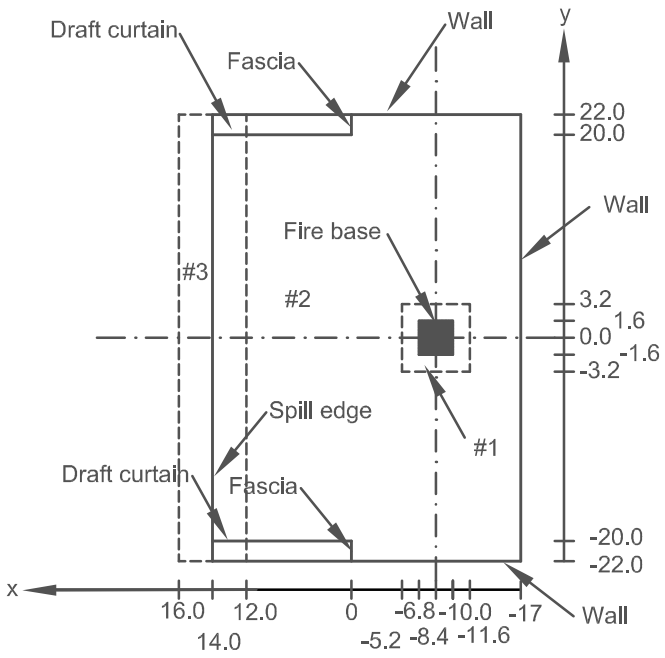

(b) Horizontal section.

Figure 4.1 *Full-scale CFD model: Configuration W.*

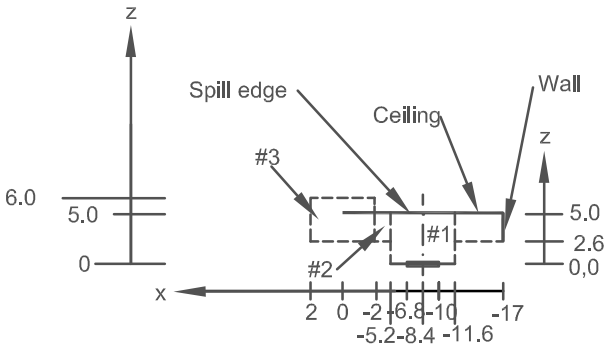

(a) Vertical section.

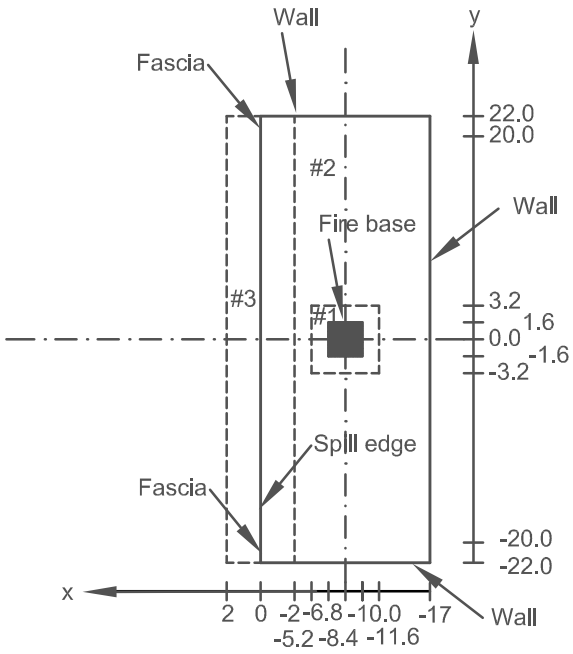

(b) Horizontal section.

Figure 4.2 *Full-scale CFD model: Configuration WO.*

	$\{\Delta x, \Delta y, \Delta z\}$ mm		
Simulation ID	**Grid #1**	**Grid #2**	**Grid #3**
B4138-XXX	{100,100,100}	{200,200,100}	{200,200,100}

Table 4.3 *Grid spacings in the full-scale CFD-model according to designations in Figures 4.1 and 4.2.*

Convective heat $\dot{Q}_{c,w}$ and $\dot{m}_w$ mass flow rates are computed from the temperature and velocity profiles using the numerical integration method outlined in Section 2.6, Eqns. (2.6.4) and (2.6.6), p. 43.

4.5 Assessing Radiation Dependency

Thermal radiation does not obey the scaling laws, attributed to temperatures being preserved whereas distances are not. A study designated B4138-108 was prepared to assess the discrepancy associated with neglecting radiation in the full-scale model of test B4138-108. Test B4138-108 was chosen because it represented the shortest distance from the fire base to the compartment opening and the highest heat release rate addressed in the study. The resulting approach flow mass flow rate $\dot{m}_w$ and the convective heat flow rate in the compartment opening $\dot{Q}_{c,w}$ are plotted in Figure 4.3. In general a 10% over prediction of convective heat flow rate $\dot{Q}_{c,w}$ by the full-scale base setup B4138-108 is observed in Figure 4.3(b). The impact on the approach flow mass flow rate $\dot{m}_w$ is limited to less than 1% as seen on Figure 4.3(a). The general conclusion is that the CFD model slightly over predicts mass flow rates and temperatures leading to conservative estimates for approach flow mass flow rates.

The complete series of temperature and velocity profiles can be found in Appendix H. The discussion on impacts of radiation correction in Section 3.8 is also relevant to the present study of the full-scale setup. The essence of the discussion was that temperatures far from the center line would be over predicted by up to 10-20% in the base setup B4138-108 without radiation correction.

4.6 Results

4.6.1 Temperature Profiles

To reduce the number of plots in the main body of the present thesis, only temperature and velocity profiles on the center line in the compartment opening are included in this section. Supporting plots can be found in Appendix F and G.

From Figure 4.4 and Appendix F it is clear that the best agreement is observed for the scaling of small-scale CFD predictions to the full-scale. Throughout the test series predictions are within 10% of the full-scale predictions. This was obviously expected because of the identical model setup, and clearly verifies the scaling laws of Section 4.3.

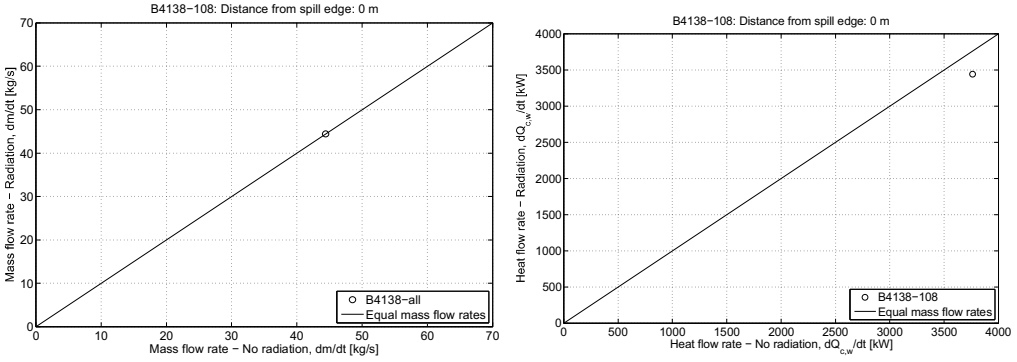

(a) B4138-108 - Full-scale: Mass flow rates for base setup and applying radiation submodel.

(b) B4138-108 - Full-scale: Heat flow rates for base setup and applying radiation submodel.

Figure 4.3 *B4138-108: Assessing impact from including radiation in the full-scale CFD model.*

Poor agreements are observed between tests and CFD predictions for B4138-{105-106} with the balcony and draft curtains attached. Full-scale temperatures from the small-scale tests are under predicted by up to 25% compared to temperatures predicted by the full-scale CFD model. This is attributed to the heat conduction through the balcony and draft curtains not being modeled correctly, i.e. heat conduction is under predicted. The agreement is considerably improved for tests B4138-{107-108} with flows emanating from the experimental fire compartment lined with insulating ceramic fiber, i.e. nearly adiabatic surfaces. Here temperature predictions are within -20% of the measured full-scale temperatures from the experimental program with the highest discrepancies far from the center line, where radiation from the smoke layer removes energy from the approach flow. See Section 3.8 for a discussion on the impact of modeling radiation from the smoke layer.

4.6.2 Velocity Profiles

Very good agreement is also observed by comparing predictions of the velocity profiles in the small-scale and full-scale CFD models, attributed to the identical model setup. Agreement are within 5% of full-scale predictions.

No reliable direct measurements of the velocities in tests B4138-{105-106} are available, because of the inconsistent velocity profiles observed using the thermal anemometer. Hence only temperature derived velocities are provided for comparison with full-scale predictions. Agreement is typically within -20% of full-scale predictions. By comparing velocity measurements in tests B4138-{107-108} with full-scale CFD predictions, one can identify discrepancies limited to -10% to -20% of full-scale CFD predictions.

CFD predictions at positions 20.0 m from the center line are abutting the fascia surface and hence heavily influenced by the boundary conditions on the

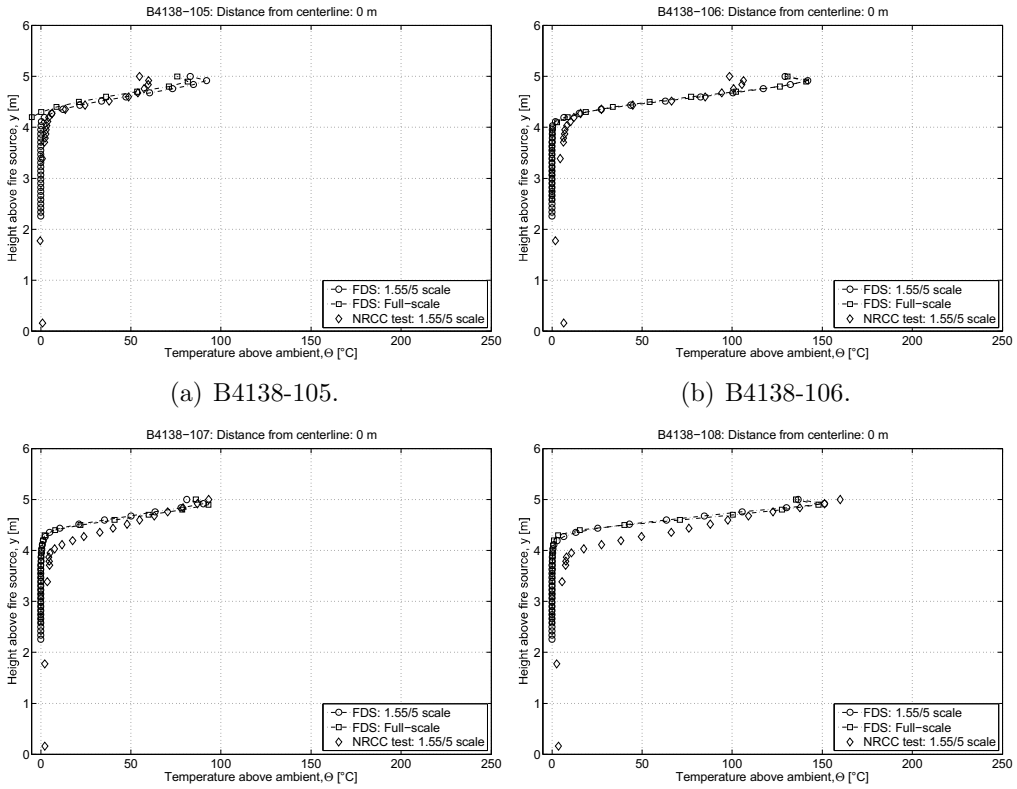

(a) B4138-105. (b) B4138-106.

(c) B4138-107. (d) B4138-108.

Figure 4.4 *Comparing modeling and experiment: Temperature profiles at location THCP0.*

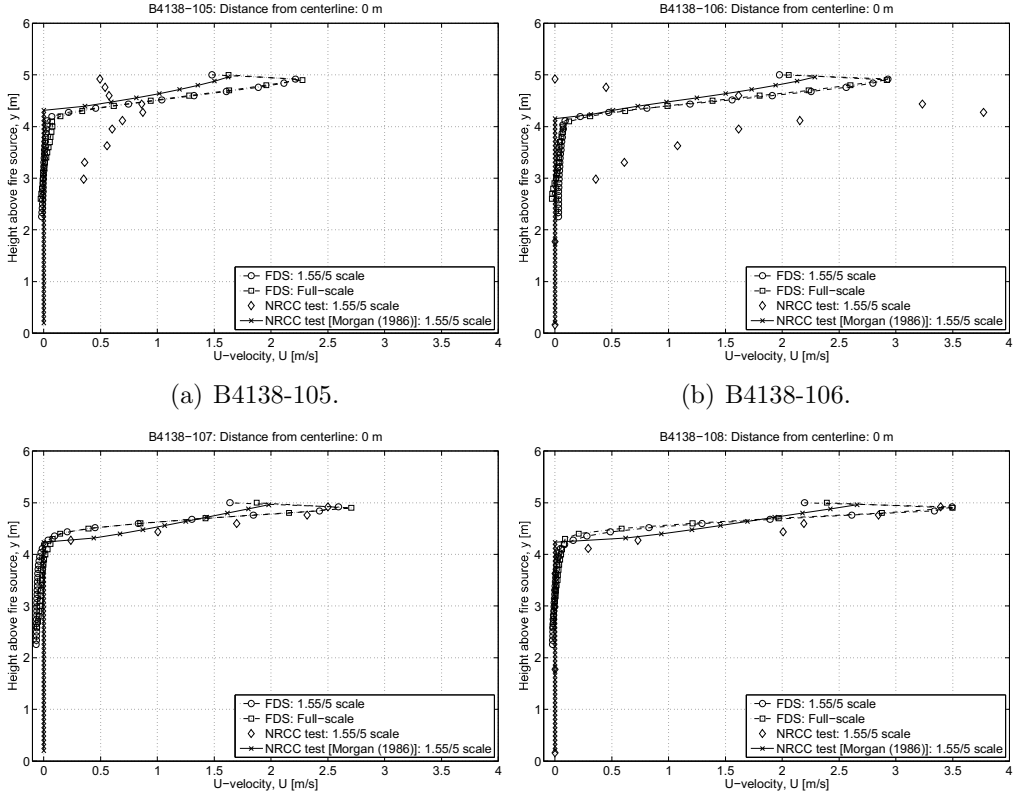

(a) B4138-105. (b) B4138-106.

(c) B4138-107. (d) B4138-108.

Figure 4.5 *Comparing modeling and experiment: Velocity profiles at location THCP0.*

fascia, and therefore not considered applicable for comparison.

4.6.3 Heat Flow Rates

A very good agreement between predicted full-scale and small-scale convective heat flow rates in the compartment opening is observed in Figure 4.6. Agreement is within 10% of full-scale predictions. For tests B4138-{105-106} agreements are somewhat poor, under predicting the convective heat flow rate by about 20% compared to full-scale CFD predictions. This is clearly attributed to the insufficient heat conduction applied in the modeling of the balcony and draft curtains, thus over predicting temperatures in the compartment opening.

4.6.4 Mass Flow Rates

Scalings of the mass flow rates predicted by the CFD model are within 5% of full-scale predictions. Mass flow rates for tests B4138-{107-108} are in general scaled to within +5% of the full-scale CFD predictions. Scaling the measured mass flow rates in tests B4138{105-106} leads to an under prediction by 30% compared to

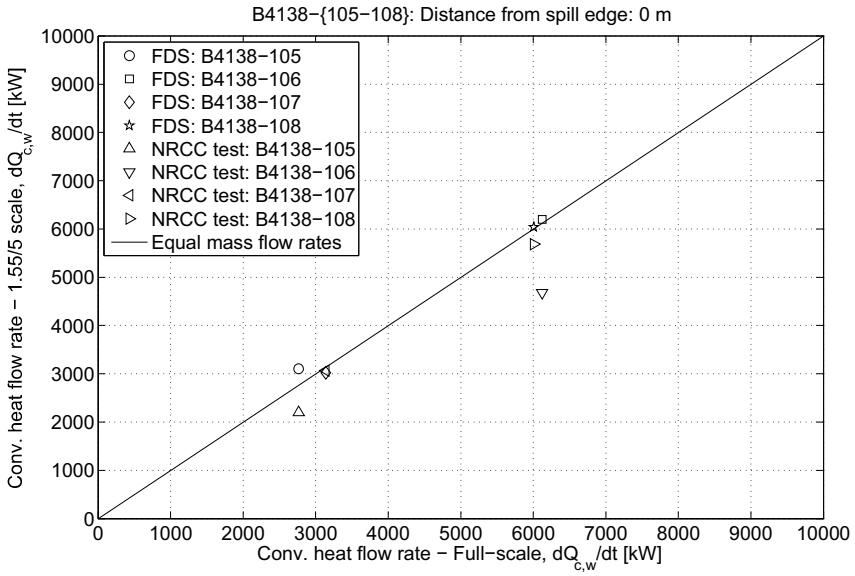

Figure 4.6 *B4138-{105-108}: Scaling of heat flow rate.*

full-scale CFD predictions, which is largely attributed to the insufficient modeling of heat conduction through the balcony and draft curtains in the CFD model.

4.7 Conclusion

The results obtained in the small-scale experimental and numerical program are scaled using Froude modeling to assess the applicability of the CFD model in predicting mass flow rates in full-scale approach flows in wide openings.

A very high degree of agreement was observed for the scaling of small-scale CFD predictions to full-scale, supporting confidence in the application of the CFD model on the full-scale. The good agreements were observed for all quantities investigated and were within 5-10% of full-scale CFD predictions, even observed to be lower in the scaling of mass flow rates and velocities.

In comparing experimental measurements of temperature and velocities, poor agreement were observed for tests B4138-{105-106} attributed to the insufficient implementation of heat conduction in the applied CFD model, i.e. energy conducted through the balcony and draft curtains were inadequate compared to the real conditions in the experimental small-scale setup. Agreements improved for tests B4138-{107-108} where heat conduction can be neglected because of the use of insulating ceramic fiber in the experimental fire compartment. Disregarding scaling of the temperature profiles in tests B4138-{105-106}, agreement between small-scale measurements and full-scale predictions of temperatures and velocities were typically within -20% of the full-scale CFD predictions.

Agreement in the scaling of mass flow rates from experiment was observed to

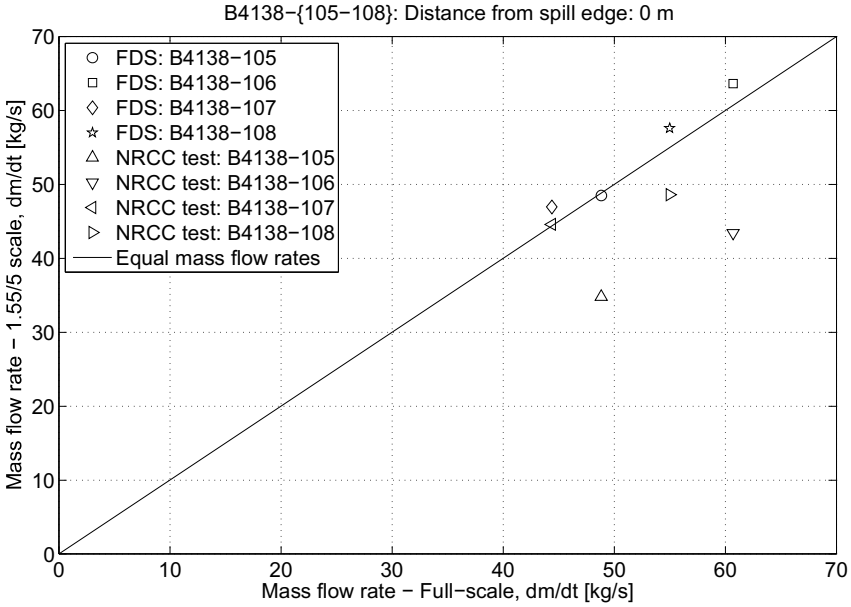

Figure 4.7 *B4138-{105-108}: Scaling of mass flow rate.*

be very good, within 5% of full-scale predictions, disregarding mass flow rates in tests B4138-{105-106}.

The general conclusion is that the CFD model can be applied with confidence in the prediction of mass flow rates in full-scale approach flows. Discrepancies of up to +20% of experimental measurements are expected for temperatures far from the center line, whereas only 10% to 20% over predictions of velocities compared to experimental measurements are expected. Mass flow rates are expected to be predicted within +20% of experimental measurements.

Chapter 5

Full-scale Approach Flows in Wide Openings

5.1 Present Research

In extension to the experimental and numerical program on small-scale approach flows, see Chapter 3, a full-scale numerical study is conducted. The study addresses compartment opening widths W_w ranging from 7.2 m to 87.2 m with and without a downstand, and distances from the fire base to the compartment opening D_{fb} ranging from 7.8 m to 22.4 m.

The objectives of the present research are:

Study distribution of mass flow rate - The mass flow rate per unit length along the compartment opening is investigated to identify correlations between the total approach flow mass flow rate $\dot{m}_w$ and the presence of a downstand d_d, distance from fire base to compartment opening D_{fb}, opening width W_w and convective heat flow rate $\dot{Q}_{c,w}$.

Derive engineering relation for mass flow rate - A new method to determine the approach flow mass flow rate from wide openings is proposed.

5.2 Full-scale Model Studies

5.2.1 Modeling Objective

The objective of the present full-scale CFD modeling is to predict temperature and velocity profiles in the fire compartment opening for use in deriving mass $\dot{m}_w$ and heat flow rates $\dot{Q}_{c,w}$ in the approach flow.

5.2.2 Modeling Parameters

The present numerical modeling program investigates the approach flow mass flow rate in wide fire compartment openings as a function of the heat release rate

$\dot{Q}_T$, the distance to the fire base D_{fb}, the width of the fire compartment opening W_w and presence of a downstand with the depth d_d.

The experimental parameters are:

Fire size $\dot{Q}_T$ - Lee & Emmons (1961) found based on dimensional analysis, that the mass flow rate from line sources scale with the convective heat release rate raised to 1/3 power, $\dot{Q}_c^{1/3}$. This is assumed also to be valid in this study, thus a fixed fire size of $\dot{Q}_T \in \{5700\}$ kW is applied in the majority of the simulations. The fire size was chosen based on the maximum size of common design fires for office buildings and sprinklered retail malls in Denmark, and in the vicinity of recommendations in Milke (2000). However an additional six simulations with $\dot{Q}_T \in \{2800, 8500\}$ kW were conducted to verify the correlation with the heat release rate derived by Lee & Emmons (1961).

Distance to fire base D_{fb} - Correlations between the approach flow mass flow rate and the distance from the fire base to the compartment opening were not addressed in any of the publications cited in Section 3.1. To allow for a correlation, the distance D_{fb} was varied through $\{7.8, 15.6, 22.4\}$ m.

The opening width W_w - The fire compartment opening width impacts the perimeter of the spill plume and hence the entrainment. Investigated opening widths W_w range from the original narrow openings originally investigated to very wide openings $W_w \in \{7.2, 14.4, 28.0, 40.0, 58.0, 87.2\}$ m.

Downstand depth d_d - Only downstands completely obstructing the ceiling jet are investigated. According to Klote & Milke (2002) the depth of ceiling jets in fire compartments with reflected flows are about 10-20% of the compartment height to ceiling. In the present study downstand depths d_d were varied through $\{0.0, 1.0\}$ m, corresponding to 20% of the fire compartment height.

Fire compartment size - The present study employs a fire compartment with a fixed depth of 31 m (rear wall to compartment opening) and a fixed height to ceiling of 5 m. The width of the fire compartment is changed with the compartment opening over the range $W_{fc} \in \{32, 44, 62, 91.2\}$ m. The compartment floor is assumed completely open, i.e. ambient properties, hence the entrainment into the axisymmetric plume in the fire compartment is not influenced by the fire compartment geometry.

Fixed parameters also expected to impact the approach flow mass flow rate, but not addressed explicitly in this study, are termed secondary parameters and include:

Fire compartment height H_{fc} - The height of the fire compartment clearly determines the rising height of the axisymmetric plume and hence the mass flow rate in the compartment opening. The present study employs a fixed

compartment height of $H_{fc} = 5.0$ m. Changing the compartment opening width W_w, clearly influences the depth of the smoke layer and hence the rising height of the axisymmetric plume, i.e. the correlation with the rising height is indirectly addressed.

Heat transfer in fire compartment - Heat transfer through compartment walls subtracts energy from the approach flow, slowing down the flow, and hence decrease the mass flow rate in the opening. To derive conservative estimates for the mass flow rate, the fire compartment is lined with adiabatic boundary conditions to neglect any heat conduction through the enclosure, leading to conservative estimates for the mass flow rate.

5.3 Modeling Program

5.3.1 Simulations Breakdown

A total of 42 simulations were carried out in the full-scale approach flow modeling program. A list of simulations are prepared in Table 5.1 with applied total heat release rate $\dot{Q}_T$ $[kW]$, ambient temperature T_∞ $[^\circ C]$, downstand depth d_d $[m]$, distance from fire base to compartment opening D_{fb} $[m]$, compartment opening width W_w $[m]$, compartment depth D_{fc} $[m]$, compartment width W_{fc} $[m]$, compartment height H_{fc} $[m]$, height above compartment base of boundary condition below smoke layer z_{sl} $[m]$ and averaging time interval $\bar{t}$ [s].

5.3.2 Description of CFD Model

Modeling Procedure

The CFD model *Fire Dynamics Simulator ver. 4.06*, described in Section 2.4, was applied in the modeling of the full-scale approach flow setup.

Heat release rates are increased linearly to the prescribed test values according to Table 5.1 over a time period of 1 s. Computations are run until at least 120 s of steady state has been achieved. Quantities of temperature and velocity are recorded at positions listed in Table 5.5. Measured quantities are averaged over the steady state time period $\bar{t}$ (at least 60 s) with the conversion program *fds2ascii* and saved for external data processing.

Computational Grid and Boundary Conditions

Sketches of the computational grids along with geometrical dimensions applied in the CFD model of the full-scale approach flow setup are shown in Figure 5.1. The fire source is elevated 0.1 m above the compartment floor.

Grid spacings are determined from the characteristic length scales in the plume region D_p^* and the approach flow/ceiling jet D_{cj}^*, see Table 5.2, and recommendations provided in Chapter 2.

All grids are rectilinear and grid spacings are provided in Table 5.3 applying the notation $\Delta\mathbf{x} = \{\Delta x, \Delta y, \Delta z\}$. A multiple of the largest grid spacing, i.e.

$\Delta \mathbf{x} = 0.2$ m, is applied in the CFD model. Grids overlap by one or two grid cells depending on local grid spacings.

To save computational cost, the lower thermal zone in the fire compartment is not resolved and boundary conditions are applied outside the base of the smoke layer, z_{sl} $[m]$. Energy conservation is checked to make sure smoke does not migrate to the lower thermal zone.

The location of the fire base on Figure 5.1 is designated x_{fb} $[m]$ and expressed in terms of the distance from the fire base to the compartment opening D_{fb}:

$$x_{fb} = D_{fb} - 14 \tag{5.3.1}$$

Measuring Positions

Measurements are recorded using the slice file (SLCF) output option in FDS at positions listed in Table 5.5 along with recorded quantities.

Data Processing

Convective heat flow rates $\dot{Q}_{c,w}$ and mass flow rates $\dot{m}_w$ are computed from the temperature and velocity profiles using the numerical integration method outlined in Section 2.6, Eqns. (2.6.4) and (2.6.6), p. 43. Mass flow rates per unit length $\dot{m}'_w$ are computed adopting the same approach evidently only performing a one dimensional numerical integration according to Eqn. (2.6.5). Smoke layer depths d_w are computed from the buoyancy profiles applying the method in Section 3.4, Eqn. (3.4.1), p. 91.

CFD Model Inputs

The full-scale approach flow CFD model employs the full hydrodynamic model including LES turbulence model, propane combustion, no radiation model and adiabatic surface boundary conditions, see model inputs in Table 5.6.

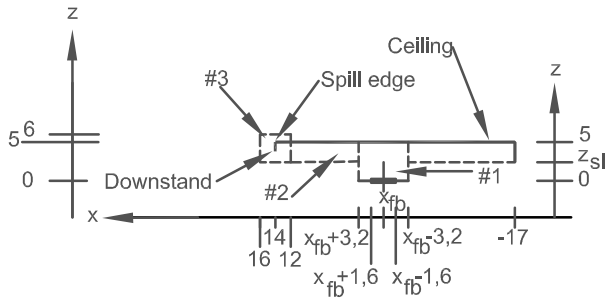

(a) Vertical section.

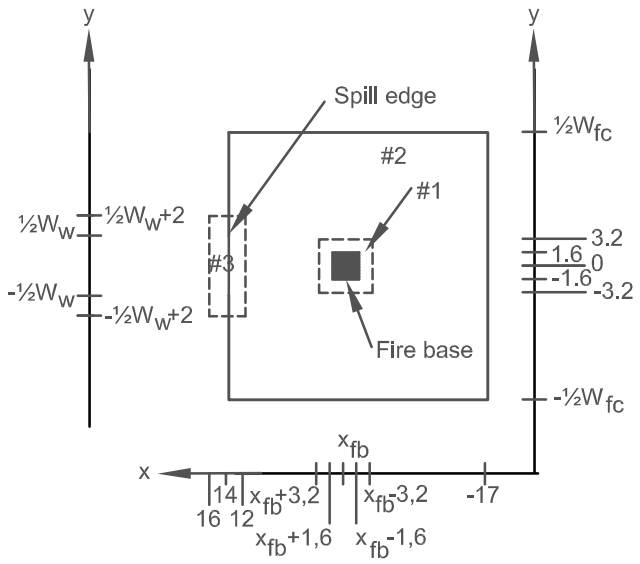

(b) Horizontal section.

Figure 5.1 *CFD model: Full-scale approach flow setup.*

Simulation ID	$\dot{Q}_T$	T_∞	d_d	D_{fb}	W_w	D_{fc}	W_{fc}	H_{fc}	z_{sl}	$\bar{t}$
WOSP007-075-ND	5700	20	0.0	22.4	7.2	31.0	32.0	5.0	0.0	60
WOSP014-075-ND	5700	20	0.0	22.4	14.4	31.0	32.0	5.0	1.4	60
WOSP028-075-ND	5700	20	0.0	22.4	28.0	31.0	32.0	5.0	2.6	60
WOSP040-075-ND	5700	20	0.0	22.4	40.0	31.0	44.0	5.0	2.6	60
WOSP058-075-ND	5700	20	0.0	22.4	58.0	31.0	62.0	5.0	2.6	60
WOSP087-075-ND	5700	20	0.0	22.4	87.2	31.0	91.2	5.0	2.6	60
WOSP007-050-ND	5700	20	0.0	15.6	7.2	31.0	32.0	5.0	0.0	60
WOSP014-050-ND	5700	20	0.0	15.6	14.4	31.0	32.0	5.0	1.4	60
WOSP028-050-ND	5700	20	0.0	15.6	28.0	31.0	32.0	5.0	2.6	60
WOSP040-050-ND	5700	20	0.0	15.6	40.0	31.0	44.0	5.0	2.6	60
WOSP058-050-ND	5700	20	0.0	15.6	58.0	31.0	62.0	5.0	2.6	60
WOSP087-050-ND	5700	20	0.0	15.6	87.2	31.0	91.2	5.0	2.6	60
WOSP007-025-ND	5700	20	0.0	7.8	7.2	31.0	32.0	5.0	0.0	60
WOSP014-025-ND	5700	20	0.0	7.8	14.4	31.0	32.0	5.0	1.4	60
WOSP028-025-ND	5700	20	0.0	7.8	28.0	31.0	32.0	5.0	2.6	60
WOSP040-025-ND	5700	20	0.0	7.8	40.0	31.0	44.0	5.0	2.6	60
WOSP058-025-ND	5700	20	0.0	7.8	58.0	31.0	62.0	5.0	2.6	60
WOSP087-025-ND	5700	20	0.0	7.8	87.2	31.0	91.2	5.0	2.6	60
WOSP007-075-D	5700	20	1.0	22.4	7.2	31.0	32.0	5.0	0.0	60
WOSP014-075-D	5700	20	1.0	22.4	14.4	31.0	32.0	5.0	1.4	60
WOSP028-075-D	5700	20	1.0	22.4	28.0	31.0	32.0	5.0	2.6	60
WOSP040-075-D	5700	20	1.0	22.4	40.0	31.0	44.0	5.0	2.6	60
WOSP058-075-D	5700	20	1.0	22.4	58.0	31.0	62.0	5.0	2.6	60
WOSP087-075-D	5700	20	1.0	22.4	87.2	31.0	91.2	5.0	2.6	60
WOSP007-050-D	5700	20	1.0	15.6	7.2	31.0	32.0	5.0	0.0	60
WOSP014-050-D	5700	20	1.0	15.6	14.4	31.0	32.0	5.0	1.4	60
WOSP028-050-D	5700	20	1.0	15.6	28.0	31.0	32.0	5.0	2.6	60
WOSP040-050-D	5700	20	1.0	15.6	40.0	31.0	44.0	5.0	2.6	60
WOSP058-050-D	5700	20	1.0	15.6	58.0	31.0	62.0	5.0	2.6	60
WOSP087-050-D	5700	20	1.0	15.6	87.2	31.0	91.2	5.0	2.6	60
WOSP007-025-D	5700	20	1.0	7.8	7.2	31.0	32.0	5.0	0.0	60
WOSP014-025-D	5700	20	1.0	7.8	14.4	31.0	32.0	5.0	1.4	60
WOSP028-025-D	5700	20	1.0	7.8	28.0	31.0	32.0	5.0	2.6	60
WOSP040-025-D	5700	20	1.0	7.8	40.0	31.0	44.0	5.0	2.6	60
WOSP058-025-D	5700	20	1.0	7.8	58.0	31.0	62.0	5.0	2.6	60
WOSP087-025-D	5700	20	1.0	7.8	87.2	31.0	91.2	5.0	2.6	60
WOSP014-075-ND-2800	2800	20	0.0	22.4	14.4	31.0	32.0	5.0	1.4	60
WOSP028-075-ND-2800	2800	20	0.0	22.4	28.0	31.0	32.0	5.0	2.6	60
WOSP040-075-ND-2800	2800	20	0.0	22.4	40.0	31.0	44.0	5.0	2.6	60
WOSP040-075-ND-8500	8500	20	0.0	22.4	40.0	31.0	44.0	5.0	2.6	60
WOSP058-075-ND-8500	8500	20	0.0	22.4	58.0	31.0	62.0	5.0	2.6	60
WOSP087-075-ND-8500	8500	20	0.0	22.4	87.2	31.0	91.2	5.0	2.6	60

Table 5.1 *Full-scale approach flow modeling: List of simulations.*

Config.	Plume D_p^*	Approach flow D_{cj}^*	Spill Plume D_l^*
WOSP0XX-007-XX	1.7	0.5	0.77
WOSP0XX-014-XX	1.7	0.5	0.58
WOSP0XX-028-XX	1.7	0.5	0.45
WOSP0XX-040-XX	1.7	0.5	0.39
WOSP0XX-058-XX	1.7	0.5	0.33
WOSP0XX-087-XX	1.7	0.5	0.28
WOSP075-014-ND-2800	1.3	0.5	0.44
WOSP075-028-ND-2800	1.3	0.5	0.34
WOSP075-040-ND-2800	1.3	0.5	0.29
WOSP075-040-ND-8500	2.0	0.5	0.45
WOSP075-058-ND-8500	2.0	0.5	0.39
WOSP075-087-ND-8500	2.0	0.5	0.33

Table 5.2 *Characteristic length scales in the full-scale approach flow model.*

	$\{\Delta x, \Delta y, \Delta z\}$ mm		
Simulation ID	**Grid #1**	**Grid #2**	**Grid #3**
WOSP0XX-XXX-XX-XXXX	{100,100,100}	{200,200,100}	{200,200,100}

Table 5.3 *Grid spacings according to designations in Figure 5.1.*

Designation	Line type	BC type	FDS type
Outflow	Dashed	Passive vent	*OPEN*
Smoker layer interface (z_{sl})	Dashed	Passive vent	*OPEN*
Floor	Dashed	Passive vent	*OPEN*
Walls	Solid	Adiabatic/partial slip	*ADIABATIC*
Ceiling	Solid	Adiabatic/partial slip	*ADIABATIC*
Fire base	Solid	Steady HRR	*HRRPUA*

Table 5.4 *Boundary conditions according to designations in Figure 5.1.*

Simulation ID	Quantity	Location	Position
WOSPXXX-XXX-XX	T,u,v,w	Compartment opening	$x \in \{14.0\}$ m

Table 5.5 *Measured quantities and positions applied in the full-scale approach flow CFD model relative to dimensions in Figure 5.1.*

Turbulence model		
Smagorinsky constant	C_s	0.2
Prandtl number	Pr	0.5
Schmidt number	Sc	0.5
Combustion model		
Material	Propane	Default FDS v. 4.06
Heat of combustion	ΔH_c	47,251 kJ/kg
Radiative fraction	χ_r	0.286
Molecular weight	M_w	44.00 g/mol
Soot yield	y_s	0.01 kg/kg
Fire source		
Fire base area	A_f	3.2^2 m^2
Specific HRR	$\dot{Q}''_T$	see Table 5.1
Flame sheet correction	*AUTOMATIC_Z*	*TRUE*
Radiation model		
Radiative model		Not applied
Surface BCs		
Thermal model		Adiabatic
Ghost cell temperature	T_{ghost}	T_g
Velocity model		Partial slip
Wall velocity	u_τ	$0.5u_i$
Flow BCs		
Flow model	Passive vent	*OPEN*
Ambient temperature	T_∞	$20°C$
Ambient velocity	$\mathbf{u}$	0 m/s
Ambient perturbed pressure	$\tilde{p}$	0 Pa
Ambient static pressure	p_0	1.013 10^5 Pa

Table 5.6 *Full-scale approach flow setup: Model input parameters.*

5.4 Results

5.4.1 Conservation of Energy

Because the entire CFD model is lined with adiabatic surfaces, convective heat input must equal the convective heat flow in the compartment opening to obey the conservation of energy. Figure 5.2 verifies this requirement, and it is clear that the boundary conditions below the smoke layer are valid, i.e. the boundary condition is not submerged in the smoke layer. The minor deviations from the line of equality are attributed to the averaging process and the filtering of the core flow, see Section 2.6.

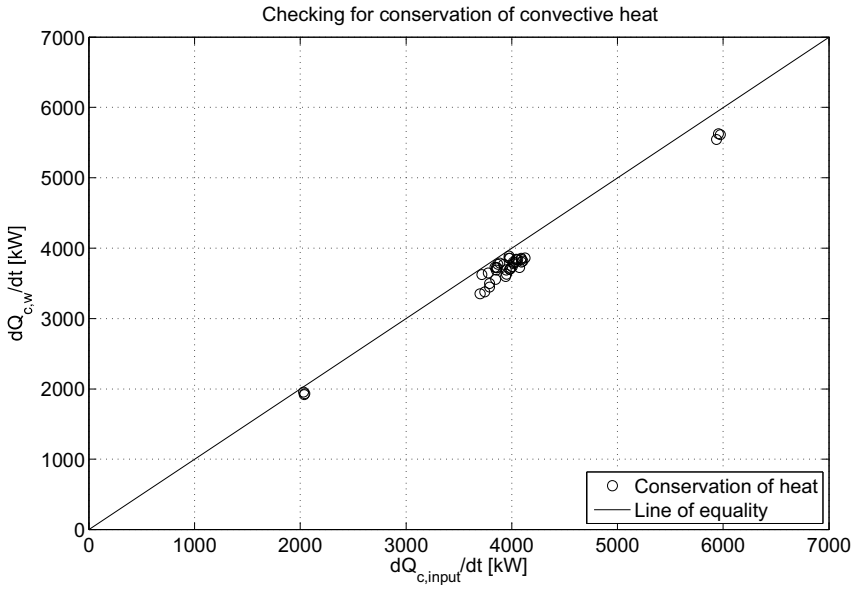

Figure 5.2 *Conservation of energy in the CFD model: Convective heat release rate input $\dot{Q}_c$ vs. $\dot{Q}_{c,w}$ in the compartment opening.*

5.4.2 Mass Flow Rates per Unit Length

The mass flow rates per unit length $\dot{m}'_w$ along the fire compartment opening is plotted as the deviation from the average mass flow rate per unit length, $\bar{\dot{m}}'_w$, across the entire opening width W_w, i.e. assuming an even distribution in accordance with previous studies by Thomas et al. (1963) and Morgan (1986):

$$\frac{\dot{m}'_w - \bar{\dot{m}}'_w}{\bar{\dot{m}}'_w} \tag{5.4.1}$$

where $\bar{\dot{m}}'_w$ is the average mass flow rate per unit length over the entire compartment opening width, W_w:

$$\bar{\dot{m}}'_w = \frac{\dot{m}_w}{W_w} \tag{5.4.2}$$

This makes it possible to assess if an assumption of an even distribution is valid over the entire range of compartment widths investigated in the current program. Each plot contains the three investigated distances from the fire base to the compartment opening D_{fb}, to allow for an assessment of the dependency on the location of the fire base.

The mass flow rates in Figure 5.3 are computed without any downstand to obstruct the flow out of the fire compartment. It is clear that for narrow opening widths, e.g. $W_w \in \{7.2, 14.2\}$ m, the deviations from an even distribution are smaller compared to wide openings $W_w \geq 40.0$ m. Except at the ends of the compartment openings, deviations without a downstand are restricted to $\pm 20\%$ of the average mass flow rate $\dot{m}'_w$. Looking at the mass flow rates with the downstand $d_d = 1$ m the resemblance to an even distribution is evident, as the deviation from the average mass flow rate decreases to $\pm 10\%$.

From Alpert (1972) it is known that a ceiling jet approaching a straight spill edge will be mapped as a Gaussian shaped profile along the spill edge, due to the radial velocity distribution emanating from the point source. This shape can be identified for opening widths $W_w \geq 28.0$ m, see Figure 5.3, but is clearly influenced by the reflecting flow from the compartment walls at the ends of the compartment opening, where the mass flow rate is increased. It is clear that this type of flow pattern is attributed to the nature of the ceiling jet, and thus not clearly identifiable from the mass flow rates per unit length with downstand $d_d = 1.0$ m. In this case the radial distribution is almost completely obstructed by the downstand, yielding a more even mass flow rate distribution along the compartment opening. Low W_w/W_{fc} ratios, i.e. the opening is much smaller than the fire compartment width, in the present study for $W_w \in \{7.2, 14.2\}$, yield an even distribution, mainly because the opening represents a very small arc length on the equivalent radial distribution.

5.4.3 Location of Fire Base

From both series of plots in Figures 5.3 and 5.4 there seem to be no clear dependency of the mass flow rate per unit length $\dot{m}'_w$ on the distance from the fire base to the compartment opening D_{fb}. Because of the modeling approach, the compartment floor was assumed to be open and at ambient conditions, i.e. the fire compartment is assumed well-ventilated and air entrained into the axisymmetric plume can be considered independent of the extents of the fire compartment. For very narrow openings the entrainment would obviously be affected, and the assumption of well-ventilated conditions is no longer valid.

Looking at Figure 5.5 it is clear that a weak correlation between the mass flow rate $\dot{m}_w$ and the distance from the fire base to the compartment opening D_{fb} can not be ignored, which makes sense because of the radial velocity distribution in a ceiling jet migrating under a ceiling. The impact is obviously more distinct with out the downstand, due to the deep downstand completely obstructing the ceiling jet flow. From Figure 5.6 the smoke layer depth d_w is observed to also correlate weakly with the distance to the fire base D_{fb}.

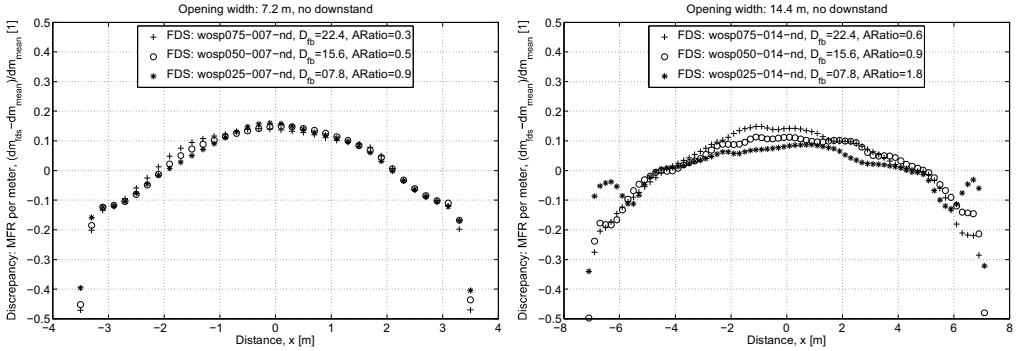

(a) $W_w = 7.2$ m. (b) $W_w = 14.4$ m.

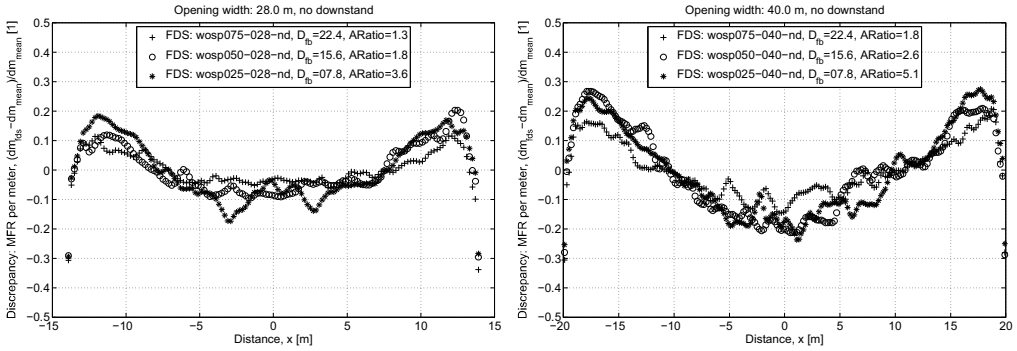

(c) $W_w = 28.0$ m. (d) $W_w = 40.0$ m.

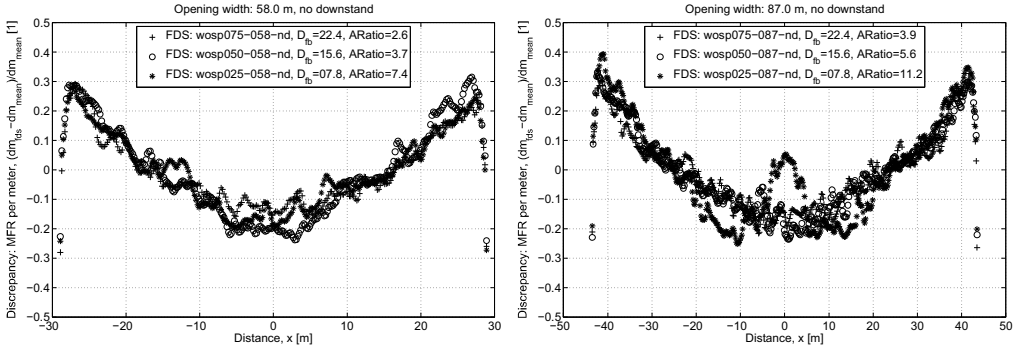

(e) $W_w = 58.0$ m. (f) $W_w = 87.2$ m.

Figure 5.3 *Downstand $d_d = 0$ m : Mass flow rates per unit length.*

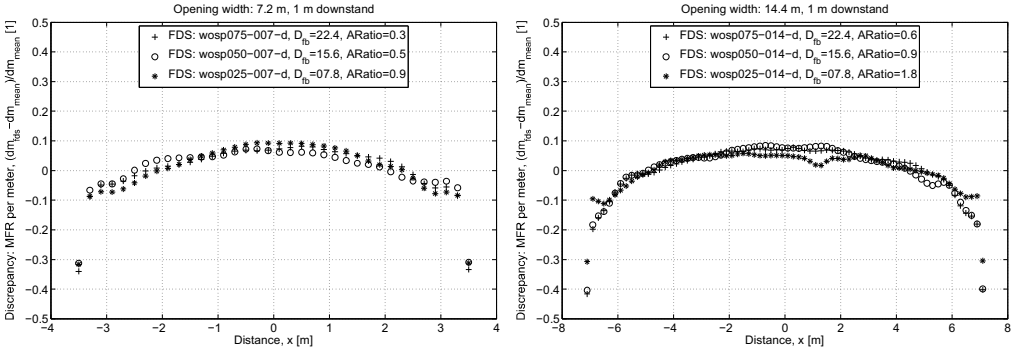

(a) $W_w = 7.2$ m.

(b) $W_w = 14.4$ m.

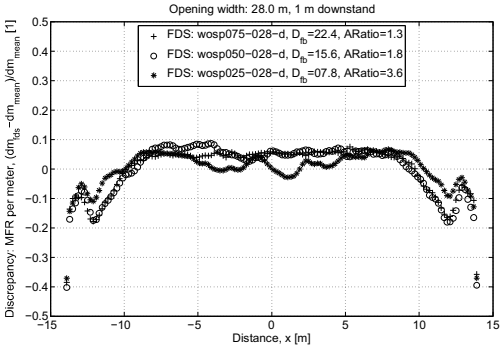

(c) $W_w = 28.0$ m.

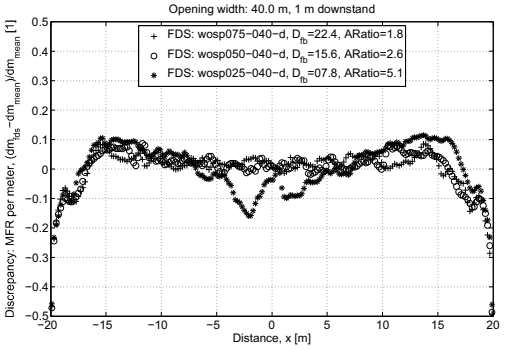

(d) $W_w = 40.0$ m.

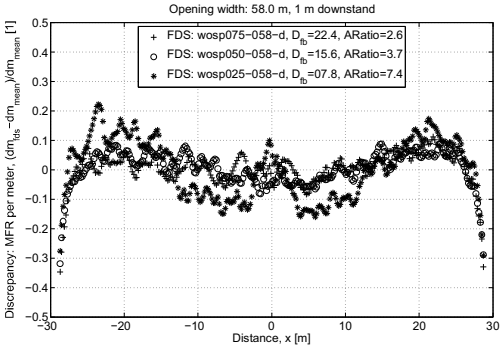

(e) $W_w = 58.0$ m.

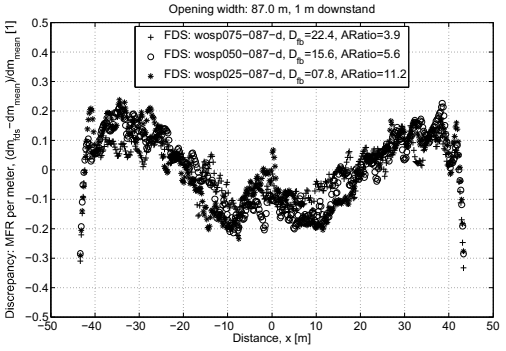

(f) $W_w = 87.2$ m.

Figure 5.4 *Downstand $d_d = 1$ m: Mass flow rates per unit length.*

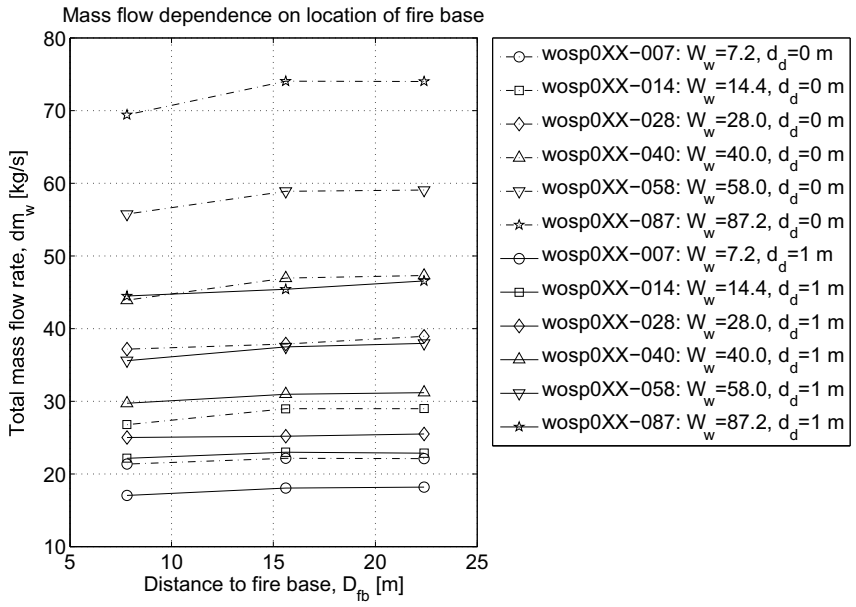

Figure 5.5 *Mass flow rate dependency on location of fire base.*

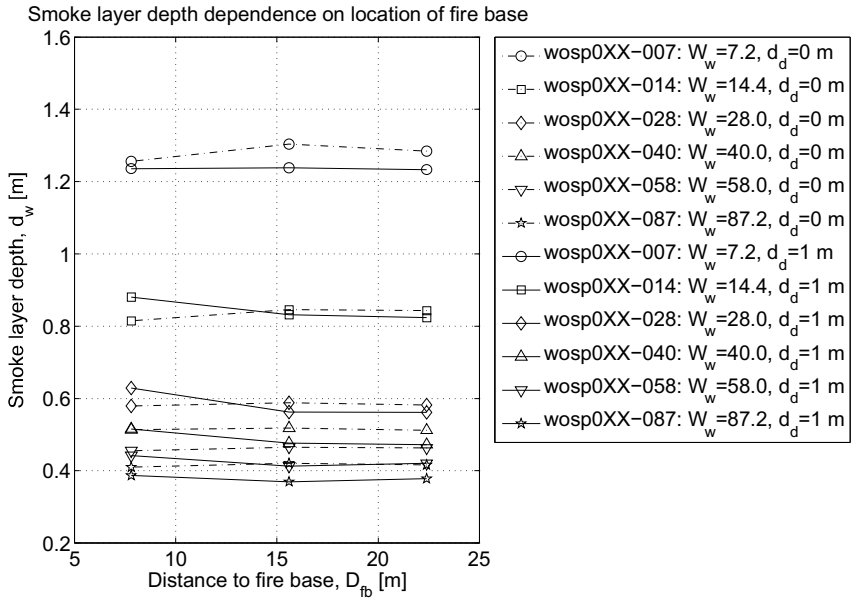

Figure 5.6 *Smoke layer depth dependency on location of fire base.*

5.5 Development of New Approach Flow Method

5.5.1 Methodology

A new method for deriving the approach flow mass flow rate in wide openings is proposed. The scaling laws were verified for a ∼1/3 scaling in Chapter 4, thus the scaling laws are expected to be valid for scalings 3/5 and 4/5. Allowing for a more robust method, the predicted mass and heat flow rates along with geometrical compartment dimensions from the present CFD modeling program are scaled according to the scaling laws derived in Section 4.3 using a 3/5 and 4/5 scaling. The entire set of scaled quantities can be found in Appendix I, p. 291. Applying the scaled predictions from the CFD model does not exactly extend the data set, because predictions are only scaled, i.e. bigger fires in smaller compartments are not covered and vice versa. However it allows for a more robust data fit, addressing smaller fires in compartments with lower ceiling heights.

5.5.2 Assumptions and Limitations

Assumptions and limitations applied in developing the new method are:

Fire sizes - Heat release rates ranging from $\dot{Q}_T$=700 kW to 8500 kW.

Fire compartment heights - Ceiling heights H_{fc}=3 m to 5 m covering typical ceiling heights in office spaces and retail shops.

Fire compartment openings - Opening widths ranging from W_w=4.3 m to 87.2 m are used in deriving the method, representing the smallest openings (except window/door plumes) usually applied in shop units and very wide openings, e.g. an open plan office opening up into an atrium.

Downstands - The method addresses approach flows flowing unhindered out of the fire compartment, and flows with an appreciable downstand completely obstructing the ceiling jet flow, i.e. with a depth corresponding to 20% of the compartment height.

Balcony flow - Smoke flowing under a balcony before spilling into an atrium is not considered, only the approach flow mass flow rate in the fire compartment opening is covered by the method.

Stable smoke layer interface - Opening widths are assumed wide enough to prevent makeup air entering the fire compartment from obstructing the smoke layer interface with increased mixing as a result.

Well-ventilated conditions - Complete combustion and well-ventilated conditions are assumed throughout the method.

No heat loss - Heat loss through the fire compartment enclosure is neglected, leading to conservative estimates of the mass flow rate, see Section 3.8.

Radiation - The method does not include radiative effects on the smoke layer flow, thus care should be taken for smoke flows where radiation is important. Neglecting radiative effects leads to conservative estimates for the mass flow rates, see Section 3.8.

Dimensional units - The method is developed using the SI system with the following modifications: kW and kJ.

5.5.3 Approach Flow Method

From looking at Figure 5.7 it is clear that the approach flow mass flow rate $\dot{m}_w$ can be decoupled from the compartment height, assuming an axisymmetric plume (dependent on the rising height) acts as a source of mass flow into the approach flow smoke layer. Hence writing the mass flow rate in the compartment opening

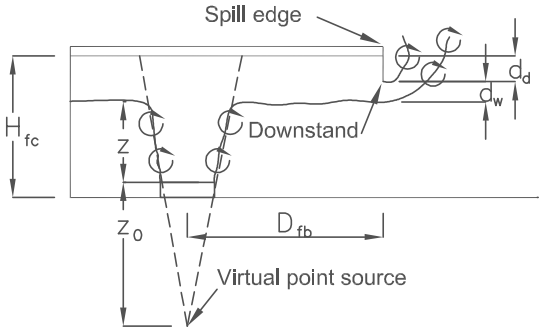

Figure 5.7 *Nomenclature adopted in deriving the mass flow rate in approach flows.*

$\dot{m}_w$:

$$\dot{m}_w = \dot{m}_p + \dot{m}_c \tag{5.5.1}$$

where $\dot{m}_p$ is the axisymmetric plume mass flow rate $[kg/s]$ and $\dot{m}_c$ is the mass flow rate under the ceiling $[kg/s]$.

Modifying the correlation proposed by Heskestad (1986) for the mass flow rate in the axisymmetric plume $\dot{m}_p$ we get:

$$\dot{m}_p = 0.076\dot{Q}_c^{1/3}\left(z - z_0\right)^{5/3}\ldots \tag{5.5.2a}$$

$$\dot{m}_p = 0.076\dot{Q}_c^{1/3}\left(H_{fc} - (d_w + d_d) - z_0\right)^{5/3}\ldots \tag{5.5.2b}$$

where $\dot{Q}_c$ is the convective heat release rate $[kW]$, d_w is the smoke layer depth in the compartment opening $[m]$, d_d is the depth of the downstand $[m]$, z is the rising height of the plume $[m]$ and the distance to the virtual fire origin z_0 $[m]$ proposed by Heskestad (1983) is:

$$z_0 = 0.083\dot{Q}_T^{2/5} - 1.02D \tag{5.5.3}$$

Here D is the fire diameter $[m]$ and $\dot{Q}_T$ is the total heat release rate $[kW]$.

Subtracting the mass flow rate in the axisymmetric plume $\dot{m}_p$ from the total approach flow mass flow rate $\dot{m}_w$ predicted by the CFD model, yields the net mass flow rate under the ceiling $\dot{m}_c$. The mass flow rate under the ceiling approaching the compartment opening depends on not only the mass flow rate supplied by the axisymmetric plume, but evidently also the depth of the smoke layer and inherently the presence of any downstand. It was previously shown in Figure 5.5 and Figure 5.6 that the distance to the fire base had an impact on the mass flow rate and therefore must be included in the correlation. Dimensional analyses in investigations of line sources, e.g. Lee & Emmons (1961) and Thomas (1987), have shown that mass flow rates scale with the heat release rate raised to the power 1/3, i.e. $\dot{Q}^{1/3}$. The derived scaling is applied for the convective heat flow rate $\dot{Q}_{c,w}$ in the current derivation of a correlation for the mass flow rate.

Based on the above discussion a correlation for the mass flow rate below the ceiling $\dot{m}_c$ is proposed in Eqn. (5.5.4):

$$\dot{m}_c = C_m \dot{Q}_c^{1/3} W_w^m D_{fb}^n \left(\frac{d_w}{d_w + d_d} \right)^k \left| \begin{array}{rcl} C_m & = & 0.0243 \\ m & = & 0.9926 \\ n & = & 0.1679 \\ k & = & 0.3937 \end{array} \right. \tag{5.5.4}$$

Correlation coefficients are computed by an unconstrained nonlinear optimization using the *Nelder-Mead Simplex Method* to find the minimum of a multi-variable scalar function, please refer to Lagarias, et al. (1998) for more information. The optimization algorithm is provided with the mathematical software package *Matlab ver. 7.1.*

The quality of the correlation proposed in Eqn. (5.5.4) can be assessed in Figure 5.8, where fitted data are plotted against predicted data from the CFD modeling program. The correlation coefficient R^2=0.98 is fairly high, indicating that the fitted variables are highly correlated by Eqn. (5.5.4).

From Eqn. (5.5.4) it is clear that the net mass flow rate under the ceiling does not depend on the ceiling height H_{fc}, because this parameter has been decoupled and included in the correlation for the axisymmetric plume, Eqn. (5.5.2b). The presence of a downstand restricts and decreases the approach flow through the ratio $d_w/(d_w + d_d)$ as expected.

The smoke layer depth impacts the approach flow mass flow rate $\dot{m}_w$ through the rising height of the axisymmetric plume and hence the plume mass flow rate $\dot{m}_p$. The smoke layer depth in the compartment opening d_w is inherently impacted by the total approach flow mass flow rate $\dot{m}_w$ and not only the net mass flow rate under the ceiling $\dot{m}_c$. The presence of an appreciable downstand will certainly increase the total smoke layer depth $(d_w + d_d)$ but also the smoke layer depth in the compartment opening d_w. Not only due to smoke building up in the fire compartment, but also because the smoke flow below the ceiling is forced down upon impact with the downstand, preventing smoke from flowing unhindered out of the fire compartment. Morgan (1986) and Morgan et al. (1999) proposes a discharge coefficient C_d to be used in describing the contraction of the approach

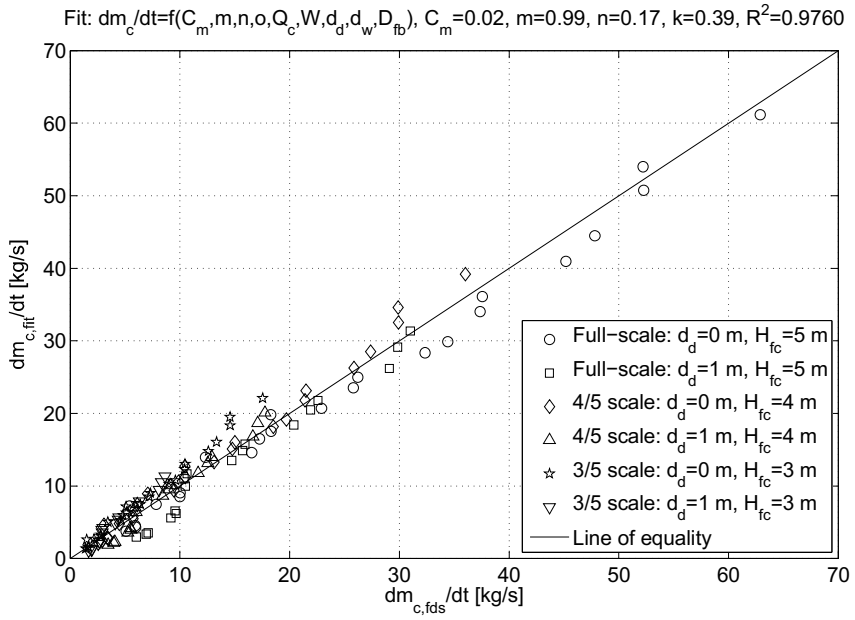

Figure 5.8 *Correlating mass flow rates in the compartment opening* $\dot{m}_w$.

flow as it flows under a downstand. The same approach is adopted in the present method.

Once again based on the above discussion a correlation for the smoke layer depth d_w in the compartment opening is proposed in Eqn. (5.5.5):

$$d_w = C_d C_m W_w^m D_{fb}^n \dot{m}_w^l \left(1 + d_d^k\right) \left| \begin{array}{rcl} C_m & = & 0.7128 \\ m & = & -0.7958 \\ n & = & -0.0415 \\ k & = & 0.1012 \\ l & = & 0.7197 \end{array} \right. \tag{5.5.5}$$

where the discharge coefficients according to Morgan et al. (1999) are $C_d = 0.6$ for flow obstructed by a downstand and $C_d = 1.0$ for approach flows leaving the fire compartment unhindered. The correlation coefficients where computed using the previous mentioned unconstrained nonlinear optimization method. The quality of the correlation proposed in Eqn. (5.5.5) can be assessed in Figure 5.9, where fitted data are plotted against CFD predictions from the full-scale CFD modeling program. A correlation coefficient of R^2=0.99 indicates a strong correlation between the fitted variables in Eqn. (5.5.5).

Looking at the steps involved in the method, i.e. Eqn. (5.5.2b), Eqn. (5.5.4), Eqn. (5.5.1) and Eqn. (5.5.5), it is evident that the approach flow mass flow rate $\dot{m}_w$ must be computed iteratively from an initial guess for the smoke layer depth d_w in the compartment opening. An initial guess is proposed by Klote & Milke

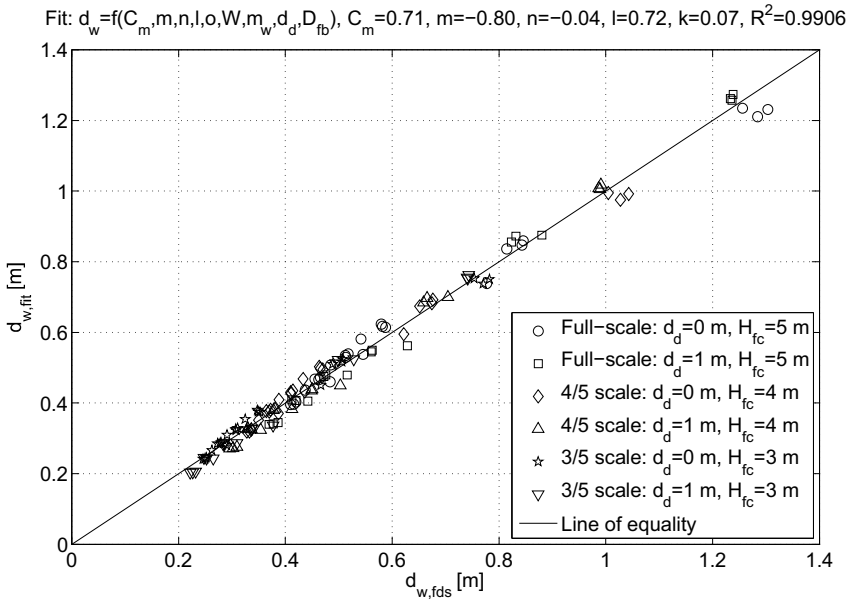

Figure 5.9 *Correlating smoke layer depths in the compartment opening* d_w.

(2002) using the depth of a ceiling jet in the range 10%-20% of the compartment height. The application of the proposed method is outlined below:

(1) - Make initial guess for smoke layer depth d_w^0 **-** Use $d_w^0 = 0.2H_{fc}$.

(2) - Compute mass flow rate in axisymmetric plume $\dot{m}\left(d_w^{n-1}\right)_p^n$ **-** Use Eqn. (5.5.2b) with the smoke layer depth d_w^{n-1} from the previous iteration (or initial guess).

(3) - Compute net mass flow rate under ceiling $\dot{m}\left(d_w^{n-1}\right)_c^n$ **-** Use Eqn. (5.5.4) with the smoke layer depth d_w^0 from the previous iteration.

(4) - Compute the total approach flow mass flow rate $\dot{m}\left(\dot{m}_p^n, \dot{m}_c^n\right)_w^n$ **-** Use Eqn. (5.5.1) and the values computed in Step (2) and (3) above.

(5) - Update the smoke layer depth $d_w^n\left(\dot{m}\right)_w^n$ **-** Use Eqn. (5.5.5) with the approach flow mass flow rate $\dot{m}_w^n$ computed in Step (4) above.

(6) - Return to Step (2) and continue until convergence has been reached - Usually convergence is reached within five iterations.

Superscripts refer to iterations $n = 0, 1, 2, 3, \ldots$. Because of the inherently empirical nature of the derived method, any application must be within the limits of the present research and meet the underlying assumptions, see Section 5.5.2.

5.5.4 Testing the New Method for Mass Flow Rate

The new method proposed for calculating the approach flow mass flow rate in wide openings is tested against the predicted mass flow rates from the full-scale CFD program using the parameters outlined in Table 5.1. Correlations using the simplified coefficients proposed in Eqns. (5.5.6) and (5.5.7) are also plotted against the predicted mass flow rates from the full-scale CFD modeling program:

$$\dot{m}_c = C_m \dot{Q}_c^{1/3} W_w^m D_{fb}^n \left(\frac{d_w}{d_w + d_d} \right)^k \qquad \begin{array}{rcl} C_m & = & 0.025 \\ m & = & 1.0 \\ n & = & 0.17 \\ k & = & 0.40 \end{array} \tag{5.5.6}$$

$$d_w = C_d C_m W_w^m D_{fb}^n \dot{m}_w^l \left(1 + d_d^k\right) \qquad \begin{array}{rcl} C_m & = & 0.72 \\ m & = & -0.80 \\ n & = & -0.05 \\ k & = & 0.11 \\ l & = & 0.72 \end{array} \tag{5.5.7}$$

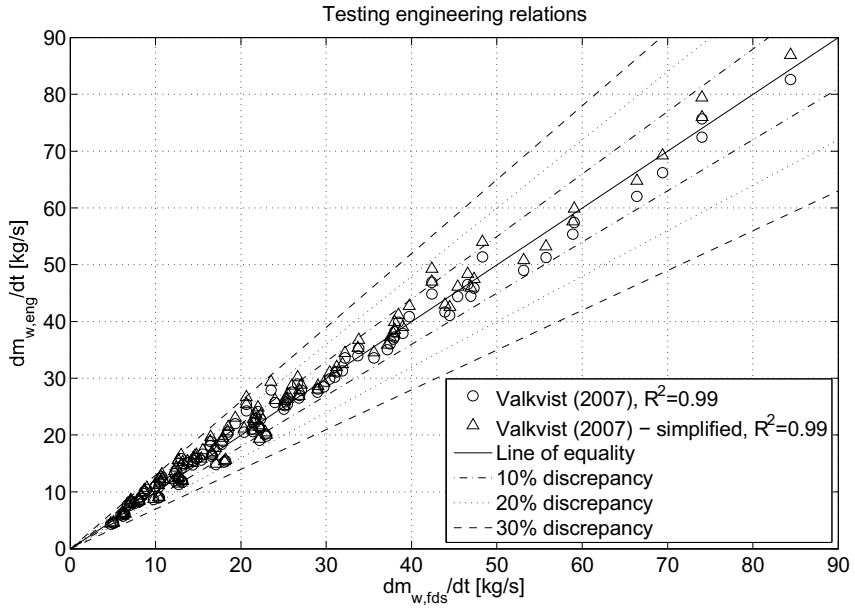

Figure 5.10 *Testing new approach flow correlations.*

From Figure 5.10 it is clear that a high coefficient of correlation is obtained, R^2=0.99, even with the simplified method, R^2=0.99. In the low range the full method predicts mass flow rates within ±20% improving to ±10% in the intermediate to high range of mass flow rates, see also Figure 5.11. The simplified method performs a little worse with ±30% improving to ±20% respectively.

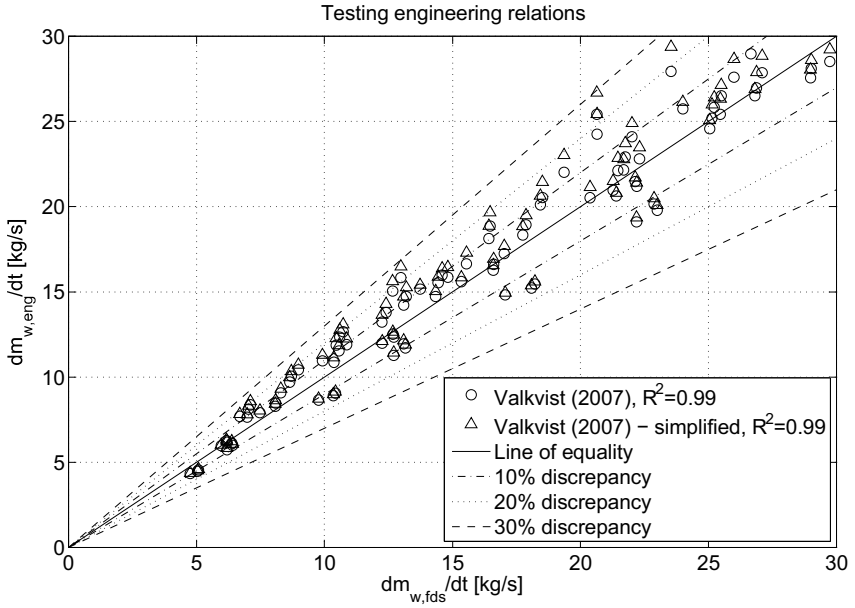

Figure 5.11 *Testing new approach flow correlations - close up.*

A method for calculating the approach flow mass flow rate $\dot{m}_w$ in wide openings was proposed by Morgan et al. (1999):

$$\dot{m}_w = \frac{2}{3} C_d^{2/3} \left(2g\Theta_{cw} T_\infty\right)^{1/2} \frac{W_w \rho_\infty}{T_{cw}} d_w \kappa_m \tag{5.5.8}$$

where C_d is the coefficient of discharge (C_d=1.0 for compartments without a downstand and C_d=0.6 if a downstand is present), Θ_{cw} $[K]$ and T_{cw} $[K]$ are the temperature above ambient and absolute temperature below the ceiling respectively, T_∞ $[K]$ and ρ_∞ $[kg/m^3]$ are the ambient temperatures and density respectively, W_w is the compartment opening width $[m]$, d_w is the smoke layer depth $[m]$ and $\kappa_m = 1.3$ is a profile correction factor applied because real flow profiles deviates from triangular and step profiles used in the derivation of the method. The method is evaluated in Figure 5.12 using input from the CFD predictions in the full-scale approach flow program, see Table 5.1. The method performs poorly over the entire range, even though the CFD predictions are based on adiabatic walls and ceilings, maximizing the temperature T_{cw} in the smoke layer (a parameter in the method). Since the assumptions applied in deriving Eqn. (5.5.8), see Morgan (1986), do not restrict it to narrow openings, the poor agreement can not be completely attributed to the method being applied to wide openings. This is also supported by the fact, that the model performs poorly in the narrow opening range. The smoke layer depth d_w is computed according to Morgan (1986), see Eqn. (3.4.1), and should hence provide the correct input, since this approach was proposed along with the derivation of the method in Eqn. (5.5.8).

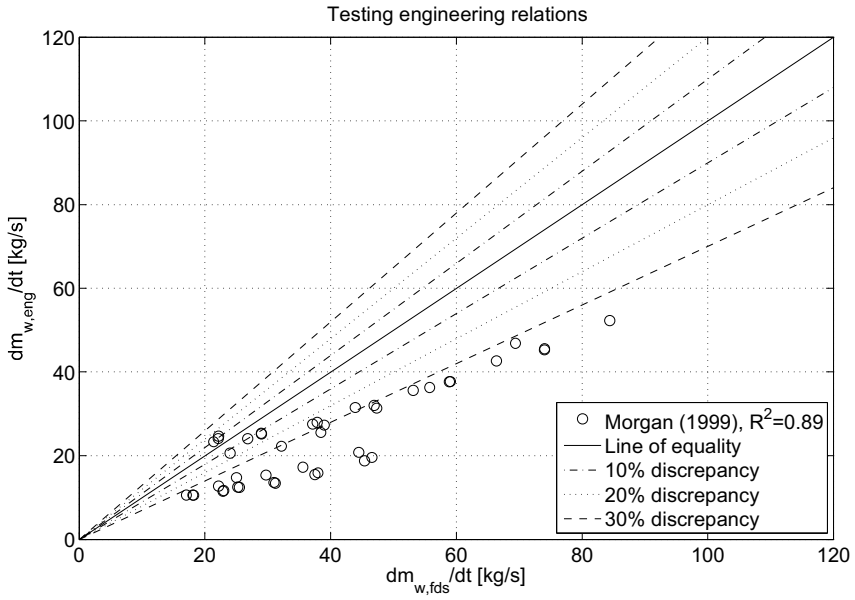

Figure 5.12 *Evaluating mass flow rates predicted by the method in Eqn.* (5.5.8).

5.6 Conclusions

A full-scale CFD modeling study was conducted to develop a new method for calculating the approach flow mass flow rate $\dot{m}_w$ in wide compartment openings. The CFD modeling program consisted of 42 full-scale models addressing heat release rates $\dot{Q}_T$ from 2800 kW to 8500 kW, opening widths W_w from 7.2 m to 87.2 m, fire sources located 7.8 to 22.4 m from the compartment opening D_{fb} and the impact of a downstand in the opening d_d. Throughout the CFD modeling program a fixed compartment height H_{fb} of 5 m was used. In developing the new method the full-scale predictions were scaled using Froude modeling with scalings of 3/5 and 4/5 respectively. This provided a total of 126 data points, to account for smaller fires in smaller fire compartments with ceiling heights scaling accordingly. Bigger fires in smaller fire compartments and vice versa were not addressed with this scaling methodology.

A new method using a five step iterative procedure was developed. A new approach was proposed for describing the approach flow mass flow rate $\dot{m}_w$, where an axisymmetric plume acts as a source of mass flow rate in the approach flow, i.e. coupling the impact of the compartment height H_{fb} to the mass flow rate for an axisymmetric plume $\dot{m}_p$. The total approach flow mass flow rate $\dot{m}_w$ hence consists of mass flow rates from an axisymmetric plume $\dot{m}_p$ and a net mass flow rate under the ceiling $\dot{m}_c$:

$$\dot{m}_w = \dot{m}_p + \dot{m}_c \tag{5.6.1}$$

Two new correlations for the net mass flow rate under the ceiling $\dot{m}_c$ and the

smoke layer depth d_w in the compartment opening have been proposed:

$$\dot{m}_c = C_m \dot{Q}_c^{1/3} W_w^m D_{fb}^n \left(\frac{d_w}{d_w + d_d} \right)^k \qquad \begin{array}{rcl} C_m & = & 0.0243 \\ m & = & 0.9926 \\ n & = & 0.1679 \\ k & = & 0.3937 \end{array}$$

$$d_w = C_d C_m W_w^m D_{fb}^n \dot{m}_w^l \left(1 + d_d^k\right) \qquad \begin{array}{rcl} C_m & = & 0.7128 \\ m & = & -0.7958 \\ n & = & -0.0415 \\ k & = & 0.1012 \\ l & = & 0.7197 \end{array}$$

The proposed method has been validated against predicted mass flow rates from the full-scale CFD modeling program and a correlation coefficient of R^2=0.99 achieved.

5.7 Future Research

The present study only addresses a fixed fire size of $\dot{Q}_T$=5700 kW in fire compartments with a fixed ceiling height of H_{fb}=5 m and a few additional fire sizes $\dot{Q}_T$=2800 kW and 8500 kW. Scaled CFD predictions are applied in developing a new method for calculating mass flow rates, but does not extend the data sets to increased fire sizes in smaller fire compartments. Verification of the method for a wide range of fire sizes $\dot{Q}_T$, compartment heights H_{fc} and opening widths W_w should be performed to verify the versatility of the method.

Chapter 6

Wide Opening Spill Plumes

6.1 Introduction

The existing research on balcony spill plumes are extensive, but not exhaustive, and a complete review will not be presented in the present chapter. An introduction to the most common spill plume methods are provided in Chapter 2, Section 2.10.4, and only main findings are repeated in the present section.

The existing renowned methods for calculating mass flow rates in spill plumes are based on 1/10 scale experiments of smoke flow from shop units with compartment opening widths restricted to $W_w = 14$ m and rising heights of up to $z_l = 9$ m on the full-scale. Experimental data are provided in Morgan & Marshall (1975), Morgan & Marshall (1979), Marshall & Harrison (1996) and the most recent in Harrison (2004). The first and so far only full-scale experiments have been published recently in McCartney (2006).

The most comprehensive "simple" spill plume model was developed by the British Building Research Establishment (BRE method) applying the pioneering work by Lee & Emmons (1961). The method is by many practicing fire protection engineers not considered a simple engineering relation due to it's multi-step iterative construction. Law (1995) used data from Morgan & Marshall (1975) and Morgan & Marshall (1979) and additional data from Marshall & Harrison (1996) to propose a simple one-step engineering correlation, which was later adopted and slightly modified by Milke (2000) and CIBSE (2003), probably comprising the three most widely applied set of spill plume models. Using the set of data by Marshall & Harrison (1996), Poreh et al. (1998) and Thomas et al. (1998) derived new entrainment coefficients, including end entrainment in the latter case, proposing a new set of spill plume models. A new experiment was developed by Harrison (2004) to update the methods proposed by Poreh and Thomas, providing an updated entrainment coefficient including end entrainment. Recently McCartney (2006) published the first engineering relation for spill plume mass flow rates based on full-scale experimental data.

The shortcomings of all the above mentioned existing spill plume models are the limited validation range. Modern buildings often have spill edges and tall open spaces beyond the validated opening widths of $W_w \leq 14$ m and rising

heights $z_l \leq 9$ m limiting the applicability of the existing spill plume models. Computational fluid dynamics (CFD) is a useful tool in trying to extend the validation range of the existing spill plume models or even develop new ones. The fatality in this approach is the lack of any validation data for wide openings and large rising heights. The applicability of the CFD fire model *Fire Dynamics Simulator* (FDS) in predicting mass flow rates in spill plumes limited by the extensions given above, have been shown in numerous publications, the most recent and comprehensive being Harrison (2004) and McCartney (2006). In Chapter 5 a new method for calculating mass flow rates in wide opening approach flows was proposed using CFD predictions validated against experiment. The fluid dynamics of spill plumes emanating from wide openings are identical to that of spill plumes from narrow openings (here interpreted as openings within the limits of existing data), and Harrison and McCartney showed that the CFD fire model *Fire Dynamics Simulator* could be applied with confidence in predicting mass flow rates in the investigated spill plumes from narrow openings. The current modeling program applies FDS in calculating mass flow rates in wide opening spill plumes (WOSP) and attempts to validate the CFD predictions against existing engineering relations.

6.2 Present Research

In the full-scale CFD modeling program in Chapter 5 a new method for calculating the approach flow mass flow rate in wide openings was proposed. The present research incorporates the findings in Chapter 5 in the development of a complete model for calculating mass flow rates in spill plumes emanating from wide openings. A full-scale modeling program employing compartment opening widths W_w ranging from 7.2 m to 87.2 m with and without a downstand, and distances D_{fb} 7.8 m and 22.4 m from the fire base to the compartment opening.

The objectives of the present research are:

Study mass flow rates in wide opening spill plumes - Investigations of mass flow rates as a function of compartment opening width, rising height, presence of a downstand and location of the fire base are conducted. Mass flow rates are computed using computational fluid dynamics.

Study collapse of spill plume - The inherent line plume property of a spill plume is investigated as a function of rising height to study the expected collapse into an axisymmetric plume.

Derive engineering relation for mass flow rate - A new method to calculate the mass flow rate in spill plumes emanating from wide openings is proposed based on CFD predictions.

6.3 Full-scale Model Studies

6.3.1 Modeling Objective

The objective of the present full-scale numerical modeling program is to record temperature T and velocity profiles $\mathbf{U}$ in horizontal cross-sections of the wide opening spill plumes as a function of rising height z_l for use in deriving mass $\dot{m}_l$ $[kg/s]$ and heat flow rates $\dot{Q}_{c,l}$ $[kW]$.

6.3.2 Modeling Parameters

The present numerical modeling program investigates the mass flow rate $\dot{m}_l$ in the wide opening spill plume as a function of the total heat release rate $\dot{Q}_T$, the distance to the fire base D_{fb}, the width of the fire compartment opening W_w and presence of a downstand with depth d_d.

The experimental parameters are:

Fire size $\dot{Q}_T$ - Dimensional analysis by Lee & Emmons (1961) has shown that the mass flow rate $\dot{m}_l$ from line sources scale with the convective heat release rate $\dot{Q}_c^{1/3}$. A reasonable assumption is to conserve this scaling in the present spill plume modeling program. The fire size was chosen based on common design fires for office buildings and sprinklered retail malls in Denmark, and in the vicinity of recommendations in Milke (2000) and is limited to the range $\dot{Q}_{c,w} \in [3500 : 6900]$.

Rising height z_l - Rising heights in the range $z_l \in [0 : 56.8]$ m were investigated. The computational domain extended 24 control volumes beyond the investigated rising heights to avoid impact from the boundary conditions.

The opening width W_w - The fire compartment opening width impacts the perimeter of the spill plume and hence the entrainment. Investigated opening widths W_w range from the original narrow openings to very wide openings $W_w \in \{7.2, 14.4, 40.0, 87.2\}$ m.

Distance to fire base D_{fb} - Correlation with the distance to the fire base was not addressed in any of the publications addressed in Section 2.10.4. To allow for investigation of a correlation, the distance D_{fb} was varied through $\{7.8, 22.4\}$ m.

Downstand depth d_d - Only downstands completely obstructing the ceiling jet are investigated. According to Klote & Milke (2002) the depth of ceiling jets in fire compartments with reflected flows are about 10-20% of the compartment height to ceiling. In the present study downstand depths were varied through $d_d \in \{0.0, 1.0\}$ m, i.e. corresponding to 20% of the fire compartment height.

Fire compartment size - The present study employs a fire compartment with a fixed depth of 31 m (rear wall to compartment opening) and a fixed height to ceiling of 5 m. The width of the fire compartment is changed

with the compartment opening over the range $W_{fc} \in \{32, 44, 91.2\}$ m. The compartment floor is assumed completely open, i.e. ambient conditions, hence the entrainment into the axisymmetric plume in the fire compartment is not influenced by the fire compartment geometry.

Fixed parameters also expected to impact the approach flow mass flow rate, but not addressed explicitly in this study, are termed secondary parameters and include:

Fire compartment height H_{fc} - The height of the fire compartment clearly determines the rising height of the axisymmetric plume in the fire compartment and hence the approach flow mass flow rate in the compartment opening. The full-scale modeling program on approach flow mass flow rates in Chapter 5 indirectly addresses rising heights. The present study employs a fixed compartment height of $H_{fc} = 5.0$ m.

Heat transfer in fire compartment - Heat transfer through compartment walls removes energy from the approach flow, slowing down the flow, and hence decrease the mass flow rate in the opening. To derive conservative estimates for the mass flow rate, the fire compartment is lined with insulating surfaces to minimize heat conduction and maximize the mass flow rate.

6.4 Modeling Program

6.4.1 Simulations Breakdown

The final full-scale modeling program comprised 14 simulations, all listed in Table 6.1 with computed convective heat flow $\dot{Q}_{c,w}$ $[kW]$, ambient temperature T_∞ $[^\circ C]$, downstand depth d_d $[m]$, distance from fire base to compartment opening D_{fb} $[m]$, compartment opening width W_w $[m]$, compartment depth D_{fc} $[m]$, compartment width W_{fc} $[m]$, compartment height H_{fc} $[m]$, height above compartment base of boundary condition below smoke layer z_{sl} $[m]$ and averaging time interval $\overline{t}$ [s].

6.4.2 Description of CFD Model

Modeling Procedure

The CFD model *Fire Dynamics Simulator ver. 4.06*, described in Section 2.4, was applied in the modeling of the full-scale approach flow setup. For a simple validation assessment of the CFD model in spill plume modeling, please refer to Section 6.6.7.

Heat release rates are increased linearly to the prescribed test values according to Table 6.1 over a time period of 1 s. Computations are run until at least 90 s of steady state has been achieved. Quantities of temperature and velocities are recorded at positions listed in Table 6.5. Measured quantities are averaged over the steady state time period $\overline{t}$ (at least 60 s) with the conversion program *fds2ascii* and saved for external data processing.

Simulation ID	$\dot{\mathbf{Q}}_{\mathbf{c,w}}$	$\mathbf{T}_\infty$	$\mathbf{d_d}$	$\mathbf{D_{fb}}$	$\mathbf{W_w}$	$\mathbf{D_{fc}}$	$\mathbf{W_{fc}}$	$\mathbf{H_{fc}}$	$\mathbf{z_{sl}}$	$\bar{\mathbf{t}}$
WOSP007-075-ND-BSP	4500	20	0.0	22.4	7.2	31.0	32.0	5.0	0.0	60
WOSP007-075-D-BSP	3882	20	1.0	22.4	7.2	31.0	32.0	5.0	0.0	60
WOSP014-075-ND-BSP	4603	20	0.0	22.4	14.4	31.0	32.0	5.0	1.4	60
WOSP014-075-D-BSP	6886	20	1.0	22.4	14.4	31.0	32.0	5.0	1.4	60
WOSP040-075-ND-BSP	3651	20	0.0	22.4	40.0	31.0	44.0	5.0	2.6	60
WOSP040-075-D-BSP	4703	20	1.0	22.4	40.0	31.0	44.0	5.0	2.6	60
WOSP087-075-ND-BSP	3631	20	0.0	22.4	87.2	31.0	91.2	5.0	2.6	60
WOSP087-075-D-BSP	4266	20	1.0	22.4	87.2	31.0	91.2	5.0	2.6	60
WOSP014-025-ND-BSP	4051	20	0.0	7.8	14.4	31.0	32.0	5.0	1.4	60
WOSP014-025-D-BSP	5595	20	1.0	7.8	14.4	31.0	32.0	5.0	1.4	60
WOSP040-025-ND-BSP	3554	20	0.0	7.8	40.0	31.0	44.0	5.0	2.6	60
WOSP040-025-D-BSP	3926	20	1.0	7.8	40.0	31.0	44.0	5.0	2.6	60
WOSP087-025-ND-BSP	3492	20	0.0	7.8	87.2	31.0	91.2	5.0	2.6	60
WOSP087-025-D-BSP	3529	20	1.0	7.8	87.2	31.0	91.2	5.0	2.6	60

Table 6.1 *Full-scale wide opening spill plume modeling: List of simulations.*

To adequately resolve all model setups outlined in Table 6.1 throughout the entire computational domain would require excessive computational costs. Exploiting the methodology of flow regions outlined in Chapter 2, the approach flow mass flow rate investigated in Chapter 5 could act as a line source term in the compartment opening of the full-scale spill plume modeling program, i.e. applied as a boundary condition. This would require recording of all dependent quantities, e.g. velocities $\mathbf{U}$, density ρ, viscosity μ, mixture fraction Z etc., in all control volume faces of the compartment opening. However FDS does not allow for specifying viscosity as a boundary condition, and the implementation of a non-uniform boundary condition over the entire opening would require comprehensive preprocessing of the recorded data.

As an alternative and still keeping the computational cost in mind, it was decided to use the entire fire compartment as a source term to the balcony spill plume. Allowing for minimal sub-adequately grid sizes in the fire compartment, the computation time could be decreased and still provide an acceptable "boundary condition" in the fire compartment opening to the spill plume. This would allow for velocities and temperatures to be distributed correctly in the compartment opening and the approach flow heat and mass flow rates accordingly. Convective heat flow rates $\dot{Q}_{c,w}$ and mass flow rates $\dot{m}_w$ were derived in the compartment opening and applied in the development of the spill plume correlation.

In the present study the approach flow mass flow rate $\dot{m}_w$ is subtracted from the spill plume mass flow rate $\dot{m}_l$ to decouple the approach flow mass flow rate from the spill plume mass flow rate $\dot{m}_l$, hence introducing the net mass flow rate $\dot{m}_{l,net}$. The sub-adequately resolved axisymmetric plume was shown in Section

Config.	Plume D_p^*	Approach flow D_{cj}^*	Spill Plume D_l^*
WOSP075-007-ND-BSP	1.8	0.5	0.80
WOSP075-007-D-BSP	1.7	0.5	0.75
WOSP075-014-ND-BSP	1.8	0.5	0.61
WOSP075-014-D-BSP	2.1	0.5	0.72
WOSP075-040-ND-BSP	1.6	0.5	0.37
WOSP075-040-D-BSP	1.8	0.5	0.41
WOSP075-087-ND-BSP	1.6	0.5	0.27
WOSP075-087-D-BSP	1.7	0.5	0.29
WOSP025-014-ND-BSP	1.7	0.5	0.58
WOSP025-014-D-BSP	1.9	0.5	0.66
WOSP025-040-ND-BSP	1.6	0.5	0.37
WOSP025-040-D-BSP	1.7	0.5	0.38
WOSP025-087-ND-BSP	1.6	0.5	0.27
WOSP025-087-D-BSP	1.6	0.5	0.27

Table 6.2 *Characteristic length scales in the full-scale approach flow model.*

2.10.1 to yield a higher entrainment rate, but since the approach flow mass flow rate $\dot{m}_w$ is decoupled from the spill plume mass flow rate $\dot{m}_l$ this can be neglected.

Computational Grid and Boundary Conditions

Sketches of the computational grids along with geometrical dimensions applied in the CFD model of the full-scale approach flow setup are shown in Figures 6.1 and 6.2. The fire source is located flush with the floor of the fire compartment.

Grid spacings in the spill plume region are determined from the characteristic length scales D_l^*, see Table 6.2, and recommendations provided in Chapter 2. Grid spacings in the fire compartment are chosen to provide a sufficiently resolved "boundary condition" for the approach flow mass flow rate $\dot{m}_w$. A grid spacing of 0.2 m was assessed adequate for the present study.

All grids are rectilinear and grid spacings are provided in Table 6.3 applying the notation $\Delta\mathbf{x} = \{\Delta x, \Delta y, \Delta z\}$. A multiple of the largest grid spacing, i.e. $\Delta\mathbf{x} = 0.8$ m, is applied in the CFD model. Grids overlap by one to four grid cells depending on local grid spacings.

To save computational cost, the lower thermal zone in the fire compartment is not resolved and boundary conditions are applied outside the base of the smoke layer, z_{sl} $[m]$. Energy conservation is checked to make sure smoke does not migrate to the lower thermal zone.

The location of the fire base on Figure 6.2 is designated x_{fb} $[m]$ and expressed in terms of the distance from the fire base to the compartment opening D_{fb}:

$$x_{fb} = D_{fb} - 14 \tag{6.4.1}$$

	$\{\Delta x, \Delta y, \Delta z\}$ **mm**	
	WOSP0XX-007/...	**WOSP0XX-040/...**
Grid	**014-XX-BSP**	**087-XX-BSP**
#1	{200,200,200}	{200,200,200}
#2	{200,200,200}	{200,200,200}
#3	{100,200,100}	{100,200,100}
#4	{200,200,200}	{200,200,200}
#5	{200,200,200}	{200,200,200}
#6	{200,200,200}	{200,200,200}
#7	{400,400,400}	{400,400,400}
#8	{400,400,400}	{400,400,400}
#9	{400,400,400}	{400,400,400}
#10	{800,800,800}	{800,800,800}
#11	{800,800,800}	{800,800,800}
#3*	Not applied	{200,200,200}
#4*	Not applied	{800,800,800}
#5*	Not applied	{800,800,800}
#6*	Not applied	{800,800,800}
#7*	Not applied	{800,800,800}
#8*	Not applied	{800,800,800}
#9*	Not applied	{800,800,800}
#10*	Not applied	{800,800,800}
#11*	Not applied	{800,800,800}

Table 6.3 *Grid spacings according to designations in Figures 6.1 and 6.2.*

As mentioned earlier in this section computational costs are important because of the size of the computational domain in the present study. As the spill plume rises, more air is entrained, and the turbulent length scale hence increased. The spill plume flow was described in Section 2.10.4, where the widening of the rising spill plume was documented. A preprocessing tool was developed in the mathematical software package *Matlab ver. 7.1* to process input for computational grids to FDS. This provided an easy way to construct grids that mimic the basic flow pattern of a spill plume with increasing turbulent length scales as a function of rising height. An example of a computed grid can be found in Figures 6.1 and 6.2.

FDS supports continuous and piecewise linear stretching of computational grids. One of the shortcomings of the feature is the limited number of directions that can be stretched, only two of the three coordinate directions. Another problem is the difficulty in ensuring a monotonic map of the computational control volumes into the stretched grid space, which is a distinct challenge in non-symmetric stretches and multi-grid designs. Based on extensive runs and the previous mentioned shortcomings, the stretch feature provided with FDS was deemed inapplicable in the present study.

Another approach to address the computational costs was to exploit the symmetry of the model setup about the center line. Initial studies applying the symmetry flow boundary condition provided with FDS (designated *MIRROR*) resulted in fatal predictions of the mass flow rate along the center line. The result was an increased numerical diffusion attributed to the cancellation of turbulent eddies across the symmetry boundary condition, see discussion in Section 2.4.7.

An alternative approach was adopted for compartment openings $W_w > 14.4$ m. Here the spill plume and rotation region were divided into a computational grid (i.e. grid # $[3:11]$) and a boundary grid (i.e. grid # $[3*:11*]$ marked with an asterisk and cross hatched in Figure 6.2). The boundary grid serves as a "symmetric boundary condition" based on a lower grid resolution. It is important to note that numerical effects from the interpolation between grids in the computational region (grid # $[3:11]$) and boundary region (grid # $[3*:11*]$) are minimized by allowing at least 24 control volumes in the computational grid region to dampen out any numerical interpolation perturbations. This is the reason for the stair-stepped grid interface across the spill plume region in Figure 6.2).

To avoid any numerical disturbance from the boundary conditions at the top of the spill plume region (grids # 11 and 11*) to propagate upstream and impact the core flow, a boundary grid approach has also been adopted in the top of the spill plume, where grids # $[10:11]$ and $[10*:11*]$) are boundary grids with low grid resolutions and no data recording, see Figure 6.1. Numerical boundary perturbations are hence damped out before reaching the core flow in the computational region, grid # $[3:9]$, by propagating through at least 24 control volumes.

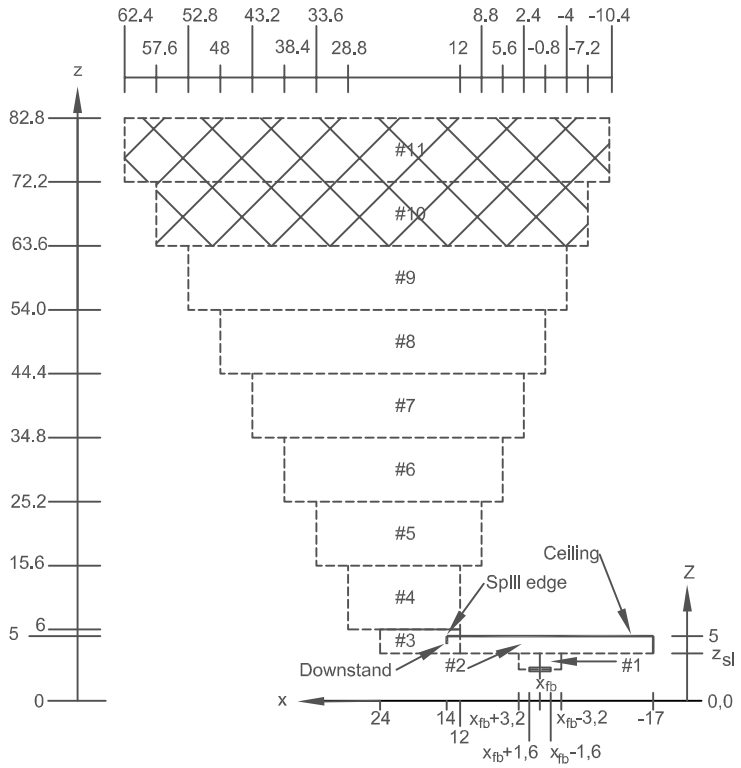

Figure 6.1 *CFD model: Full-scale spill plume setup, vertical section.*

Designation	**Line type**	**BC type**	**FDS type**
Outflow	Dashed	Passive vent	*OPEN*
Smoker layer interface (z_{sl})	Dashed	Passive vent	*OPEN*
Floor	Solid	Adiabatic/partial slip	*ADIABATIC*
Walls	Solid	Adiabatic/partial slip	*ADIABATIC*
Ceiling	Solid	Adiabatic/partial slip	*ADIABATIC*
Fire base	Solid	Steady HRR	*HRRPUA*

Table 6.4 *Boundary conditions according to designations in Figures 6.1 and 6.2.*

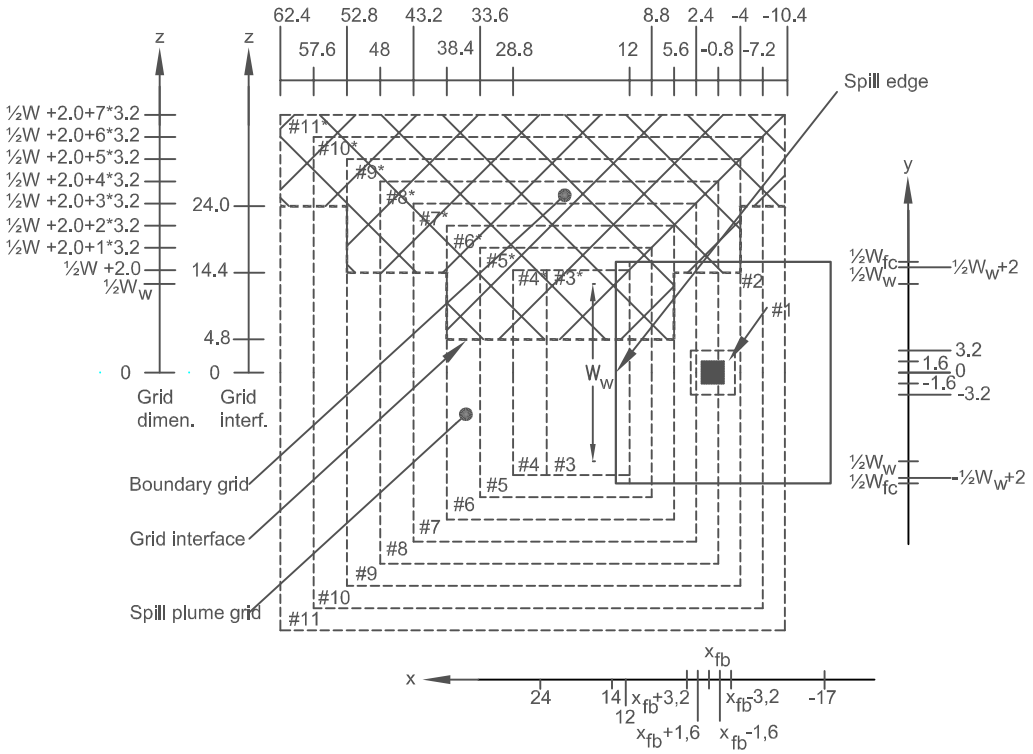

]

Figure 6.2 *CFD model: Full-scale spill plume setup, horizontal section.*

Measuring Positions

Measurements are recorded using the slice file (SLCF) output option in FDS at positions listed in Table 6.5 along with recorded quantities.

Simulation ID	Quantity	Location	Position
WOSPXXX-XXX-XX-BSP	T,u,v,w	Opening	$x \in \{14.0\}$ m
WOSPXXX-XXX-XX-BSP	T,u,v,w	Spill plume	$z \in \{3.6, 8.8, 13.2, \ldots$
			$18.4, 22.8, 28.0, \ldots$
			$32.4, 37.6, 42.0, \ldots$
			$47.2, 51.6, 56.8\}$ m

Table 6.5 *Measured quantities and positions applied in the full-scale approach flow CFD model relative to dimensions in Figures 6.1 and 6.2.*

Data Processing

All quantities applied in the present study are recorded in the computational grid (i.e. grid # [3 : 9]) and then mirrored about the center line, discarding quantities recorded from the center line to the grid interface between the computational grid and the boundary grid, see Figure 6.2. The inherent symmetric flow pattern of the approach flow and thus balcony spill plume was documented in Section 3.9.5, supporting the mirroring approach in the present modeling program.

Convective heat flow rates $\dot{Q}_c$ and $\dot{m}_l$ mass flow rates are computed from the temperature and velocity profiles using the numerical integration method outlined in Section 2.6, Eqns. (2.6.4) and (2.6.6), p. 43. Smoke layer depths in the fire compartment opening d_w are computed from the buoyancy profiles applying the method in Section 3.4, Eqn. (3.4.1), p. 91.

CFD Model Inputs

The full-scale approach flow CFD model employs the full hydrodynamic model including LES turbulence model, propane combustion, no radiation model and adiabatic surface boundary conditions, see model inputs in Table 6.6.

Turbulence model		
Smagorinsky constant	C_s	0.2
Prandtl number	Pr	0.5
Schmidt number	Sc	0.5
Combustion model		
Material	Propane	Default FDS v. 4.06
Heat of combustion	ΔH_c	47,251 kJ/kg
Radiative fraction	χ_r	0.286
Molecular weight	M_w	44.00 g/mol
Soot yield	y_s	0.01 kg/kg
Fire source		
Fire base area	A_f	3.2^2 m^2
Specific HRR	$\dot{Q}''_T$	see Table 6.1
Flame sheet correction	*AUTOMATIC_Z*	*TRUE*
Radiation model		
Radiative model		Not applied
Surface BCs		
Thermal model		Adiabatic
Ghost cell temperature	T_{ghost}	T_g
Velocity model		Partial slip
Wall velocity	u_τ	$0.5u_i$
Flow BCs		
Flow model	Passive vent	*OPEN*
Ambient temperature	T_∞	$20°C$
Ambient velocity	$\mathbf{u}$	0 m/s
Ambient perturbed pressure	$\tilde{p}$	0 Pa
Ambient static pressure	p_0	1.013 10^5 Pa

Table 6.6 *Full-scale approach flow setup: Model input parameters.*

6.5 Results

6.5.1 Conservation of Energy

The conservation of energy in the spill plume is checked to make sure the entire spill plume is resolved within the computational grid. From Figure 6.3 it is clear that the profiles are almost horizontal implying that the convective heat flow rate $\dot{Q}_c$ is constant in the spill plume. Deviations are within 5% of the mean convective heat flow rate, considered acceptable the averaging process taken into consideration.

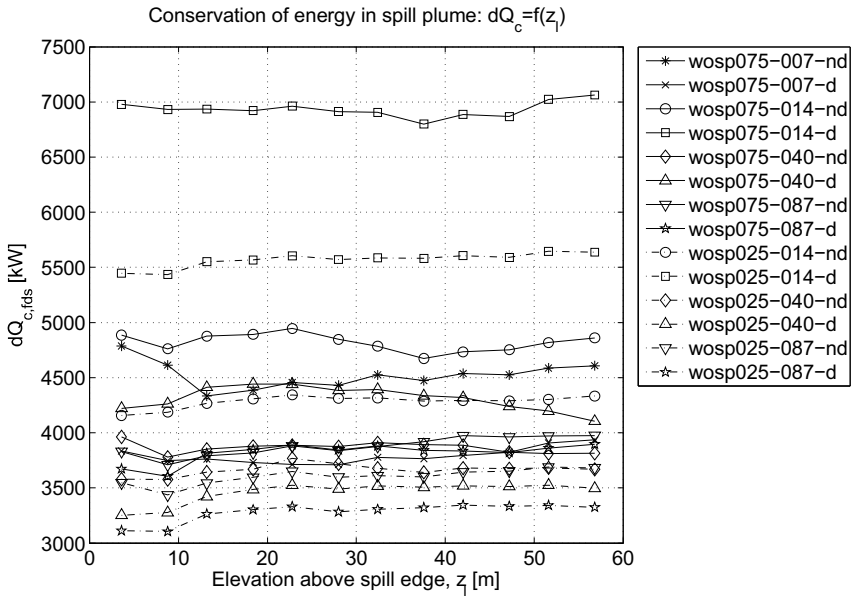

Figure 6.3 *Conservation of energy in CFD model: Convective heat flow in the spill plume* $\dot{Q}_c$.

6.5.2 Lateral Temperature Distribution in Spill Plume

The lateral temperature distributions in the spill plume are investigated to assess if the core flow filtering, see Section 2.6, should be relaxed to avoid disintegration of the spill plume. The wide spill plumes are expected to reach temperatures above ambient in the vicinity of the cut-off filter $\Delta T_i \geq 1$ K, see Figure 6.4. Mean lateral temperature distributions in the figure are obtained using the $\Delta T_i \geq 1$ K cut-off filter, i.e. yielding conservative mean temperatures:

$$\bar{T}_j = \frac{\sum_i^N T_{i,j}}{N} \; \forall \; \{i,j\} \in \Omega_{\Delta T \geq 1\,\mathrm{K}} \tag{6.5.1}$$

where $\Omega_{\Delta T \geq 1\,\mathrm{K}}$ is the spill plume core. The temperature distributions in the extreme setups ($W_w = 87.2$ m), see Figure 6.4, implies that the spill plume will begin to numerically collapse for rising heights $z_l > 8.8$ m above the spill edge.

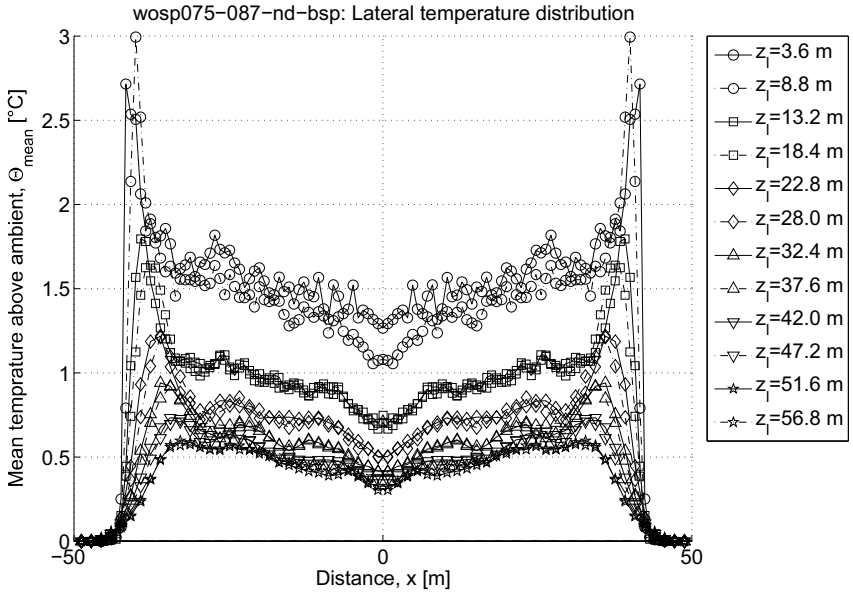

(a) WOSP075-087-ND-BSP: $W_w = 87.2$ m, $d_d = 0$ m.

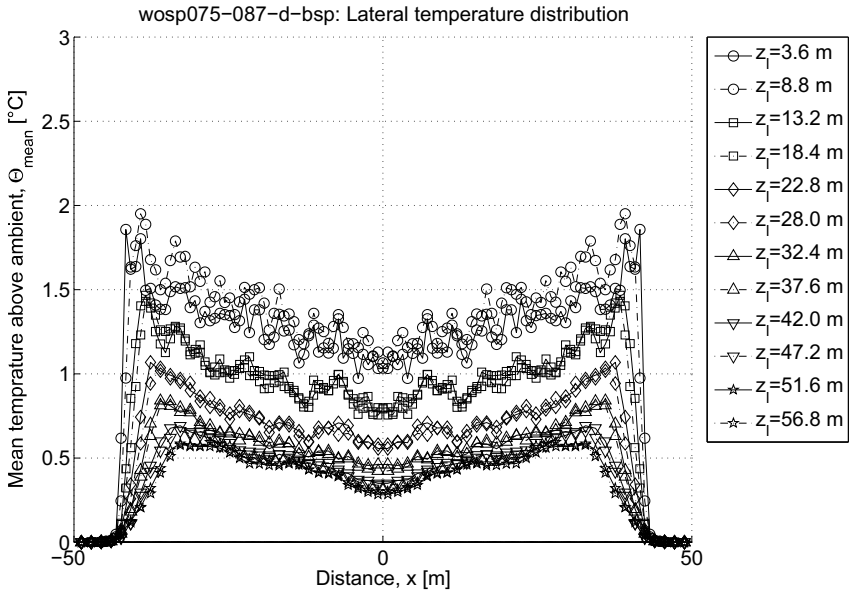

(b) WOSP075-087-D-BSP: $W_w = 87.2$ m, $d_d = 1$ m.

Figure 6.4 *WOSP075-XXX-XX-BSP: Lateral mean temperature distributions.*

The complete series of lateral temperature distributions can be found in Appendix J.

The magnitude of the temperature cut-off filter was chosen based on investigations of the mass flow rates for different cut-off filters. The objective was to arrive at a cut-filter that would produce zero mass flux outside the spill plume without forcing the plume to numerically collapse at low elevations. Lateral mass flow rates per unit length are shown for cut-off filters $\Delta T \in \{10^{-6}, 10^{-2}, 1\}$ K in Figure 6.6. Looking at Figures 6.6(a) and 6.6(b) it is clear that the mass flow rate outside the spill plume region is not close to zero, as opposed to Figures 6.6(c)-6.6(f). From the above discussion it was clear that a cut-off filter of $\Delta T \geq 1$ K was not applicable because of the numerical collapsing plume, thus it was decided to relax the temperature cut-off filter to $\Delta T \geq 10^{-2}$ K:

$$\tilde{\rho}_i = \begin{cases} \rho_i & \forall\ \Delta T_i \geq 10^{-2}\ K \\ 0 & \forall\ \Delta T_i < 10^{-2}\ K \end{cases} \tag{6.5.2}$$

with i designating the local control volume index. The velocity cut-off filter remained unchanged, i.e. according to Section 2.6.

It should be noted that Klote & Milke (2002) without further documentation proposed a temperature rise of $\Theta \geq 2$ K for a buoyant plume to be considered strongly buoyant. Obviously this criterion is not applicable in the present study as it would lead to a premature numerical plume collapse.

6.5.3 Mass Flow Rates Per Unit Length in Spill Plume

The lateral mass flow rates per unit length $\dot{m}'_l$ in the spill plume are derived from the predicted velocity and temperature fields applying the cut-off filter described in Section 6.5.2 and the numerical method outlined in Section 2.6. The complete series of lateral mass flow rate distributions can be found in Appendix K. Looking at the plot series it is clear that the mass flow rate distributions resemble the distribution emanating from the fire compartment, see Section 5.4.2.

Figure 6.5 shows the difference in end entrainment for regular ($W_w \in \{7.2, 14.4\}$ m) and wide ($W_w \in \{40.0, 87.2\}$ m) spill plumes. For regular spill plumes air is entrained into the ends of the spill plume, hereby increasing the lateral extent of the spill plume. For wide spill plumes it is implied that the ends are eroded, hence decreasing the lateral extent of the wide spill plume. The trend is supported by Appendix K. This questions the approach by Thomas (1987), where end entrainment was addressed by adding a half axisymmetric plume to each end of the spill plume. Obviously this approach can be adopted for regular spill plumes, but is expected to over predict the mass flow rate in wide spill plumes.

The total mass flow rate $\dot{m}_l$ is clearly impacted by the plume cut-off filter ΔT, but from Figure 6.6 it is observed that this does not impact the edge erosion for the wide spill plume.

As the approach flow emanates from the compartment opening it has a considerable amount of horizontal momentum that inherently affects the entrainment on the back and front of the spill plume. The use of an appreciable downstand

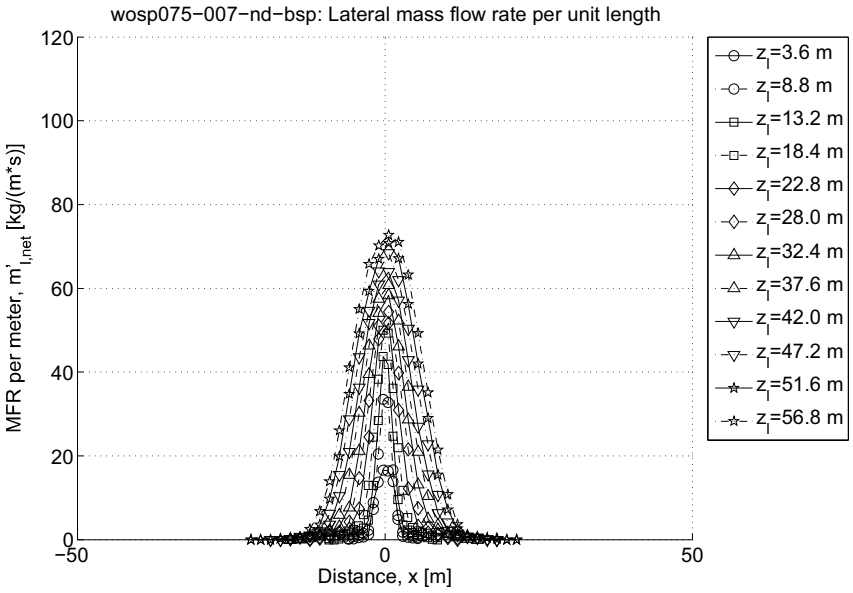

(a) WOSP075-007-ND-BSP.

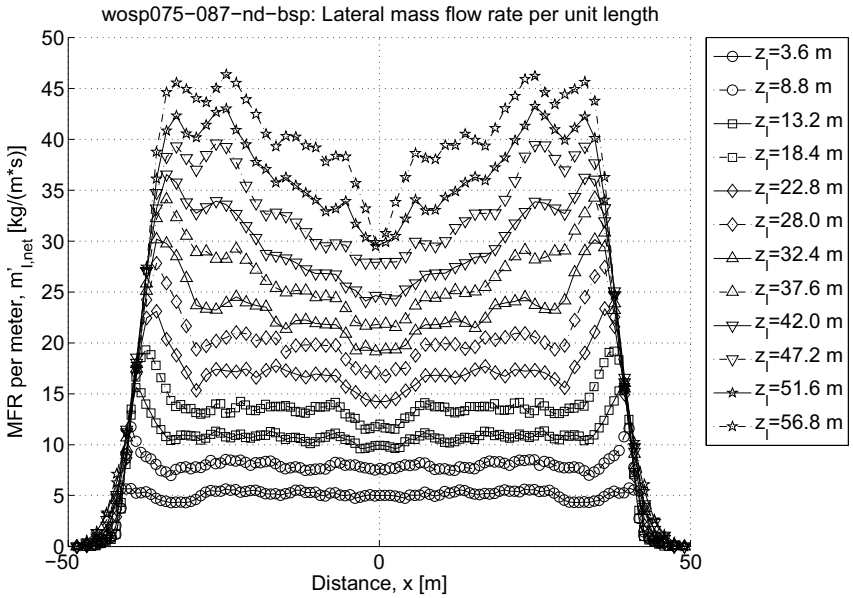

(b) WOSP075-087-ND-BSP.

Figure 6.5 *Edge erosion in wide spill plumes.*

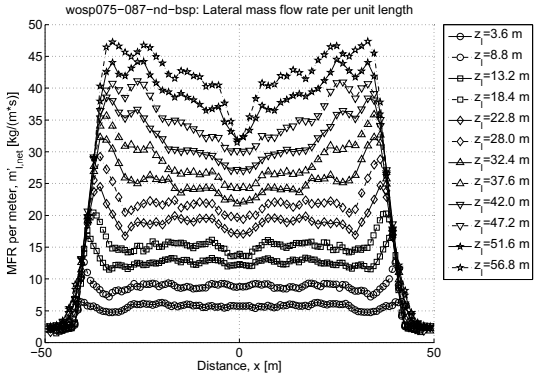

(a) WOSP075-087-ND-BSP, $\Delta T \geq 1E-6$ K.

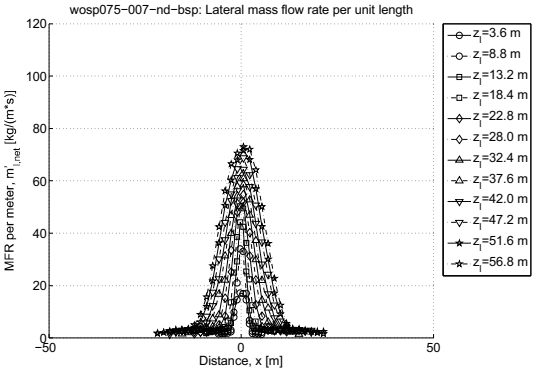

(b) WOSP075-007-ND-BSP, $\Delta T \geq 1E-6$ K.

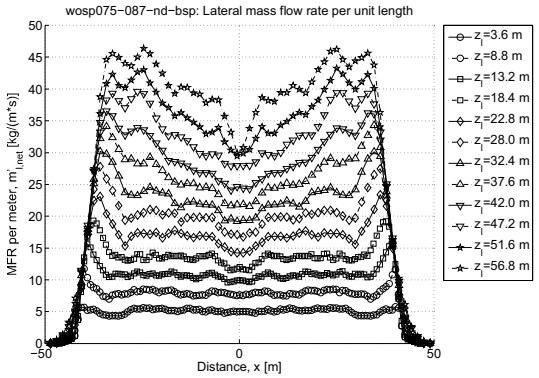

(c) WOSP075-087-ND-BSP, $\Delta T \geq 1E-2$ K.

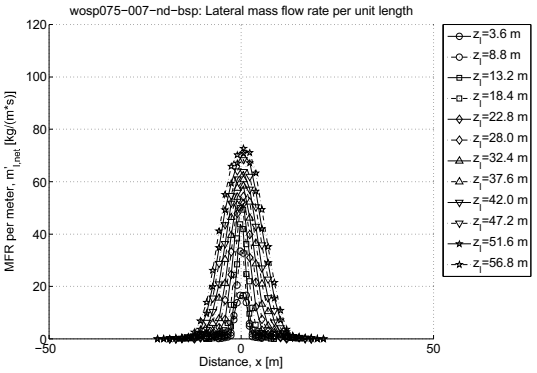

(d) WOSP075-007-ND-BSP, $\Delta T \geq 1E-2$ K.

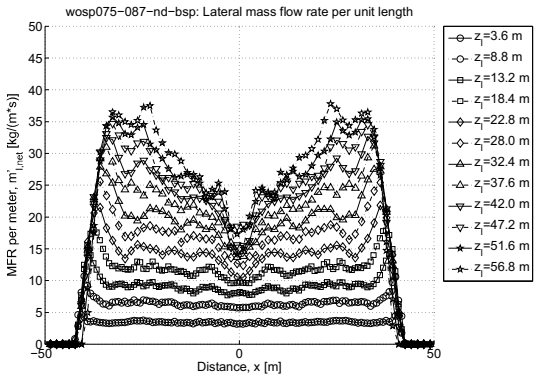

(e) WOSP075-087-ND-BSP, $\Delta T \geq 1$ K.

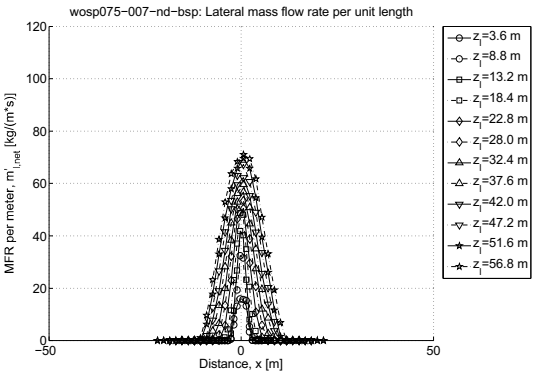

(f) WOSP075-007-ND-BSP, $\Delta T \geq 1$ K.

Figure 6.6 *Lateral mass flow rate distributions as a function of temperature cut-off filter magnitude.*

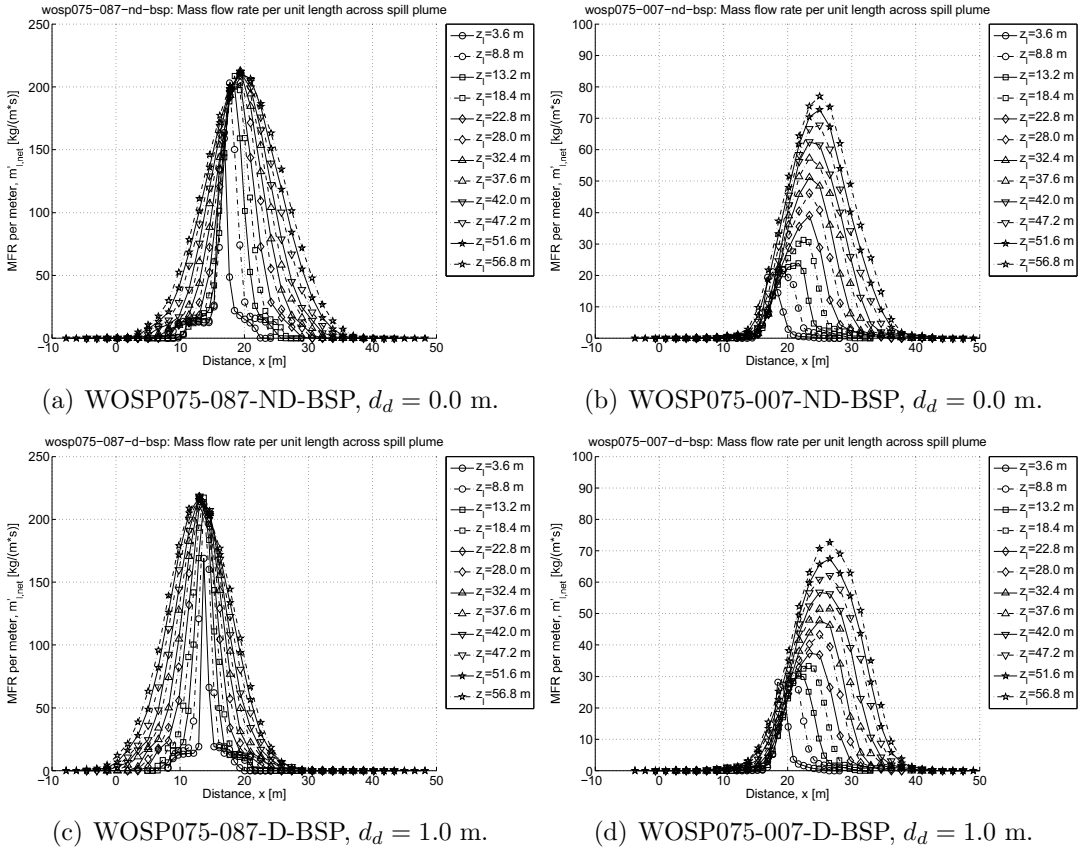

(a) WOSP075-087-ND-BSP, $d_d = 0.0$ m.

(b) WOSP075-007-ND-BSP, $d_d = 0.0$ m.

(c) WOSP075-087-D-BSP, $d_d = 1.0$ m.

(d) WOSP075-007-D-BSP, $d_d = 1.0$ m.

Figure 6.7 *Cross-sectional mass flow rates per unit length.*

completely obstructing the ceiling jet, yields a more uniform entrainment profile and hence vertically aligned mass flow rate profiles as can be seen in Figure 6.7. Due to the depth of the smoke layer (a result of a large fire in a small fire compartment), the mass flow rate profiles in Figures 6.7(b) and 6.7(d) do not differ considerably, because the smoke layer extends considerably below the downstand. A complete series of cross-sectional mass flow rates per unit length profiles can be found in Appendix L.

6.5.4 Spill Plume Collapse

The collapse of the thermal spill plume has already been mentioned in the previous sections, where it was regarded a numerical artifact. Real thermal plumes however are also subjected to the same disintegration due to entrainment of the ambient air into the spill plume, see e.g. Klote & Milke (2002), leading to a stagnating spill plume controlled by the existing ambient air currents.

Lateral temperature distributions are shown for a wide ($W_w = 87.2$ m) and narrow spill plume ($W_w = 14.4$ m) in Figure 6.8. The deviations from an even

mass flow rate distribution along the spill edge for approach flows in wide openings were discussed in Chapter 5, and were partly attributed to the flows reflected from the compartment walls. Because no energy is conducted through the compartment enclosure, temperatures and hence mass flow rates are expected to have local extrema at the ends of the spill plume. However as the fire base is located closer to the compartment opening, the ceiling jet momentum impacts the flow emanating from the compartment opening, and another local extrema can be observed on the center line for $D_{fb} = 7.8$ m, see Figure 6.9.

Using a temperature cut-off filter of $\Delta T \geq 1$ K it is possible to observe the collapse of a spill plume. Looking at Figure 6.6(f) it is clear that the strongly buoyant spill plume is not subjected to disintegration of the spill plume, i.e. the shape of the mass flow rate profiles is preserved with rising height z_l. In contrast it is obviously from Figure 6.6(e) that the mass flow rate profiles collapse on the center line $x = 0$, represented by the spike penetrating down through the profiles. This can be explained by looking at the temperature profiles in Figure 6.4, where it is obvious that for $z_l > 8.8$ m the mean temperature $\bar{T}$ descends below the cut-off filter magnitude $\Delta T \geq 1$, hence vanishing from the surface integral applied in deriving the mass flow rate, see Section 2.6, and thus decreasing the total mass flow rate $\dot{m}_l$.

The observed spike is not a result of the mirrored boundary condition, which can be deduced from looking at the preserved mass flow rate profiles with cut-off filters $\Delta T \geq \{10^{-6}, 10^{-2}\}$ K in Figures 6.6(a) and 6.6(c). Looking at the mean temperature profile for the wide spill plume $W_w = 87.2$ m close to the compartment opening $D_{fb} = 7.8$ m in Figure 6.9, a small perturbation on the order $\bar{\Theta} \sim 0.2$ K on the center line is observed. The perturbation is attributed to the mirrored boundary condition and assumed to be negligible in deriving the total mass flow rate $\dot{m}_l$ (through the density ρ). This is supported by the mass flow rate per unit length profiles $\dot{m}'_l$ depicted in Figure 6.10, where the impact of the perturbation can be identified to be of the order $\dot{m}'_l \sim 3$ kg/(s*m).

Using a cut-off filter of $\Delta T \geq 1$ K, and computing the lateral and cross-sectional extents of the spill plume, it is possible to monitor the transformation of the spill plume by simply plotting the aspect ratio AR_l [1]:

$$AR_l = \frac{D_l}{W_l} \tag{6.5.3}$$

where D_l is the cross-sectional and W_l is the lateral extent of the spill plume $[m]$ respectively. The extents of the spill plume are computed from:

$$D_l = \max_j \left(\max_i (x_{ij}) - \min_i (x_{ij}) \right) \ \forall \ \{i, j\} \in \Omega_{\Delta T \geq 1\,\mathrm{K}} \tag{6.5.4a}$$

$$W_l = \max_i \left(\max_i (y_{ij}) - \min_i (y_{ij}) \right) \ \forall \ \{i, j\} \in \Omega_{\Delta T \geq 1\,\mathrm{K}} \tag{6.5.4b}$$

where $\Omega_{\Delta T \geq 1\,\mathrm{K}}$ is the spill plume core using the cut-off filter $\Delta T \geq 1$ K. It is obvious that for $AR_l \to 1$ the spill plume approaches an axisymmetric plume and a line plume for $AR_l \to 0$. From Figure 6.11 it can be seen that the regular

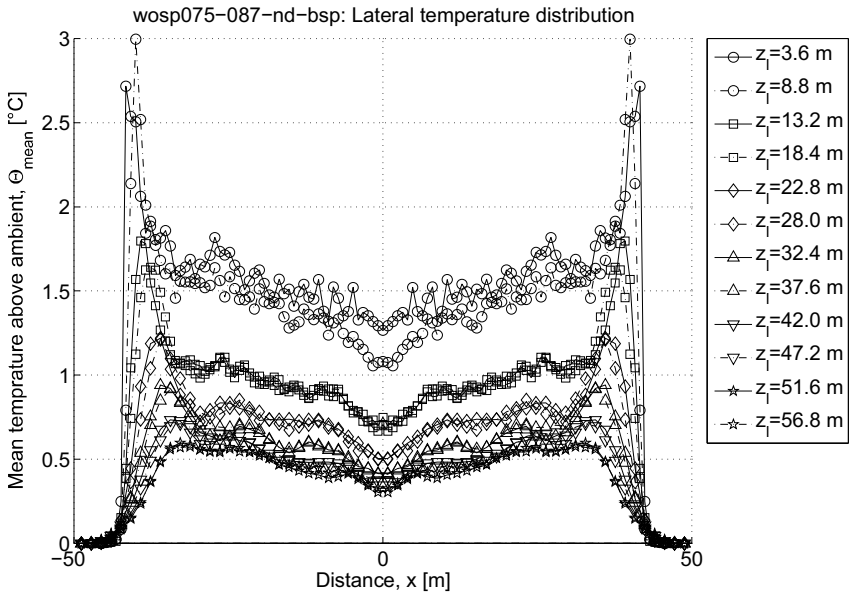

(a) WOSP075-087-ND-BSP: $D_{fb} = 22.4$ m, $W_w = 87.2$ m, $d_d = 0$ m.

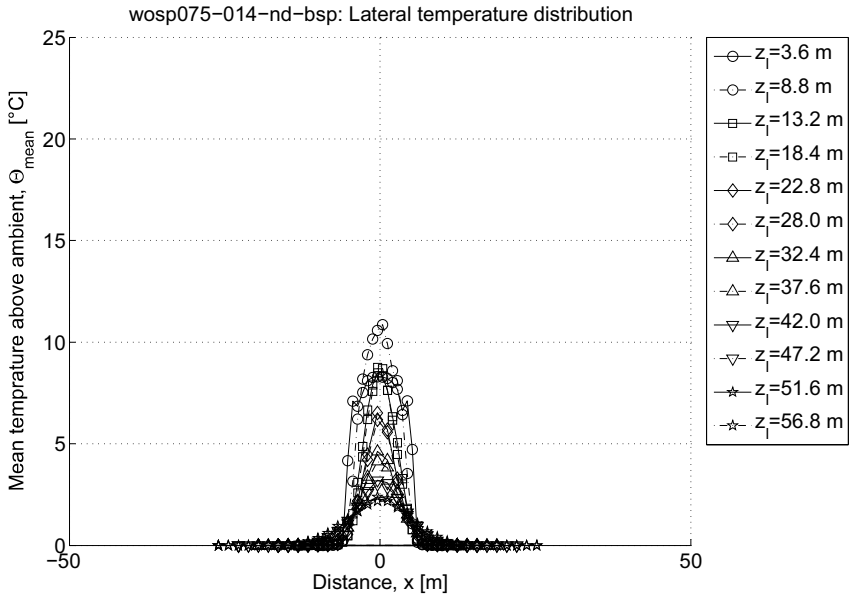

(b) WOSP075-007-ND-BSP: $D_{fb} = 22.4$ m, $W_w = 14.4$ m, $d_d = 0$ m.

Figure 6.8 *WOSP075-XXX-ND-BSP: Lateral mean temperature distributions.*

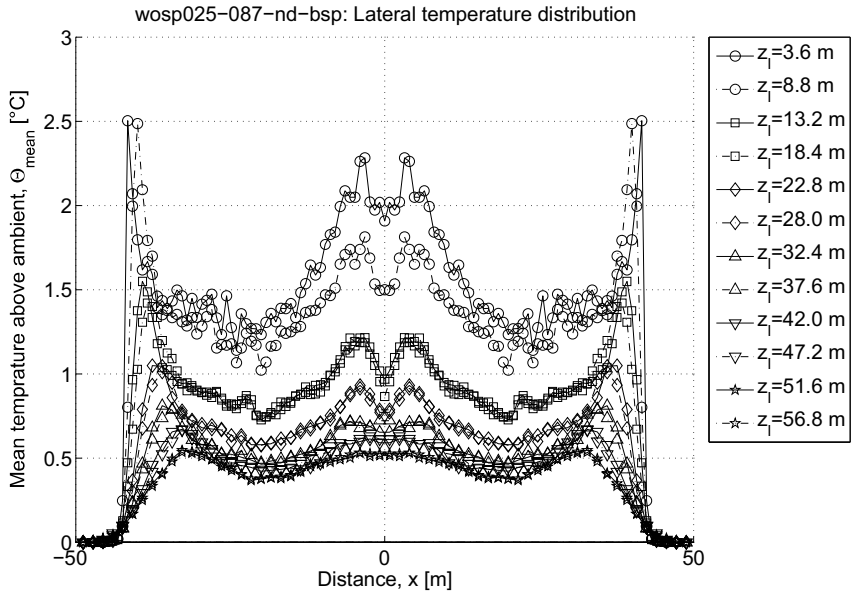

Figure 6.9 *WOSP025-087-ND-BSP, D_{fb} = 7.8 m, W_w = 87.2 m, d_d = 0 m: Lateral mean temperature distributions.*

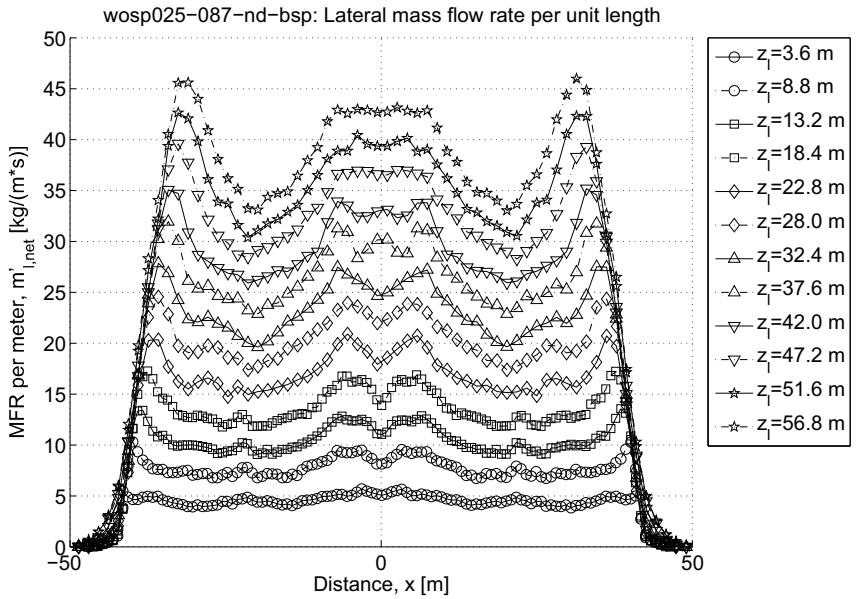

Figure 6.10 *WOSP025-087-ND-BSP, D_{fb} = 7.8 m, W_w = 87.2 m, d_d = 0 m: Lateral mass flow rate per unit length distributions.*

spill plumes investigated, i.e. ($W_w \in \{7.2, 14.4\}$ m), approaches an axisymmetric plume for $z_l \gtrsim 30$ m, whereas the wide spill plumes, i.e. ($W_w \in \{40.0, 87.2\}$ m), changes the aspect ratio very slowly, mainly because of the low end entrainment discussed in Section 6.5.3.

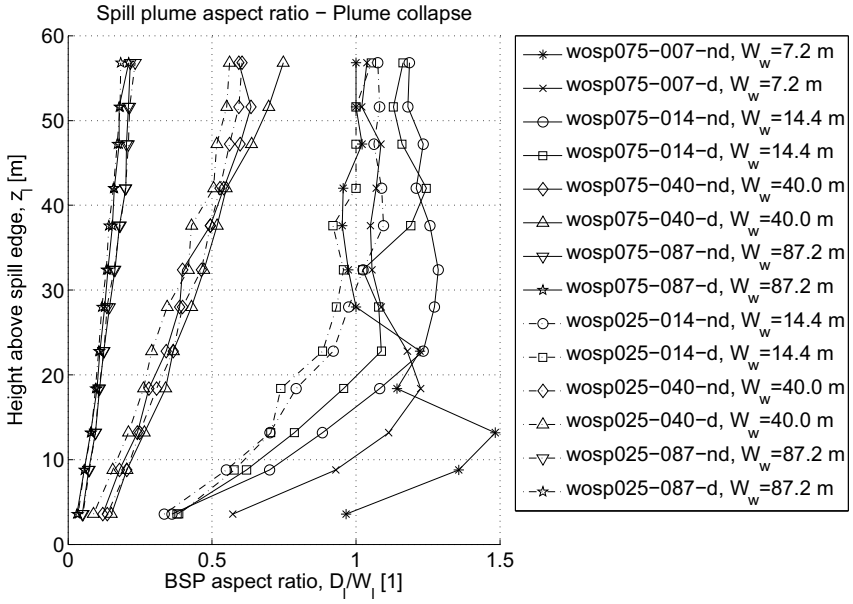

Figure 6.11 *Spill plume transformation: Aspect ratio D_l/W_l.*

6.6 Development of Spill Plume Method for Wide Openings

6.6.1 Functional Form

The functional form of the wide opening spill plume method is adopted from most of the previous research programs on spill plumes, e.g. Law (1986) and McCartney (2006), and based on the nomenclature in Figure 6.12:

$$\dot{m}_l = \dot{m}_{l,net}\left(\dot{Q}_{c,w}, W_w, z, z_e\right) + \dot{m}_e\left(d_w, W_w, \dot{m}_w\right) \tag{6.6.1a}$$

$$= C_l\left(\dot{Q}_{c,w}, W_w, \right)\left[z - z_e\right] + \dot{m}_e\left(d_w, W_w, \dot{m}_w\right) \tag{6.6.1b}$$

$$= C_l\left(\dot{Q}_{c,w}, W_w, \right) z_l + \dot{m}_e\left(d_w, W_w, \dot{m}_w\right) \tag{6.6.1c}$$

where $\dot{m}_l$ is the gross mass flow rate in the spill plume $[kg/s]$, $\dot{m}_{l,net}$ is the net mass flow rate in the spill plume $[kg/s]$, $\dot{m}_e$ is the mass flow rate at the elevation of the spill edge $[kg/s]$, $\dot{m}_w$ is the approach flow mass flow rate $[kg/s]$, C_l is

the entrainment coefficient $[kg/(m * s)]$, W_w is the compartment opening width (i.e. the lateral extent of the spill edge) $[m]$, d_w is the smoke layer depth in the compartment opening $[m]$, $\dot{Q}_{c,w}$ is the convective heat flow rate into the spill plume $[W]$, z is the height above the compartment floor $[m]$, z_l is the rising height above the spill edge $[m]$ and z_e is the elevation of the spill edge $[m]$.

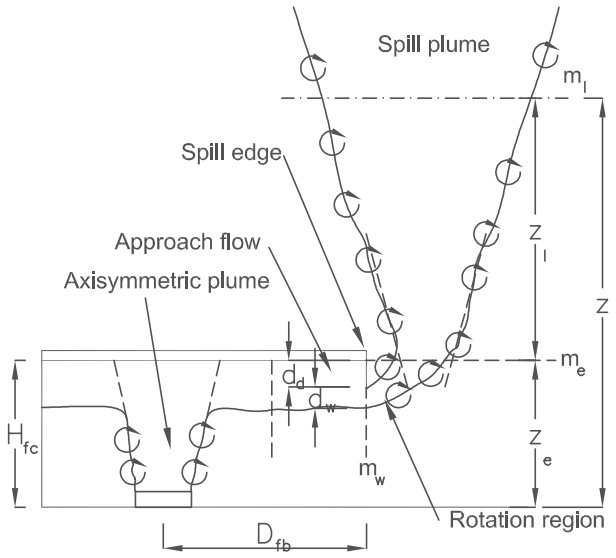

Figure 6.12 *Nomenclature adopted in deriving the spill plume mass flow rate.*

6.6.2 Assumptions and Limitations

Assumptions and limitations applied in developing the new method are:

Convective heat flows - Convective heat flows into the spill plume are evaluated in the compartment opening based on the convective heat flow in the approach flow and ranges from $\dot{Q}_{c,w}$=3492 kW to 6886 kW.

Fire compartment heights - The compartment ceiling height H_{fc} was fixed at 5 m throughout the tests, but does not impact the net flow rate in the spill plume, since the approach flow mass flow rate is decoupled and calculated separately, see Chapter 5.

Fire compartment openings - Opening widths ranging from W_w=7.2 m to 87.2 m is used in deriving the method, representing opening widths investigated in earlier spill plume programs ($W_w = \{7.2, 14.4\}$ m) and extended to wide openings often associated with open plan offices or large retail shop units opening up into an atrium.

Balcony depth - The present research does not address approach flows emanating from a fire compartment and migrating under a balcony to the spill edge, only flows spilling from the fire compartment into the atrium is comprised by the new method. Harrison (2004) investigated smoke flows under balconies.

Downstands - The method addresses flows flowing unhindered out of the fire compartment and flows with an appreciable downstand completely obstructing the ceiling jet flow, i.e. at least 20% of the compartment height.

Stable smoke layer interface - Opening widths are assumed wide enough to prevent makeup air entering the fire compartment from obstructing the smoke layer interface with increased mixing as a result.

Well-ventilated conditions - Complete combustion and well-ventilated conditions are assumed throughout the method.

No heat loss - Heat loss through the fire compartment enclosure is neglected, leading to conservative estimates of the mass flow rate, see Section 3.8.

Radiation - The method does not include radiative effects on the smoke layer and spill plume flow, thus care should be taken for smoke flows where radiation is paramount. Neglecting radiative effects leads to conservative estimates of the mass flow rates, see Section 3.8.

Free spill plume - The method is derived for a free spill plume and inherently includes entrainment into the ends. The method is expected to over predict mass flow rates for spill plumes restricted by atrium walls because of the reduced entrainment perimeter.

Buoyant plume - The plume is considered buoyant throughout it's extents, i.e. also at the highest elevations. For temperatures above ambient below $\Theta = 1$ C$^\circ$ it is questionable if the plume can be considered strongly buoyant, hence being extremely sensitive to ambient air currents that can increase mixing. The method is derived without any external airflow impacting the plume, thus the method should be applied with caution for temperatures above ambient close to $\Theta = 1$ C$^\circ$ since real flow conditions in an atrium may impact the entrainment in weakly buoyant plumes.

Dimensional units - The method is developed using the SI system with the following modifications: kW and kJ.

6.6.3 Mass Flow Rate at the Spill Edge Elevation

Mass flow rates are derived from the velocity and temperature fields predicted by the CFD model using the numerical method outlined in Section 2.6 and the core plume filtering discussed in Section 6.5.2. The total mass flow rates $\dot{m}_l$ predicted by the CFD model are plotted against the rising height z_l above the spill edge in

Figure 6.13. A clear linear dependence on the rising height z_l is observed implying that the mass flow rate at the spill edge $\dot{m}_e$ at $z_l = 0$ can be determined by linear extrapolation.

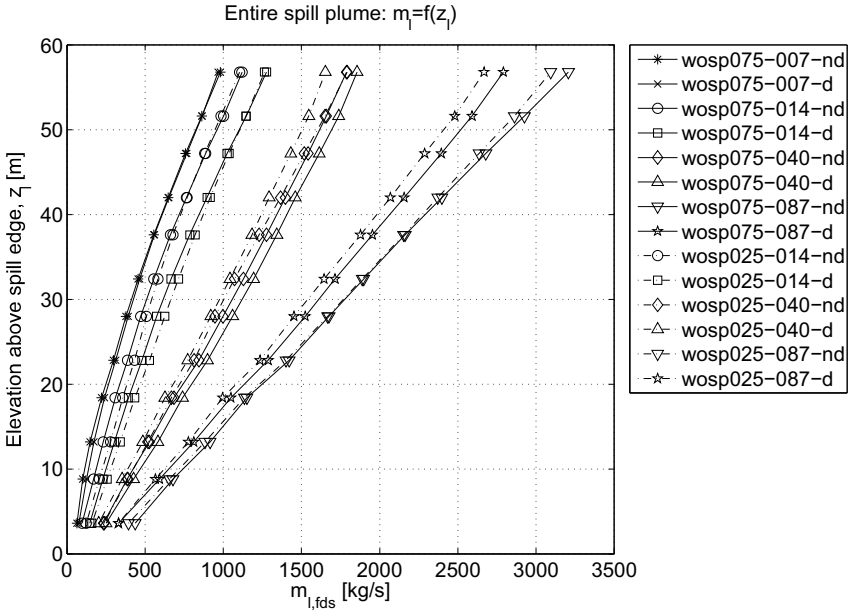

Figure 6.13 *Total mass flow rate in spill plume $\dot{m}_l$.*

By looking at the linear mass flow rate profiles in Figure 6.13, a slight non-linear behavior is observed in the lower spill plume region for $z_l \lesssim 15$ m, attributed to the flow not being completely vertically aligned, i.e. not completely rotated, hence entraining less ambient air. The best fit to derive $\dot{m}_e$ is obtained from only considering the mass flow rates in the lower spill plume, see Figure 6.14.

The mass flow rate at the spill edge $\dot{m}_e$ is found by simple linear extrapolation of the functional form:

$$\dot{m}_l = C_{l,low} z_l \qquad z_l \in [3.6 : 8.8] \tag{6.6.2}$$

The linear data fits $\dot{m}_{l,fit}$ are plotted against predicted values of mass flow rates $\dot{m}_l$ in the lower spill plume and can be found in Figure 6.15 along with the linear coefficients $C_{l,low}$ for the respective simulations.

The derived mass flow rates at the elevation of the spill edge $\dot{m}_e$ using Eqn. (6.6.2) and the corresponding approach flow mass flow rates $\dot{m}_w$ are listed in Table 6.7.

6.6.4 Entrainment in the Rotation Region

The mass flow rate at the elevation of the spill edge $\dot{m}_e$ is obviously dependent on the rotation of the horizontal approach flow rate $\dot{m}_w$ to the vertical position

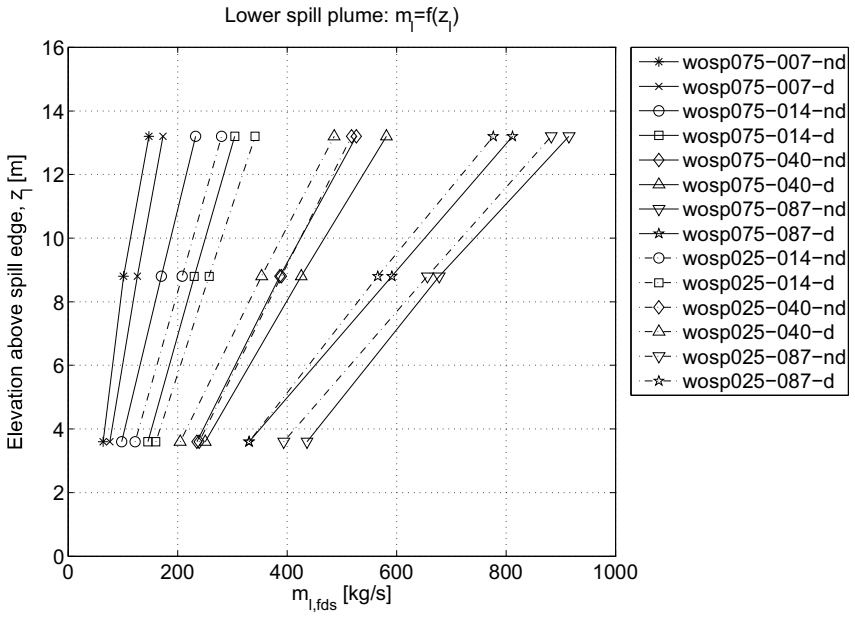

Figure 6.14 *Mass flow rate in lower spill plume $\dot{m}_l$ - close up.*

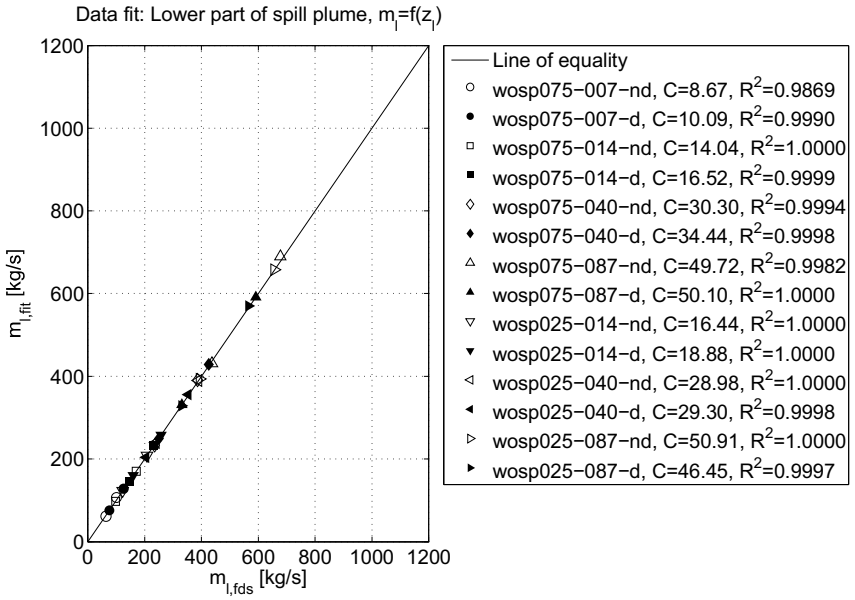

Figure 6.15 *Fitted vs. predicted mass flow rates in the lower spill plume.*

Simulation ID	$\dot{m}_e$ [kg/s]	$\dot{m}_w$ [kg/s]
WOSP075-007-ND-BSP	38.40	32.19
WOSP075-007-D-BSP	41.83	30.92
WOSP075-014-ND-BSP	47.82	41.48
WOSP075-014-D-BSP	87.45	41.34
WOSP075-040-ND-BSP	130.19	66.02
WOSP075-040-D-BSP	129.11	48.78
WOSP075-087-ND-BSP	269.56	109.57
WOSP075-087-D-BSP	150.05	59.42
WOSP025-014-ND-BSP	63.24	37.70
WOSP025-014-D-BSP	92.51	36.02
WOSP025-040-ND-BSP	135.70	54.63
WOSP025-040-D-BSP	101.45	40.53
WOSP025-087-ND-BSP	211.88	89.96
WOSP025-087-D-BSP	167.47	52.28

Table 6.7 *Computed mass flow rates in approach flow $\dot{m}_w$ and at the elevation of the spill edge $\dot{m}_e$.*

z_e. As the flow is rotated air is entrained on the two sides of the rotated flow and at the ends. Air is assumed to be entrained as a function of the distance along the streamlines in the rotated flow. For the method to be applicable in engineering, it must be simple to use. Deriving the streamlines require detailed information about the approach flow velocity field. This is not available from the simple approach flow method proposed in Chapter 5, hence a simple correlation between the approach flow mass flow rate $\dot{m}_w$ and the mass flow rate at the spill edge $\dot{m}_e$ is desired.

Based on statistical analysis of $\dot{m}_e$ and $\dot{m}_w$, see Table 6.7, as a function of the variables available from the calculation of the approach flow mass flow rate from Chapter 5, significant correlations are found between $\dot{m}_e$, the width of the compartment opening W_w, the depth of the smoke layer in the compartment opening d_w and the approach flow mass flow rate $\dot{m}_w$. A correlation of this type was expected since d_w and W_w describes the area of the approach flow being rotated and $\dot{m}_w$ the source potential. A simple correlation for the spill edge mass flow rate $\dot{m}_e$ is proposed based on the aforementioned variables:

$$\dot{m}_e = C_m \dot{m}_w^m W_w^n d_w^k \quad \left| \begin{array}{rcl} C_m & = & 2.2628 \\ m & = & 0.5780 \\ n & = & 0.4923 \\ k & = & 0.2426 \end{array} \right. \tag{6.6.3}$$

where $\dot{m}_w$ is the approach flow mass flow rate $[kg/s]$ calculated from Eqn. (5.5.4), Eqn. (5.5.2b) and Eqn. (5.5.1), $\dot{m}_e$ is the mass flow rate at the elevation of the spill edge $[kg/s]$, W_w is the compartment opening width $[m]$, d_w is the depth of the

smoke layer in the compartment opening $[m]$ calculated from Eqn. (5.5.5). The distance from the fire base to the compartment opening D_{fb} and the downstand depth d_d were not found to correlate significantly with the spill edge flow $\dot{m}_e$. The smoke layer depth d_w however correlates significantly with the downstand depth d_d, see Section 5.5.3, and is also weakly correlated to the distance from the fire base to the compartment opening D_{fb}, hence $\dot{m}_e$ indirectly depends on D_{fb} and d_d. Correlation coefficients are again computed by an unconstrained nonlinear optimization using the *Nelder-Mead Simplex Method* to find the minimum of a multi-variable scalar function, see Lagarias et al. (1998).

Fitted values of the mass flow rate at the spill edge $\dot{m}_{e,fit}$ are plotted against predicted values $\dot{m}_e$ in Figure 6.16 to assess the quality of the correlation. A correlation coefficient of $R^2 = 0.95$ was obtained indicating a strong correlation between the variables in Eqn. (6.6.3).

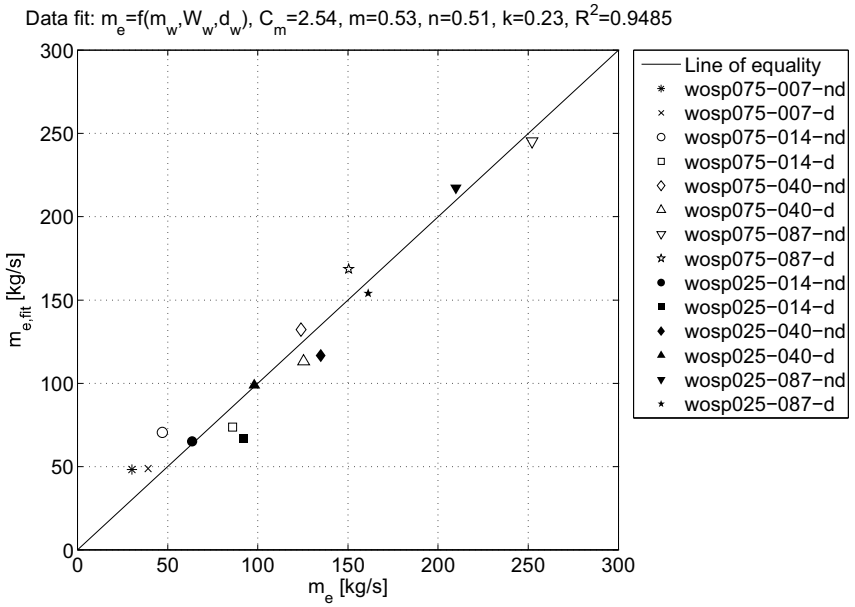

Figure 6.16 *Correlating mass flow rate at elevation of spill edge $\dot{m}_e$ to approach flow mass flow rate $\dot{m}_w$.*

6.6.5 Entrainment in the Wide Spill Plume

From looking at the total mass flow rate profiles $\dot{m}_l$ in Figure 6.13 it is clear that an intermediate region exists where the entrainment is almost constant and the profiles close to linear. The intermediate region $z_l \in [18.2 : 47.0]$ m is plotted in Figure 6.17.

Using a simple linear functional form for $\dot{m}_l$, the entrainment coefficients $C_{l,int}$ in the intermediate spill plume region can be derived from simple linear regression:

$$\dot{m}_l = C_{l,int} z_l + m_e \qquad z_l \in [18.2 : 47.0] \tag{6.6.4}$$

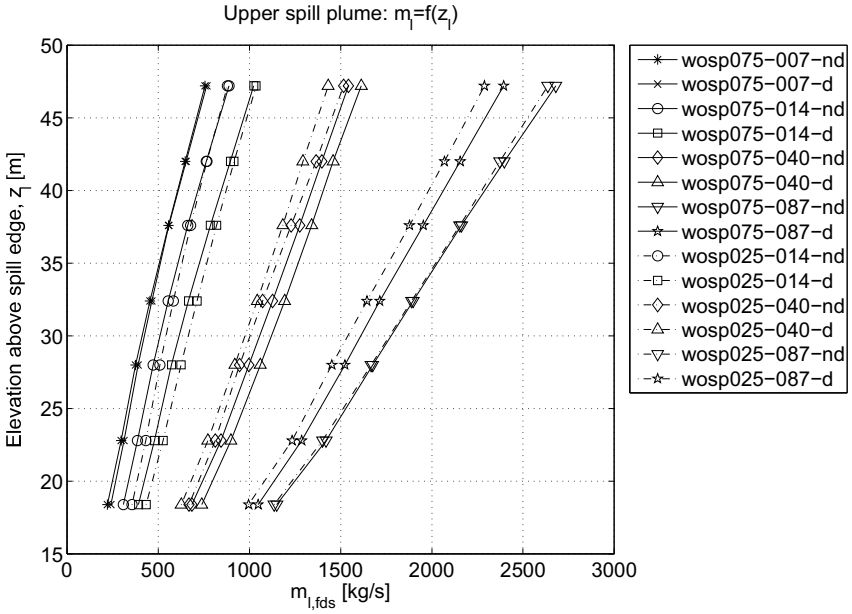

Figure 6.17 *Total mass flow rate in intermediate spill plume region* $\dot{m}_l$.

Resulting entrainment coefficients $C_{l,int}$ are displayed in the legends of Figures 6.18 and 6.19. The difference in entrainment coefficients clearly depends on the fire size $\dot{Q}_{c,w}$ and the compartment opening width W_w, which is supported by numerous publications on spill plume correlations, e.g. Lee & Emmons (1961), Law (1986) and Thomas (1987). By applying simple dimensional analysis to the mass flow rate $\dot{m}_l$ above a line source, Lee & Emmons (1961) found that the mass flow rate scaled with $\dot{Q}^{1/3}$. This is considered a well renowned scaling and will also be employed in the current study. A simple entrainment coefficient $C_{l,sim}$ addressing wide spill plumes is proposed to correlate with the width of the compartment opening W_w and the convective heat flow in the approach flow $\dot{Q}_{c,w}$ in accordance with the aforementioned findings in the literature:

$$C_{l,sim} = C_m W_w^m \dot{Q}_{c,w}^{1/3} \left| \begin{array}{rcl} C_m & = & 0.1936 \\ m & = & 0.6174 \end{array} \right. \tag{6.6.5}$$

Testing the correlation for the simple entrainment coefficient $C_{l,sim}$, Eqn. (6.6.5), against predicted coefficients $C_{l,fds}$ yields a correlation coefficient of $R^2 = 0.97$, see Figure 6.18, indicative of a strong correlation.

The depth of the downstand d_d is expected to have an impact on the mass flow rate because of it's obvious impact on the entrainment profiles discussed in Section 6.5.3. From statistical testing, the correlation between the entrainment coefficient $C_{l,int}$ and the downstand depth d_d was found to be very weak and insignificant. Simulations WOSP025-087-ND-BSP and WOSP025-087-D-BSP are subjected to almost identical convective heat flow rates in the approach flow ($\dot{Q}_{c,w} = 3492$ kW

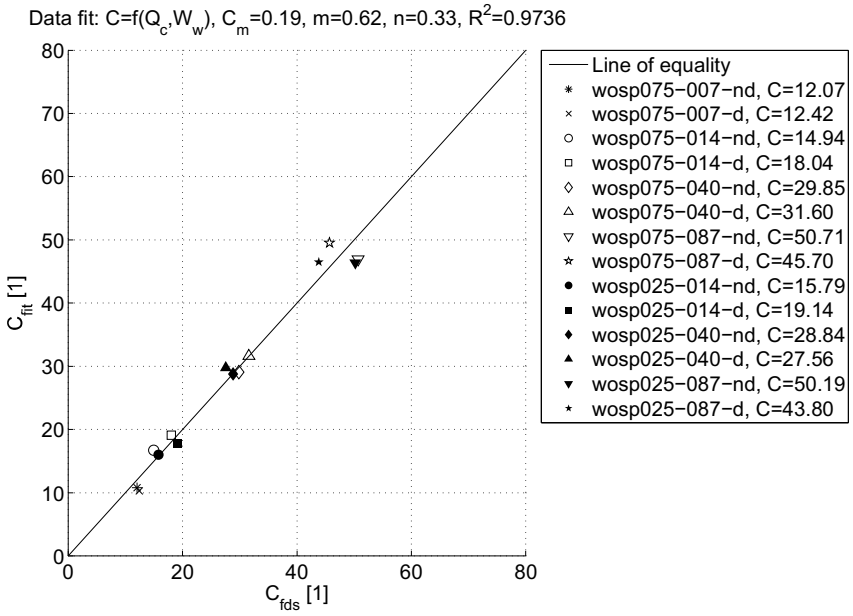

Figure 6.18 *Entrainment coefficients in the intermediate spill plume region $C_{l,int}$ using the simple spill plume method Eqn.* (6.6.5).

and $\dot{Q}_{c,w} = 3529$ kW) and are thus suitable for comparison with respect to the impact of the downstand depth, $d_d = 0.0$ m and $d_d = 1.0$ m respectively. Mass flow rates for the simulations are depicted in Figure 6.17, where a significant difference can be observed, thus not supporting the findings from the statistical analysis. Testing for a correlation between the mass flow rate $\dot{m}_l$ and the smoke layer depth d_w, implied a significant correlation, supported by Figure 6.17 as previously mentioned. From the research on the approach flow, see Section 5.5.3, the smoke layer depth, d_w was found to correlate with the downstand depth d_d, i.e. the entrainment coefficient C_l correlates indirectly with the downstand depth d_d by correlating with the smoke layer depth d_w. Based on this discussion a new entrainment coefficient $C_{l,mod}$ is proposed using the depth of the smoke layer d_w divided by the width of the compartment opening W_w, i.e. the smoke layer aspect ratio, as a variable in the spill plume method:

$$C_{l,mod} = C_m W_w^m \dot{Q}_{c,w}^{1/3} \left(\frac{d_w}{W_w}\right)^k \left| \begin{array}{rcl} C_m & = & 0.1060 \\ m & = & 1.2523 \\ k & = & 0.4151 \end{array} \right. \tag{6.6.6}$$

Testing the correlation, Eqn. (6.6.6), for the modified entrainment coefficient $C_{l,mod}$ against predicted coefficients $C_{l,fds}$ yields a correlation coefficient of $R^2 = 0.99$, see Figure 6.19. The modified correlation Eqn. (6.6.6) thus have a slightly better fit than the simple correlation Eqn. (6.6.5).

Looking at simulations WOSP075-087-ND-BSP and WOSP025-087-ND-BSP in Figure 6.17 subjected to convective heat flow rates $\dot{Q}_{c,w} = 3631$ kW and

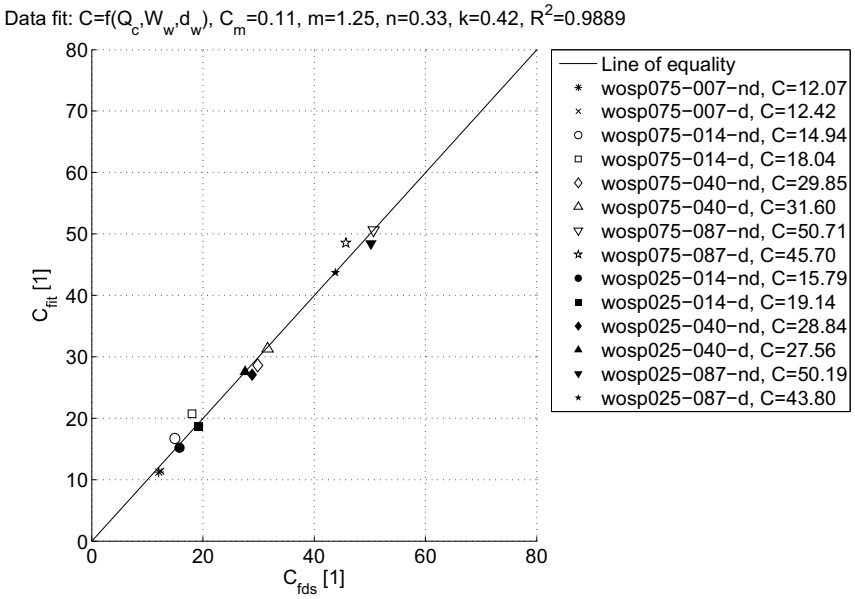

Figure 6.19 *Entrainment coefficients in the intermediate spill plume region* $C_{l,int}$ *using the modified spill plume method Eqn.* (6.6.6).

$\dot{Q}_{c,w} = 3492$ kW respectively, the distance from the fire base to the compartment opening D_{fb} can be seen not to have any significant effect on the spill plume mass flow rate $\dot{m}_l$, supported by a low correlation coefficient from the statistical analysis. In the derivation of the new spill plume method, see Eqn. (6.6.6), the entrainment coefficient C_l was found to correlate with the smoke layer depth d_w. In the derivation of the new method for the smoke layer depth in the approach flow opening d_w, see Section 5.5.3, a correlation between d_w and the distance to the fire base D_{fb} was observed. This implies that the gross mass flow rate in the spill plume $\dot{m}_l$ also correlates with the distance to the fire base D_{fb} through the source term for the approach flow mass flow rate $\dot{m}_w$ and hence the smoke layer depth d_w.

Combining the two proposed correlations for the entrainment coefficients, Eqns. (6.6.5) and (6.6.6), with the functional form of the spill plume method, see Eqn. (6.6.1c) yield two new methods for calculating the mass flow rate $\dot{m}_l$ in wide spill plumes, the simple method:

$$\dot{m}_{l,sim} = C_m W_w^m \dot{Q}_{c,w}^{1/3} z_l + \dot{m}_e \left| \begin{array}{rcl} C_m & = & 0.1936 \\ m & = & 0.6174 \end{array} \right. \tag{6.6.7}$$

and the modified method:

$$\dot{m}_{l,mod} = C_m W_w^m \dot{Q}_{c,w}^{1/3} \left(\frac{d_w}{W_w}\right)^k z_l + \dot{m}_e \left| \begin{array}{rcl} C_m & = & 0.1060 \\ m & = & 1.2523 \\ k & = & 0.4151 \end{array} \right. \tag{6.6.8}$$

where $\dot{m}_e$ is the mass flow rate at the elevation of the spill edge z_e calculated from Eqn. (6.6.3). Eqn. (6.6.8) provides the best correlation and should be used over

the simple method Eqn. (6.6.7). In deriving the spill edge mass flow rate $\dot{m}_e$, the user must have computed the approach flow mass flow rate $\dot{m}_w$ and smoke layer depth d_w, thus the application of the modified method is no more complicated than the simple method, since all variables are calculated beforehand. Other methods exist for calculating the mass flow rate at the spill edge $\dot{m}_e$, e.g. Morgan et al. (1999).

6.6.6 Application of Spill Plume Method

The application of the updated spill plume method is outlined below:

(1) - Compute approach flow mass flow rate $\dot{m}_w$ and smoke layer depth d_w - Use Eqns. (5.5.4), (5.5.2b) and (5.5.1) derived in Chapter 5.

(2) - Compute mass flow rate at the spill edge $\dot{m}_e$ - Use Eqn. (6.6.3) with the smoke layer depth d_w and approach flow mass flow rate $\dot{m}_w$ from the previous step.

(3) - Compute mass flow rate in spill plume $\dot{m}_l$ - Use Eqn. (6.6.8) with the spill edge mass flow rate $\dot{m}_e$ from the previous step.

Because of the inherently empirical nature of the derived method, any application must be within the limits of the present research and meet the underlying assumptions, see Section 6.6.2.

6.6.7 Testing Spill Plume Methods for Mass Flow Rate

The new methods for calculating the net mass flow rate in the spill plume, $\dot{m}_{l,net}$, are tested against CFD predictions and existing spill plume methods. The tested spill plume methods are presented in Section 2.10.4. For convenience the tested methods are listed in Eqns. (6.6.9)-(6.6.14) written on net mass flow rate form $\dot{m}_{l,net}$: Valkvist (2007) - simple:

$$\dot{m}_{l,net} = \dot{m}_{l,sim} - \dot{m}_e = 0.1936 W_w^{0.6174} \dot{Q}_{c,w}^{1/3} z_l \tag{6.6.9}$$

Valkvist (2007) - modified:

$$\dot{m}_{l,net} = \dot{m}_{l,mod} - \dot{m}_e = 0.1060 W_w^{1.2523} \dot{Q}_{c,w}^{1/3} \left(\frac{d_w}{W_w} \right)^{0.4151} z_l \tag{6.6.10}$$

Law (1995):

$$\dot{m}_{l,net} = \dot{m}_l - \dot{m}_e = 0.31 \dot{Q}_c^{1/3} W_w^{2/3} z_l \tag{6.6.11}$$

Thomas et al. (1998):

$$\dot{m}_{l,net} = \dot{m}_l - \dot{m}_e = 0.159 \dot{Q}_c^{1/3} W_w^{2/3} z_l + 0.09 \left(\frac{\dot{Q}_c}{W_w} \right)^{1/3} z_l \tag{6.6.12}$$

Harrison (2004):

$$\dot{m}_{l,net} = \dot{m}_l - \dot{m}_e = 0.20\dot{Q}_T^{1/3} W_w^{2/3} z_l + 0.0017\dot{Q}_T \tag{6.6.13}$$

McCartney (2006):

$$\dot{m}_{l,net} = \dot{m}_l - \dot{m}_e = 0.52\dot{Q}_T^{1/3} W_w^{1/5} z_l \tag{6.6.14}$$

The tests of the two new methods Eqns. (6.6.9) and (6.6.10) can be found in Figures 6.20(a) and 6.20(b) respectively. Correlation coefficients of $R^2 = 0.98$ and $R^2 = 0.99$ were achieved. Based on the correlation coefficients alone there is no clear reason for choosing one method over the other. However looking at the data for the regular compartment widths, i.e. $W_w \in \{7.2, 14.4\}$ m, it is clear that none of the methods predicts this range very well. The best performance is achieved by the modified method, under predicting the mass flow rate with up to 30% for high elevations and narrow openings $W_w = 7.2$. The methods are developed for wide spill plumes, hence the low performance in the range of narrow openings $W_w \sim 7.2$ must be accepted.

Looking at the performances of Eqn. (6.6.11) (Figure 6.21(a)), Eqn. (6.6.13) (Figure 6.22(a)) and Eqn. (6.6.14) (Figure 6.22(b)) they all perform poorly for wide openings, whereas performances are quite good within the range where the empirical relations were derived, i.e. $W_w \in \{7.2, 14.4\}$ m. This serves as a simple validation of the applied CFD model (FDS) in modeling spill plume mass flow rates $\dot{m}_l$. The confidence is highly supported by looking at the performance of Eqn. (6.6.14) in Figure 6.22(b), derived from full-scale experimental data, where the range $W_w \in \{7.2, 14.4\}$ m is predicted by the CFD model to be within 20% of the correlation Eqn. (6.6.14). This clearly implies that the CFD model predicts mass flow rates within experimental accuracy.

The spill plume methods in Eqn. (6.6.11) (Figure 6.21(a)), Eqn. (6.6.13) and Eqn. (6.6.12) (Figure 6.21(b)) all exhibit a high correlation coefficient of $R^2 \sim 0.98$ which indicates that the applied CFD model correlates very well with the data used in the development of the former spill plume methods. The coefficients in the engineering relations are clearly off, since the data does not align with the line of equality.

Eqn. (6.6.12) was derived for wide spill plumes, see Thomas et al. (1998), and from Figure 6.21(b) this is evident as the mass flow rates from wide openings $W_w \in \{40.0, 87.2\}$ m are in much better agreement compared to the other investigated methods.

Eqn. (6.6.14) in Figure 6.22(b) is found to perform very bad for large opening widths, i.e. $W_w \in \{40.0, 87.2\}$ m, attributed to the low scaling of the compartment width ($W_w^{0.20}$) relative to the other spill plume methods, i.e. only weakly dependent on the compartment opening. McCartney implied that the weak dependence on the compartment opening width was attributed to the spill plume transforming into an axisymmetric plume at high elevations, which is partly supported by Section 6.5.4 for narrow spill plumes, but not for the investigated wide spill plumes $W_w \in \{40.0, 87.2\}$.

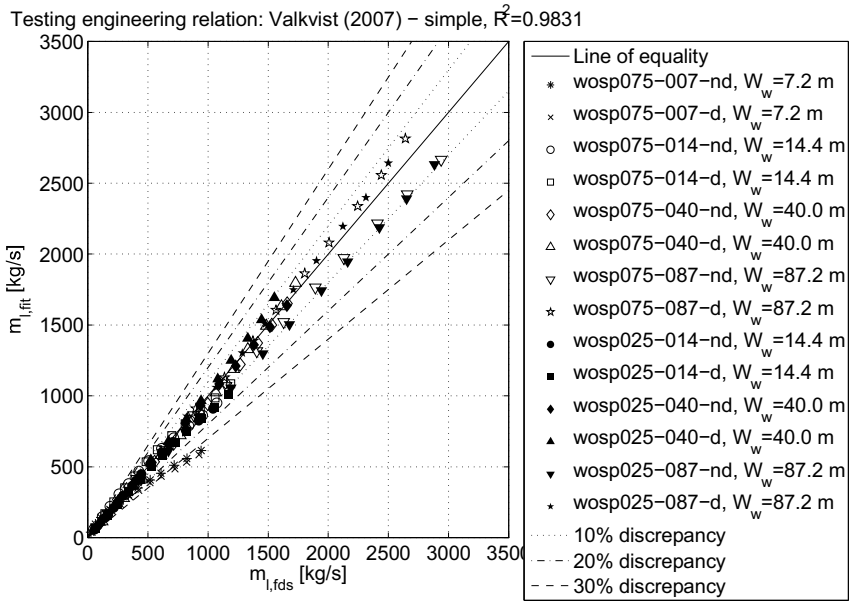

(a) Valkvist (2007), Eqn. (6.6.9) - simple.

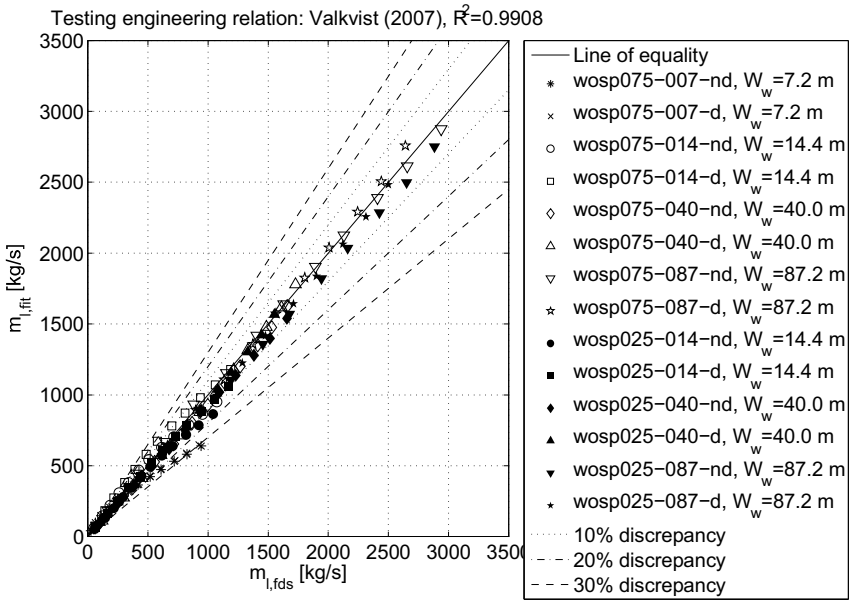

(b) Valkvist (2007), Eqn. (6.6.10) - modified.

Figure 6.20 *Testing spill plume methods against predicted net mass flow rates* $\dot{m}_{l,net}$.

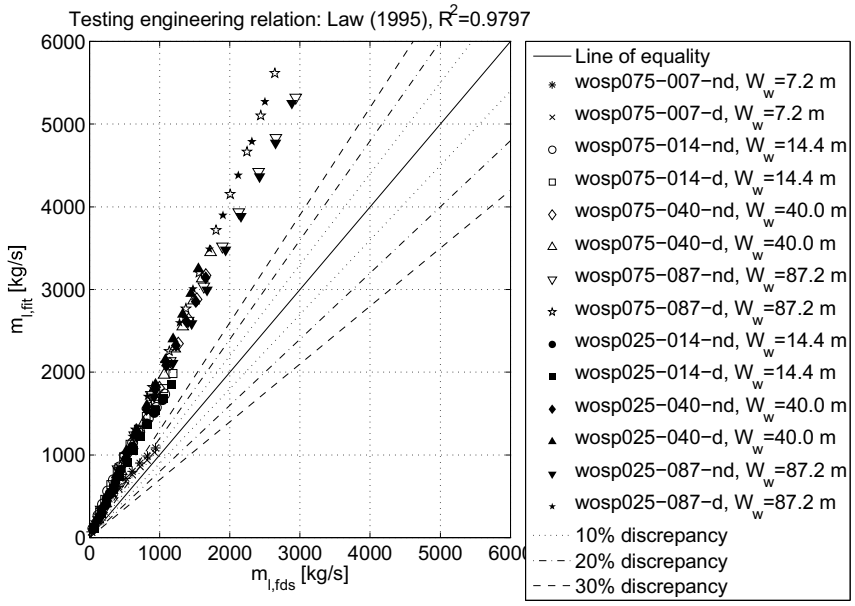

(a) Law (1986), Eqn. (6.6.11).

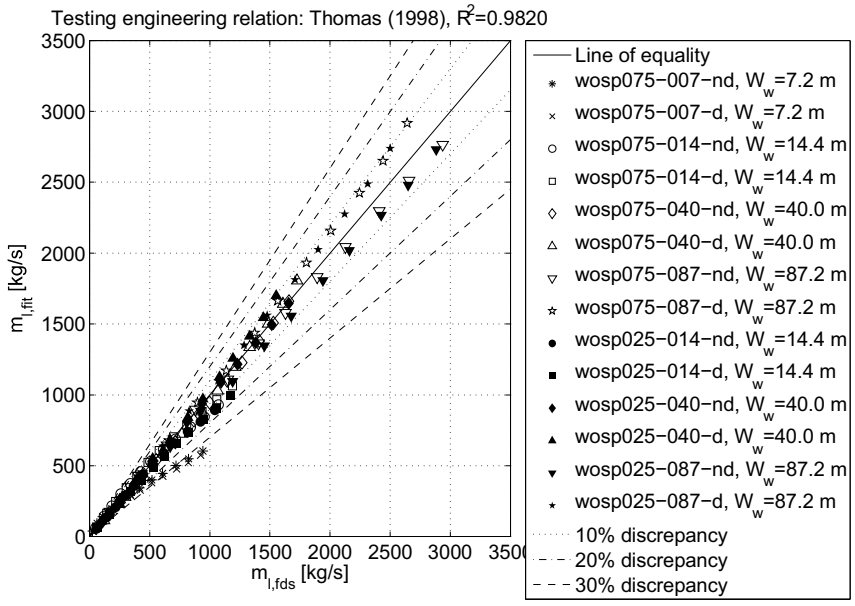

(b) Thomas et al.(1998), Eqn. (6.6.12).

Figure 6.21 *Testing spill plume methods against predicted net mass flow rates* $\dot{m}_{l,net}$.

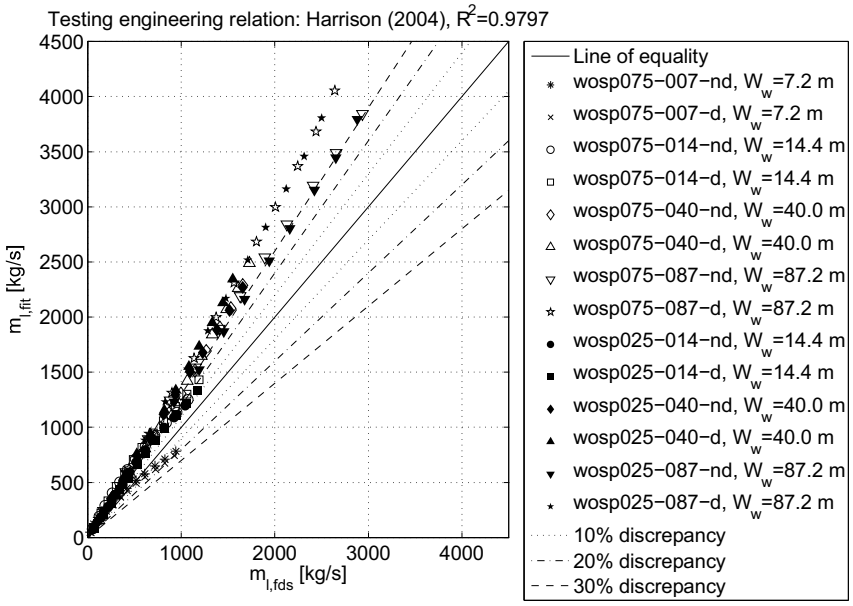

(a) Harrison (2004), Eqn. (6.6.13).

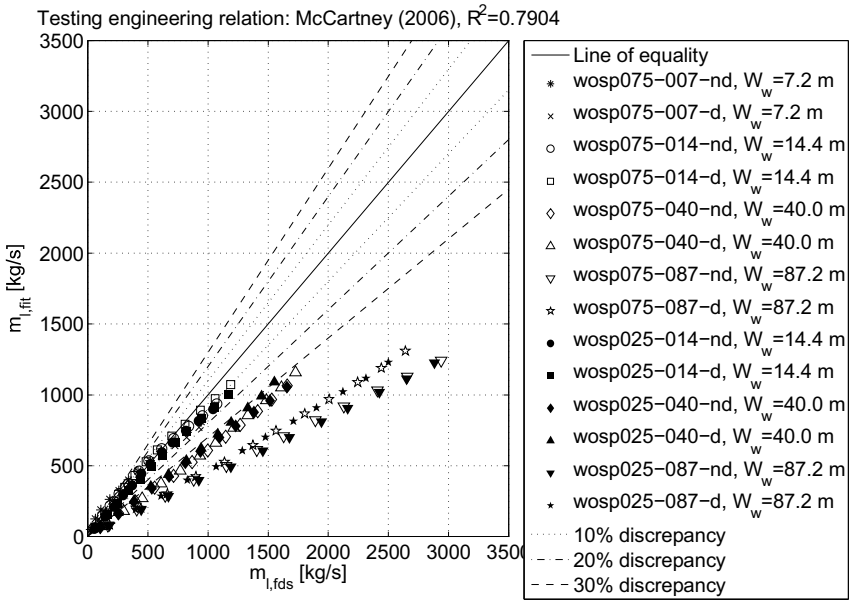

(b) McCartney (2006), Eqn. (6.6.14).

Figure 6.22 *Testing spill plume methods against predicted net mass flow rates* $\dot{m}_{l,net}$.

6.7 Conclusion

A full-scale CFD modeling study was conducted to develop a new method for calculating the mass flow rate in wide spill plumes. A limited CFD modeling program consisting of 14 full-scale simulations where carried out, addressing convective heat release rates $\dot{Q}_{c,w}$ ranging from 3492 kW to 6886 kW, opening widths W_w from 7.2 m to 87.2 m, fire sources located 7.8 and 22.4 m from the compartment opening D_{fb} and the impact of a downstand in the compartment opening d_d. The fire compartment height H_{fb} was fixed at 5 m in all simulations. Only spill plumes rising immediately from the compartment opening were considered, i.e. no channeled flows or flows under a projecting balcony are considered.

Two new methods were proposed for calculating the mass flow rate in wide spill plumes $\dot{m}_l$. A simple method adopting the functional form of most existing spill plume methods depending on rising height above the spill edge z_l, mass flow rate at the elevation of the spill edge $\dot{m}_e$, compartment opening width W_w and convective heat release rate $\dot{Q}_{c,w}$. A modified method applying the former functional form and additionally the smoke layer depth d_w in the compartment opening smoke layer ratio d_w/W_w as a variable in the correlation. Both methods are based on a linear dependence on the rising height from the spill edge z_l. For the simple method:

$$\dot{m}_{l,sim} = C_m W_w^m \dot{Q}_{c,w}^{1/3} z_l + \dot{m}_e \left| \begin{array}{rcl} C_m & = & 0.1936 \\ m & = & 0.6174 \end{array} \right. \tag{6.7.1}$$

And the modified method:

$$\dot{m}_{l,mod} = C_m W_w^m \dot{Q}_{c,w}^{1/3} \left(\frac{d_w}{W_w}\right)^k z_l + \dot{m}_e \left| \begin{array}{rcl} C_m & = & 0.1060 \\ m & = & 1.2523 \\ k & = & 0.4151 \end{array} \right. \tag{6.7.2}$$

The proposed methods were validated against predicted net mass flow rates in the spill plume $\dot{m}_{l,net}$ from the full-scale CFD modeling program, and correlation coefficients of R^2=0.98 and R^2=0.99 were achieved for the simple and modified methods respectively.

The methods for the mass flow rate require the mass flow rate at the elevation of the spill edge $\dot{m}_e$ as a source term. A simple correlation for the entrainment in the rotation region was proposed to calculate the mass flow rate at the spill edge $\dot{m}_e$ from the approach flow mass flow rate $\dot{m}_w$, smoke layer depth d_w and compartment opening width W_w:

$$\dot{m}_e = C_m \dot{m}_w^m W_w^n d_w^k \left| \begin{array}{rcl} C_m & = & 2.2628 \\ m & = & 0.5780 \\ n & = & 0.4923 \\ k & = & 0.2426 \end{array} \right. \tag{6.7.3}$$

The input parameters for the approach flow mass flow rate $\dot{m}_w$ and the smoke layer depth d_w required to calculate the mass flow rate at the spill edge $\dot{m}_e$ can be calculated using the principles presented in Chapter 5.

A limited study of the collapse of spill plumes was conducted. The study implied that spill plumes emanating from compartment openings of regular widths $W_w \leq \{7.2, 14.4\}$ m will transform into an axisymmetric plume at high elevations. Wide spill plumes are expected to exhibit the same behavior, however at much higher elevations, where the integrity of the spill plume is questionable because of the low buoyancy and expected stagnation.

6.8 Future Research

The rotation region is highly dependent on the momentum in the approach flow, a fact that is not well implemented in the current spill plume methods. Almost all the present methods use a linear dependence from the spill edge elevation z_e to describe the mass flow rate $\dot{m}_l$ at higher elevations z_l, inherently assuming that the flow is fully rotated (vertically aligned) as it reaches the elevation of the spill edge. This is not true and can be seen from the non-linear profile shape in the lower spill plume region, see e.g. Figure 6.13. Entrainment rate and extents of the rotation region should be investigated further.

The biggest shortcoming of the current research and all other derived spill plume methods are the lack of full-scale (or near full-scale) experimental data to support the predictions. No full-scale experiments address rising heights $z_l > 4$ m, see McCartney (2006), which is very close to the vertical extent of the rotation region. The fire research society is highly encouraged to support the development of experimental data for mass flow rates in order to validate the existing spill plume methods and CFD tools at rising heights where they are actually applied in the fire safety design of buildings.

The collapse of the spill plume was only investigated based on the numerical filtering of the spill plume. An experimental study must be conducted to provide information about the stagnation of high-elevation buoyant plumes. The present study implied that the spill plume may transform into an axisymmetric plume, but no experimental data for high-elevation spill plumes exist to support the findings.

No high-bay facilities that could accommodate a close to full-scale spill plume setup have been available previously. Carleton University, Ottawa (ON), and National Research Council Canada (NRCC) have recently begun to operate a ten-story full-scale atrium facility located in Almonte (ON) in connection with the existing NRCC test facility. The facility allows for the design of experimental high-elevation atrium setups, if not at full-scale then at a 1/2 scale. Studies of buoyant plumes at high elevations can be conducted at the facility to address the aforementioned problems with lacking validation data and spill plume collapse.

Figure 6.23 *Photo taken from the base of the ten-story atrium facility in Almonte (ON, Canada) by the author during an internship at NRCC, Fire Research Program in 2005.*

Chapter 7

Modeling Buoyancy Driven Vent Flows

7.1 Introduction

Atrium fire safety designs often encompass a smoke management system comprising e.g. smoke and heat exhaust ventilators (SHEVs) and inlets for make-up air. SHEVs can be mechanical, i.e. smoke is exhausted by a fan (centrifugal or axial), or driven by buoyancy. In Denmark smoke management systems must provide tenable conditions at least throughout the time required for safe egress and generally ensure safe fire fighting conditions, i.e. prevent flash-over and increase visibility. The exhaust capacity of the system is determined from the amount of smoke produced by a design fire in the building. The smoke production is predicted by fire safety design methods, generally being simple engineering relations, numerical zone models or computational fluid dynamics (CFD). Focus in the current research is on modeling buoyancy driven SHEVs using computational fluid dynamics.

In CFD modeling of smoke movement in a building, vents (mechanical or buoyancy driven) are generally described using simple boundary conditions. To describe the flow passing through the vent correctly, detailed information is required about the flow field (velocities, turbulence, pressure and densities). A common approach to model mechanical exhaust fans is to simply describe an exhaust volume/mass flux or flow rate on the boundary of the computational domain. Detailed information about the turbulence is often not available and is hence neglected in the description of the exhaust boundary condition, under the assumption that the impact is negligible compared to the over all smoke production and the associated uncertainties.

To reduce computational costs buoyancy driven exhaust vents are often modeled as simple passive vents with a homogeneous *Neumann* boundary condition for the velocity flowing out and subjected to ambient pressures and temperatures, see a description of the boundary condition in Section 2.4.7. This approach ignores the flow field outside the vent, because it is simply not included in the computational domain, and inherently ignores the contraction of the flow as it leaves the

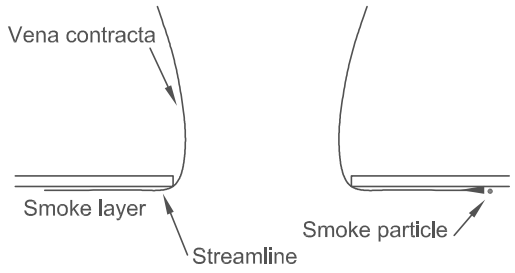

Figure 7.1 *Example of the formation of a vena contracta outside the buoyancy driven exhaust vent.*

vent. The contraction reduces the effective vent area by the formation of a *vena contracta*, see example in Figure 7.1. The result is a reduced performance and capacity of the real vent compared to the modeled vent, i.e. a non-conservative design in contradiction with best-practice in fire safety engineering.

7.2 Orifice Flow Formulas

The present research is focused on one-way flows, and hence far from lazy flooding flow, where the direction of the flow passing through the vent alternates. Two setups are considered, the horizontal and vertical vents respectively.

The velocity controlling an incompressible flow through a vent is governed by *Bernoulli's principle*:

$$\underbrace{\frac{1}{2}\rho_p U_p^2}_{p_d} + \underbrace{\rho_p \mathbf{g} h_p}_{p_s} + p_p = const. \tag{7.2.1}$$

where ρ_p is the density $[kg/m^3]$, U_p is the mean velocity $[m/s]$, $\mathbf{g}$ is the gravitational acceleration $[m/s^2]$, h_p is the elevation $[m]$, p_p is the pressure and index p designates the position in the flow. Dynamic and static pressures are designated by p_d and p_s $[Pa]$ respectively.

Applying the nomenclature for the horizontal vent, see Figure 7.2, the velocity W_a at the vena contracta can be written:

$$\frac{1}{2}\rho_a W_a^2 - \frac{1}{2}\rho_i W_i^2 = \rho_i g h_i - \rho_a g h_a + p_i - p_a \tag{7.2.2a}$$

$$\frac{1}{2}\rho_a W_a^2 = -g\left(\rho_i - \rho_a\right)\left(h_a - h_i\right) + \left(p_i - p_a\right) \tag{7.2.2b}$$

$$W_a = \left[2\frac{g\Delta\rho h_a + \Delta p}{\rho_a}\right]^{1/2} \tag{7.2.2c}$$

where the smoke layer velocity is assumed at rest $U_i = 0$ m/s and $h_a > h_i$. Assuming that h_i=0, the buoyancy force acts over the distance from the top

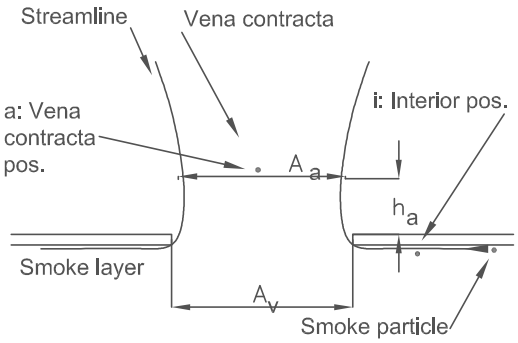

Figure 7.2 *Nomenclature applied for the horizontal vent.*

of the vent to the vena contracta h_a. The buoyancy force acts in the vertical direction along the stream line. Due to lack of information about the stream lines, a common approach is to consider the distance from the top of the vent to the vena contracta (i.e. $h_a - h_i$) as the distance over which the buoyancy force impacts the contraction of the flow. The pressure difference is $\Delta p = p_i - p_a$ and the density difference is $\Delta\rho = \rho_a - \rho_i$.

Mass flow rates through the vent $\dot{m}_a$ are derived by multiplying the vent velocity W_a, Eqn. (7.2.2c), by the flow density ρ_a and the area of the vena contracta A_a:

$$\dot{m}_a = \rho_a W_a A_a \tag{7.2.3a}$$

$$= \left[2\rho_a \left(g\Delta\rho h_a + \Delta p\right)\right]^{1/2} A_a \tag{7.2.3b}$$

The area of the vena contracta A_a $[m^2]$ is not known, and in correspondence with normal procedure the area is described by the geometric area of the vent A_v $[m^2]$ corrected by a coefficient of contraction C_v [1]:

$$C_v = \frac{A_a}{A_v} \tag{7.2.4}$$

The *Bernoulli equation*, Eqn. (7.2.1), is based on an ideal fluid flow, e.g. inviscid, incompressible and ignoring boundary layer effects, which must be corrected by a coefficient of viscosity C_μ. The correction coefficients C_v and C_μ are often collected in the coefficient of discharge:

$$C_d = C_v C_\mu \tag{7.2.5}$$

Most vents in fire safety engineering are considered orifices (as opposed to nozzles) with $C_\mu \sim 0.98$, see Emmons (1997), i.e. $C_d \rightarrow C_v$ is a commonly employed

assumption. Combining Eqns. (7.2.4), (7.2.5) and (7.2.3b), neglecting entrainment and density changes in the outflow over the height h_a yield the mass flow rate for the horizontal vent $\dot{m}_{v,h}$:

$$\dot{m}_{v,h} = C_{d,h} \left[2\rho_v \left(g\Delta\rho h_a + \Delta p\right)\right]^{1/2} A_v \tag{7.2.6}$$

where $C_{d,h}$ is the coefficient of discharge for the horizontal vent.

In the case of the vertical vent, see Figure 7.3, the component of the gravitational acceleration $\mathbf{g}$ normal to the vent and in the direction of the exhaust flow is zero, simplifying the expression for the velocity in the vent. Because of gravity acting perpendicular to the vent surface, interior and exterior pressures decrease with height requiring a surface integration of the pressure field to derive the pressure difference Δp:

$$\Delta p(x,y) = \Delta p_b + \int_0^y \Delta\rho(x,y) g dy \tag{7.2.7}$$

where Δp_b is the pressure increase at the base of the vent. Hence applying the zero hydrostatic component to rewrite Eqn. (7.2.6) and including the pressure, Eqn. (7.2.7), yield the mass flow rate for the vertical vent $\dot{m}_{v,v}$:

$$d\dot{m}_{v,v} = C_{d,v} \left[2\rho_v(x,y)\Delta p(x,y)\right]^{1/2} dA \tag{7.2.8a}$$

$$\dot{m}_{v,v} = C_{d,v} \int_{A_v} \left[2\rho_v(x,y)\Delta p(x,y)\right]^{1/2} dA \tag{7.2.8b}$$

where $C_{d,v}$ is the coefficient of discharge for the vertical vent.

Applying e.g. CFD modeling, predicted velocity, density and pressure fields can be employed in the computation of the coefficient of discharge for horizontal $C_{d,h}$, Eqn. (7.2.9a), and vertical $C_{d,v}$, Eqn. (7.2.9b), vents respectively:

$$C_{d,h} = \frac{\dot{m}_{v,h}}{\left[2\rho_v \left(g\Delta\rho h_a + \Delta p\right)\right]^{1/2} A_v} \tag{7.2.9a}$$

$$C_{d,v} = \frac{\dot{m}_{v,v}}{\int_{A_v} \left[2\rho_v(x,y)\Delta p(x,y)\right]^{1/2} dA} \tag{7.2.9b}$$

The European Standard on smoke and heat exhaust ventilators EN12101-2 (2003) outlines a test method for experimentally determining the coefficient of discharge C_d of a vent. In the test method the buoyancy term in Eqn. (7.2.9a) is ignored leading to the simpler Eqns. (7.2.10a) and (7.2.10b) for the horizontal and vertical vent respectively:

$$C^*_{d,h} = \frac{\dot{m}_{v,h}}{\left[2\rho_v \Delta p\right]^{1/2} A_v} \tag{7.2.10a}$$

$$C^*_{d,v} = \frac{\dot{m}_{v,v}}{\int_{A_v} \left[2\rho_v(x,y)\Delta p(x,y)\right]^{1/2} dA} \tag{7.2.10b}$$

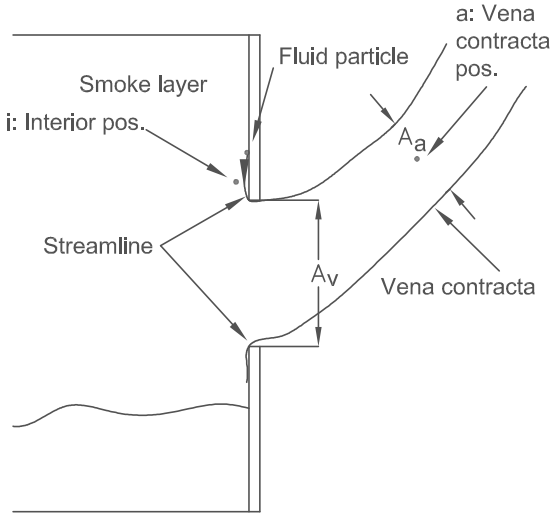

Figure 7.3 *Nomenclature applied for the vertical vent.*

7.3 Froude Number

In assessing the performance of the buoyancy driven vents, the Froude number Fr is very convenient:

$$Fr = \frac{W}{(gd_h)^{1/2}} \tag{7.3.1}$$

where W is the mean velocity of the flow in the vent $[m/s]$, g is the gravitational acceleration $[m/s^2]$ and d_h is the hydraulic diameter $[m]$. The hydraulic diameter d_h for a rectangular vent is defined as:

$$d_h = 2\frac{H_v W_v}{H_v + W_v} \tag{7.3.2}$$

where H_v and W_v is the geometrical height and width of the vent $[m]$ respectively.

The Froude number is the ratio of inertial to gravitational forces. It's convenience in plotting the performance of vent flows is based on the ratio of the velocity (a measure of the mass flow rate through the vent) and the hydraulic diameter (a measure of the potential capacity of the vent). This addresses the fact that an increased mass flow rate through a vent, can be achieved by increasing the temperature (increasing the buoyancy) at a fixed vent area, or increasing the vent area at a fixed temperature.

7.4 Present Research

The present research objective is to determine a correlation between the exhaust capacity predicted using a CFD model with simple passive vents as boundary conditions and the capacity including the vena contracta outside the exhaust vent in the model.

7.5 Full-scale Model Studies

7.5.1 Modeling Objective

The objective of the present full-scale numerical study is to measure temperature and velocity profiles in the vent opening for use in deriving mass flow rates, $\dot{m}_v$, and discharge coefficients, C_d, in the opening. Additional point recordings in the computational domain are conducted to allow for predictions of the discharge coefficients for the considered vent configurations.

7.5.2 Modeling Parameters

The present numerical modeling program investigates mass flow rates through vents applying boundary conditions of simple passive type and vents where the complete outflow is modeled, thus taking the contraction outside the vent into consideration. Mass flow rates are derived as a function of vent area A_v, aspect ratio $AR_v = H_v/W_v$ and convective heat release rate $\dot{Q}_c$.

The modeling parameters are:

Convective heat release rate $\dot{Q}_c$ - The convective heat release rate is not a dependent variable, but only serves to raise the temperature above ambient in the smoke layer Θ to provide a buoyant flow.

Vent area A_v - The vent area controls the mass flux through the vent and is varied in the range $A_v \in [1.0 : 5.6]$ m^2 and $A_v \in [1.0 : 3.2]$ m^2 for the horizontal and vertical vents respectively.

Vent aspect ratio AR_v - The aspect ratio $AR_v = H_v/W_v$ of the vent controls the capacity for narrow openings, i.e. a very narrow opening having a large area, is not considered as effective as a wider but shorter vent having the exact same area. This can be explained by the fact that contraction is controlled by the shortest geometrical length scale in the flow. Vents with aspect ratios in the range $AR_v \in [0.4 : 1.0]$ and $AR_v \in [0.3 : 1.0]$ for the horizontal and vertical vents respectively are investigated.

Vent width and heights W_v and H_v - Geometrical dimensions obviously controls the geometric vent area A_v. Vent widths $W_v \in [0.6 : 2.8]$ m and heights $H_v \in [1.0 : 2.0]$ m are investigated in the present research.

Computational domain - Two configurations are determined, one employing a simple passive vent, see Section 2.4.7, as a model for the buoyancy driven

vent, and another model taking the exterior flow and the vena contracta into consideration.

Vent position - The discharge coefficients of horizontal and vertical vents differ ($C_{d,h} \sim 0.61$ and $C_{d,v} \sim 0.68$, see e.g. Emmons (1997)), hence the two configurations must be investigated separately.

Fixed parameters also expected to impact the approach flow mass flow rate, but not addressed explicitly in this study, are termed secondary parameters and include:

Compartment dimensions - Compartment dimensions are fixed throughout the modeling program. Any change is considered irrelevant to the outcome of the test, because the research only addresses local vent flows, e.g. mass flow rate through the vent. In both investigated configurations the foot print of the compartment is roughly 16 m^2 with a compartment height of 2.4 m and 4.0 m for the horizontal and vertical configurations respectively.

Smoke layer depth d_s - The depth of the smoke layer inherently impacts the mass flow rate through the vent. A shallow smoke layer is prone to exhibit a "plughole-like" behavior. This is not to be confused with the real plughole effect associated with mechanical exhaust vents, where low buoyant ambient air from the lower thermal zone is exhausted, significantly decreasing the exhaust mass flow rate of hot smoke gases. The "plughole-like" behavior in the former case, refers to the fact that a shallow smoke layer will only exploit the edge/circumference of the vent, leaving a "hole" in the center of the vent with a low mass flux (approaching zero) or maybe subjected to lazy flooding conditions (i.e. low buoyant flow with alternating direction). In the present study a uniform smoke layer is formed below the vent.

Heat transfer in fire compartment - All solid boundaries are adiabatic. The thermal properties of the compartment are irrelevant since the dependent variables are restricted to the mass flow rate, pressure and density differences, and geometrical parameters in the vent.

7.6 Modeling Program

7.6.1 Simulations Breakdown

A total of 216 simulations were carried out in the full-scale vent flow program. A list of simulations is prepared in Table 7.1 with applied convective heat release rate $\dot{Q}_c$ $[kW]$, ambient temperature T_∞ $[^\circ C]$, vent area A_v $[m^2]$, vent height H_v $[m]$, vent width W_v $[m]$, hydraulic diameter d_h $[m]$, aspect ratio AR_v [1] and averaging time interval $\bar{t}$ [s]. The applied configuration (Conf.) refers to the computational domain using a simple passive vent (designated *Pass.*) or the full vent flow including the vena contracta (designated *Full*).

Each horizontal configuration was subjected to 7 different convective heat release rates, $\dot{Q}_{c,hor}$:

$$\dot{Q}_{c,hor} = \{55, 110, 275, 550, 1100, 1650, 2200\}\,\text{kW} \tag{7.6.1}$$

whereas the vertical vents were only subjected to a range of 6 convective heat release rates, $\dot{Q}_{c,ver}$:

$$\dot{Q}_{c,ver} = \{90, 225, 450, 900, 1350, 1800\}\,\text{kW} \tag{7.6.2}$$

Simulation ID	**Pos.**	**Conf.**	$\dot{\mathbf{Q}}_\mathbf{c}$	$\mathbf{A_v}$	$\mathbf{H_v}$	$\mathbf{W_v}$	$\mathbf{d_h}$	$\mathbf{AR_v}$	$\bar{\mathbf{t}}$
DC-HOR-10-10-F	Hori.	Full	Eqn. (7.6.1)	1.0	1.0	1.0	1.0	1.0	30
DC-HOR-10-12-F	Hori.	Full	Eqn. (7.6.1)	1.2	1.0	1.2	1.1	0.8	30
DC-HOR-10-14-F	Hori.	Full	Eqn. (7.6.1)	1.4	1.0	1.4	1.2	0.7	30
DC-HOR-10-16-F	Hori.	Full	Eqn. (7.6.1)	1.6	1.0	1.6	1.2	0.6	30
DC-HOR-10-18-F	Hori.	Full	Eqn. (7.6.1)	1.8	1.0	1.8	1.3	0.6	30
DC-HOR-10-20-F	Hori.	Full	Eqn. (7.6.1)	2.0	1.0	2.0	1.3	0.5	30
DC-HOR-10-28-F	Hori.	Full	Eqn. (7.6.1)	2.8	1.0	2.8	1.5	0.4	30
DC-HOR-20-20-F	Hori.	Full	Eqn. (7.6.1)	4.0	2.0	2.0	2.0	1.0	30
DC-HOR-20-28-F	Hori.	Full	Eqn. (7.6.1)	5.6	2.0	2.8	2.3	1.4	30
DC-HOR-14-28-F	Hori.	Full	Eqn. (7.6.1)	3.9	1.4	2.8	1.9	0.5	30
DC-HOR-10-10-P	Hori.	Pass.	Eqn. (7.6.1)	1.0	1.0	1.0	1.0	1.0	30
DC-HOR-10-12-P	Hori.	Pass.	Eqn. (7.6.1)	1.2	1.0	1.2	1.1	0.8	30
DC-HOR-10-14-P	Hori.	Pass.	Eqn. (7.6.1)	1.4	1.0	1.4	1.2	0.7	30
DC-HOR-10-16-P	Hori.	Pass.	Eqn. (7.6.1)	1.6	1.0	1.6	1.2	0.6	30
DC-HOR-10-18-P	Hori.	Pass.	Eqn. (7.6.1)	1.8	1.0	1.8	1.3	0.6	30
DC-HOR-10-20-P	Hori.	Pass.	Eqn. (7.6.1)	2.0	1.0	2.0	1.3	0.5	30
DC-HOR-10-28-P	Hori.	Pass.	Eqn. (7.6.1)	2.8	1.0	2.8	1.5	0.4	30
DC-HOR-20-20-P	Hori.	Pass.	Eqn. (7.6.1)	4.0	2.0	2.0	2.0	1.0	30
DC-HOR-20-28-P	Hori.	Pass.	Eqn. (7.6.1)	5.6	2.0	2.8	2.3	1.4	30
DC-HOR-14-28-P	Hori.	Pass.	Eqn. (7.6.1)	3.9	1.4	2.8	1.9	0.5	30
DC-VER-10-10-F	Vert.	Full	Eqn. (7.6.2)	1.0	1.0	1.0	1.0	1.0	30
DC-VER-10-18-F	Vert.	Full	Eqn. (7.6.2)	1.8	1.8	1.0	1.3	1.8	30
DC-VER-12-06-F	Vert.	Full	Eqn. (7.6.2)	0.7	0.6	1.2	0.8	0.5	30
DC-VER-18-06-F	Vert.	Full	Eqn. (7.6.2)	1.1	0.6	1.8	0.9	0.3	30
DC-VER-18-10-F	Vert.	Full	Eqn. (7.6.2)	1.8	1.0	1.8	1.3	0.6	30
DC-VER-18-18-F	Vert.	Full	Eqn. (7.6.2)	3.2	1.8	1.8	1.8	1.0	30
DC-VER-10-10-P	Vert.	Pass.	Eqn. (7.6.2)	1.0	1.0	1.0	1.0	1.0	30
DC-VER-10-18-P	Vert.	Pass.	Eqn. (7.6.2)	1.8	1.8	1.0	1.3	1.8	30
DC-VER-12-06-P	Vert.	Pass.	Eqn. (7.6.2)	0.7	0.6	1.2	0.8	0.5	30
DC-VER-18-06-P	Vert.	Pass.	Eqn. (7.6.2)	1.1	0.6	1.8	0.9	0.3	30
DC-VER-18-10-P	Vert.	Pass.	Eqn. (7.6.2)	1.8	1.0	1.8	1.3	0.6	30
DC-VER-18-18-P	Vert.	Pass.	Eqn. (7.6.2)	3.2	1.8	1.8	1.8	1.0	30

Table 7.1 *Full-scale vent flow modeling: List of simulations.*

Designation	Line type	BC type	FDS type
Outflow	Dashed	Passive vent	*OPEN*
Floor	Dashed	Passive vent	*OPEN*
Walls	Solid	Adiabatic/partial slip	*ADIABATIC*
Ceiling	Solid	Adiabatic/partial slip	*ADIABATIC*
Heat base	Solid	Steady convective heat flux	*HEAT_FLUX*
Vent (only DC-...-P)	Solid	Passive vent	*OPEN*

Table 7.2 *Boundary conditions according to designations in Figures 7.4 and 7.5.*

7.6.2 Description of CFD Model

Modeling Procedure

The CFD model *Fire Dynamics Simulator ver. 4.06*, described in Section 2.4, was applied in the modeling of the full-scale vent flow.

Convective heat release rates are increased linearly to the prescribed test values according to Table 7.1 over a time period of 1 s. Computations are run until at least 60 s of steady state has been achieved. Quantities of temperature, T, and velocities, $\mathbf{u}$, are recorded at positions listed in Table 7.5. Additional point recordings of temperature, T, and perturbation pressure, $\tilde{p}$, are conducted at positions also listed in Table 7.5. Measured quantities are averaged over the steady state time period $\overline{t}$ (at least 30 s) with the conversion program *fds2ascii* and saved for external data processing.

Computational Grid and Boundary Conditions

Sketches of the computational grids along with geometrical dimensions applied in the CFD model of the full-scale vent flow setups are shown in Figures 7.4 and 7.5. The heat source is located flush against the base of the compartment.

The computational domain outside the vent applied in modeling the complete outflow region (full vent including the vena contracta - DC-XXX-XX-XX-F) is reduced in the models applying the simple boundary condition (passive vent - DC-XXX-XX-XX-P) in accordance with Figures 7.6(a) and 7.6(b) for the horizontal and vertical vent configurations respectively.

Grid spacings are determined from a simple grid convergence study of the vent mass flow rate $\dot{m}_v$. The vent mass flow rate $\dot{m}_v$ was chosen for the grid convergence study because of it's universal information about the outflow, taking the exhaust capacity and contraction into consideration. A series of 4 simulations were conducted for a horizontal vent setup with a geometrical vent diameter $A_v = 1.0$ m^2 and using a fixed convective heat release rate $\dot{Q}_c = 1100$ kW. Grid spacings in the range $\Delta x \in \{25, 50, 100, 200\}$ mm were applied, see Table 7.3. Predicted mass flow rates $\dot{m}_v$ are plotted against grid resolution $n^* = W_v/\Delta x$ in Figure 7.7.

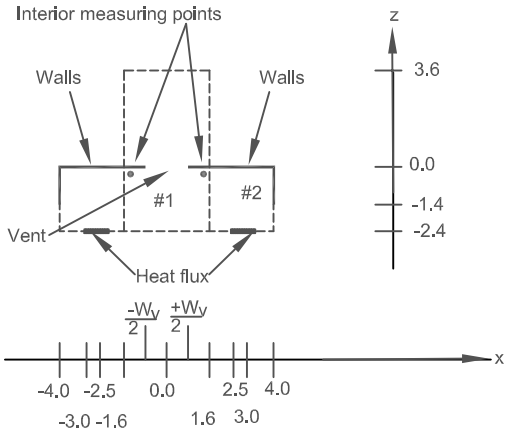

(a) Vertical section.

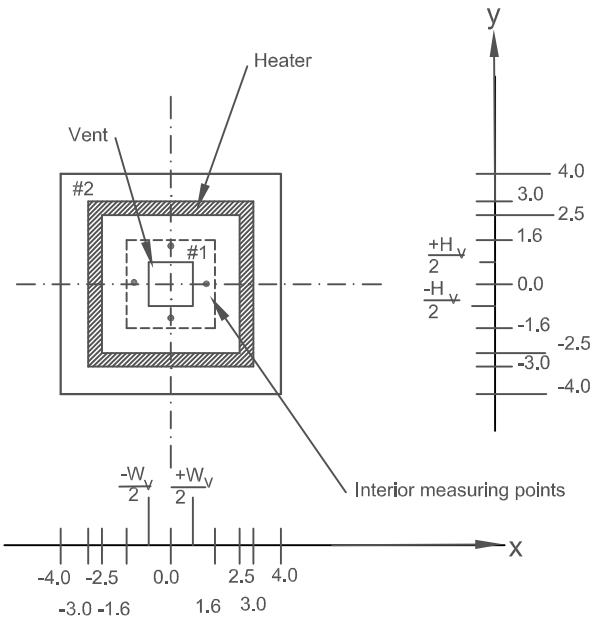

(b) Horizontal section.

Figure 7.4 *CFD model: Horizontal vent, full outflow.*

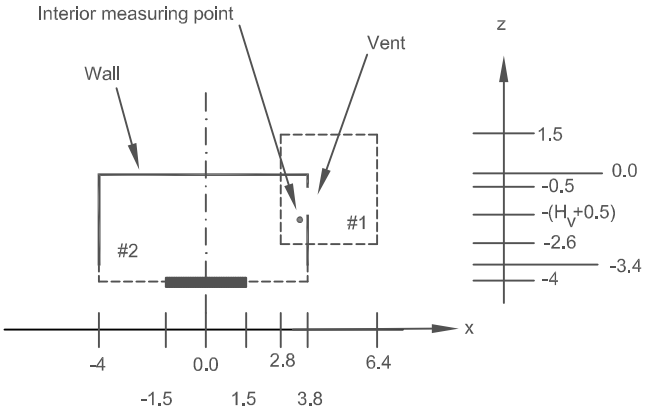

(a) Vertical section.

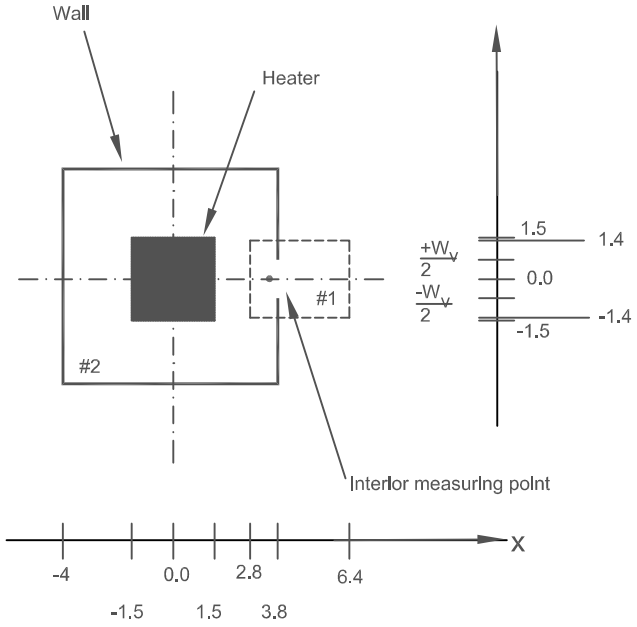

(b) Horizontal section.

Figure 7.5 *CFD model: Vertical vent, full outflow.*

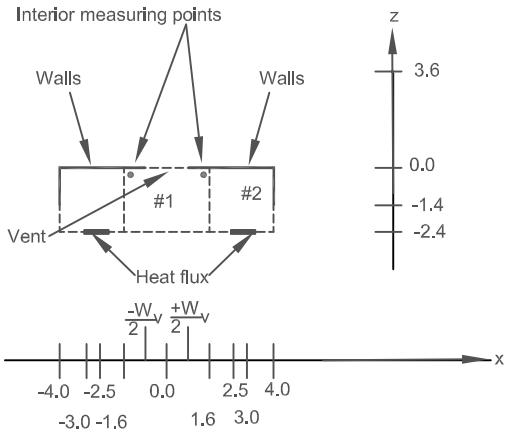

(a) Horizontal vent: Vertical section, see Figure 7.4(b) for top view.

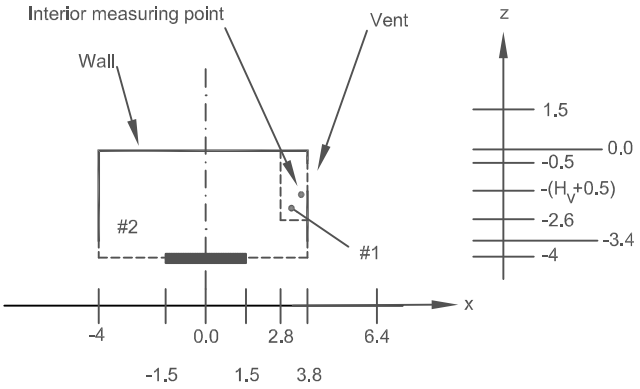

(b) Vertical vent: Vertical section, see Figure 7.5(b) for top view.

Figure 7.6 *CFD model: Horizontal and vertical vents, simple passive boundary condition applied in modeling the vent.*

Simulation ID	Pos.	Conf.	$\dot{Q}_c$	A_v	H_v	W_v	d_h	Δx	$\bar{t}$
DC-HOR-10-10-GCI-0025	Hori.	Full	1100	1.0	1.0	1.0	1.0	25	30
DC-HOR-10-10-GCI-0050	Hori.	Full	1100	1.0	1.0	1.0	1.0	50	30
DC-HOR-10-10-GCI-0100	Hori.	Full	1100	1.0	1.0	1.0	1.0	100	30
DC-HOR-10-10-GCI-0200	Hori.	Full	1100	1.0	1.0	1.0	1.0	200	30

Table 7.3 *Full-scale vent flow modeling: Grid convergence study.*

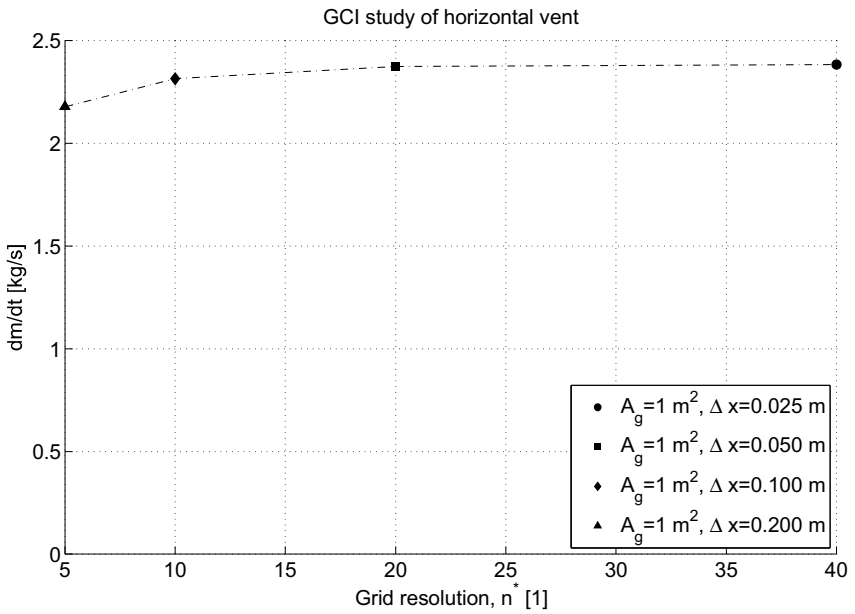

Figure 7.7 *Grid convergence study of horizontal vent flow.*

Based on the grid convergence study depicted in Figure 7.7 a grid size of $\Delta x = 50$ mm (grid # 1) was chosen for the vent flow and $\Delta x = 200$ mm for adjacent grids (grid # 2). All grids are rectilinear and grid spacings are provided in Table 7.4 applying the notation $\Delta \mathbf{x} = \{\Delta x, \Delta y, \Delta z\}$. A multiple of the largest grid size, i.e. $\Delta \mathbf{x} = 200$ mm is applied in the CFD model. Grids overlap by one or four control volumes depending on local grid sizes.

Measuring Positions

Measurements are recorded using the slice file (SLCF) output option in FDS at positions listed along with output quantities in Table 7.5.

	$\{\Delta x, \Delta y, \Delta z\}$ mm	
Simulation ID	**Grid #1**	**Grid #2**
DC-XXX-XX-XX-X	{50,50,50}	{200,200,200}

Table 7.4 *Grid spacings according to designations in Figures 7.4 and 7.5.*

Sim. ID	**Quantity**	**Location**	**Position**
DC-HOR-...	T,u,v,w	Center line	$x \in \{0.0\}$ m
DC-HOR-...	T,u,v,w	Center line	$y \in \{0.0\}$ m
DC-HOR-...	T,u,v,w	Vent	$z \in \{0.0\}$ m
DC-HOR-...	T,$\tilde{p}$	Vent perim.	$\mathbf{x} \in \{-1.5, 0.0, -0.05\}$ m
DC-HOR-...	T,$\tilde{p}$	Vent perim.	$\mathbf{x} \in \{1.5, 0.0, -0.05\}$ m
DC-HOR-...	T,$\tilde{p}$	Vent perim.	$\mathbf{x} \in \{0.0, 0.0, -0.05\}$ m
DC-HOR-...	T,$\tilde{p}$	Vent perim.	$\mathbf{x} \in \{0.0, 0.0, -0.05\}$ m
DC-VER-...	T,u,v,w	Vent	$x \in \{0.0\}$ m
DC-VER-...	T,u,v,w	Center line	$y \in \{0.0\}$ m
DC-VER-...	T,$\tilde{p}$	Vent top	$\mathbf{x} \in \{3.7, 0.0, -(H_v + 0.5 + 0.05)\}$ m

Table 7.5 *Measured quantities and positions applied in the full-scale vent flow CFD models relative to dimensions in Figures 7.4 and 7.5. Here* $\mathbf{x} = \{x, y, z\}$ *represents a point position.*

Data Processing

Mass flow rates in the vent $\dot{m}_v$ are computed from temperature and velocity profiles using the numerical integration method outlined in Section 2.6, Eqns. (2.6.4), p. 43.

For use in calculating the coefficient of discharge C_d, see e.g. Eqn. (7.2.9), the pressure must be provided. From Eqn. (2.4.5) we get the total pressure using FDS:

$$p = \underbrace{\frac{1}{2}\rho |\mathbf{U}|^2}_{p_d} + \frac{\rho}{\rho_\infty}\tilde{p} \tag{7.6.3}$$

where p_d is the dynamic pressure explicitly addressed in *Bernoulli's equation*, see Eqn. (7.2.1). The static pressure p_s is subtracted in Eqn. (2.4.1c), hence arriving at Eqn. (2.4.4). Thus the perturbation pressure $\tilde{p}$ does not include the static pressure p_s, see Eqn. (2.4.2), used in *Bernoulli's equation*. Thus we write the pressure increase Δp:

$$\Delta p = \frac{\rho}{\rho_\infty}\tilde{p} \tag{7.6.4}$$

McGrattan (2005a) provides a comprehensive description of the hydrodynamic model employed in FDS.

The distance to the vena contracta h_a required in Eqn. (7.2.9a) is derived

from the vertical velocity field W predicted by the CFD model. Applying a cut-off filter for the velocity W, defines the width of the outflow $W_f(z)$:

$$\tilde{W} = \begin{cases} W & \forall\, W \geq 0.1 \\ 0 & \forall\, W < 0 \end{cases} \tag{7.6.5}$$

where the bulk flow is directed upward. The width of the outflow $W_f(z)$, see Figure 7.8, is derived from:

$$W_f(k) = \max_i (x_{ik}) - \min_i (x_{ik}) \;\; \forall \, \{i,k\} \in \Omega_{W \geq 0.1 \text{ m/s}} \tag{7.6.6}$$

where $\Omega_{W \geq 0.1 \text{ m/s}}$ is the core flow defined according to Eqn. (7.6.5). The largest contraction, i.e. the minimum width $W_{f,\min}(z)$ identifies the vena contracta and hence the height h_a above the vent, see Figure 7.8:

$$h_{a,p} = z \,\Big|_{\min_k (W_{f,k})} \tag{7.6.7}$$

where index p refers to the position of the vertical plane along which the width W_f is computed, i.e. $p \in \{x, y\}$. Only the relative width of the outflow W_f is relevant in determining h_a, hence any inaccuracies associated with the applied cut-off filter can be ignored. The width of the outflow W_f is derived on the vertical center planes through the horizontal vent, see Table 7.5. The distance h_a to the vena contracta is derived as the average of the two computed values for each vertical center plane:

$$h_a = \frac{1}{2} \left(h_{a,x} + h_{a,y} \right) \tag{7.6.8}$$

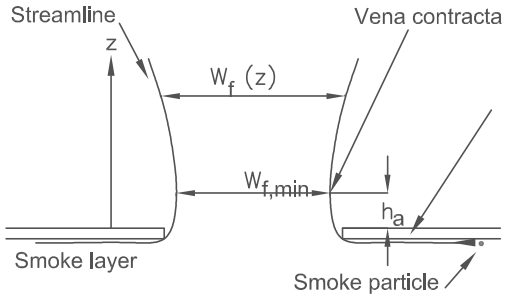

Figure 7.8 *Calculating the distance to the vena contracta h_a.*

CFD Model Inputs

The full-scale numerical model employs the full hydrodynamic model including LES turbulence model, no combustion, convective heat release rate, no radiation model and adiabatic surface boundary conditions, see model inputs in Table 7.6.

Turbulence model		
Smagorinsky constant	C_s	0.2
Prandtl number	Pr	0.5
Schmidt number	Sc	0.5
Combustion model		
Combustion model		Not applied
Heat source		
Heat base area (horizontal vent)	A_f	11.0 m^2
Heat base area (vertical vent)	A_f	3.2^2 m^2
Specific HRR	$\dot{Q}''_c$	see Table 7.1
Radiation model		
Radiative model		Not applied
Surface BCs		
Thermal model		Adiabatic
Ghost cell temperature	T_{ghost}	T_g
Velocity model		Partial slip
Wall velocity	u_τ	$0.5u_i$
Flow BCs		
Flow model	Passive vent	*OPEN*
Ambient temperature	T_∞	$20°C$
Ambient velocity	$\mathbf{u}$	0 m/s
Ambient perturbed pressure	$\tilde{p}$	0 Pa
Ambient static pressure	p_0	$1.013\ 10^5$ Pa

Table 7.6 *Full-scale vent flow setup: Model input parameters.*

7.7 Results

7.7.1 Coefficients of Discharge

As a simple validation study of the applied CFD model in predicting mass flow rates through buoyancy driven vents, the coefficients of discharge C_d computed from Eqn. (7.2.9) are plotted against the Reynolds number Re in Figures 7.9(a) and 7.9(b) for horizontal and vertical vents respectively. The flows are in both cases considered fully turbulent $Re >> 10000$, and hence according to Emmons (1997) the discharge coefficient for the horizontal vent of orifice type is $C_d \sim 0.6$ and for the vertical vent is $C_d \sim 0.68$, which are supported by the plots. CFD predictions are in general within 5% of the proposed discharge coefficients, with a few data points outside but within 10%, for both the horizontal and vertical vents. This serves as a simple validation study of the CFD model, implying that it can be applied with confidence in modeling vent flows within the framework of the present study. Distances to the vena contracta h_a applied in deriving the coefficient of discharge $C_{d,h}$ are plotted in Figure 7.10.

As mentioned previously EN12101-2 (2003) neglects the buoyancy term in the equation for the coefficient of discharge $C^*_{d,h}$ for a horizontal vent (the term cancels out for the vertical vent). The influence of the buoyancy term is shown in Figure 7.11. The simple approach in Eqn. (7.2.10a) is observed to over predict the discharge coefficient and hence the exhaust capacity by less than 2.5% compared to the universal flow formula Eqn. (7.2.9a), hence the buoyancy term can be neglected within the range of the investigated data.

7.7.2 Vent Exhaust Capacities

Vent exhaust capacities are evaluated from the mass flux through the opening $\dot{m}''_v$ $[kg/(m^2 * s)]$ assuming a uniform velocity and density distribution across the vent:

$$\dot{m}''_v = \frac{\dot{m}_v}{A_v} \tag{7.7.1}$$

Vent mass fluxes $\dot{m}''_v$ are plotted against the Froude number in Figures 7.12(a) and 7.12(b) for horizontal and vertical vents respectively. From Figure 7.12 an inherent dependence on the boundary condition is observed. Modeling the full vent flow reduces the vent exhaust capacity by 10%-20%. This implies that modeling vent flows using a simple passive boundary condition, the modeler must increase the required vent area to correct for the vena contracta.

A maximum exhaust capacity is observed in both vent configurations in Figure 7.12, attributed to the non-linear behavior of the density ρ and velocity W with temperature T (only shown for the horizontal vent) in Figure 7.13.

Using the CFD predicted values of pressure rise Δp, density difference $\Delta\rho$ and distance to the vena contracta h_a, the mass flux $\dot{m}''_v$ is derived using the universal flow formula for a horizontal vent in Eqn. (7.2.6). A fixed coefficient of discharge for fully turbulent flow of $C_d = 0.6$ is applied in accordance with Emmons (1997). The calculated mass fluxes are plotted against CFD predictions in Figure 7.14, exhibiting identical behavior as a function of Froude number.

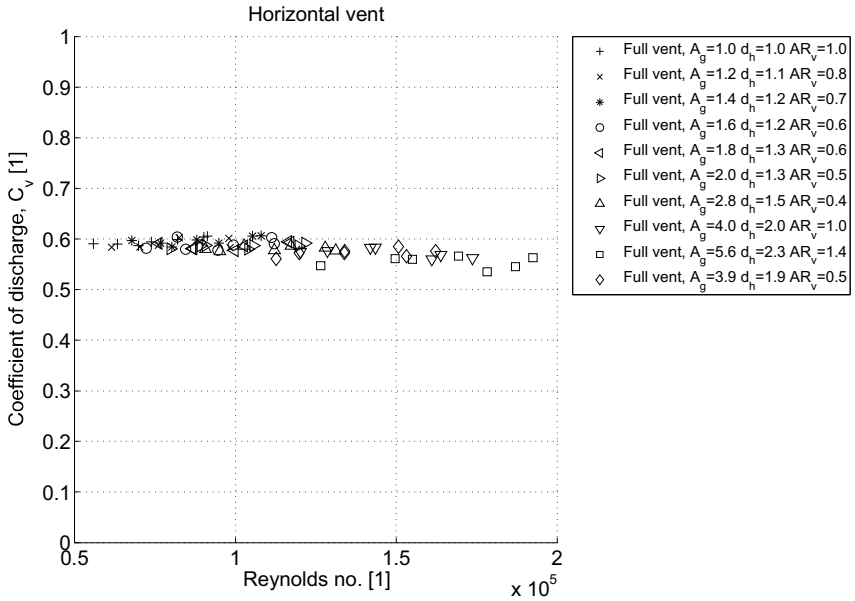

(a) Horizontal vent.

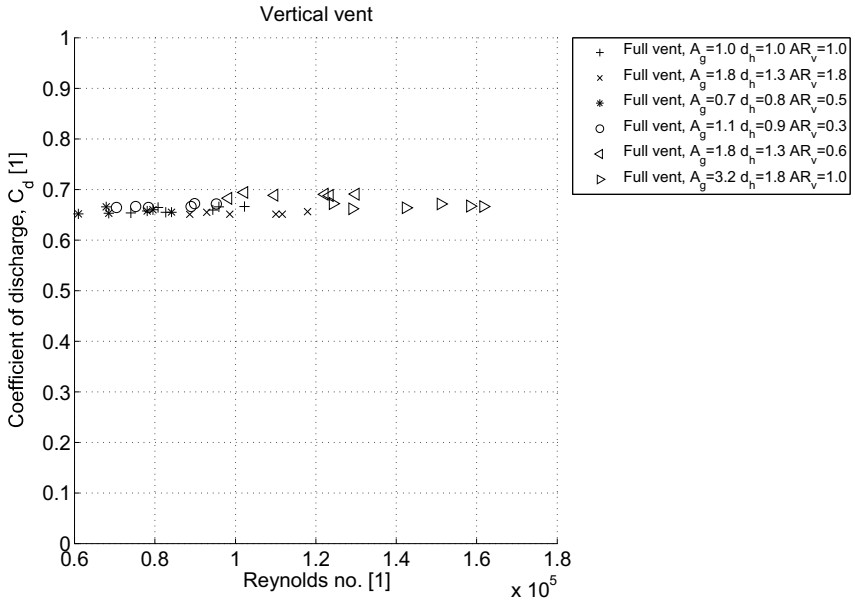

(b) Vertical vent.

Figure 7.9 *CFD model: Horizontal and vertical vents, simple passive boundary condition applied in modeling the vent.*

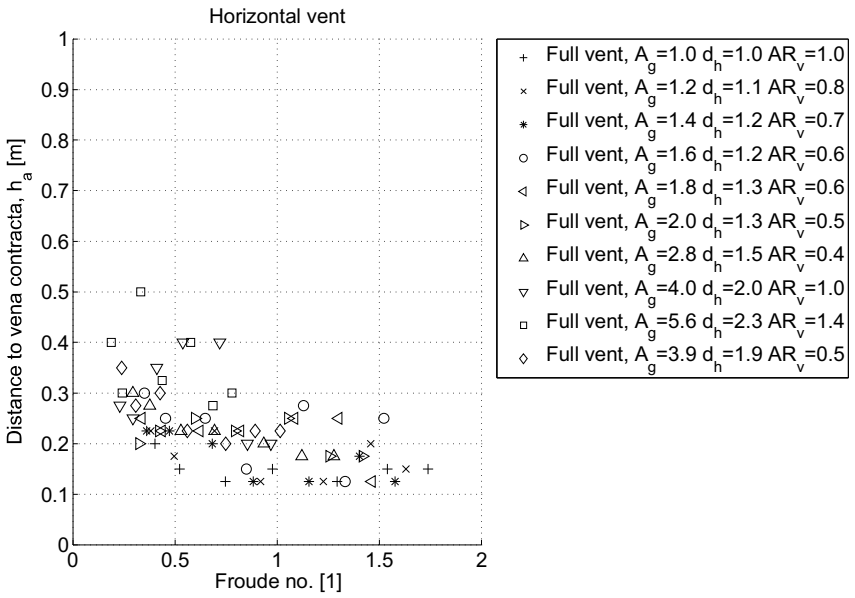

Figure 7.10 *Predicted distances to the vena contracta h_a for the horizontal vent.*

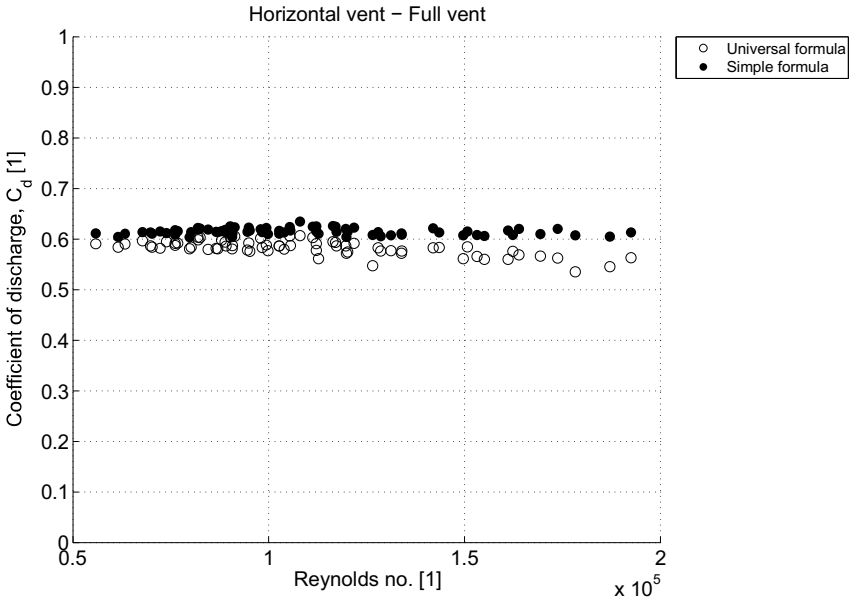

Figure 7.11 *Comparing coefficients of discharge, derived from the universal flow formula Eqn.* (7.2.9a) *or the simple formula Eqn.* (7.2.10a) *applied in EN 12101-2.*

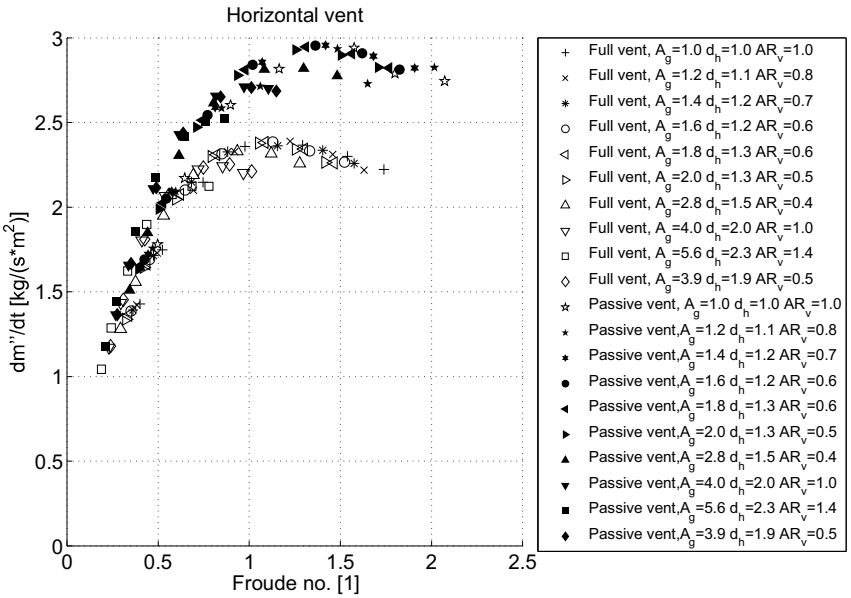

(a) Horizontal vent.

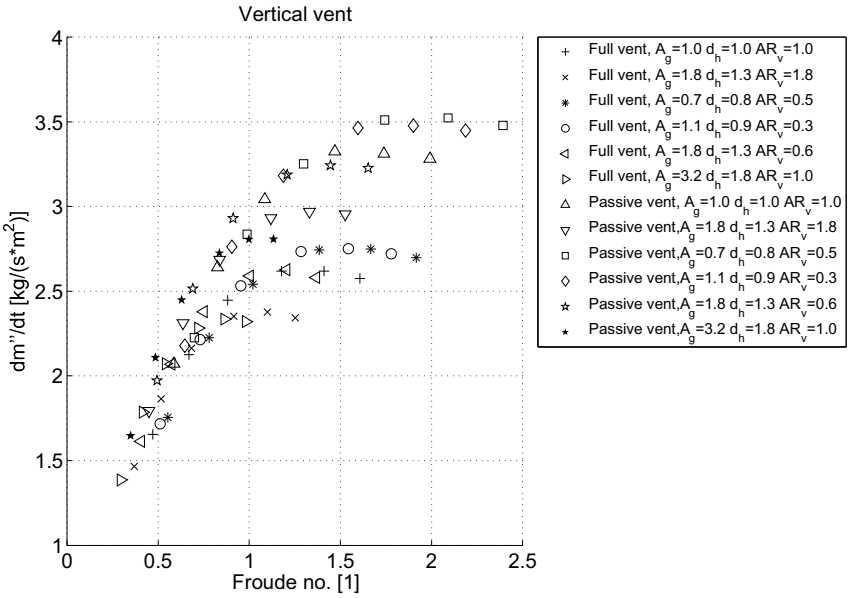

(b) Vertical vent.

Figure 7.12 *Mass fluxes in horizontal and vertical exhaust vents.*

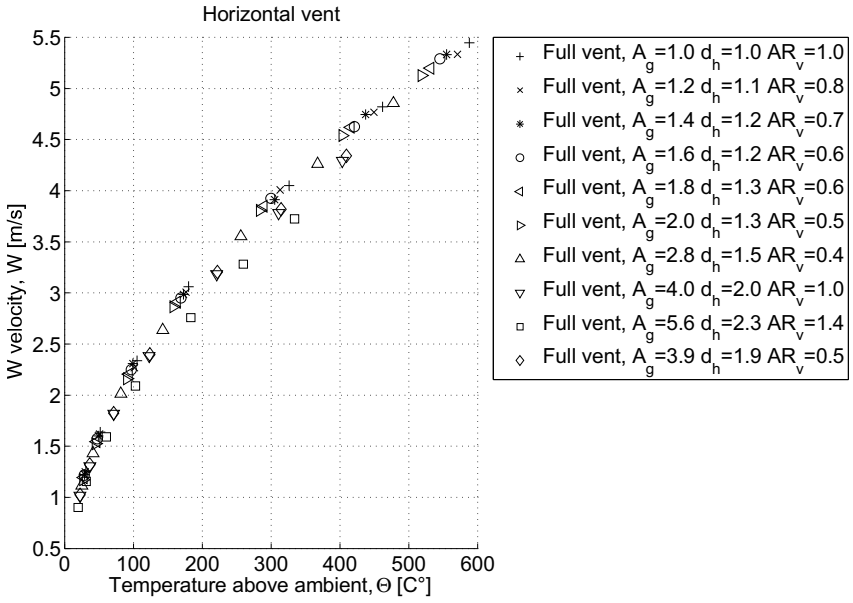

(a) W velocity.

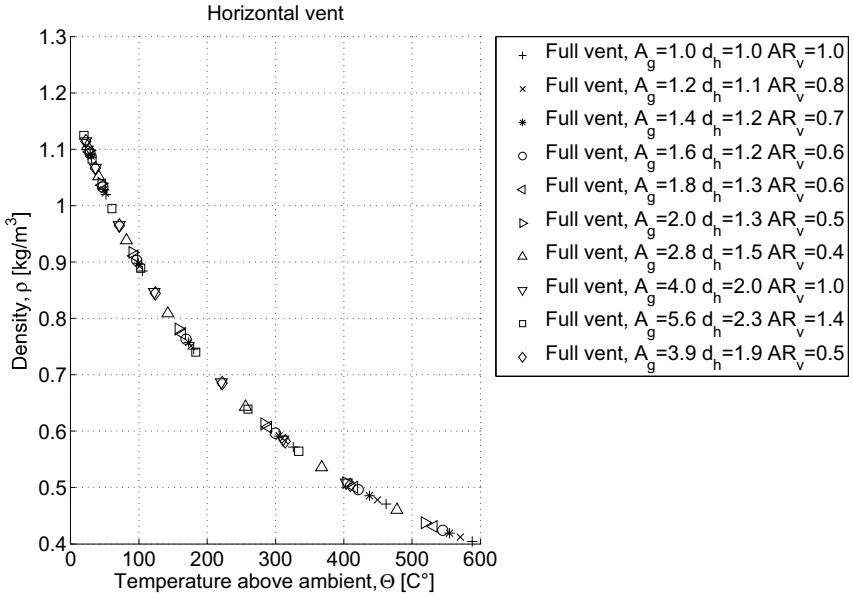

(b) Density ρ.

Figure 7.13 *Horizontal vent: Full-vent.*

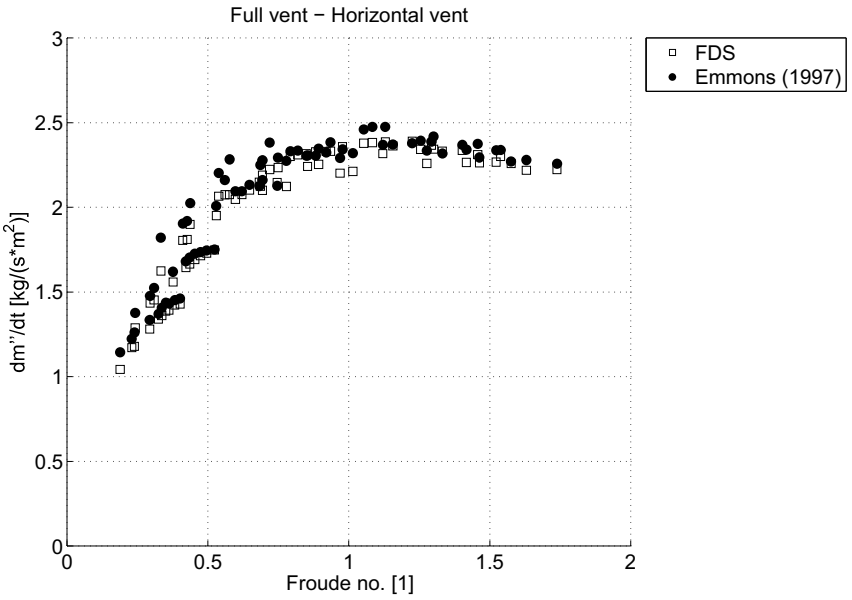

Figure 7.14 *Comparing the universal flow formula proposed by Emmons (1997) in Eqn.* (7.2.6) *with CFD predictions of mass flux through the horizontal vent.*

7.8 Development of Method for Correcting Vent Area

7.8.1 Methodology

A method to correct the vent capacity in CFD modeling of buoyancy driven vent flows using a simple passive boundary condition, see Section 2.4.7, is proposed. The proposed method corrects for the lacking contraction of exterior vent flows applying a simple passive boundary condition. Derivation of the mean Froude number through the vent Fr based on CFD predictions is required as input to the method. A correlation is proposed for the vent exhaust capacity $\dot{m}_v''$ for flows through passive vents and interior vents in a computational domain. Deriving the ratio between the vent flow capacities (full vs. passive), provides a correction coefficient $C_{i,fds}$ that must be applied to arrive at the correct geometrical vent area taking the vena contracta into consideration.

7.8.2 Assumptions and Limitations

Assumptions and limitations applied in developing the new method are:

Smoke layer temperature above ambient Θ - Temperatures above ambient in the range $\Theta \in [20 : 450]$ C° were applied in the development of the method.

Geometrical vent dimensions H_v and W_v - Geometrical extents of the vent must be within the widths $W_v \in [1.0 : 2.8]$ m and heights $H_v \in [1.0 : 2.0]$ m

for horizontal vents, and widths $W_v \in [1.0 : 1.8]$ m and heights $H_v \in [1.0 : 1.8]$ m for vertical vents.

Vent area A_v - Vent areas must be within $A_v \in [1.0 : 5.6]$ m^2 and $A_v \in [1.0 : 3.2]$ m^2 for horizontal and vertical vents respectively.

Vent aspect ratio AR_v - Vent aspect ratios $AR_v = H_v/W_v$ in the range $AR_v \in [0.4 : 1.0]$ and $AR_v \in [0.3 : 1.0]$ for the horizontal and vertical vents must be met.

Smoke layer - The smoke layer below the vent must be uniform.

Vent position - Only vents mounted in a vertical or horizontal position are addressed.

Flow outside vent, e.g. wind pressure - The method only corrects for contraction of the exterior vent flow, no impact of wind pressure is considered.

Numerical artifact - The model solely addresses a numerical artifact in CFD modeling of vent flows, and hence has nothing to do with the coefficient of discharge of the physical building component.

Inlet vents - A common assumption is that coefficients of discharge are approximately equal for in- and outflow through orifices. This can also be assumed valid for the present method, hence it also applies to inlet vents supplying makeup air to the smoke management system, obviously in the low range of temperatures above ambient. It is assumed that adequate conservatism is attained by applying the method to inlet vents where the correction is close to unity due to the low buoyancy exerted on the cold flow.

CFD model - The method is derived for application with the CFD model *Fire Dynamics Simulator* and should only be applied to other CFD models upon adequate validation.

Dimensional units - The method is developed using the SI system with the following modifications: kW and kJ.

7.8.3 Mass Flux Corrections

Horizontal vent

An obvious correlation between the mass fluxes through the vent $\dot{m}''_v$ and the Froude number Fr was observed for both the horizontal and vertical vents. From statistical analysis using the correlation coefficient R^2 to determine correlations, and an unconstrained nonlinear optimization method using the *Nelder-Mead Simplex Method* to find the minimum of the proposed multi-variable correlation, the

following correlations of the mass fluxes in the horizontal vent are derived:

$$\dot{m}''^{f}_{v,h} = \left[C_m \frac{\ln(\mathrm{Fr})}{\mathrm{Fr}} + m \right]^{-1} \left| \begin{array}{rcl} C_m & = & -0.0672 \\ m & = & 0.4447 \end{array} \right. \tag{7.8.1}$$

$$\dot{m}''^{p}_{v,h} = \left[C_m \frac{\ln(\mathrm{Fr})}{\mathrm{Fr}} + m \right]^{-1} \left| \begin{array}{rcl} C_m & = & -0.0748 \\ m & = & 0.3770 \end{array} \right. \tag{7.8.2}$$

where $\dot{m}''^{f}_{v,h}$ in Eqn. (7.8.1) and $\dot{m}''^{p}_{v,h}$ in (7.8.2) refer to the full and passive vents respectively.

The two correlations are plotted against mass flux data predicted by the CFD model in Figure 7.15. Correlation coefficients of $R^2 \sim 0.95$ implies a fairly strong correlation. However some scatter of the predicted data is observed, see also Figure 7.16(a), but considered irrelevant since only the ratio of the full vent mass flux to the passive vent mass flux is of importance.

Computing the ratio between Eqns. (7.8.1) and (7.8.2) yield the correction coefficient $C_{h,fds}$:

$$C_{h,fds} = \frac{\dot{m}''^{f}_{v,h}}{\dot{m}''^{p}_{v,h}} = 1.1 \frac{\ln(\mathrm{Fr}) - 5.0\mathrm{Fr}}{\ln(\mathrm{Fr}) - 6.6\mathrm{Fr}} \tag{7.8.3}$$

The correction coefficient $C_{h,fds}$ is plotted against the Froude number Fr in Figure 7.16(b), where a maximum reduction of ∼15% can be observed. For low Froude numbers the correction coefficient $C_{h,fds} \to 1$ as expected, because of the low contraction in low buoyant flows.

Vertical vent

The following correlations for the mass fluxes in the vertical vent were found to fit the predicted data satisfactorily:

$$\dot{m}''^{f}_{v,v} = \left[C_m \frac{\ln(\mathrm{Fr})}{\mathrm{Fr}+1} + m \right]^{-1} \left| \begin{array}{rcl} C_m & = & -0.3046 \\ m & = & 0.4122 \end{array} \right. \tag{7.8.4}$$

$$\dot{m}''^{p}_{v,v} = \left[C_m \frac{\ln(\mathrm{Fr})}{\mathrm{Fr}+1} + m \right]^{-1} \left| \begin{array}{rcl} C_m & = & -0.3063 \\ m & = & 0.3554 \end{array} \right. \tag{7.8.5}$$

where $\dot{m}''^{f}_{v,v}$ in Eqn. (7.8.4) and $\dot{m}''^{p}_{v,v}$ in (7.8.5) refers to the full and passive vents respectively.

Plotting the two correlations against the mass flux data predicted by the CFD model, see Figure 7.17, again implies a certain scatter of the predicted data about the correlation. Again only the ratio is important, hence the scatter can be neglected. Correlation coefficients of $R^2 \sim 0.90$ and $R^2 \sim 0.94$ are achieved for the horizontal and vertical vents respectively. Figure 7.18(a) depicts the distribution of the data about the correlation.

Computing the ratio between Eqns. (7.8.4) and (7.8.5) provides the correction coefficient $C_{v,fds}$ for the vertical vent:

$$C_{v,fds} = \frac{\dot{m}''^{f}_{v,v}}{\dot{m}''^{p}_{v,v}} = 1.0 \frac{\ln(\mathrm{Fr}) - 1.2\left(\ln(\mathrm{Fr}) + 1\right)}{\ln(\mathrm{Fr}) - 1.4\left(\ln(\mathrm{Fr}) + 1\right)} \tag{7.8.6}$$

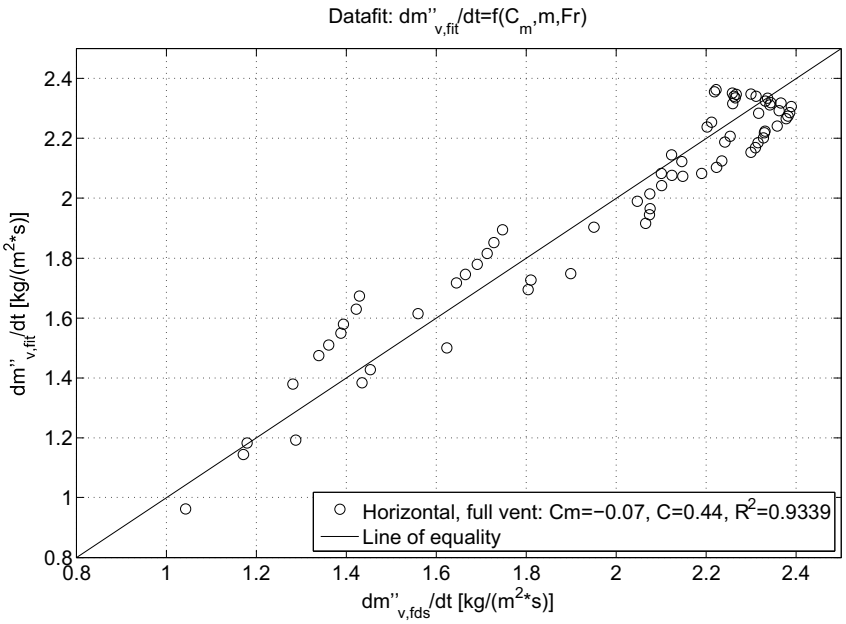

(a) Full vent.

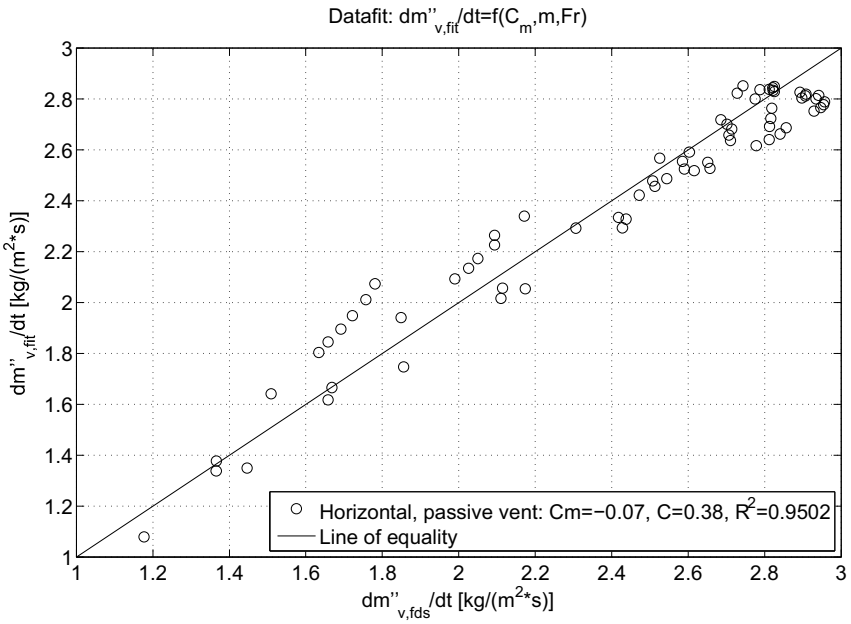

(b) Passive vent.

Figure 7.15 *Horizontal vent: Quality of correlations.*

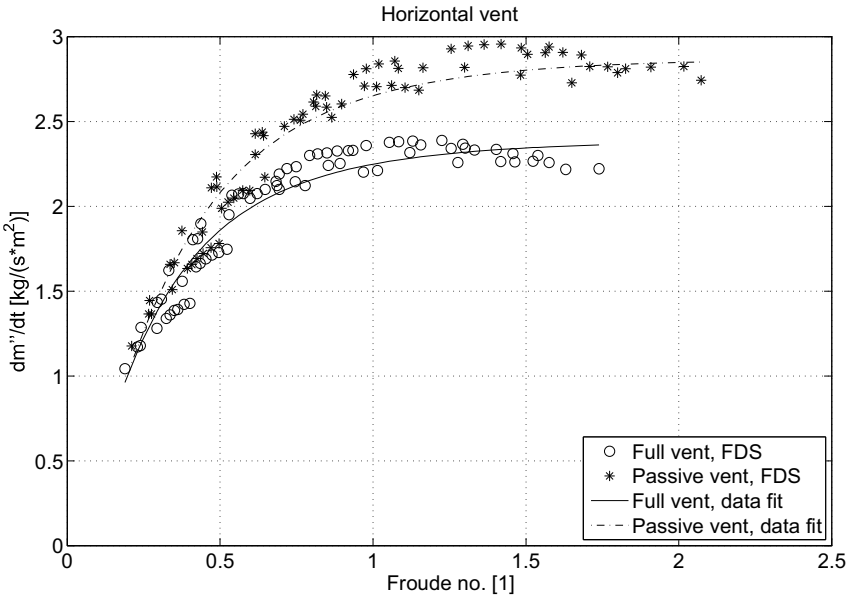

(a) Data scattering.

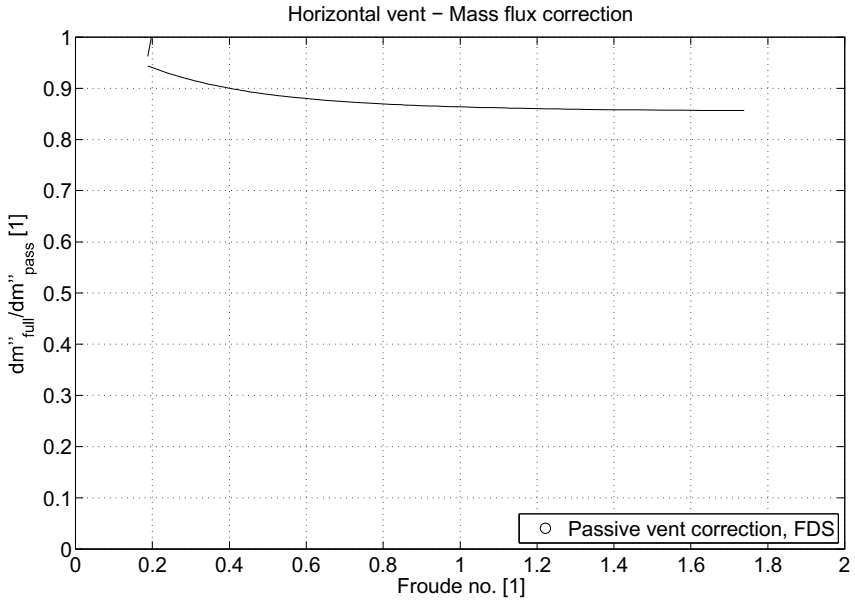

(b) Correction coefficient $C_{h,fds}$.

Figure 7.16 *Horizontal vent.*

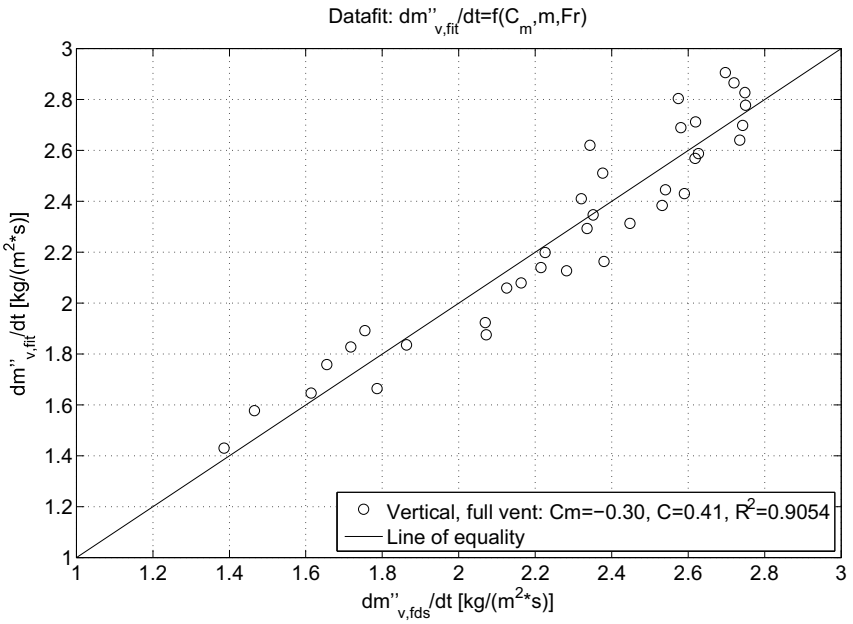

(a) Full vent.

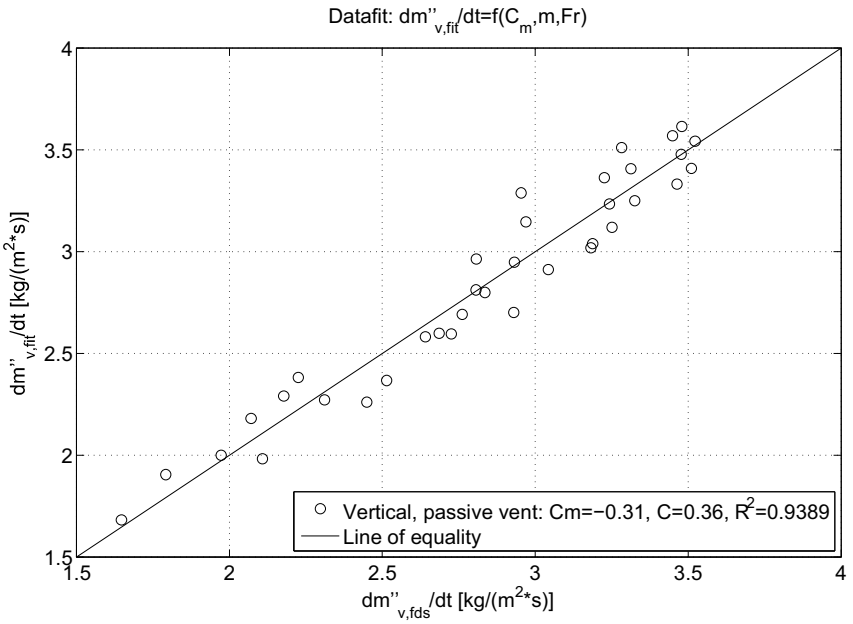

(b) Passive vent.

Figure 7.17 *Vertical vent: Quality of correlations.*

The correction coefficient $C_{v,fds}$ is plotted against the Froude number Fr in Figure 7.18(b), where a maximum reduction of ∼15% can be observed. The correction coefficient $C_{v,fds} \rightarrow 1$ as expected, because of the low contraction in low buoyant flows.

7.8.4 Application of the Method

The total mass flow rates for the two modeling approaches, passive ($\dot{m}_{i,p}$) and full ($\dot{m}_{i,f}$) vents, must be equal:

$$\dot{m}_{i,f} = \dot{m}_{i,p} \tag{7.8.7a}$$

$$A_{i,f}\dot{m}''_{i,f} = A_{i,p}\dot{m}''_{i,p} \tag{7.8.7b}$$

$$A_{i,f} = \frac{1}{C_{i,fds}} A_{i,p} \tag{7.8.7c}$$

where Eqn. (7.8.3) has been applied and $A_{i,f}$ and $A_{i,p}$ are the geometrical vent areas of the full and passive vents respectively. Subscripts f and p designate full and passive vents respectively and i represents the vent configuration, i.e. horizontal or vertical.

For the flow to be considered equivalent in the transformation from the passive to the full vent, the flow must be fully turbulent, i.e. Reynolds number $Re >$ 2300 in duct flows (see e.g. Davidson (2003)), and the Froude number must be preserved. From Figure 7.9 it is clear that the flow within the investigated range of data can be considered fully turbulent. Having derived the mass flux through the simple passive vent $\dot{m}''_{i,p}$ and calculated the corresponding Froude number Fr from the mean velocity through the vent, e.g W, the Froude number must be preserved, i.e. the point on the mass flux profile for the passive vent $\dot{m}''_{i,p}$, must be vertically displaced to the same Froude number position on the mass flux profile for the full vent $\dot{m}''_{i,f}$. Computing the ratio between $\dot{m}''_{i,p}$ and $\dot{m}''_{i,f}$ yields the correction coefficient $C_{i,fds}$, which must be inserted into Eqn. (7.8.7c) to compute the corrected geometrical vent area for the corresponding full vent $A_{i,f}$.

The application of the method is outlined below:

(1) - Compute Froude number Fr - Compute the Froude number Fr and hydraulic diameter d_h for the vent by first calculating the geometrical hydraulic diameter using Eqn. (7.3.2), and then insert the mean velocity across the vent U_i and the calculated hydraulic diameter d_h into Eqn. (7.3.1) to derive the Froude number Fr.

(2) - Compute the mass flux in the passive vent $\dot{m}''_{i,p}$ - Use the predicted mass flow rate from the CFD model $\dot{m}_{i,p}$ and the geometrical vent area for the passive vent $A_{i,p}$ applied in the CFD model.

(3) - Compute correction coefficient $C_{i,fds}$ - Using the Froude number Fr the correction coefficient $C_{i,fds}$ can be determined from Figures 7.16(b) or 7.18(b), horizontal and vertical vents respectively. From the mass flux in

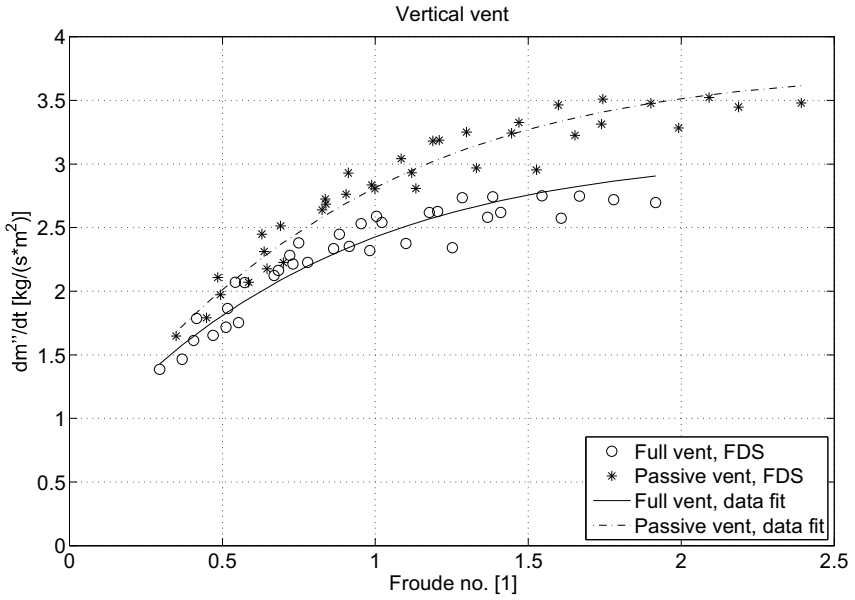

(a) Data scattering.

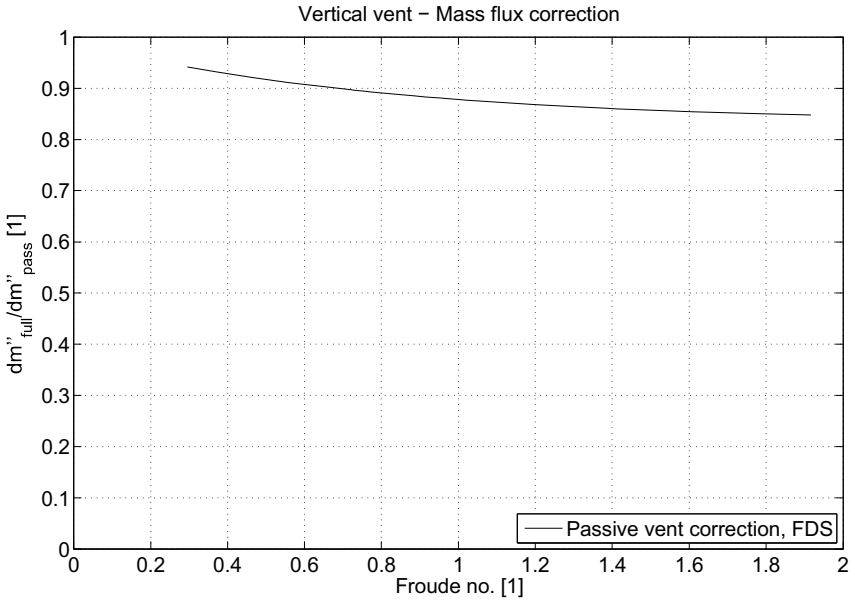

(b) Correction coefficient $C_{h,fds}$.

Figure 7.18 *Vertical vent.*

the passive vent $\dot{m}''_{i,p}$ derived in step 2 and the calculated Froude number Fr from step 1, locate the corresponding point on the profile for the passive vent in Figures 7.16(b) or 7.18(b). Displace the point vertically down to the profile for the full vent and compute the ratio of the two mass fluxes for the passive and full vents respectively using Eqn. (7.8.3) or (7.8.6) yielding the correction coefficient $C_{i,fds}$. Alternatively Eqns. (7.8.3) or (7.8.6) can be applied directly.

(4) - Compute corrected vent area for full vent $A_{i,f}$ - Calculate the corrected geometrical area of the full vent using the correction coefficient $C_{i,fds}$ from step 3 and Eqn. (7.8.7c).

(5) - Apply to individual vents in CFD model - Adequate conservatism is ensured by applying a correction coefficient of $C_{i,fds}$=0.85 to all vents in the CFD model, provided that all the assumptions and limitations in Section 7.8.2 are met.

Evidently the method must be applied to the individual passive vents in the CFD model.

7.9 Conclusions

The present research was aimed at modeling buoyancy driven vent flows using a simple approach, where the outflow region in the proximity of exhaust vents are ignored to reduce computational costs, hence ignoring the contraction of the exterior vent flow and thus reducing the vent capacity.

The CFD model *Fire Dynamics Simulator ver. 4.06* was validated against well-known and widely accepted values of discharge coefficients for horizontal and vertical vents of orifice type. It was shown that the CFD model could be applied with confidence in modeling buoyancy driven vent flows.

Discharge coefficients where derived using two approaches, a universal flow formula based on *Bernoulli's principle* and a simple formula ignoring the buoyancy term in *Bernoulli's principle*. Plotting the computed discharge coefficients, clearly supported the application of the simple approach as it only over predicted the discharge coefficient by less than ∼2.5% compared to the universal flow formula.

A method was proposed to calculate the correction of the geometrical area of a simple passive vent applied in modeling buoyancy-driven vent flows, and hence take the formation of a vena contracta outside the exhaust vent into consideration. Two correlations for the coefficient of vent area correction $C_{i,fds}$ were derived for the horizontal, Eqn. (7.9.1a), and vertical, Eqn. (7.9.1b), vents respectively:

$$C_{h,fds} = 1.1\frac{\ln(\mathrm{Fr}) - 5.0\mathrm{Fr}}{\ln(\mathrm{Fr}) - 6.6\mathrm{Fr}} \tag{7.9.1a}$$

$$C_{v,fds} = 1.0\frac{\ln(\mathrm{Fr}) - 1.2\,(\ln(\mathrm{Fr}) + 1)}{\ln(\mathrm{Fr}) - 1.4\,(\ln(\mathrm{Fr}) + 1)} \tag{7.9.1b}$$

By crude observation a vent area correction coefficient of $C_{i,fds} \sim 0.85$ can be applied for horizontal and vertical vents respectively with adequate conservatism being preserved.

The method was derived for the CFD model *Fire Dynamics Simulator ver. 4.06* and it's application with any other CFD model requires a validation study.

7.10 Future Research

The major shortcoming of the present research is it's uni-model derivation. Buoyancy driven exhaust vents are modeled with simple boundary conditions, resembling that of the passive vent applied herein, in a variety of CFD fire models for which the application of the proposed method should be validated.

Chapter 8

Conclusion

8.1 General

The present thesis concludes the research in engineering principles applied in atrium smoke management carried out under the Danish Industrial PhD Program. Research topics are based on the author's experience with shortcomings in the present engineering principles.

CFD modeling has gained widespread acceptance and application in fire safety engineering. Some of the major pitfalls in the application of the CFD models are grid design and validation studies. The present thesis proposed simple guidelines for grid design and approaches for validation studies.

The thesis proposes a complete method for deriving mass flow rates in approach flows in wide openings and the corresponding spill plumes. The method is developed using CFD modeling validated against experimental data and engineering relations derived from experimental data.

To address a widely adopted non-conservative approach in CFD modeling of buoyancy-driven vents, a new method for considering contraction of the exterior vent flows in modeling with simple passive boundary conditions was proposed.

8.2 Grid Quality Design

A simple approach to assess the adequate grid resolutions in CFD modeling of atrium smoke flows was proposed, dividing the computational domain into regions of characteristic flows for which there exist engineering relations for validation. Adequate grid resolutions are expressed in terms of the ratio of the non-dimensional characteristic fire length scale to the grid spacing $n^* = D_i^*/\Delta x$. Four distinct flow regions have been proposed:

Axisymmetric plume region - Adequately resolved for grid resolutions $n^* = D_p^*/\Delta x \gtrsim 15$. A correlation for the grid spacing $\Delta\mathbf{x}(z)$ as a function of rising height z above the fire base was proposed:

$$\frac{\Delta\mathbf{x}\,(z)}{\Delta\mathbf{x}\,(0)} = 1 - \frac{z}{z_0} \qquad \forall\, z_0 < 0 \tag{8.2.1}$$

Approach flow region - An adequately resolved flow can be obtained with grid resolutions $n^* = D^*_{cj}/\Delta x \gtrsim 5$

Rotation region - Grid resolutions of $n^* = D^*_l/\Delta x \gtrsim 3$ are considered adequate.

Spill plume region - Grid resolutions of $n^* = D^*_l/\Delta x \gtrsim 1.3$ can be considered adequate for most fire safety engineering applications. An approach to determine the grid size $\Delta \mathbf{x}\,(z_l)$ as a function of rising height z_l is proposed:

$$\frac{\Delta \mathbf{x}\,(z_l)}{\Delta \mathbf{x}\,(0)} = C_m z_l + 1 \qquad \Big| \; C_m \;=\; 0.0805 \tag{8.2.2}$$

8.3 Small-scale Approach Flows

A small-scale experimental program comprising a series of 7 tests of approach flows in a ∼1/3 scale fire compartment setup was conducted to provide validation data for CFD predictions of approach flows in wide openings. The actual experimental setup was 13.8 wide by 9.6 m deep by 1.55 m high, corresponding roughly to 44 m by 31 m by 5 m on the full-scale. Experiments were carried out using propane gas as a fire source supplied at a rate corresponding to fire sizes of 100-500 kW, corresponding to 1900-9400 kW on the full-scale.

Temperatures and velocities were recorded in the compartment opening and applied in the derivation of validation data for the CFD model. Velocities applied in the derivation of mass flow rates in the compartment opening were derived from the temperature field applying a method based on *Bernoulli's principle*. An attempt to validate temperature derived velocities against velocities measured by anemometers was carried out.

CFD predictions of temperatures, velocities and mass flow rates were validated against the obtained experimental data. Difficulties in modeling the heat conduction in part of the experimental setup were observed. However the validation study supported a high level of confidence in the applied CFD model, hence it was endorsed in the development of a new method for approach flow and spill plume mass flow rates.

8.4 Approach Flows in Wide Openings

A full-scale CFD modeling study was conducted to develop a new method for calculating the approach flow mass flow rate $\dot{m}_w$ in wide compartment openings.

A new method using a five step iterative procedure was developed for calculating the approach flow mass flow rate $\dot{m}_w$. The approach flow was divided into two components, one from an axisymmetric plume $\dot{m}_p$ (to be computed by existing axisymmetric plume models), and one from a ceiling flow $\dot{m}_c$ respectively:

$$\dot{m}_w = \dot{m}_c + \dot{m}_p \tag{8.4.1}$$

The method considers the axisymmetric plume a source for the approach flow below the ceiling.

Two new correlations for the net mass flow rate under the ceiling $\dot{m}_c$ and the smoke layer depth d_w in the compartment opening have been proposed. For the net mass flow rate under the ceiling $\dot{m}_c$:

$$\dot{m}_c = C_m \dot{Q}_c^{1/3} W_w^m D_{fb}^n \left(\frac{d_w}{d_w + d_d} \right)^k \quad \left| \begin{array}{rcl} C_m & = & 0.0243 \\ m & = & 0.9926 \\ n & = & 0.1679 \\ k & = & 0.3937 \end{array} \right.$$

and the smoke layer depth d_w in the compartment opening:

$$d_w = C_d C_m W_w^m D_{fb}^n \dot{m}_w^l \left(1 + d_d^k\right) \quad \left| \begin{array}{rcl} C_m & = & 0.7128 \\ m & = & -0.7958 \\ n & = & -0.0415 \\ k & = & 0.1012 \\ l & = & 0.7197 \end{array} \right.$$

The proposed method was tested against CFD predictions yielding a correlation coefficient of $R^2 = 0.99$. The method is inherently empirical and all assumptions and limitations must be met for the method to be applicable.

8.5 Wide Opening Spill Plumes

A comprehensive CFD model was applied in the development of two new methods for calculating the mass flow rate in wide spill plumes $\dot{m}_l$. A simple method adopting the functional form of most existing spill plume methods depending on compartment opening width W_w and convective heat release rate $\dot{Q}_{c,w}$ was proposed:

$$\dot{m}_{l,sim} = C_m W_w^m \dot{Q}_{c,w}^{1/3} z_l + \dot{m}_e \quad \left| \begin{array}{rcl} C_m & = & 0.1936 \\ m & = & 0.6174 \end{array} \right. \tag{8.5.1}$$

A modified method applying the smoke layer aspect ratio in the compartment opening AR_l as an additional variable in the correlation was proposed:

$$\dot{m}_{l,mod} = C_m W_w^m \dot{Q}_{c,w}^{1/3} \left(\frac{d_w}{W_w} \right)^k z_l + \dot{m}_e \quad \left| \begin{array}{rcl} C_m & = & 0.1060 \\ m & = & 1.2523 \\ k & = & 0.4151 \end{array} \right. \tag{8.5.2}$$

Both methods are based on a linear dependence on the rising height from the spill edge z_l.

A simple correlation for the entrainment in the rotation region was proposed to calculate the mass flow rate at the spill edge $\dot{m}_e$, applied as input for the calculation of the spill plume mass flow rate $\dot{m}_l$. The spill edge mass flow rate

$\dot{m}_e$ correlates with the approach flow mass flow rate $\dot{m}_w$, smoke layer depth d_w and compartment opening width W_w:

$$\dot{m}_e = C_m \dot{m}_w^m W_w^n d_w^k \quad \left| \begin{array}{rcl} C_m & = & 2.2628 \\ m & = & 0.5780 \\ n & = & 0.4923 \\ k & = & 0.2426 \end{array} \right. \tag{8.5.3}$$

Distance from the fire base to the compartment opening D_{fb} was found to only weakly correlate with the mass flow rate in the spill plume. The distance was however found to have a significant impact on the mass flow rate in the approach flow $\dot{m}_w$, leading to a coupling to the mass flow rate in the spill plume $\dot{m}_l$ due to the dependence on the approach flow mass flow rate $\dot{m}_w$.

The downstand depth was found to seriously impact the location of the spill plume, i.e. the distance from the cross-sectional center to the spill edge. This inherently impacts the entrainment into the spill plume. The obstruction of the approach flow by a deep downstand also influences the mass flow rate $\dot{m}_w$ and smoke layer depth d_w of the approach flow. A stronger correlation between the mass flow rate in the spill plume $\dot{m}_l$ and the smoke layer depth d_w, compared to the mass flow rate $\dot{m}_l$ and the presence of a downstand d_d was observed. Thus the spill plume mass flow rate $\dot{m}_l$ was correlated with the smoke layer depth in the compartment opening d_w, and hence indirectly the presence of a downstand d_d.

A limited study on the collapse of spill plumes was conducted. The study implied that spill plumes emanating from compartment openings of regular widths $W_w \leq \{7.2, 14.4\}$ m will transform into an axisymmetric plume at high elevations. A similar behavior for the wide opening spill plumes could not be documented, because of insufficient elevations in the computational domain, but a trend supporting the former was observed.

8.6 Buoyancy Driven Exhaust Vents

A method to correct for the lacking contraction of exterior vent flows in buoyancy driven exhaust vents modeled by simple passive vents was proposed. Two correlations for the coefficient of area correction $C_{i,fds}$ were derived for the horizontal, Eqn. (8.6.1a), and vertical, Eqn. (8.6.1b), vents respectively:

$$C_{h,fds} = 1.1 \frac{\ln(\mathrm{Fr}) - 5.0\mathrm{Fr}}{\ln(\mathrm{Fr}) - 6.6\mathrm{Fr}} \tag{8.6.1a}$$

$$C_{v,fds} = 1.0 \frac{\ln(\mathrm{Fr}) - 1.2\left(\ln(\mathrm{Fr}) + 1\right)}{\ln(\mathrm{Fr}) - 1.4\left(\ln(\mathrm{Fr}) + 1\right)} \tag{8.6.1b}$$

The geometrical area of the passive vent is thus corrected by the coefficient $C_{i,fds}$ to provide the geometrical vent area of the corresponding full vent taking the contracted vent flow into consideration:

$$A_{i,f} = \frac{1}{C_{i,fds}} A_{i,p} \tag{8.6.2}$$

By crude observation a vent area correction coefficient of $C_{i,fds} \sim 0.85$ can be applied for horizontal and vertical vents respectively with adequate conservatism being preserved.

Bibliography

R. Alpert (1972). 'Calculation of Response Time of Ceiling-mounted Fire Detectors'. *Fire Technology* **8**:181–195.

C. Beyler (2002). *SFPE Handbook of Fire Protection Engineering*, chap. Flammability Limits of Premixed and Diffusion Flames. National Fire Protection Association, Quincy, MA, 3rd edn.

C. L. Beyler (1986). 'Fire Plumes and Ceiling Jets'. *Fire Safety Journal* **11**:53–75.

A. Bounagui, et al. (eds.) (2003). *Optimizing the Grid Size Used in CFD Simulations to Evaluate Fire Safety in Houses*, National Research Council Canada, Ottawa, ON, Canada. National Research Council Canada.

M. Casey & T. Wintergerste (2000). *Best Practice Guidelines*. ERCOFTAC, Triomflaan 43, B-1160, Brussels, Belgium.

B. M. Cetegen, et al. (1984). 'Entrainment into the Near and Far Field of Fire Plumes'. *Combustion Science and Technology* **39**:305–331.

CIBSE (ed.) (2003). *CIBSE Guide E: Fire Engineering*. Chartered Institution of Building Services Engineers, London, UK.

L. Y. Cooper (1982). 'Heat Transfer from Plume to an Unconfined Ceiling'. *Journal of Heat Transfer* **104**(3):446–451.

L. Davidson (ed.) (2003). *An Introduction to Turbulence Models*. No. 97/2. Department of Thermo and Fluid Dynamics, Chalmers University of Technology, Gothenburg, Sweden.

H. W. Emmons (1997). 'Thirteenth Meeting of the UJNR Panel on Fire Reseach and Safety, March 13-20, 1996 - A Universal Orifice Flow Formula'. Tech. rep., Building and Fire Research Laboratory, National Institute of Standards and Technology. NISTIR 6030.

EN12101-2 (2003). *EN12101-2, Smoke and Heat Control Systems - Part 2: Specification for Natural Smoke and Heat Exhaust Ventilators*. European Committee for Standardization, en12101-2:2003 e edn.

J. H. Ferziger & M. Perić (2002). *Computational Methods for Fluid Dynamics*. Springer, third edn.

G. V. Hadjisophocleous & C. J. McCartney (2005). 'Guidelines for the Use of CFD Simulations for Fire and Smoke Modeling'. *ASHRAE Transactions* **111**(2):583–594.

G. O. Hansell, et al. (1993). 'Smoke Flow Experiments in a Model Atrium'. Building Research Estblishment Occasional Paper OP55, Building Research Establishment, Borehamwood, UK.

R. Harrison (2004). 'Smoke Control in Atrium Buildings: A Study of the Thermal Spill Plume'. Fire engineering research report 04/1, University of Canterbury, Christchurch, NZ.

G. Heskestad (1983). 'Luminous Heights of Turbulent Diffusion Flames'. *Fire Safety Journal* **5**:103–108.

G. Heskestad (1984). 'Engineering Relations for Fire Plumes'. *Fire Safety Journal* **7**:25–32.

G. Heskestad (1986). 'Fire Plume Entrainment According to Two Competing Assumptions'. *21st Symposium (International) on Combustion* pp. 111–120. The Combusition Insitute, Pittsburgh.

G. Heskestad & M. D. Delichatsios (eds.) (1973). *The Initial Convective Flow in Fire*, Pittsburgh, PA. Seventeenth Symposium (International) on Combustion, The Combustion Institute.

J. P. Holman (1989). *Heat Transfer*. McGraw-Hill, New York, 5th edn.

C. Huggett (1980). 'Estimation of Rate of Heat Release Rate by Means of Oxygen Consumption Measurements'. *Fire and Materials* **4**(2):61–65.

O. E. Inc. (ed.) (2004). *The OMEGA Temperature Handbook and Encyclopedia*. Omega Engineering, Inc., 5th edn. http://www.omega.com/temperature/Z/pdf/z204-206.pdf.

J. H. Klote (2002). 'Review of CFD Analysis of Smoke Management Systems'. *ASHRAE Transactions* **108**(1):687–698.

J. H. Klote & J. A. Milke (2002). *Principles of Smoke Management*. American Society of Heating, Refrigerating and Air-Conditioning Engineers, first edn.

J. Lagarias, et al. (1998). 'Convergence Properties of the Nelder-Mead Simplex Method in Low Dimensions'. *SIAM Journal of Optimization* **9**(1):112–147.

M. Law (1986). 'A Note on Smoke Plumes from Fires in Multi-level Shopping Malls'. *Fire Safety Journal* **10**:197–202.

M. Law (1995). 'Measurements of Balcony Smoke Flow'. *Fire Safety Journal* **24**:189–195.

S.-L. Lee & H. W. Emmons (1961). 'A Study of Natural Convection Above a Line Fire'. *Journal of Fluid Mechanics* **11**(3):353–368.

T. G. Ma & J. G. Quintiere (2003). 'Numerical Simulation of axi-symmetric fire plumes: Accuracy and Limitations'. *ASHRAE Transactions* **38**(5):467–492.

N. R. Marshall (1985). 'Smoke Control in Shopping Malls'. *Fire Surveyor* **14**(1):15–19.

N. R. Marshall & R. Harrison (1996). 'Experimental Studies of Thermal Spill Plumes'. Occasional Paper OP1, Building Research Establishment, Borehamwood, UK.

C. J. McCartney (2006). 'A CFD Investigation of Balcony Spill Plumes'. Master's thesis, University of Waterloo, Waterloo, ON, Canada.

K. McGrattan (2005a). 'Fire Dynamics Simulator (Version 4), Technical Reference Guide'. NIST Special Publication 1018, Fire Research Division, Building and Fire Research Laboratory, National Institute of Standards and Technology, USA.

K. McGrattan (2005b). 'Fire Dynamics Simulator (Version 4), User's Guide'. NIST Special Publication 1019, Fire Research Division, Building and Fire Research Laboratory, National Institute of Standards and Technology, USA.

J. A. Milke (ed.) (2000). *NFPA 92B: Guide for Smoke Management Systems in Malls, Atria, and Large Areas*. National Fire Protection Association, Quincy, MA, USA.

H. Morgan (1986). 'The Horizontal Flow of Buoyant Gases Toward an Opening'. *Fire Safety Journal* **11**:193–200.

H. P. Morgan, et al. (1999). *Design Methodologies for Smoke and Heat Exhaust Ventilation*. Building Research Establishment Ltd., 1st edn.

H. P. Morgan & N. R. Marshall (1975). 'Smoke Control Measures in Covered, Multi-level Shopping Malls: An Experimentally-based Theory for Smoke Production'. BRE Current Paper CP48/75, Building Research Establishment, Borehamwood, UK.

H. P. Morgan & N. R. Marshall (1979). 'Smoke Control Measures in a Covered Two-storey Shopping Mall Having Balconies as Pedestrian Walk Ways'. BRE Current Paper CP11/79, Building Research Establishment, Borehamwood, UK.

H. P. Morgan, et al. (1976). 'Smoke Hazards in Covered Multi-level Shopping Malls - Some Studies Using a Model Two-storey Mall'. BRE Current Paper CP47/76, Building Research Establishment, Borehamwood, UK.

M. Poreh, et al. (1998). 'Entrainment by two-dimensional spill plumes'. *Fire Safety Journal* **30**(1):1–19.

J. Quintiere (1984). 'A Perspective on Compartment Fire Growth'. *Combustion Science and Technology* **39**:11–54.

J. G. Quintiere (1989). 'Scaling Applications in Fire Research'. *Fire Safety Journal* **15**:3–29.

P. J. Roache (1994). 'Perspective: A Method for Uniform Reporting of Grid Refinement Studies'. *ASME Journal of Fluids Engineering* **116**:405–413.

M. H. Salley & R. P. Kassawara (2007). 'Verification and Validation of Selected Fire Models for Nuclear Power Plant Applications, Volume 7: Fire Dynamics Simulator (FDS)'. Tech. Rep. NUREG-1824 and EPRI 1011999, U.S. Nuclar Regulatory Commission, Office of Nuclear Regulatory Research (RES) and Electric Power Research Institute (EPRI), Rockville, MD:2005 and Palo Alto, CA.

J. Smagorinsky (1963). 'General Circulation Experiments with the Primitive Equations, I. The Basic Experiment'. *Monthly Weather Review* **91**(3):99–164.

D. N. Soerensen & P. V. Nielsen (2003). 'Quality Control of Computational Fluid Dynamics in Indoor Environments'. *Indoor Air* **13**:2–17.

P. H. Thomas (1987). 'On the Upward Movement of Smoke and Related Shopping Mall Problems'. *Fire Safety Journal* **12**:191–203.

P. H. Thomas, et al. (1963). 'Investigations into the Flow of Hot Gases in Roof Venting'. Fire Research Technical Paper 7, Her Majesty's Stationary Office, London, UK.

P. H. Thomas, et al. (1998). 'The Spill Plume in Smoke Control Design'. *Fire Safety Journal* **30**:21–46.

C. Yih (1952). 'Free Convection due to a Point Source of Heat'. In *Proceedings of the 1st US National Congress in Applied Mechanics*, pp. 941–947.

E. E. Zukoski (1995). *Combustion Fundamentals of Fire*, chap. Properties of Fire Plumes, pp. 101–219. Academic Press, London.

Appendix A

Multi-grid Modeling

A very simple assessment study of the multi-grid feature provided with FDS was carried out for a simple axisymmetric plume. The CFD fire model FDS was applied for the study. Simulations were conducted with two different grid designs each consisting of two grids with grid interfaces perpendicular and parallel to the direction of the bulk flow, i.e. upward direction. Grid spacings are $\Delta x = 0.10$ m and one overlap of control volumes is applied in the grid interface, i.e. two rows of interpolation grid points. Predicted temperatures and W velocities are plotted against single grid predictions at different elevations z above the fire base.

Comparing Figures A.1, A.2, A.3 and A.4 it is evident that a grid interface parallel to the bulk flow direction yields higher discrepancies from the single grid solution. This is expected because the downstream flow is subjected to a successive number of interpolations each introducing a small numerical error. With the perpendicular grid interface the flow is only interpolated at one elevation, i.e. an interpolation error is only introduced at one level in the downstream direction, thus errors are not added successively. From this very simple study it is recommended to use perpendicular over parallel grid interfaces when ever a multi-grid setup must be applied.

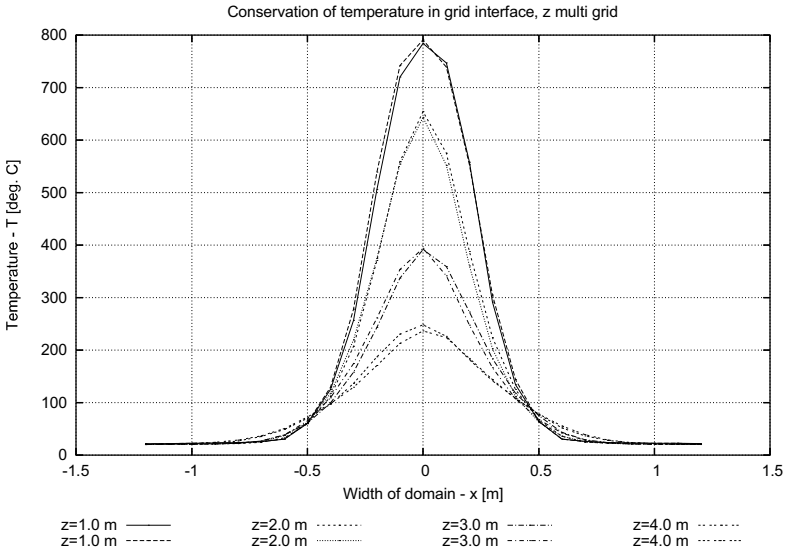

Figure A.1 *Perpendicular grid interface: Absolute temperature T.*

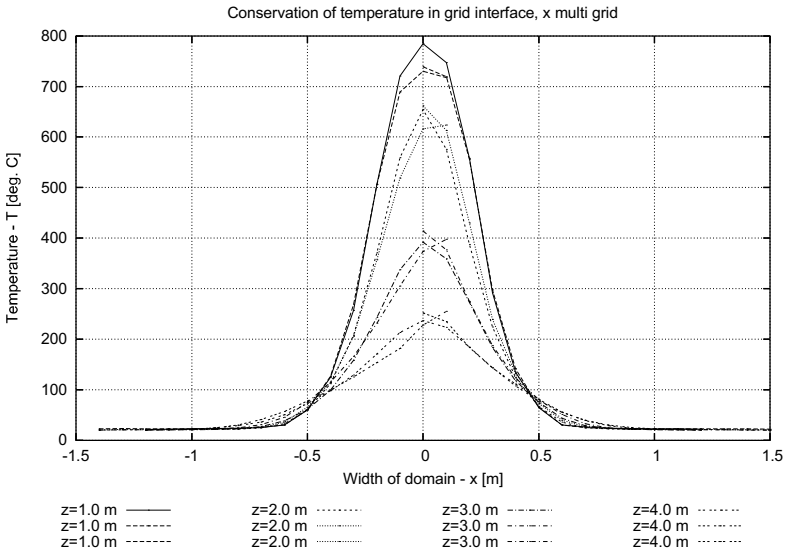

Figure A.2 *Parallel grid interface: Absolute temperature T.*

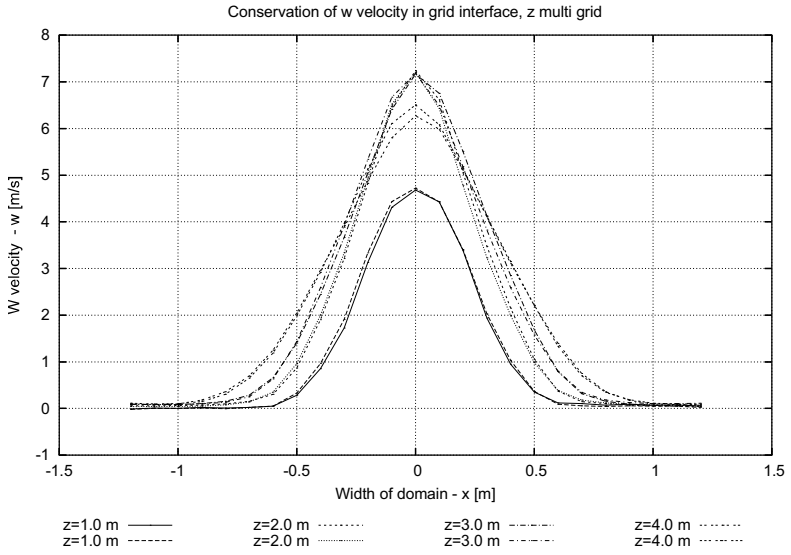

Figure A.3 *Perpendicular grid interface: W velocity W.*

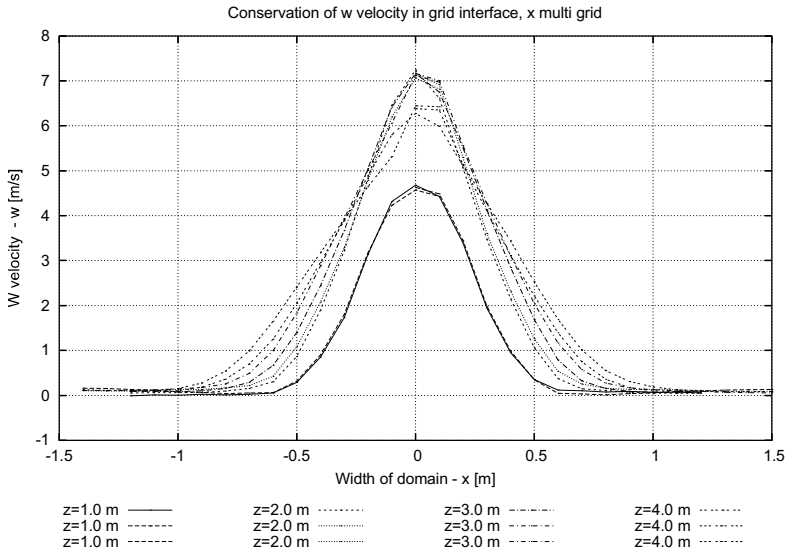

Figure A.4 *Parallel grid interface: W velocity W.*

Appendix B

Impact of Wall Velocity BC on Ceiling Jet

A simple study of the impact of the wall velocity, u_τ, boundary condition, see Section 2.4.5, has been conducted for a ceiling jet approaching a wide opening. The CFD fire model FDS was applied for the study. In this context focus is on the impact on the shape of the ceiling jet profile. Simulations have been conducted for VBC $\in \{-1.0, 0.5, 1.0\}$, i.e. no-slip, partial slip (FDS default) and free-slip condition, see Eqn. (2.4.37). Simulation designations of interest to this note is listed in Table B.1 with VBC being the only parameter changed.

From the velocity profiles in Figure B.2 it is clear that changing the BC to free-slip (fud4-10) yields a higher velocity at the top of the profile. Assuming the wall velocity is greatly reduced compared to the bulk flow (in accordance with theoretical analysis), means that the top of the velocity profile is expected to "bend backward", i.e. the highest velocity can not be located on the face of the control volumes abutting the wall. Reducing the wall velocity (fud4 and fud4-2), forces the top of the velocity profile backward as expected. The maximum velocity in the profile is also impacted by the wall boundary condition. Approaching the limit of the free-slip condition, it can be seen from Figure B.2 that the maximum velocity is no longer located in the bulk flow below the ceiling but instead in the control volume abutting the wall, which is not supported by boundary layer fluid dynamics.

From the temperature profiles in Figure B.1 it is clear that reducing the wall velocity increases the temperature in control volumes abutting the wall because

Simulation	**VBC**	**Condition**
fud4	0.5	Partial slip
fud4-2	-1.0	No-slip
fud4-10	1.0	Free-slip

Table B.1 *Simulations addressing impact of wall velocity boundary condition u_τ. Predictions are depicted in Figure B.1 and B.2.*

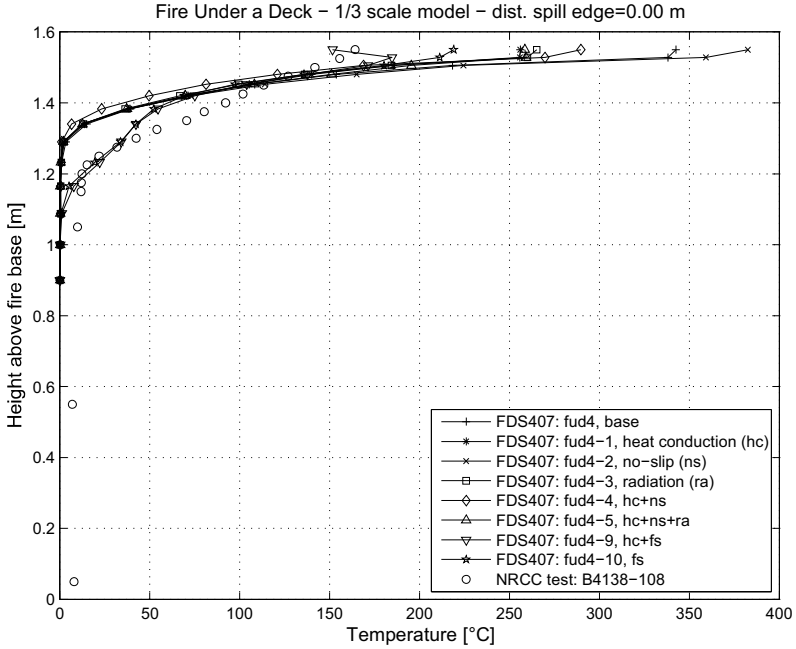

Figure B.1 *Temperature predictions: Assessing impact of the wall velocity, u_τ, boundary condition on the ceiling jet flow.*

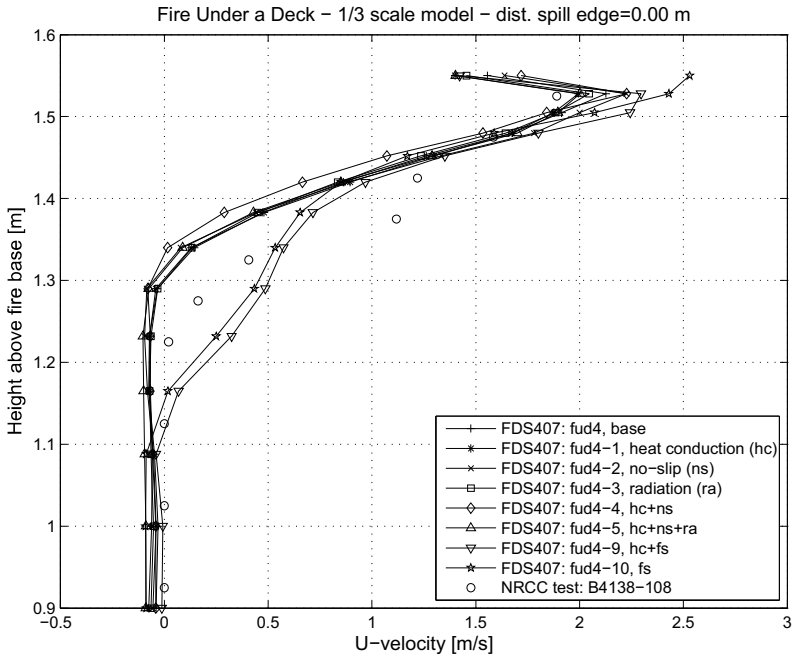

Figure B.2 *Velocity predictions: Assessing impact of the wall velocity, u_τ, boundary condition on the ceiling jet flow.*

the convective heat flow rate must be conserved at a lower velocity.

It can be concluded that the implemented wall velocity boundary conditions behave accordingly. The modeler should be aware that validating CFD simulations against boundary flows, e.g. ceiling jets, requires a comprehensive description of the boundary conditions present in the experimental setup. Since the wall velocity boundary condition is a numerical construct, it is very difficult to interpret or measure it in fire experiments and thus any applicable data are sparse (or non-existent).

Appendix C

B4138-108 Small-scale Test Program: Assessing Sub-model Dependency

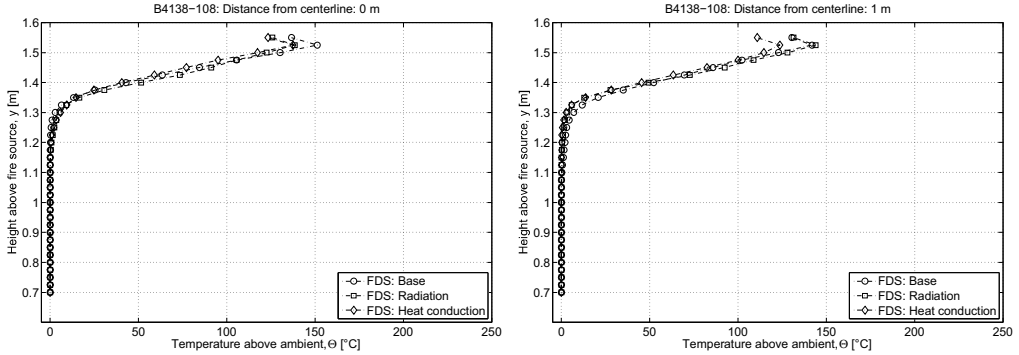

(a) Dist. from centerline: 0 m. (b) Dist. from centerline: 1 m.

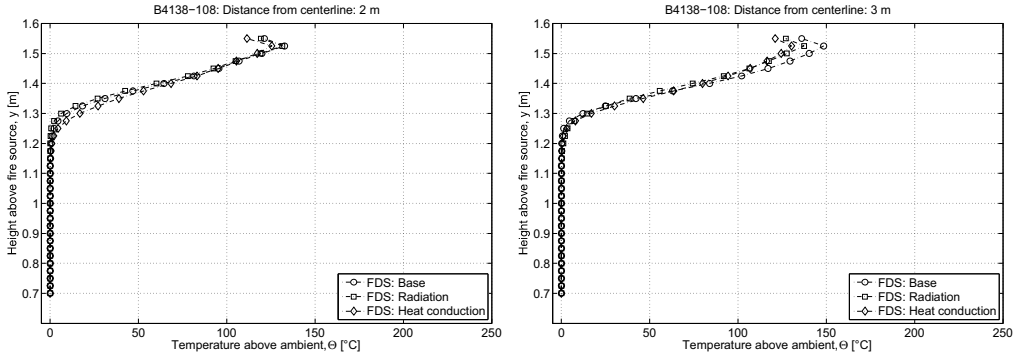

(c) Dist. from centerline: 2 m. (d) Dist. from centerline: 3 m.

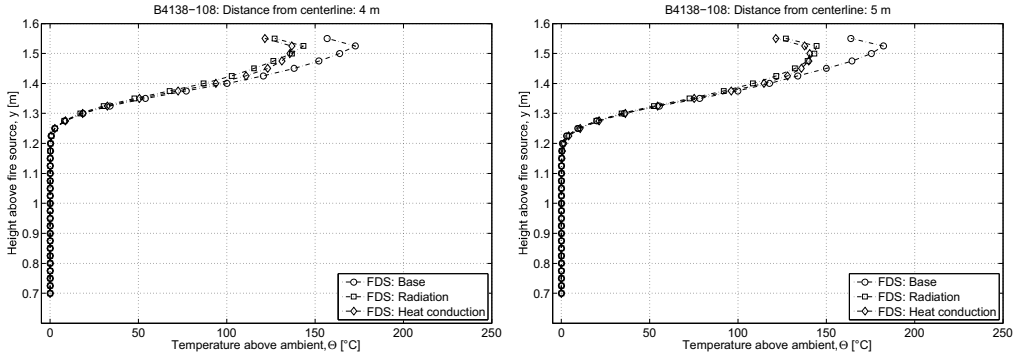

(e) Dist. from centerline: 4 m. (f) Dist. from centerline: 5 m.

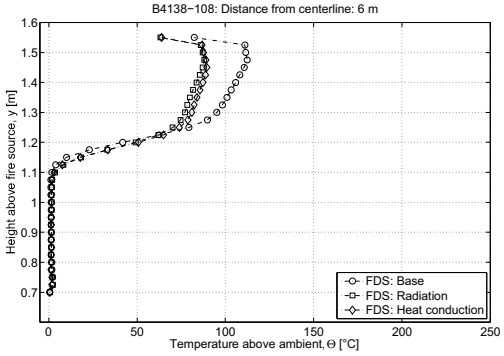

(g) Dist. from centerline: 6 m.

Figure C.1 *B4138-108 - Small-scale: Temperature profiles.*

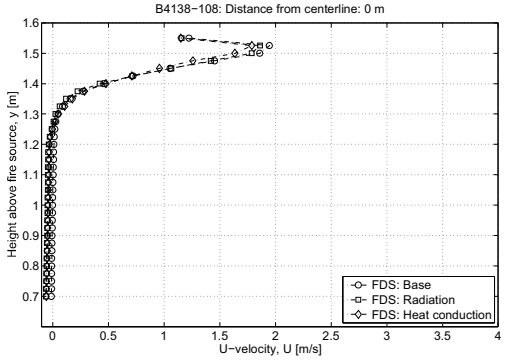

(a) Dist. from centerline: 0 m.

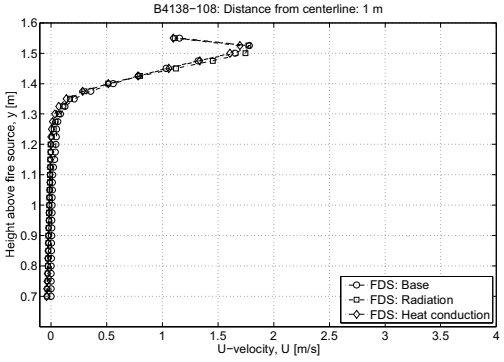

(b) Dist. from centerline: 1 m.

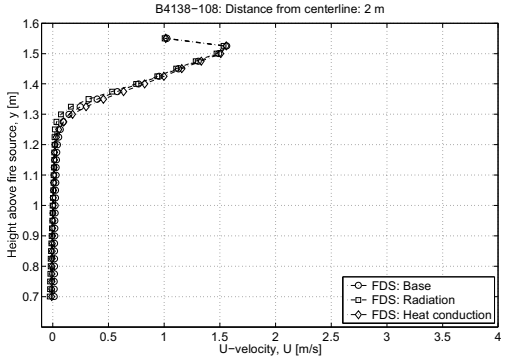

(c) Dist. from centerline: 2 m.

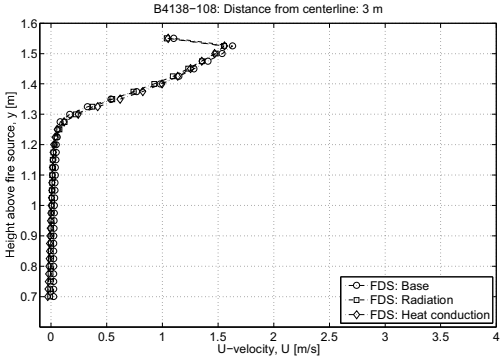

(d) Dist. from centerline: 3 m.

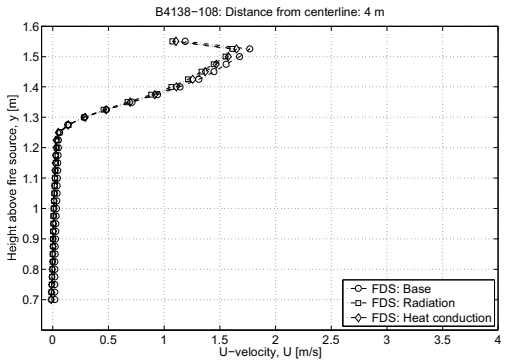

(e) Dist. from centerline: 4 m.

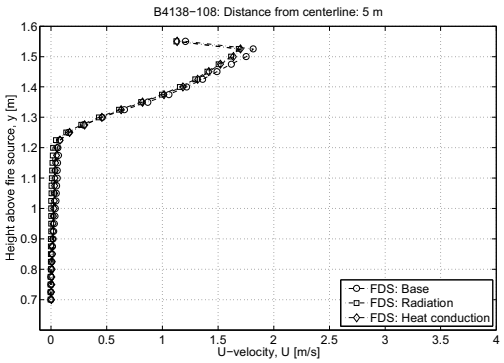

(f) Dist. from centerline: 5 m.

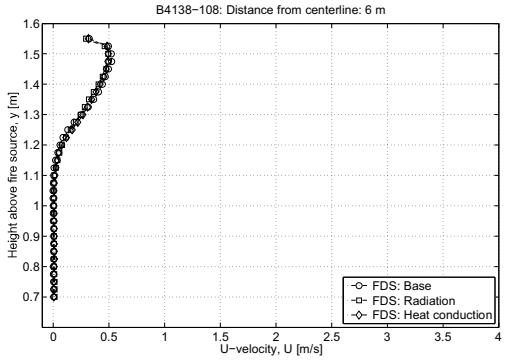

(g) Dist. from centerline: 6 m.

Figure C.2 *B4138-108 - Small-scale: U velocity profiles.*

Appendix D

B4138-XXX Small-scale Test Program: Temperature Profiles

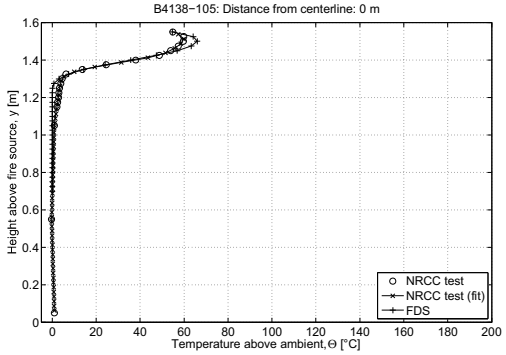

(a) Dist. from centerline: 0 m.

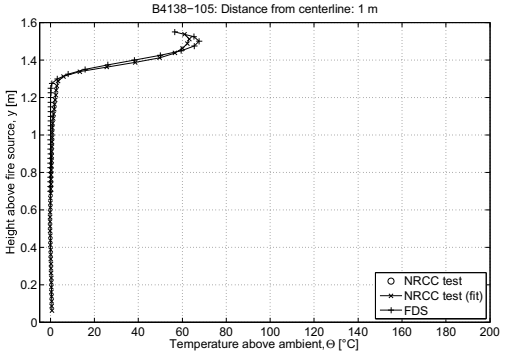

(b) Dist. from centerline: 1 m.

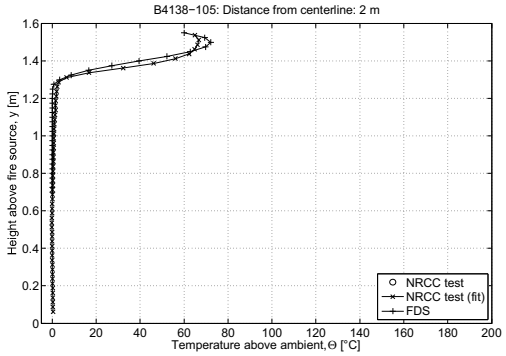

(c) Dist. from centerline: 2 m.

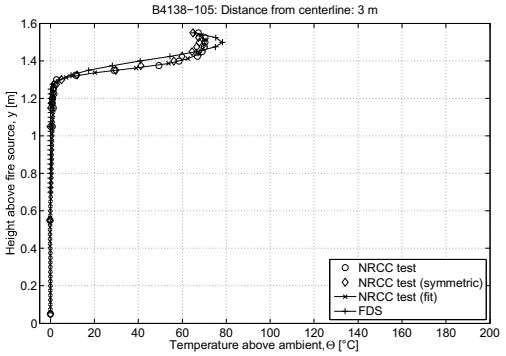

(d) Dist. from centerline: 3 m.

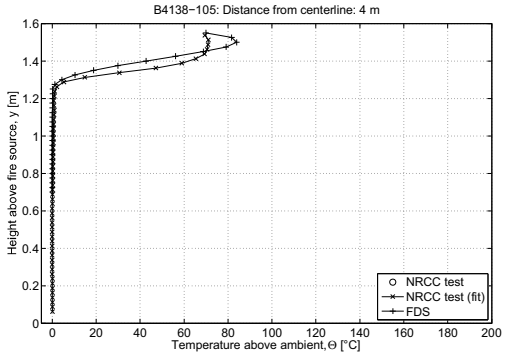

(e) Dist. from centerline: 4 m.

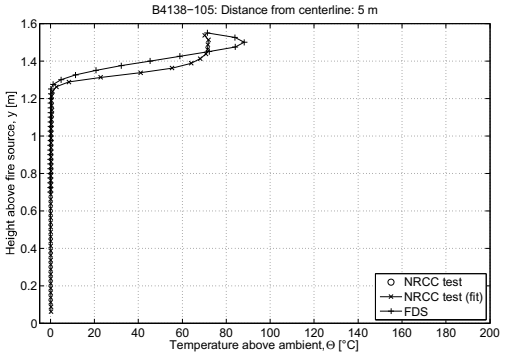

(f) Dist. from centerline: 5 m.

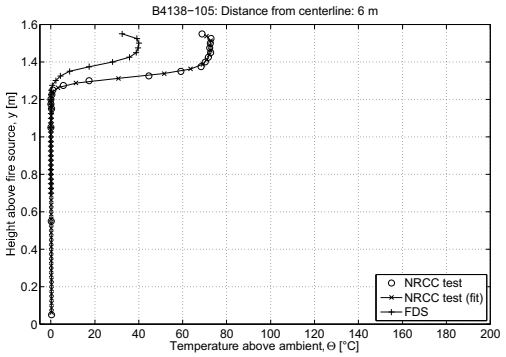

(g) Dist. from centerline: 6 m.

Figure D.1 *B4138-105 - Small-scale: Temperature profiles.*

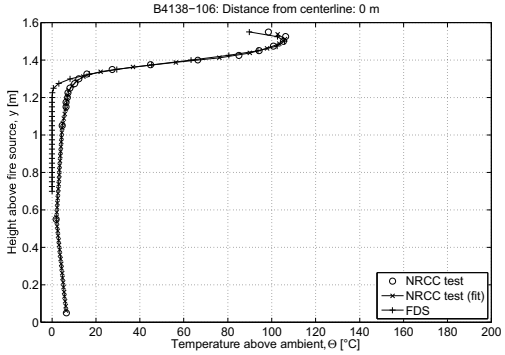

(a) Dist. from centerline: 0 m.

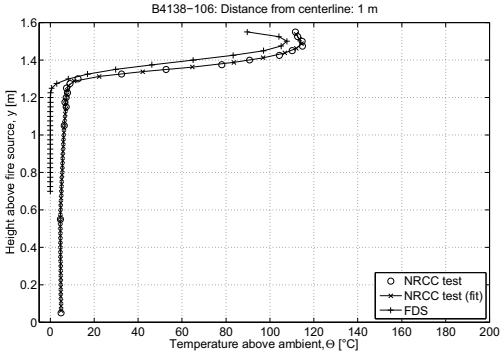

(b) Dist. from centerline: 1 m.

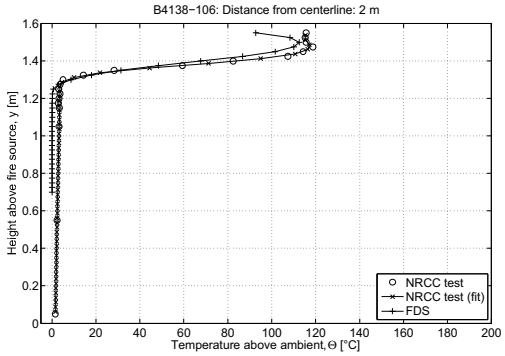

(c) Dist. from centerline: 2 m.

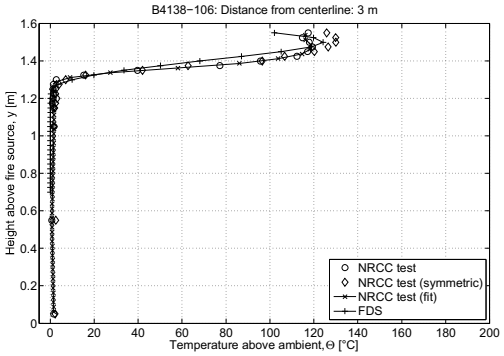

(d) Dist. from centerline: 3 m.

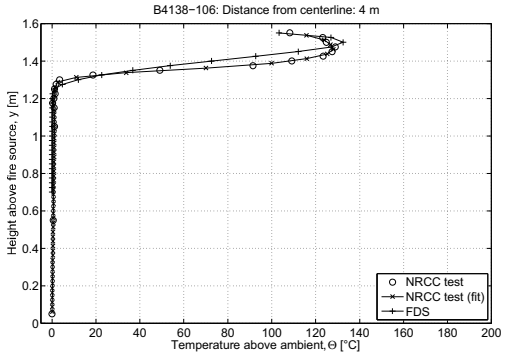

(e) Dist. from centerline: 4 m.

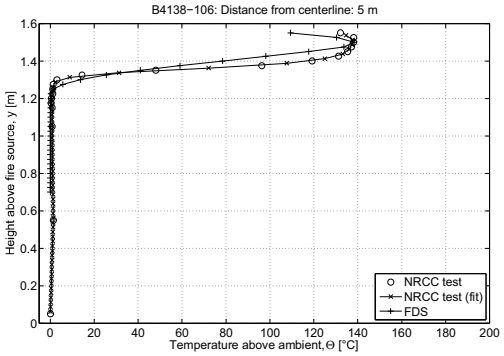

(f) Dist. from centerline: 5 m.

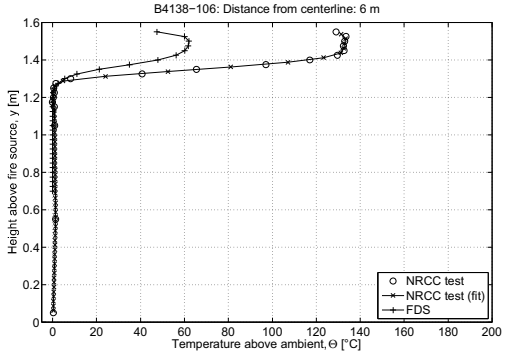

(g) Dist. from centerline: 6 m.

Figure D.2 *B4138-106 - Small-scale: Temperature profiles.*

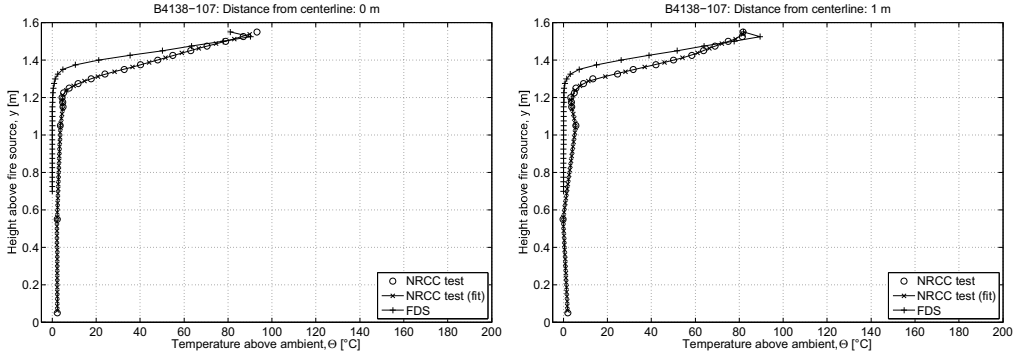

(a) Dist. from centerline: 0 m. (b) Dist. from centerline: 1 m.

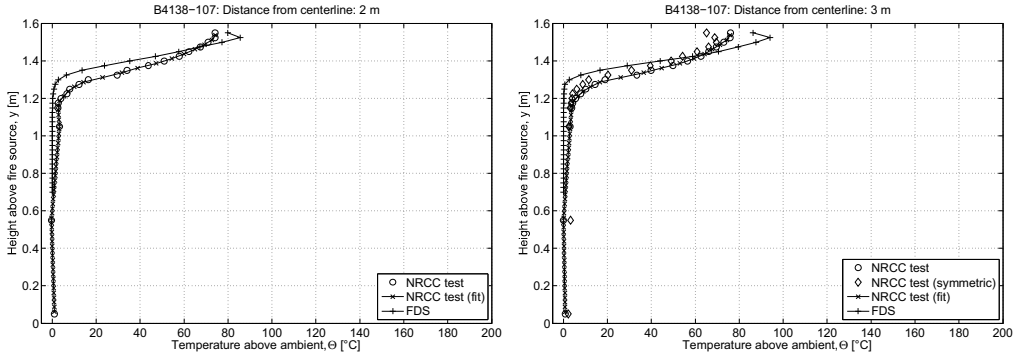

(c) Dist. from centerline: 2 m. (d) Dist. from centerline: 3 m.

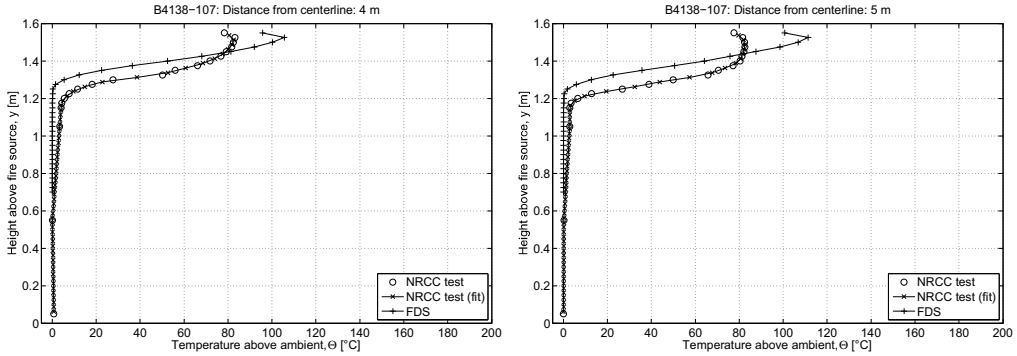

(e) Dist. from centerline: 4 m. (f) Dist. from centerline: 5 m.

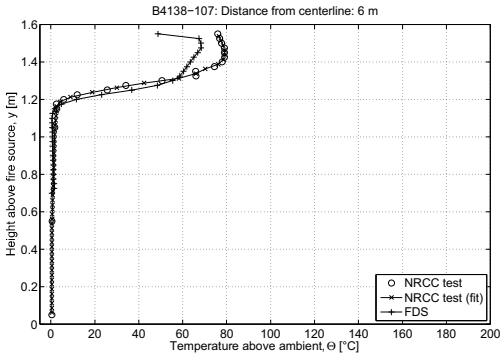

(g) Dist. from centerline: 6 m.

Figure D.3 *B4138-107 - Small-scale: Temperature profiles.*

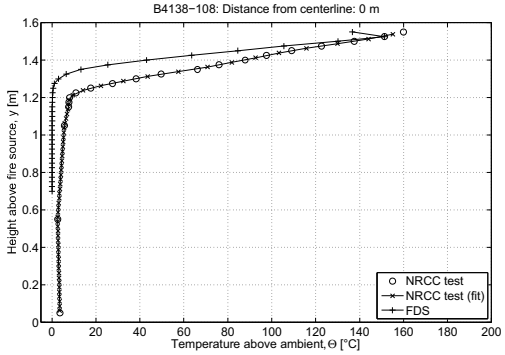

(a) Dist. from centerline: 0 m.

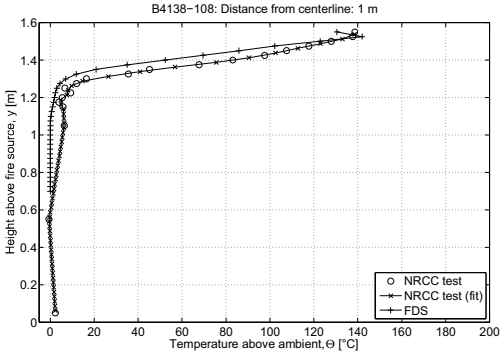

(b) Dist. from centerline: 1 m.

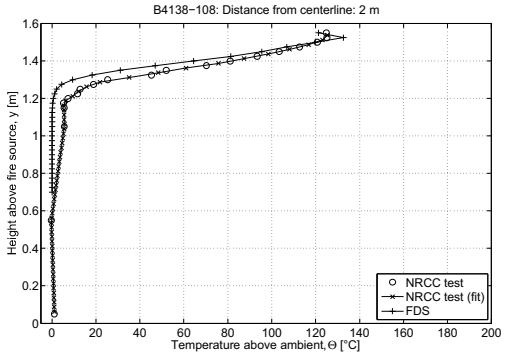

(c) Dist. from centerline: 2 m.

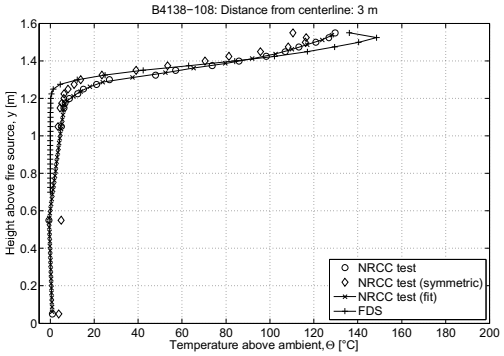

(d) Dist. from centerline: 3 m.

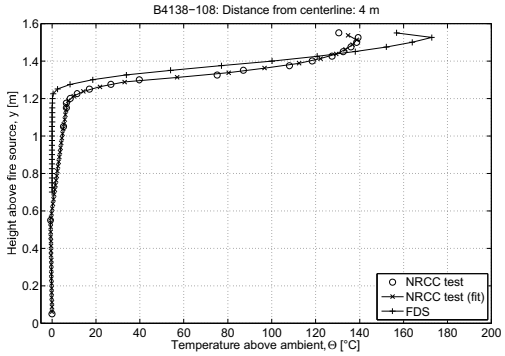

(e) Dist. from centerline: 4 m.

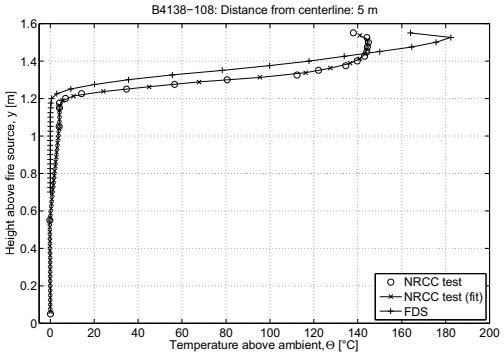

(f) Dist. from centerline: 5 m.

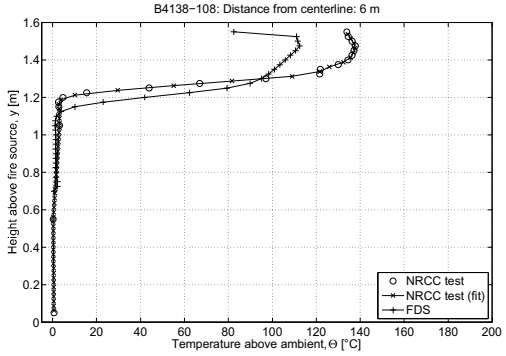

(g) Dist. from centerline: 6 m.

Figure D.4 *B4138-108 - Small-scale: Temperature profiles.*

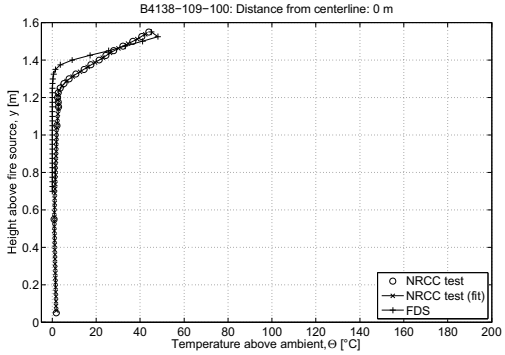

(a) Dist. from centerline: 0 m.

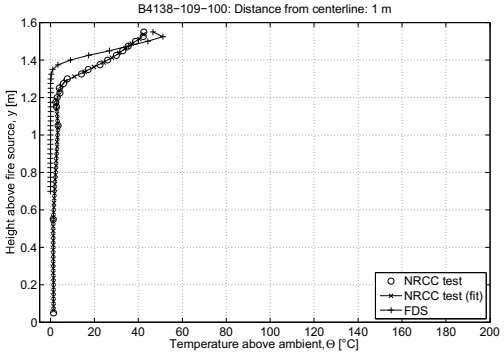

(b) Dist. from centerline: 1 m.

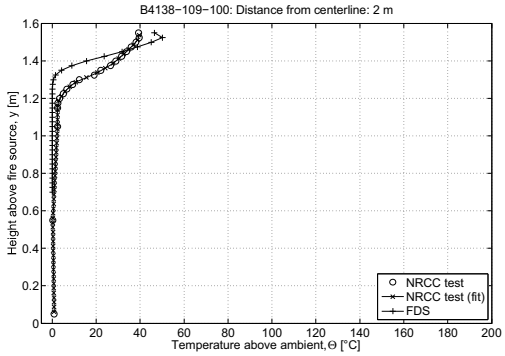

(c) Dist. from centerline: 2 m.

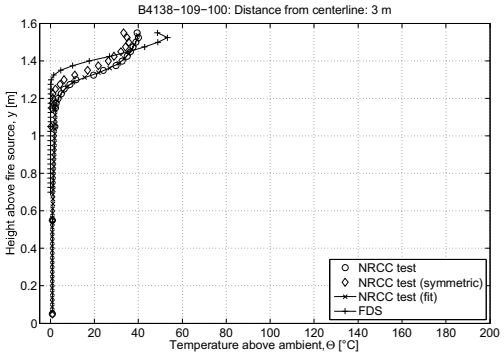

(d) Dist. from centerline: 3 m.

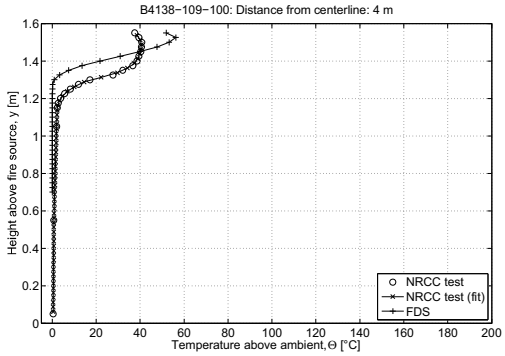

(e) Dist. from centerline: 4 m.

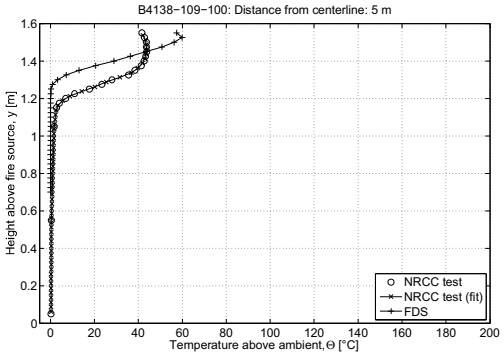

(f) Dist. from centerline: 5 m.

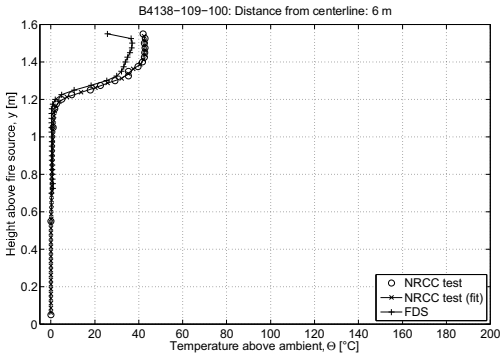

(g) Dist. from centerline: 6 m.

Figure D.5 *B4138-109-100 - Small-scale: Temperature profiles.*

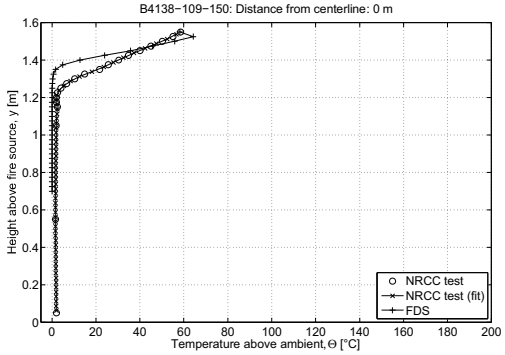

(a) Dist. from centerline: 0 m.

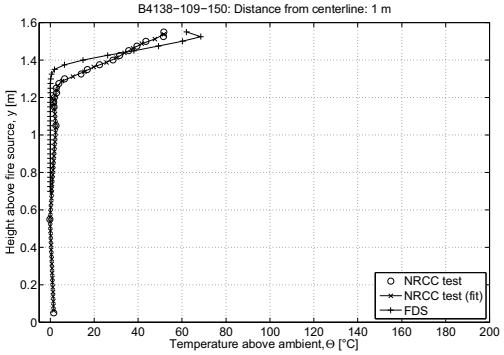

(b) Dist. from centerline: 1 m.

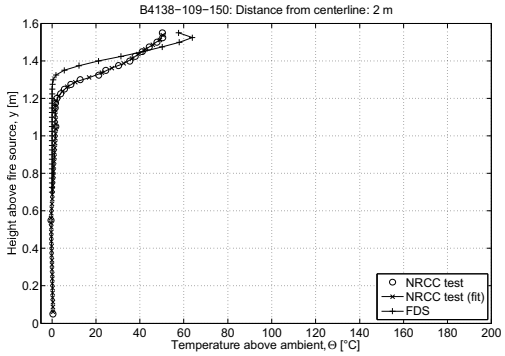

(c) Dist. from centerline: 2 m.

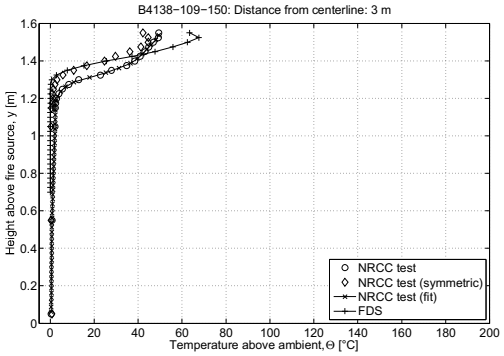

(d) Dist. from centerline: 3 m.

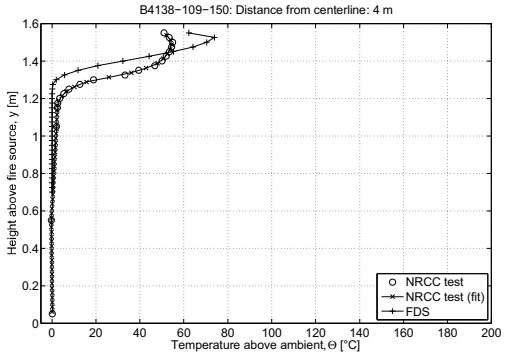

(e) Dist. from centerline: 4 m.

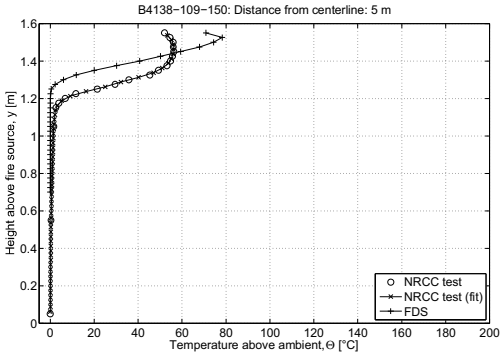

(f) Dist. from centerline: 5 m.

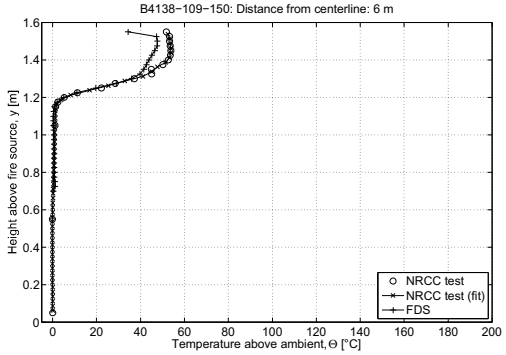

(g) Dist. from centerline: 6 m.

Figure D.6 *B4138-109-150 - Small-scale: Temperature profiles.*

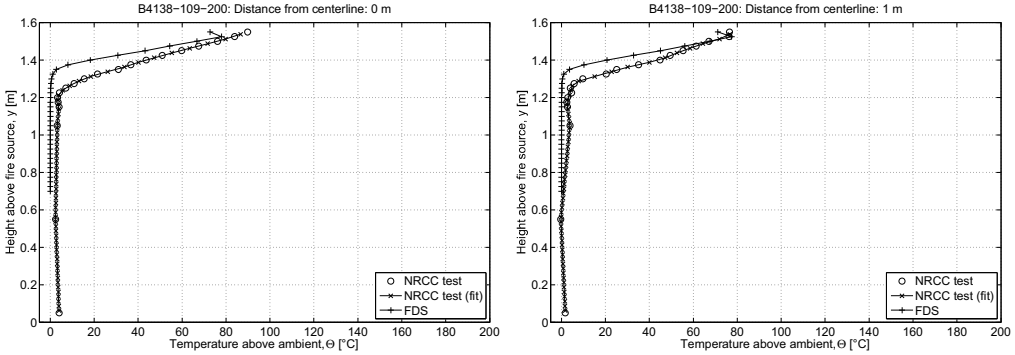

(a) Dist. from centerline: 0 m. (b) Dist. from centerline: 1 m.

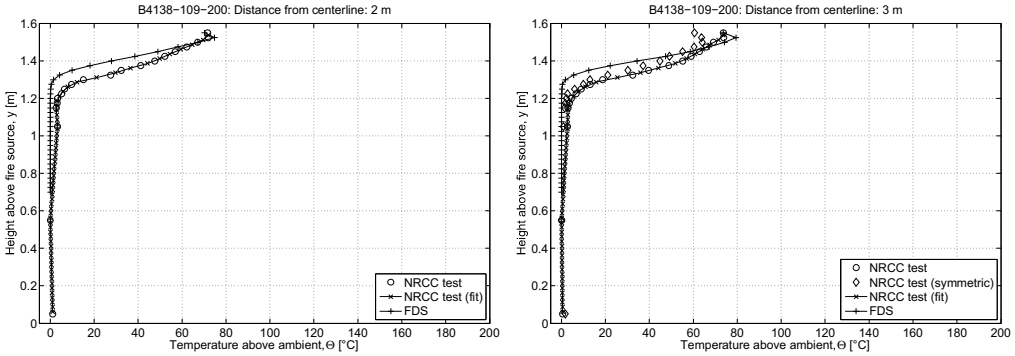

(c) Dist. from centerline: 2 m. (d) Dist. from centerline: 3 m.

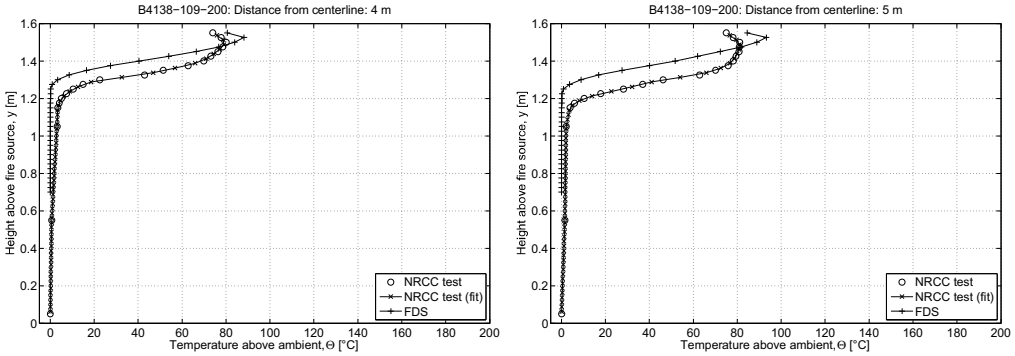

(e) Dist. from centerline: 4 m. (f) Dist. from centerline: 5 m.

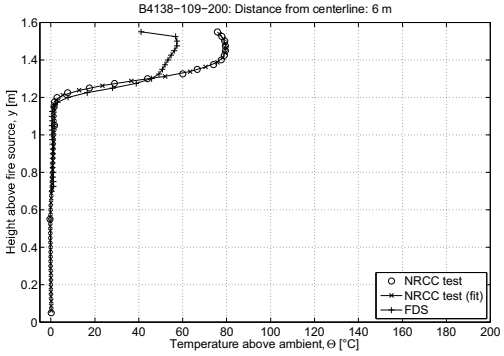

(g) Dist. from centerline: 6 m.

Figure D.7 *B4138-109-200 - Small-scale: Temperature profiles.*

Appendix E

B4138-XXX Small-scale Test Program: Velocity Profiles

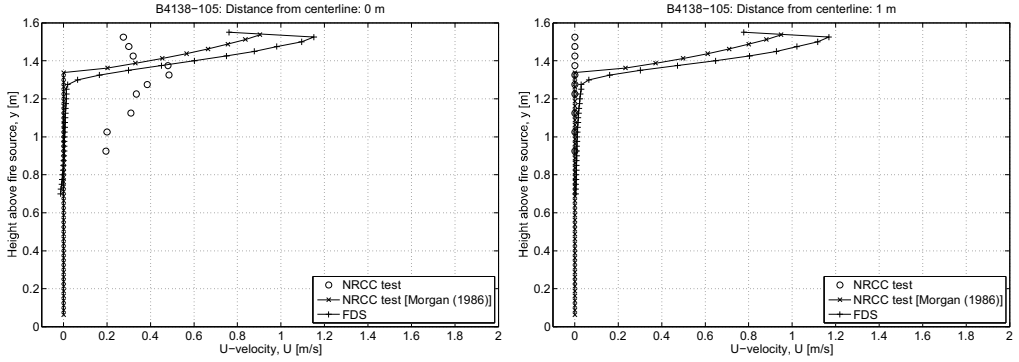

(a) Dist. from centerline: 0 m.

(b) Dist. from centerline: 1 m.

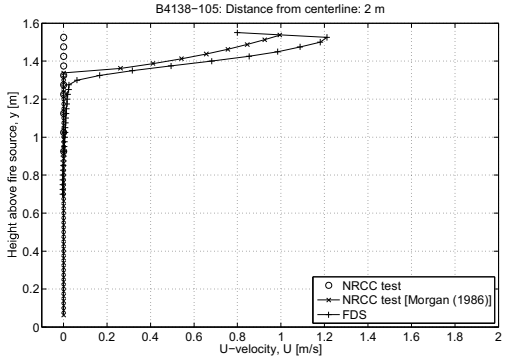

(c) Dist. from centerline: 2 m.

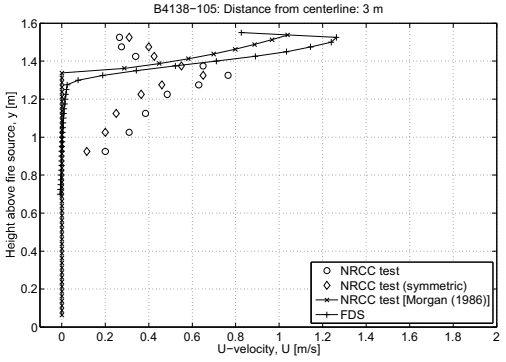

(d) Dist. from centerline: 3 m.

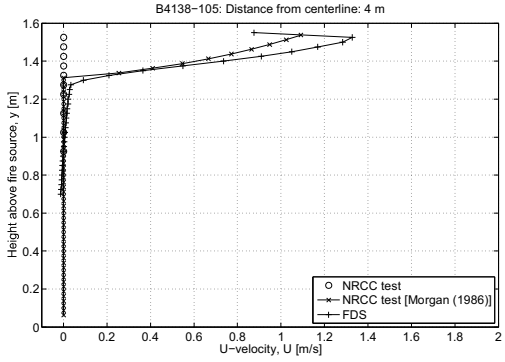

(e) Dist. from centerline: 4 m.

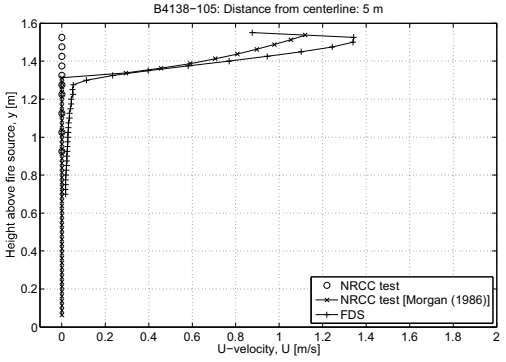

(f) Dist. from centerline: 5 m.

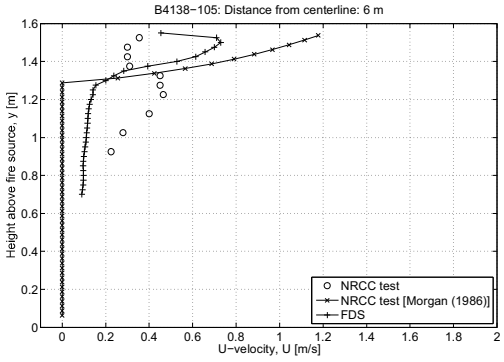

(g) Dist. from centerline: 6 m.

Figure E.1 *B4138-105 - Small-scale: U velocity profiles.*

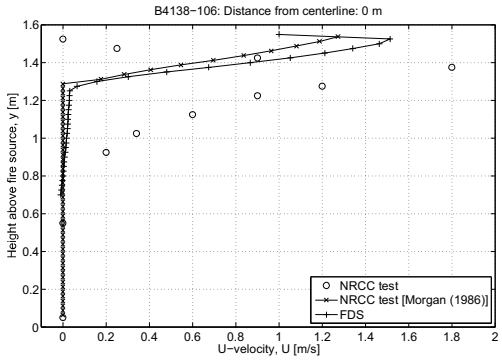

(a) Dist. from centerline: 0 m.

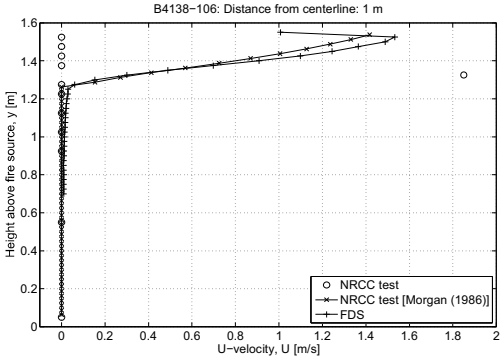

(b) Dist. from centerline: 1 m.

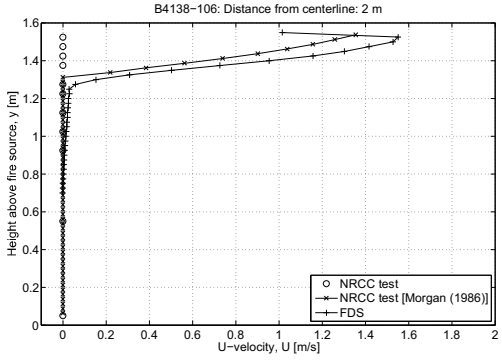

(c) Dist. from centerline: 2 m.

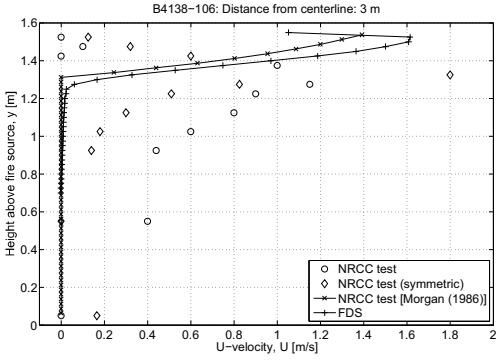

(d) Dist. from centerline: 3 m.

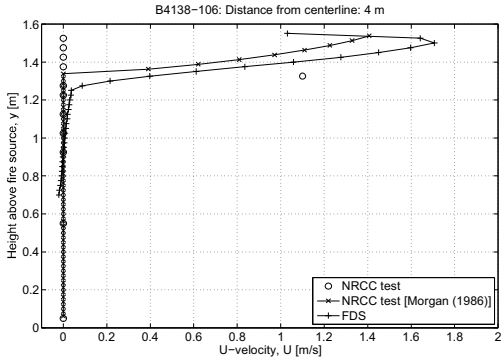

(e) Dist. from centerline: 4 m.

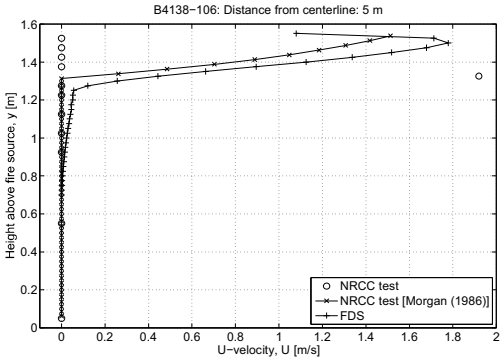

(f) Dist. from centerline: 5 m.

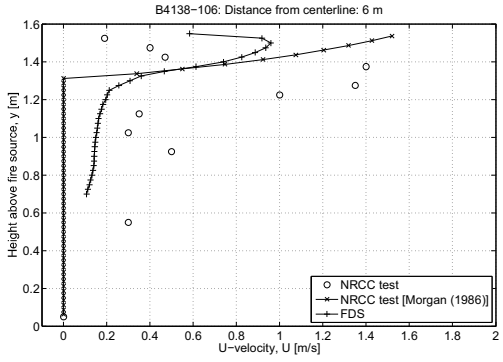

(g) Dist. from centerline: 6 m.

Figure E.2 *B4138-106 - Small-scale: U velocity profiles.*

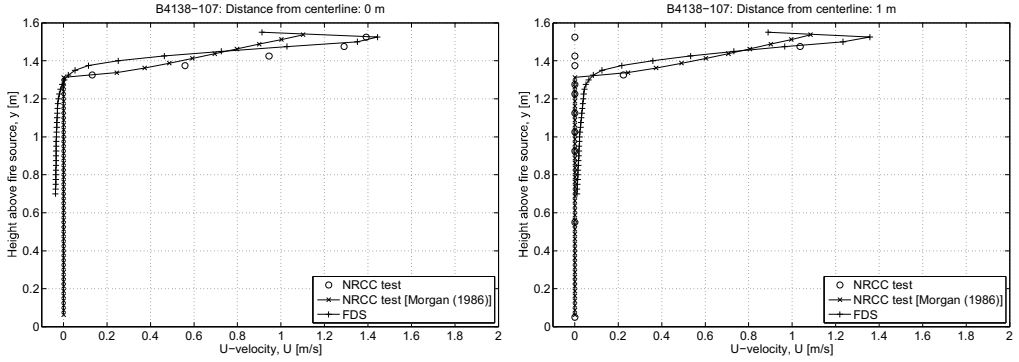

(a) Dist. from centerline: 0 m. (b) Dist. from centerline: 1 m.

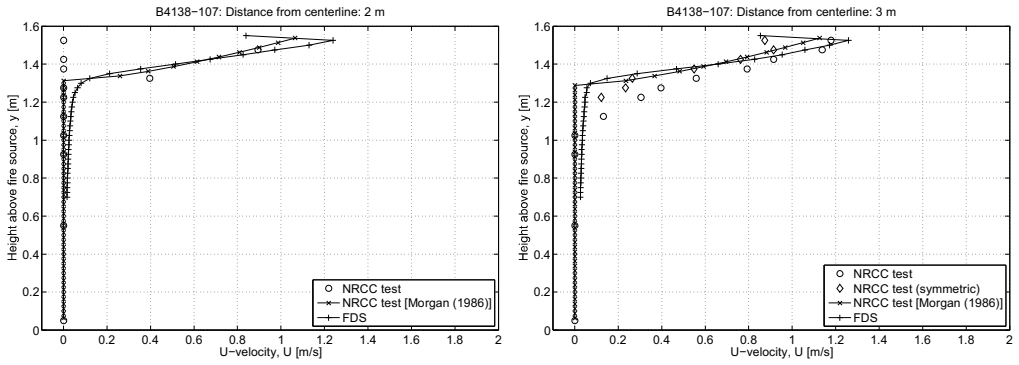

(c) Dist. from centerline: 2 m. (d) Dist. from centerline: 3 m.

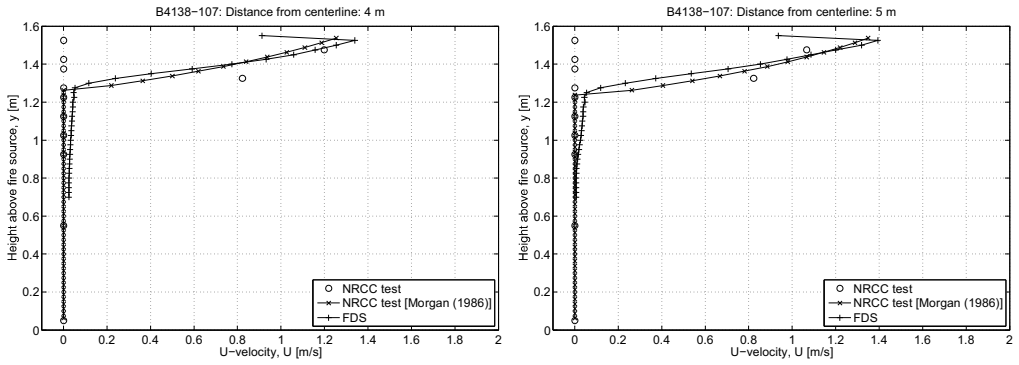

(e) Dist. from centerline: 4 m. (f) Dist. from centerline: 5 m.

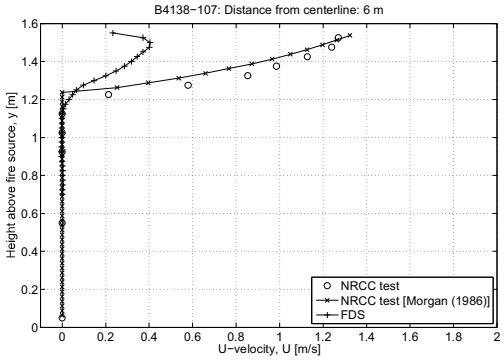

(g) Dist. from centerline: 6 m.

Figure E.3 *B4138-107 - Small-scale: U velocity profiles.*

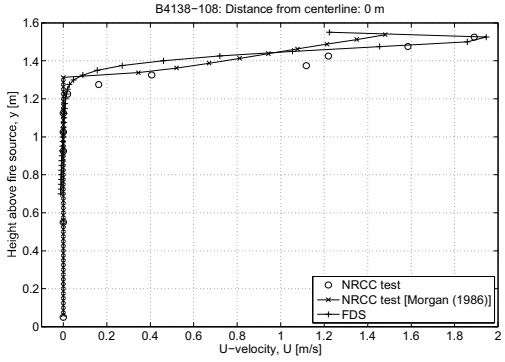

(a) Dist. from centerline: 0 m.

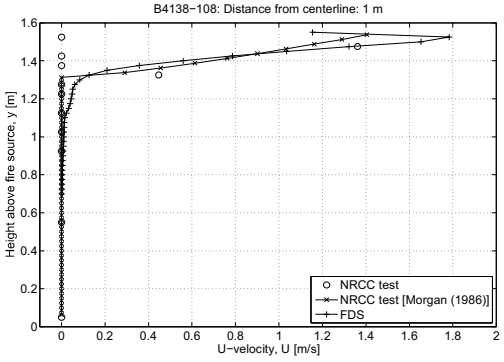

(b) Dist. from centerline: 1 m.

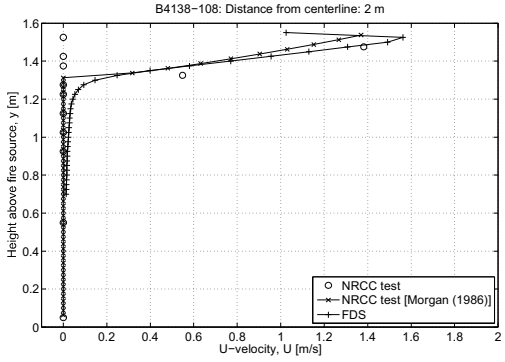

(c) Dist. from centerline: 2 m.

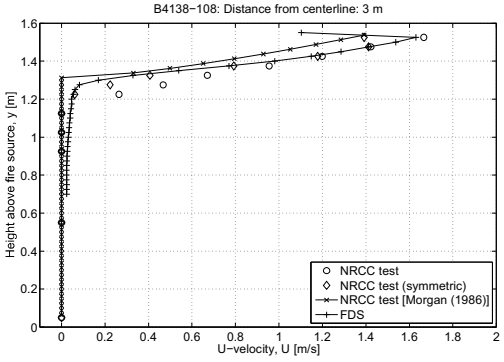

(d) Dist. from centerline: 3 m.

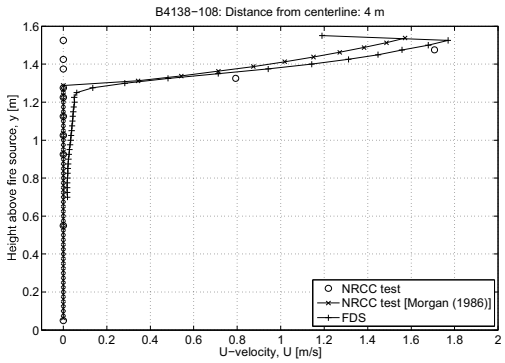

(e) Dist. from centerline: 4 m.

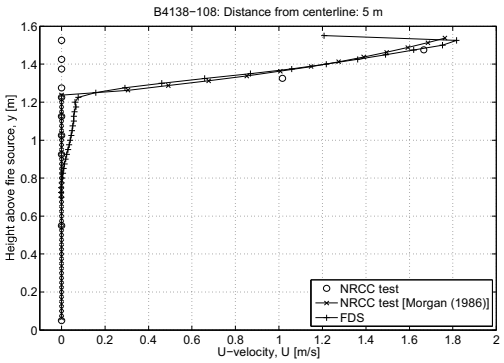

(f) Dist. from centerline: 5 m.

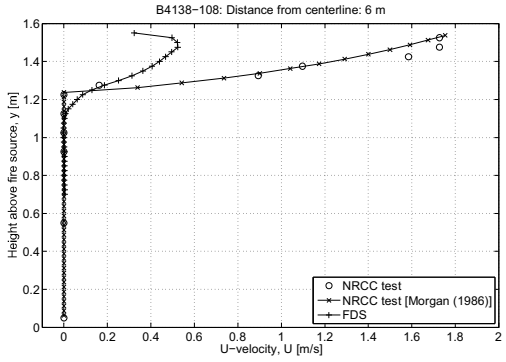

(g) Dist. from centerline: 6 m.

Figure E.4 *B4138-108 - Small-scale: U velocity profiles.*

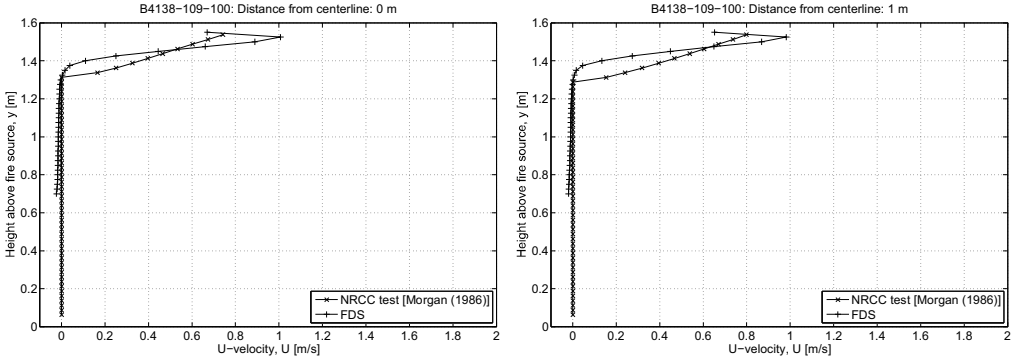

(a) Dist. from centerline: 0 m.

(b) Dist. from centerline: 1 m.

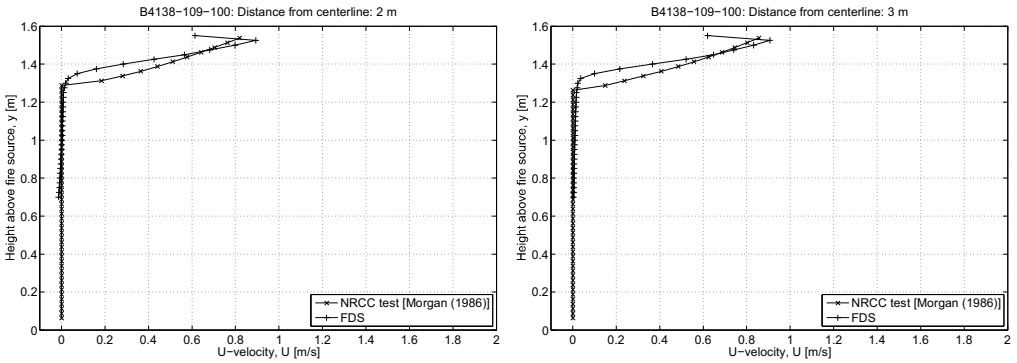

(c) Dist. from centerline: 2 m.

(d) Dist. from centerline: 3 m.

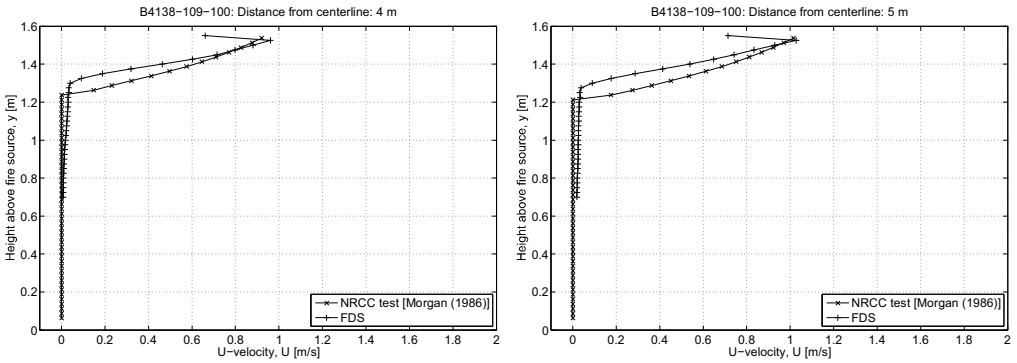

(e) Dist. from centerline: 4 m.

(f) Dist. from centerline: 5 m.

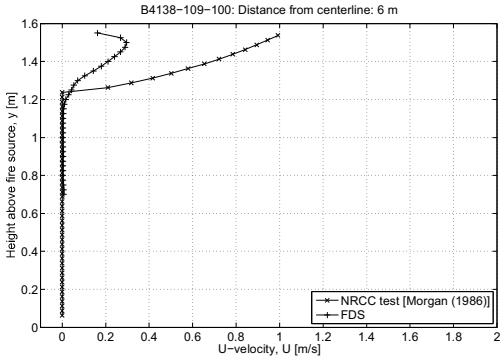

(g) Dist. from centerline: 6 m.

Figure E.5 *B4138-109-100 - Small-scale: U velocity profiles.*

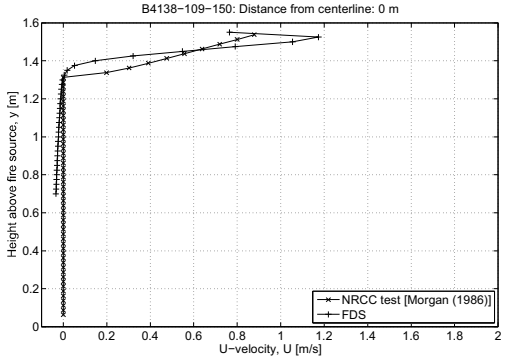

(a) Dist. from centerline: 0 m.

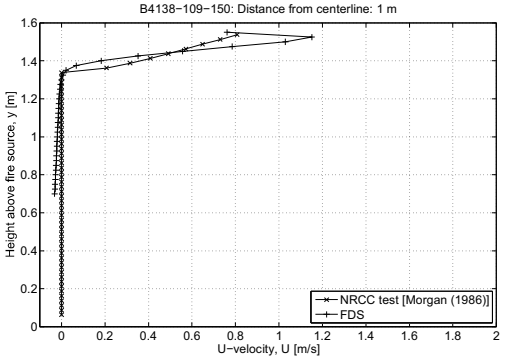

(b) Dist. from centerline: 1 m.

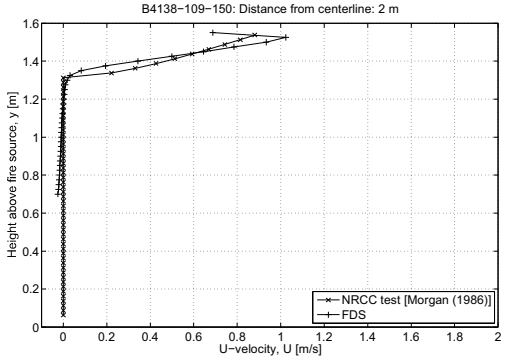

(c) Dist. from centerline: 2 m.

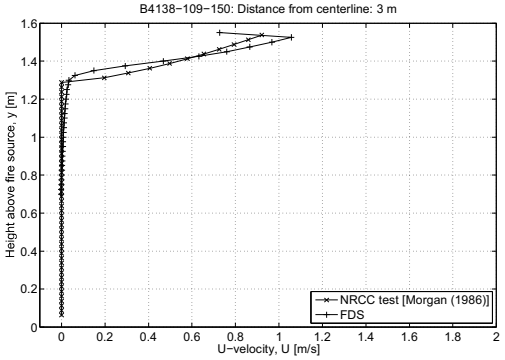

(d) Dist. from centerline: 3 m.

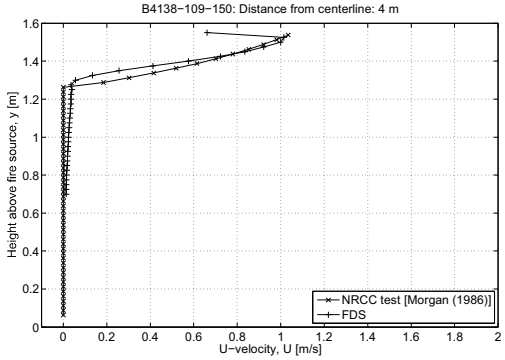

(e) Dist. from centerline: 4 m.

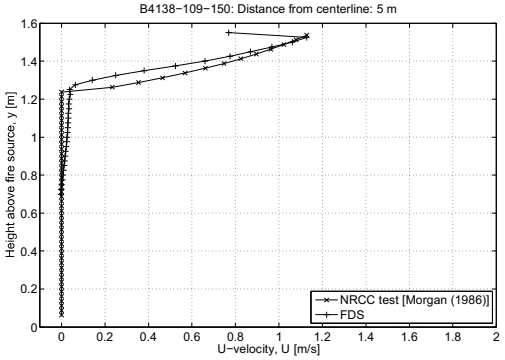

(f) Dist. from centerline: 5 m.

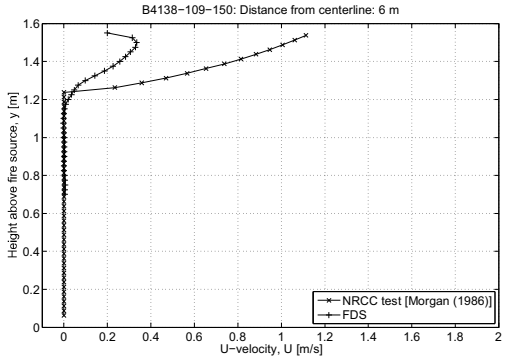

(g) Dist. from centerline: 6 m.

Figure E.6 *B4138-109-150 - Small-scale: U velocity profiles.*

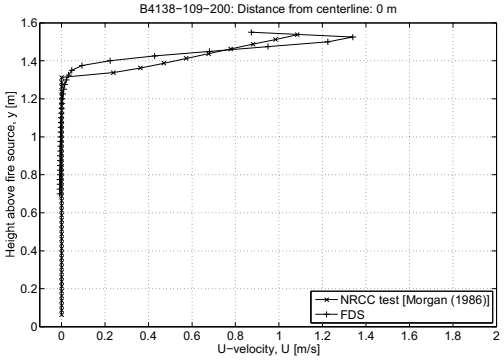

(a) Dist. from centerline: 0 m.

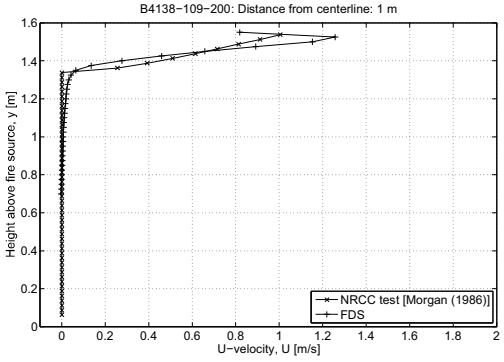

(b) Dist. from centerline: 1 m.

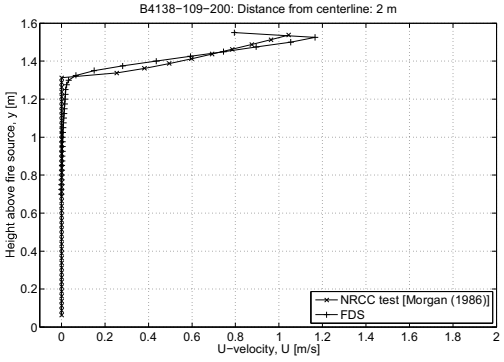

(c) Dist. from centerline: 2 m.

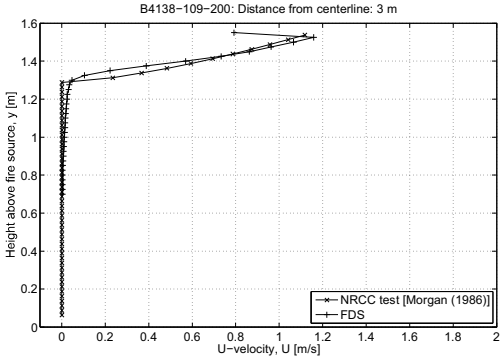

(d) Dist. from centerline: 3 m.

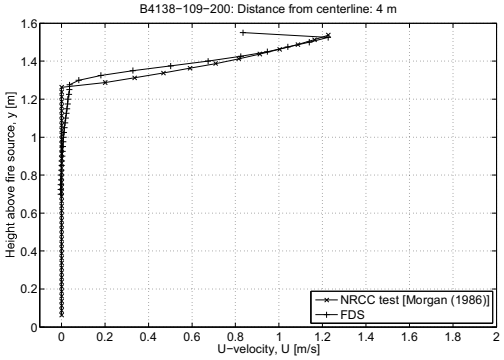

(e) Dist. from centerline: 4 m.

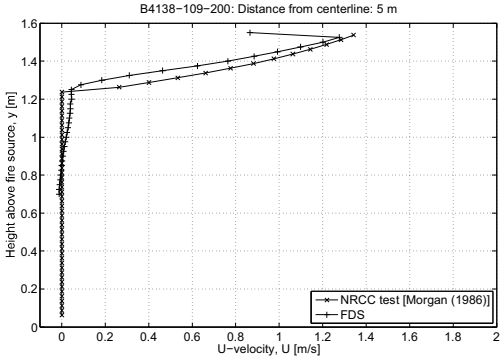

(f) Dist. from centerline: 5 m.

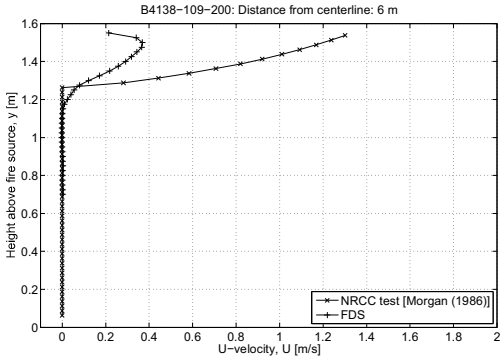

(g) Dist. from centerline: 6 m.

Figure E.7 *B4138-109-200 - Small-scale: U velocity profiles.*

Appendix F

B4138 Scaling Laws: Temperature Profiles

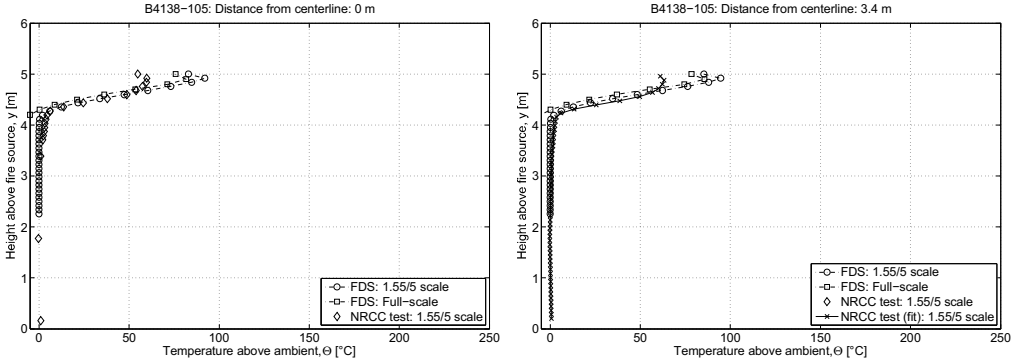

(a) Dist. from centerline: 0 m.

(b) Dist. from centerline: 3.4 m.

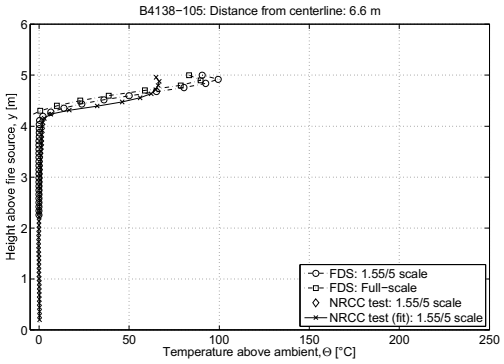

(c) Dist. from centerline: 6.6 m.

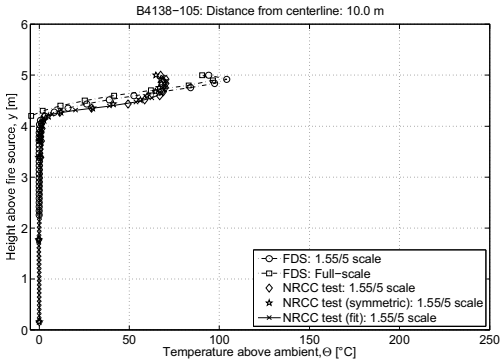

(d) Dist. from centerline: 10.0 m.

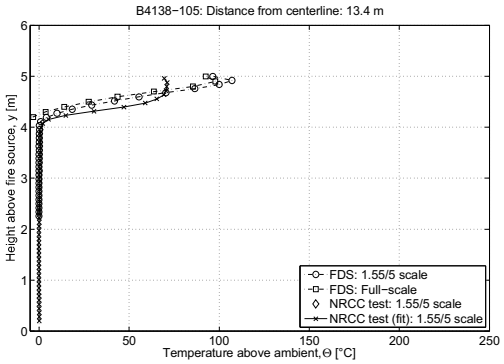

(e) Dist. from centerline: 13.4 m.

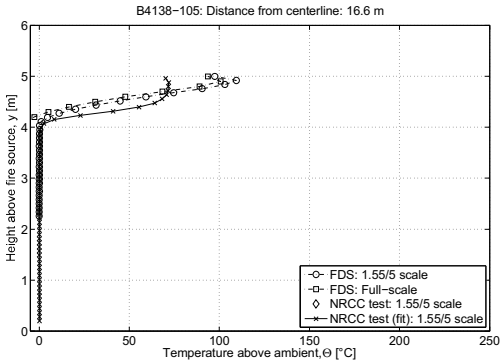

(f) Dist. from centerline: 16.6 m.

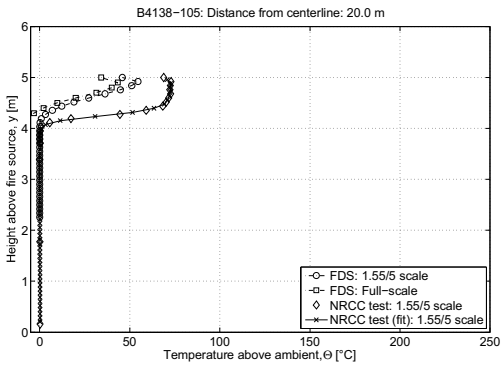

(g) Dist. from centerline: 20.0 m.

Figure F.1 *B4138-105: Temperature profiles.*

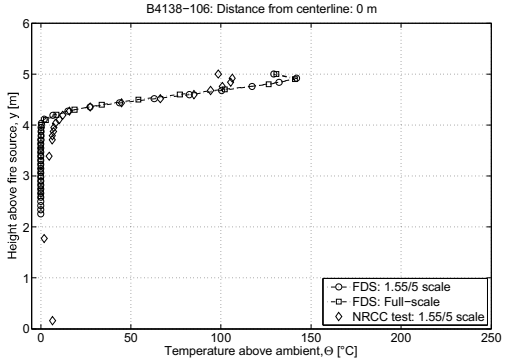

(a) Dist. from centerline: 0.0 m.

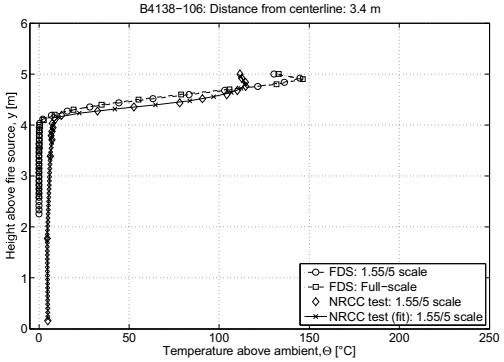

(b) Dist. from centerline: 3.4 m.

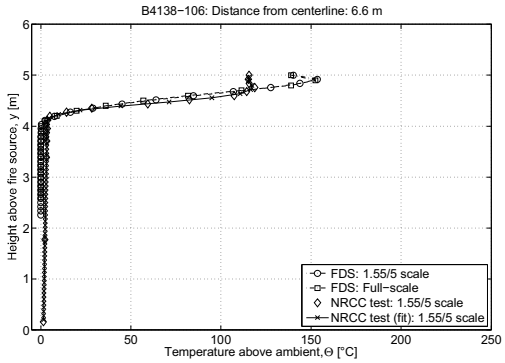

(c) Dist. from centerline: 6.6 m.

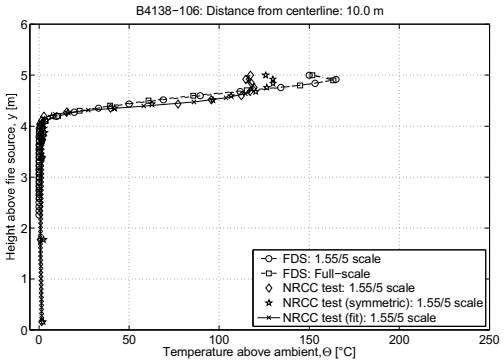

(d) Dist. from centerline: 10.0 m.

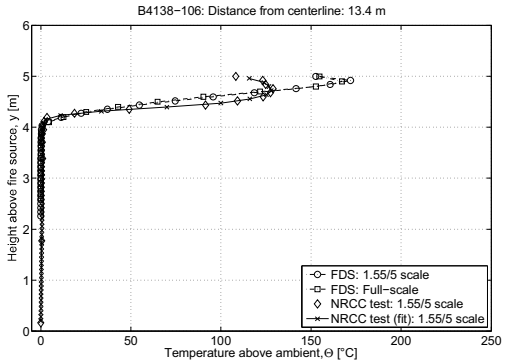

(e) Dist. from centerline: 13.4 m.

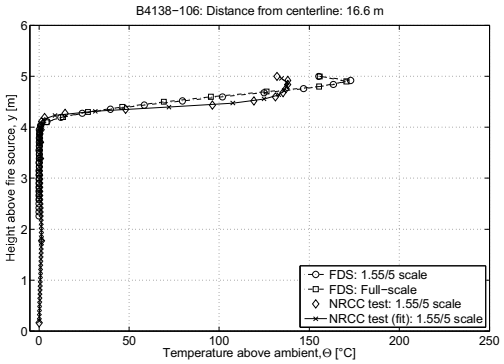

(f) Dist. from centerline: 16.6 m.

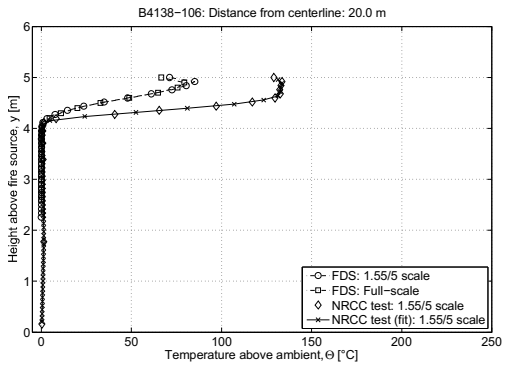

(g) Dist. from centerline: 20.0 m.

Figure F.2 *B4138-106: Temperature profiles.*

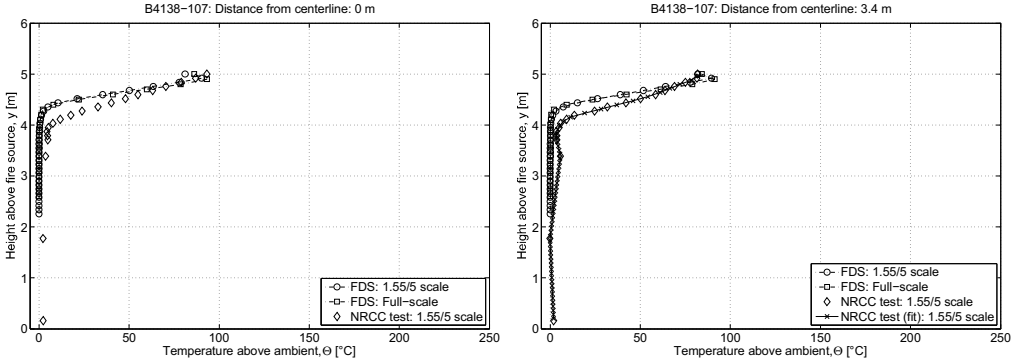

(a) Dist. from centerline: 0.0 m.

(b) Dist. from centerline: 3.4 m.

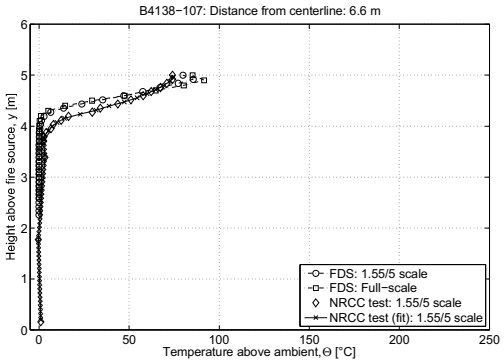

(c) Dist. from centerline: 6.6 m.

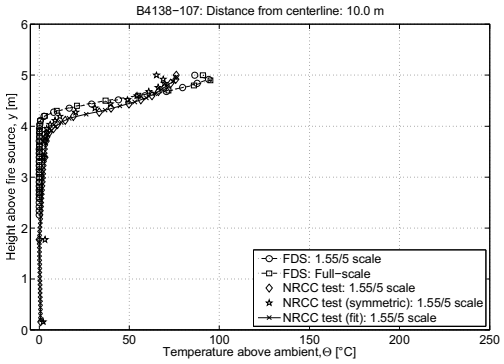

(d) Dist. from centerline: 10.0 m.

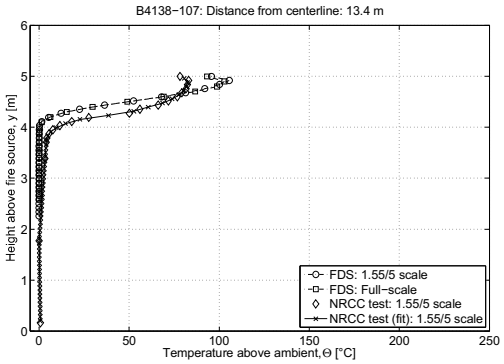

(e) Dist. from centerline: 13.4 m.

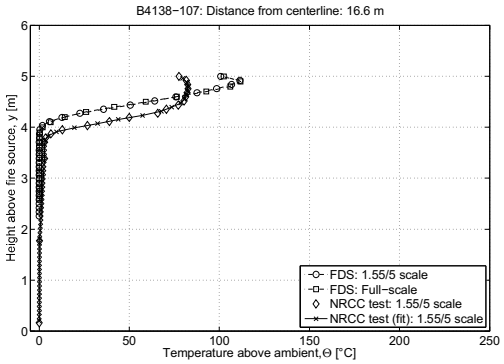

(f) Dist. from centerline: 16.6 m.

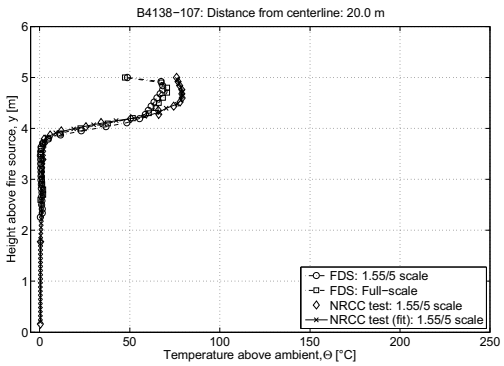

(g) Dist. from centerline: 20.0 m.

Figure F.3 *B4138-107: Temperature profiles.*

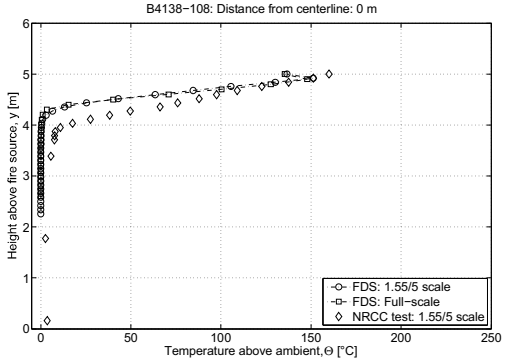

(a) Dist. from centerline: 0.0 m.

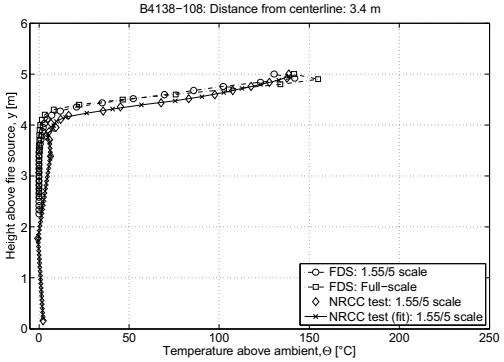

(b) Dist. from centerline: 3.4 m.

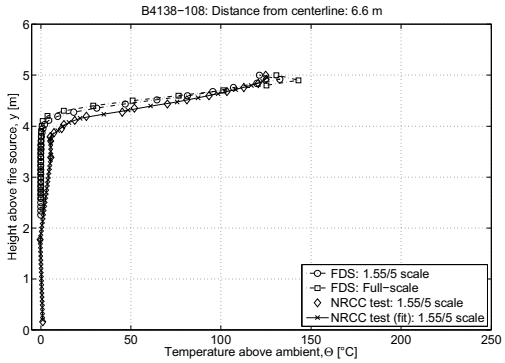

(c) Dist. from centerline: 6.6 m.

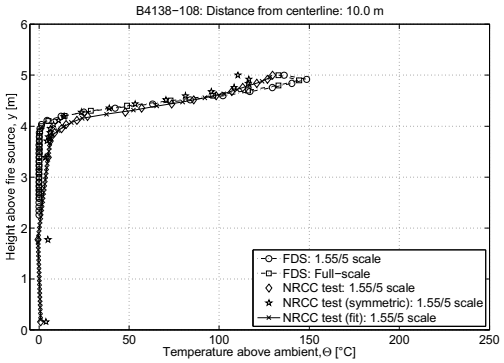

(d) Dist. from centerline: 10.0 m.

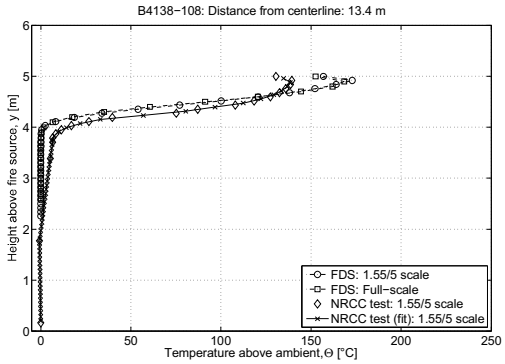

(e) Dist. from centerline: 13.4 m.

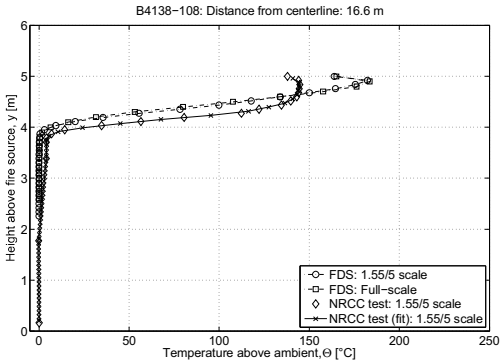

(f) Dist. from centerline: 16.6 m.

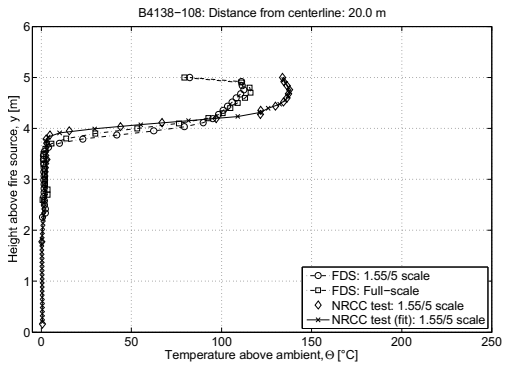

(g) Dist. from centerline: 20.0 m.

Figure F.4 *B4138-108: Temperature profiles.*

Appendix G

B4138 Scaling Laws: Velocity Profiles

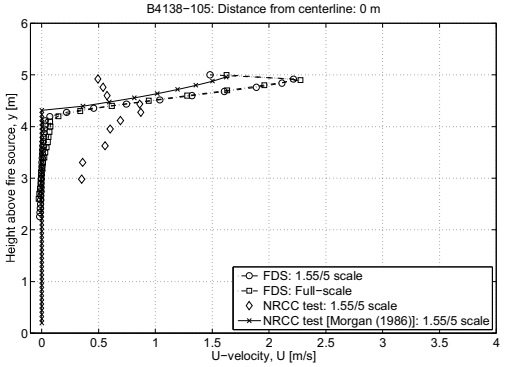

(a) Dist. from centerline: 0.0 m.

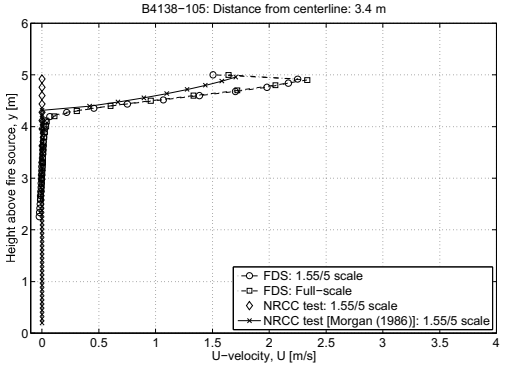

(b) Dist. from centerline: 3.4 m.

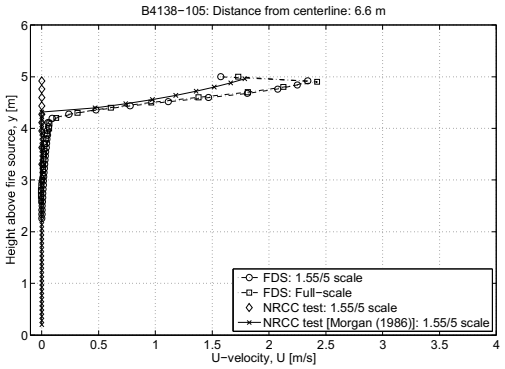

(c) Dist. from centerline: 6.6 m.

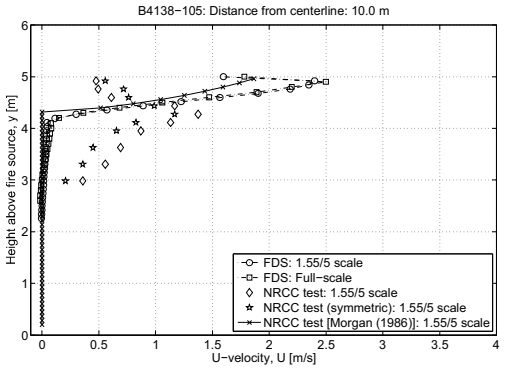

(d) Dist. from centerline: 10.0 m.

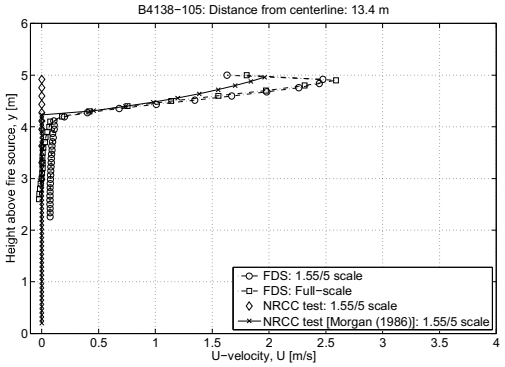

(e) Dist. from centerline: 13.4 m.

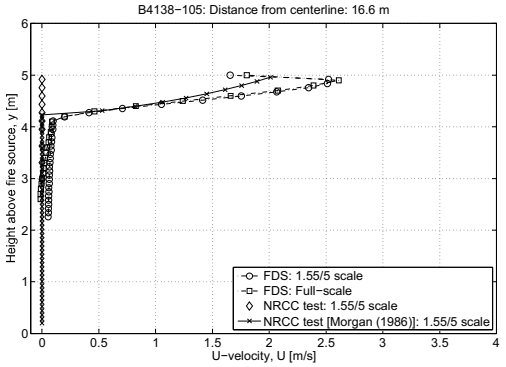

(f) Dist. from centerline: 16.6 m.

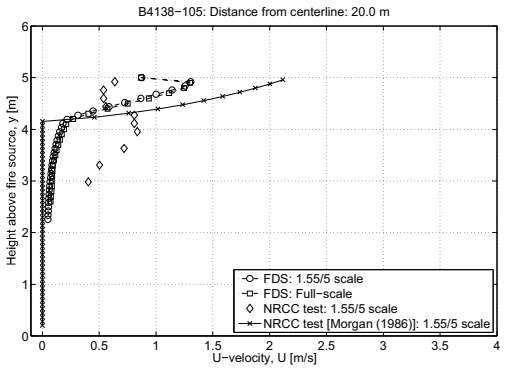

(g) Dist. from centerline: 20.0 m.

Figure G.1 *B4138-105: U velocity profiles.*

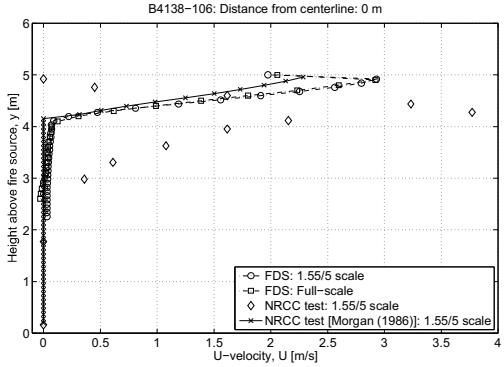

(a) Dist. from centerline: 0.0 m.

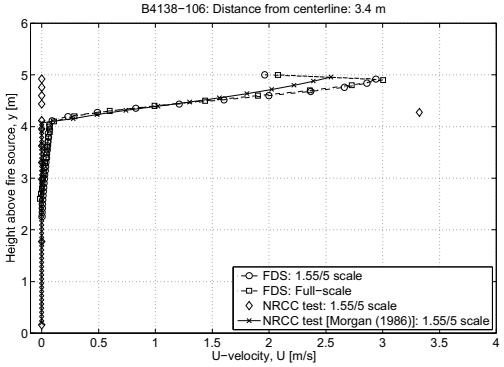

(b) Dist. from centerline: 3.4 m.

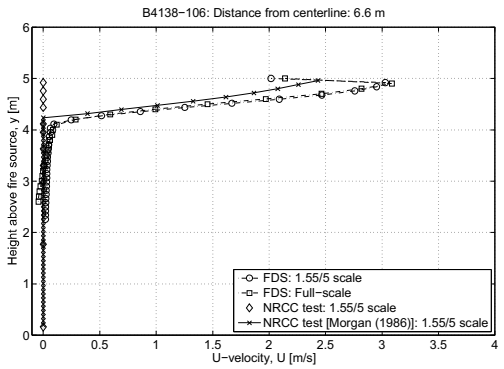

(c) Dist. from centerline: 6.6 m.

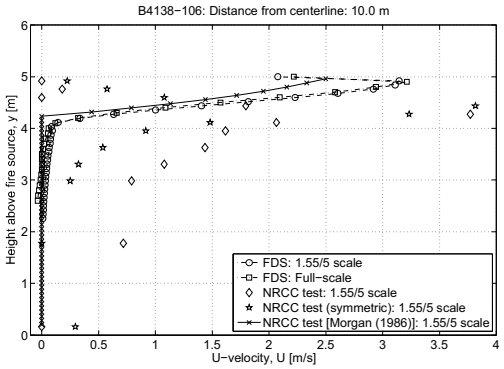

(d) Dist. from centerline: 10.0 m.

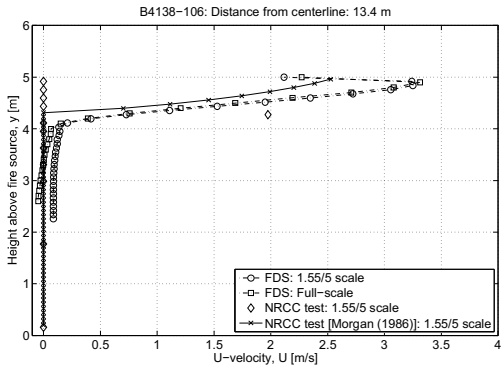

(e) Dist. from centerline: 13.4 m.

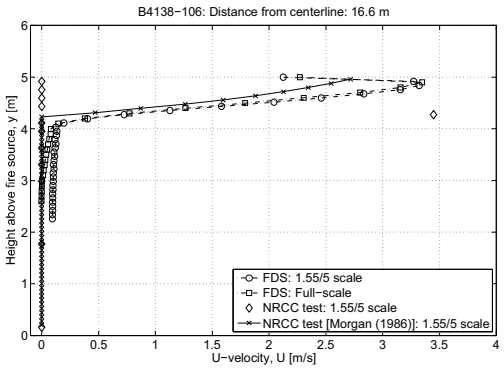

(f) Dist. from centerline: 16.6 m.

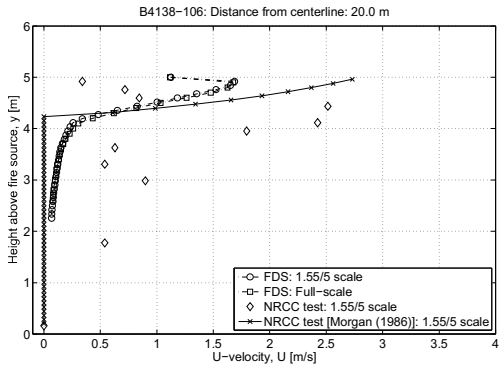

(g) Dist. from centerline: 20.0 m.

Figure G.2 *B4138-106: U velocity profiles.*

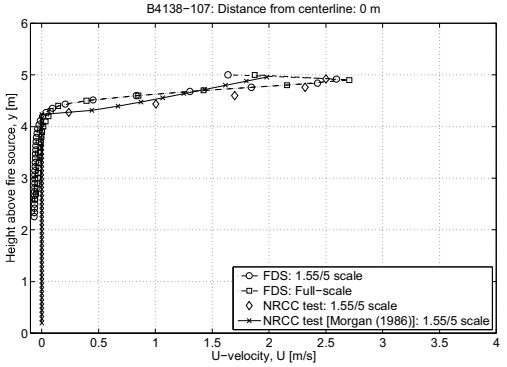

(a) Dist. from centerline: 0.0 m.

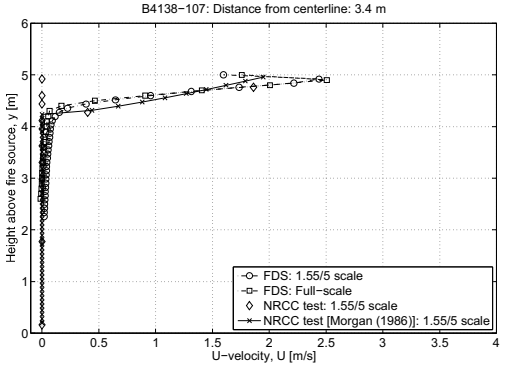

(b) Dist. from centerline: 3.4 m.

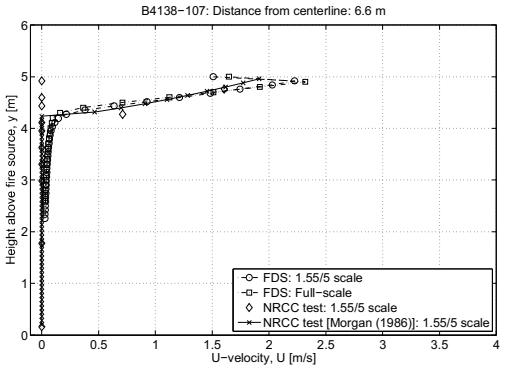

(c) Dist. from centerline: 6.6 m.

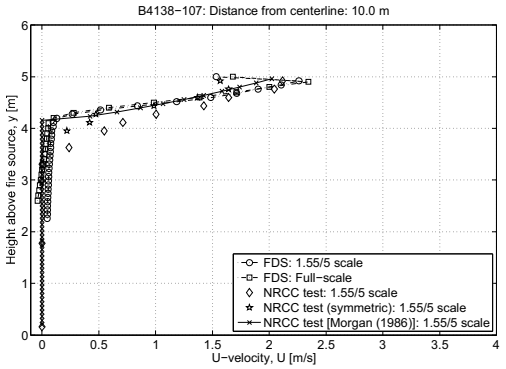

(d) Dist. from centerline: 10.0 m.

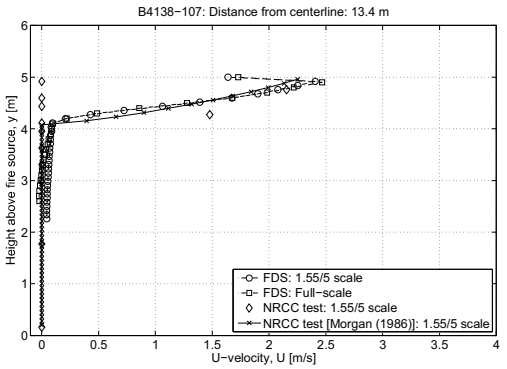

(e) Dist. from centerline: 13.4 m.

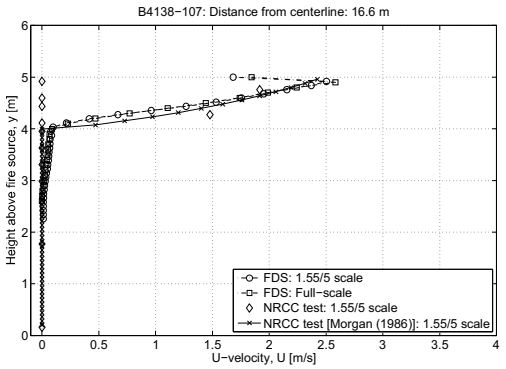

(f) Dist. from centerline: 16.6 m.

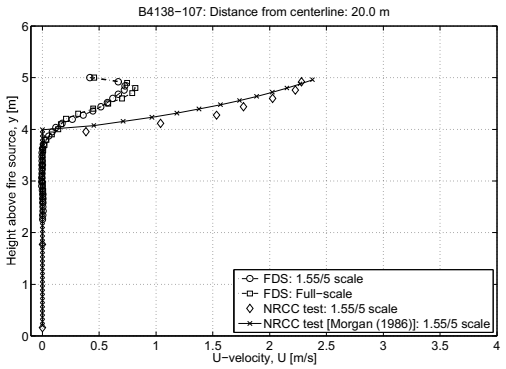

(g) Dist. from centerline: 20.0 m.

Figure G.3 *B4138-107: U velocity profiles.*

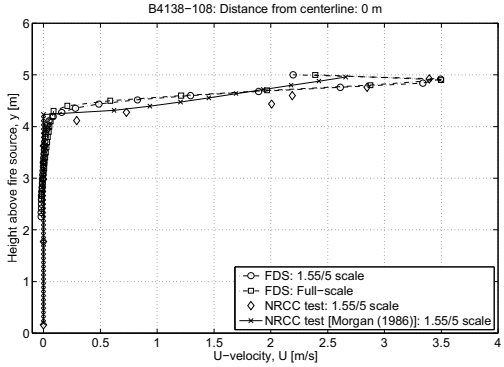

(a) Dist. from centerline: 0.0 m.

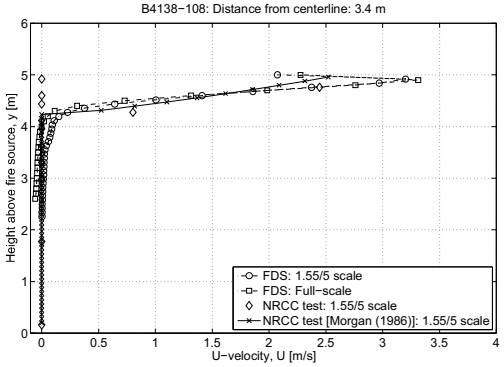

(b) Dist. from centerline: 3.4 m.

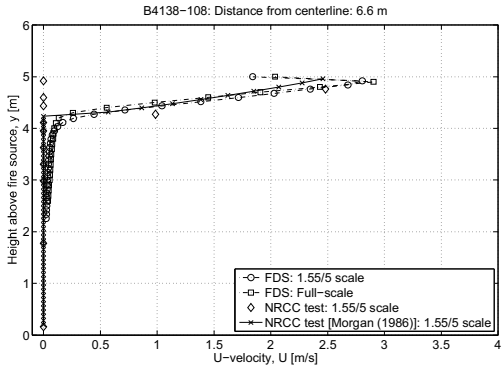

(c) Dist. from centerline: 6.6 m.

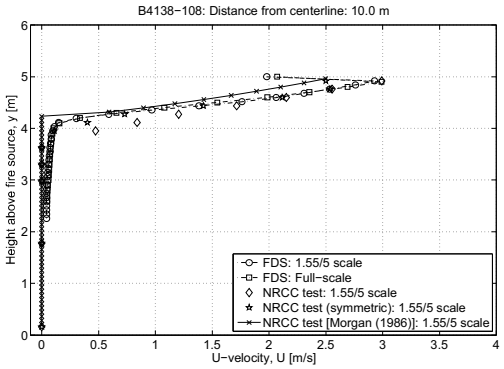

(d) Dist. from centerline: 10.0 m.

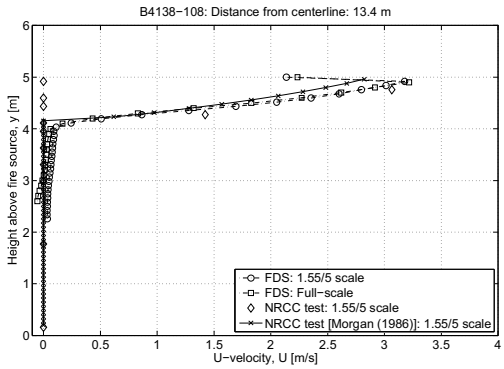

(e) Dist. from centerline: 13.4 m.

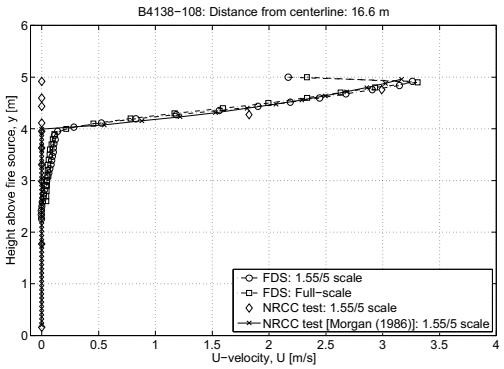

(f) Dist. from centerline: 16.6 m.

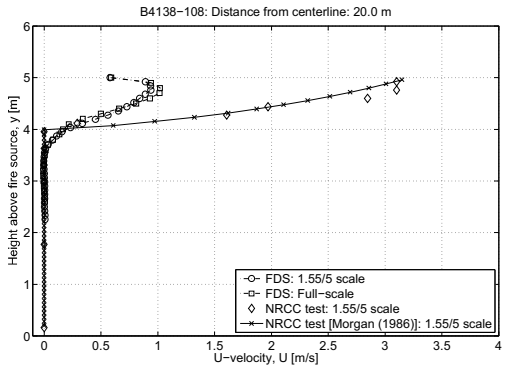

(g) Dist. from centerline: 20.0 m.

Figure G.4 *B4138-108: U velocity profiles.*

Appendix H

B4138-108 Full-scale Test Program: Assessing Sub-model Dependency

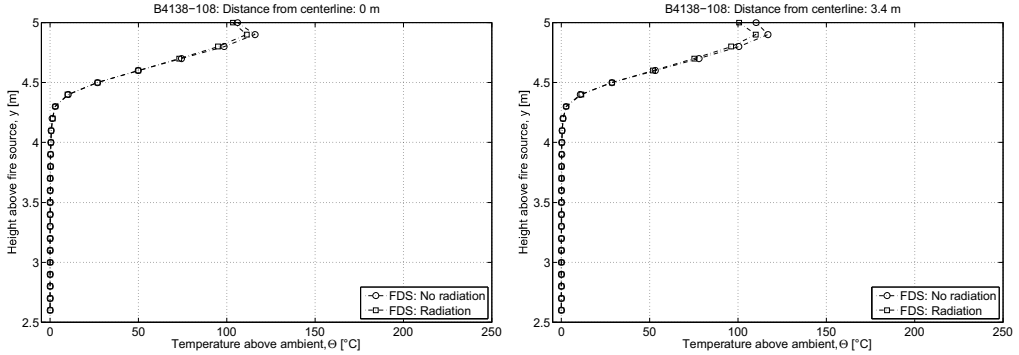

(a) Dist. from centerline: 0 m. (b) Dist. from centerline: 3.4 m.

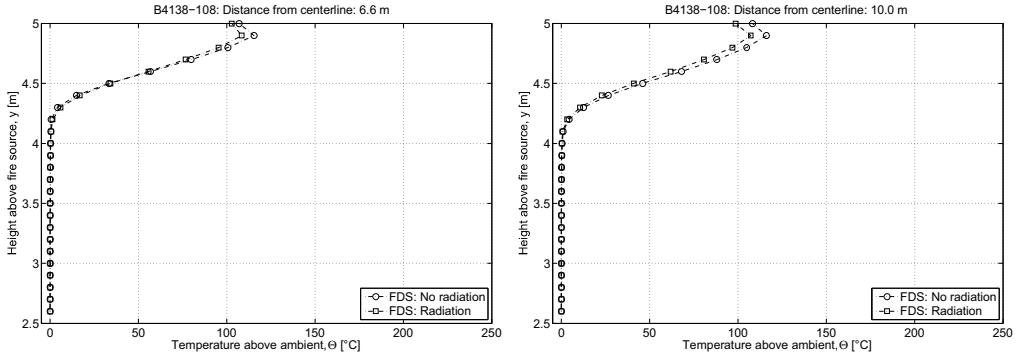

(c) Dist. from centerline: 6.6 m. (d) Dist. from centerline: 10.0 m.

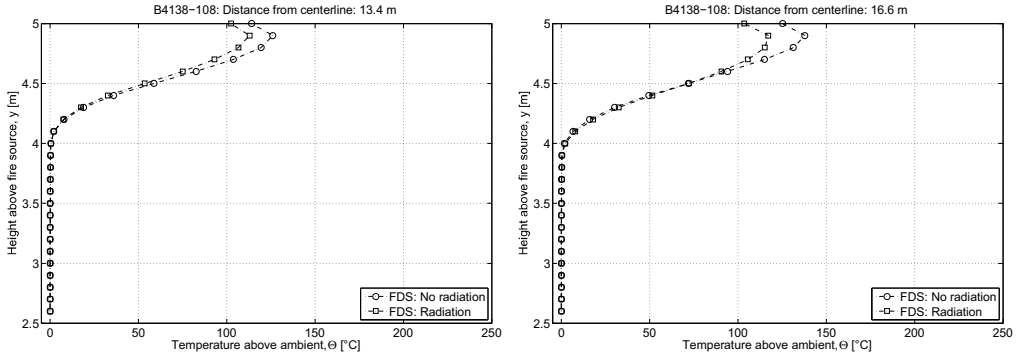

(e) Dist. from centerline: 13.4 m. (f) Dist. from centerline: 16.6 m.

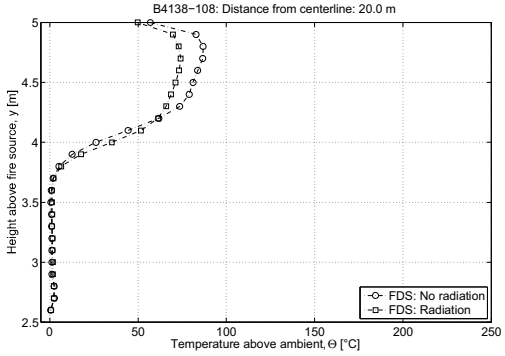

(g) Dist. from centerline: 20.0 m.

Figure H.1 *B4138-108 - Full-scale: Temperature profiles.*

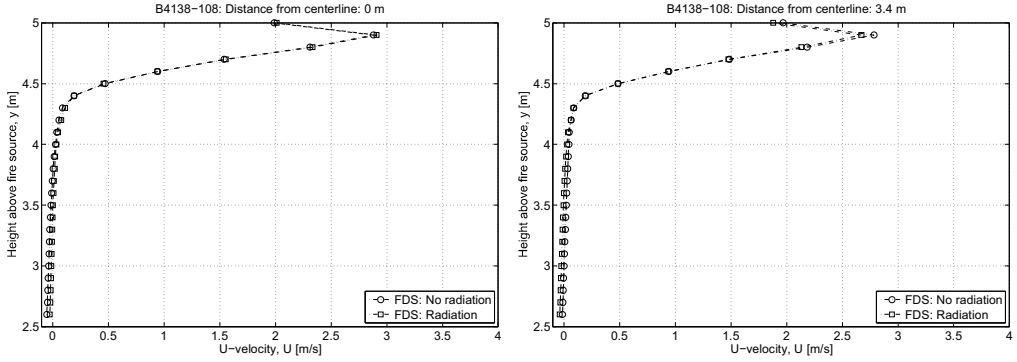

(a) Dist. from centerline: 0 m. (b) Dist. from centerline: 3.4 m.

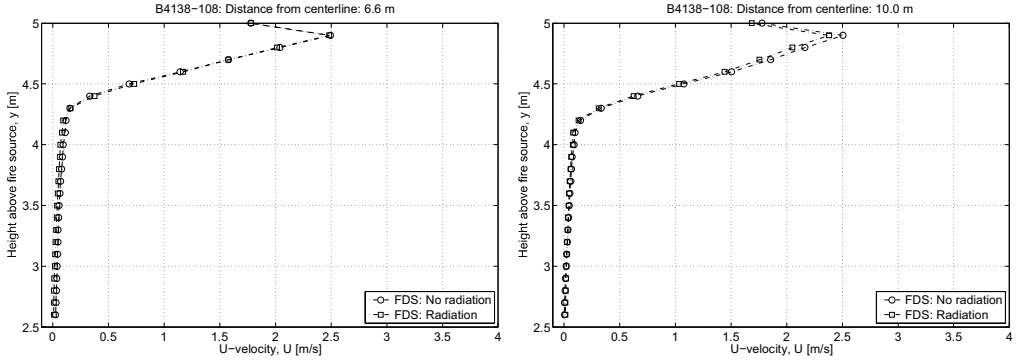

(c) Dist. from centerline: 6.6 m. (d) Dist. from centerline: 10 m.

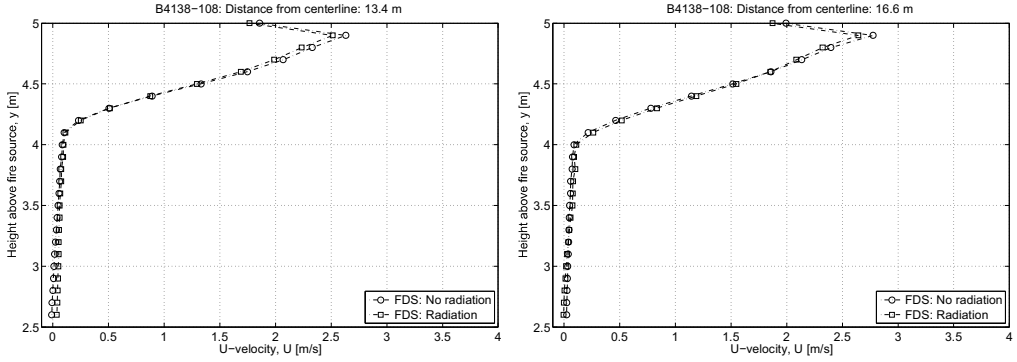

(e) Dist. from centerline: 13.4 m. (f) Dist. from centerline: 16.6 m.

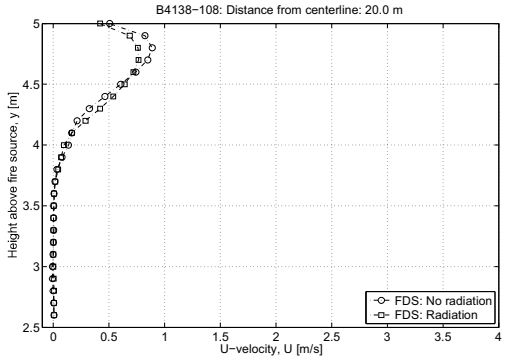

(g) Dist. from centerline: 20 m.

Figure H.2 *B4138-108 - Full-scale: U velocity profiles.*

Appendix I

Scaling the Full-scale Approach Flow CFD-model

Simulation ID	**Scaling**	$\dot{\mathbf{Q}}_{\mathbf{T}}$	$\mathbf{d_d}$	$\mathbf{D_{fb}}$	$\mathbf{W_w}$	$\mathbf{D_{fc}}$	$\mathbf{W_{fc}}$	$\mathbf{H_{fc}}$
WOSP007-075-ND	4/5	2860	0.0	18.0	5.8	24.8	25.6	4.0
WOSP014-075-ND	4/5	2860	0.0	18.0	11.5	24.8	25.6	4.0
WOSP028-075-ND	4/5	2860	0.0	18.0	22.4	24.8	25.6	4.0
WOSP040-075-ND	4/5	2860	0.0	18.0	32.0	24.8	35.2	4.0
WOSP058-075-ND	4/5	2860	0.0	18.0	46.4	24.8	49.6	4.0
WOSP087-075-ND	4/5	2860	0.0	18.0	69.8	24.8	73.0	4.0
WOSP007-050-ND	4/5	2860	0.0	12.5	5.8	24.8	25.6	4.0
WOSP014-050-ND	4/5	2860	0.0	12.5	11.5	24.8	25.6	4.0
WOSP028-050-ND	4/5	2860	0.0	12.5	22.4	24.8	25.6	4.0
WOSP040-050-ND	4/5	2860	0.0	12.5	32.0	24.8	35.2	4.0
WOSP058-050-ND	4/5	2860	0.0	12.5	46.4	24.8	49.6	4.0
WOSP087-050-ND	4/5	2860	0.0	12.5	69.8	24.8	73.0	4.0
WOSP007-025-ND	4/5	2860	0.0	6.3	5.8	24.8	25.6	4.0
WOSP014-025-ND	4/5	2860	0.0	6.3	11.5	24.8	25.6	4.0
WOSP028-025-ND	4/5	2860	0.0	6.3	22.4	24.8	25.6	4.0
WOSP040-025-ND	4/5	2860	0.0	6.3	32.0	24.8	35.2	4.0
WOSP058-025-ND	4/5	2860	0.0	6.3	46.4	24.8	49.6	4.0
WOSP087-025-ND	4/5	2860	0.0	6.3	69.8	24.8	73.0	4.0
WOSP007-075-D	4/5	2860	0.8	18.0	5.8	24.8	25.6	4.0
WOSP014-075-D	4/5	2860	0.8	18.0	11.5	24.8	25.6	4.0
WOSP028-075-D	4/5	2860	0.8	18.0	22.4	24.8	25.6	4.0
WOSP040-075-D	4/5	2860	0.8	18.0	32.0	24.8	35.2	4.0
WOSP058-075-D	4/5	2860	0.8	18.0	46.4	24.8	49.6	4.0
WOSP087-075-D	4/5	2860	0.8	18.0	69.8	24.8	73.0	4.0
WOSP007-050-D	4/5	2860	0.8	12.5	5.8	24.8	25.6	4.0
WOSP014-050-D	4/5	2860	0.8	12.5	11.5	24.8	25.6	4.0
WOSP028-050-D	4/5	2860	0.8	12.5	22.4	24.8	25.6	4.0
WOSP040-050-D	4/5	2860	0.8	12.5	32.0	24.8	35.2	4.0
WOSP058-050-D	4/5	2860	0.8	12.5	46.4	24.8	49.6	4.0
WOSP087-050-D	4/5	2860	0.8	12.5	69.8	24.8	73.0	4.0
WOSP007-025-D	4/5	2860	0.8	6.3	5.8	24.8	25.6	4.0
WOSP014-025-D	4/5	2860	0.8	6.3	11.5	24.8	25.6	4.0
WOSP028-025-D	4/5	2860	0.8	6.3	22.4	24.8	25.6	4.0
WOSP040-025-D	4/5	2860	0.8	6.3	32.0	24.8	35.2	4.0
WOSP058-025-D	4/5	2860	0.8	6.3	46.4	24.8	49.6	4.0
WOSP087-025-D	4/5	2860	0.8	6.3	69.8	24.8	73.0	4.0
WOSP014-075-ND-1430	4/5	1430	0.0	18.0	11.5	24.8	25.6	4.0
WOSP028-075-ND-1430	4/5	1430	0.0	18.0	22.4	24.8	25.6	4.0
WOSP040-075-ND-1430	4/5	1430	0.0	18.0	32.0	24.8	35.2	4.0
WOSP040-075-ND-4230	4/5	4230	0.0	18.0	32.0	24.8	35.2	4.0
WOSP058-075-ND-4230	4/5	4230	0.0	18.0	46.4	24.8	49.6	4.0
WOSP087-075-ND-4230	4/5	4230	0.0	18.0	69.8	24.8	73.0	4.0

Table I.1 *List of simulations scaled 4/5.*

Simulation ID	**Scaling**	$\dot{\mathbf{Q}}_{\mathbf{T}}$	$\mathbf{d_d}$	$\mathbf{D_{fb}}$	$\mathbf{W_w}$	$\mathbf{D_{fc}}$	$\mathbf{W_{fc}}$	$\mathbf{H_{fc}}$
WOSP007-075-ND	3/5	1400	0.0	13.4	4.3	18.6	19.2	3.0
WOSP014-075-ND	3/5	1400	0.0	13.4	8.6	18.6	19.2	3.0
WOSP028-075-ND	3/5	1400	0.0	13.4	16.8	18.6	19.2	3.0
WOSP040-075-ND	3/5	1400	0.0	13.4	24.0	18.6	26.4	3.0
WOSP058-075-ND	3/5	1400	0.0	13.4	34.8	18.6	37.2	3.0
WOSP087-075-ND	3/5	1400	0.0	13.4	52.3	18.6	54.7	3.0
WOSP007-050-ND	3/5	1400	0.0	9.4	4.3	18.6	19.2	3.0
WOSP014-050-ND	3/5	1400	0.0	9.4	8.6	18.6	19.2	3.0
WOSP028-050-ND	3/5	1400	0.0	9.4	16.8	18.6	19.2	3.0
WOSP040-050-ND	3/5	1400	0.0	9.4	24.0	18.6	26.4	3.0
WOSP058-050-ND	3/5	1400	0.0	9.4	34.8	18.6	37.2	3.0
WOSP087-050-ND	3/5	1400	0.0	9.4	52.3	18.6	54.7	3.0
WOSP007-025-ND	3/5	1400	0.0	4.7	4.3	18.6	19.2	3.0
WOSP014-025-ND	3/5	1400	0.0	4.7	8.6	18.6	19.2	3.0
WOSP028-025-ND	3/5	1400	0.0	4.7	16.8	18.6	19.2	3.0
WOSP040-025-ND	3/5	1400	0.0	4.7	24.0	18.6	26.4	3.0
WOSP058-025-ND	3/5	1400	0.0	4.7	34.8	18.6	37.2	3.0
WOSP087-025-ND	3/5	1400	0.0	4.7	52.3	18.6	54.7	3.0
WOSP007-075-D	3/5	1400	0.6	13.4	4.3	18.6	19.2	3.0
WOSP014-075-D	3/5	1400	0.6	13.4	8.6	18.6	19.2	3.0
WOSP028-075-D	3/5	1400	0.6	13.4	16.8	18.6	19.2	3.0
WOSP040-075-D	3/5	1400	0.6	13.4	24.0	18.6	26.4	3.0
WOSP058-075-D	3/5	1400	0.6	13.4	34.8	18.6	37.2	3.0
WOSP087-075-D	3/5	1400	0.6	13.4	52.3	18.6	54.7	3.0
WOSP007-050-D	3/5	1400	0.6	9.4	4.3	18.6	19.2	3.0
WOSP014-050-D	3/5	1400	0.6	9.4	8.6	18.6	19.2	3.0
WOSP028-050-D	3/5	1400	0.6	9.4	16.8	18.6	19.2	3.0
WOSP040-050-D	3/5	1400	0.6	9.4	24.0	18.6	26.4	3.0
WOSP058-050-D	3/5	1400	0.6	9.4	34.8	18.6	37.2	3.0
WOSP087-050-D	3/5	1400	0.6	9.4	52.3	18.6	54.7	3.0
WOSP007-025-D	3/5	1400	0.6	4.7	4.3	18.6	19.2	3.0
WOSP014-025-D	3/5	1400	0.6	4.7	8.6	18.6	19.2	3.0
WOSP028-025-D	3/5	1400	0.6	4.7	16.8	18.6	19.2	3.0
WOSP040-025-D	3/5	1400	0.6	4.7	24.0	18.6	26.4	3.0
WOSP058-025-D	3/5	1400	0.6	4.7	34.8	18.6	37.2	3.0
WOSP087-025-D	3/5	1400	0.6	4.7	52.3	18.6	54.7	3.0
WOSP014-075-ND-2500	3/5	700	0.0	13.4	8.6	18.6	19.2	3.0
WOSP028-075-ND-2500	3/5	700	0.0	13.4	16.8	18.6	19.2	3.0
WOSP040-075-ND-2500	3/5	700	0.0	13.4	24.0	18.6	26.4	3.0
WOSP040-075-ND-7500	3/5	3100	0.0	13.4	24.0	18.6	26.4	3.0
WOSP058-075-ND-7500	3/5	3100	0.0	13.4	34.8	18.6	37.2	3.0
WOSP087-075-ND-7500	3/5	3100	0.0	13.4	52.3	18.6	54.7	3.0

Table I.2 *List of simulations scaled 3/5.*

Appendix J

Lateral Temperature Distribution in WOSP

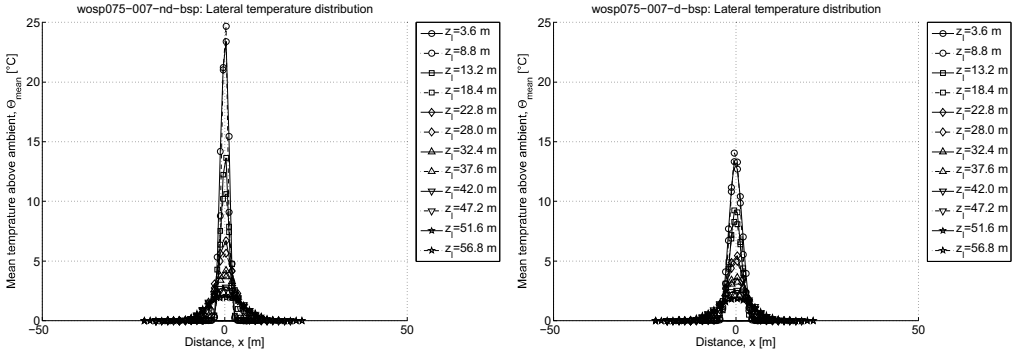

(a) WOSP075-007-ND-BSP. (b) WOSP075-007-D-BSP.

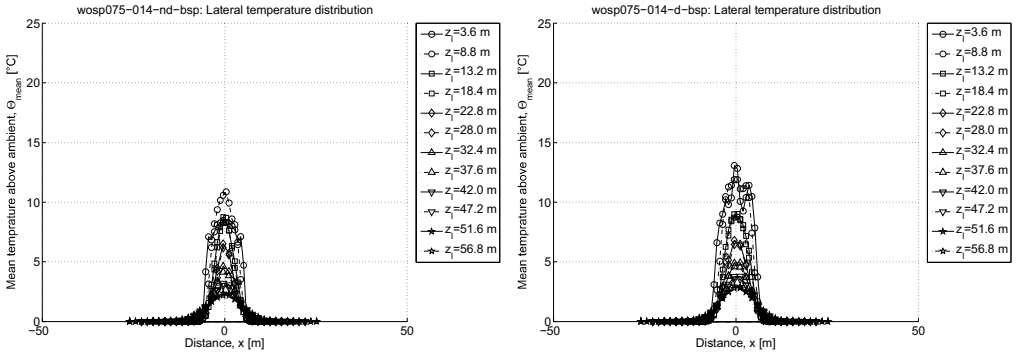

(c) WOSP075-014-ND-BSP. (d) WOSP075-014-D-BSP.

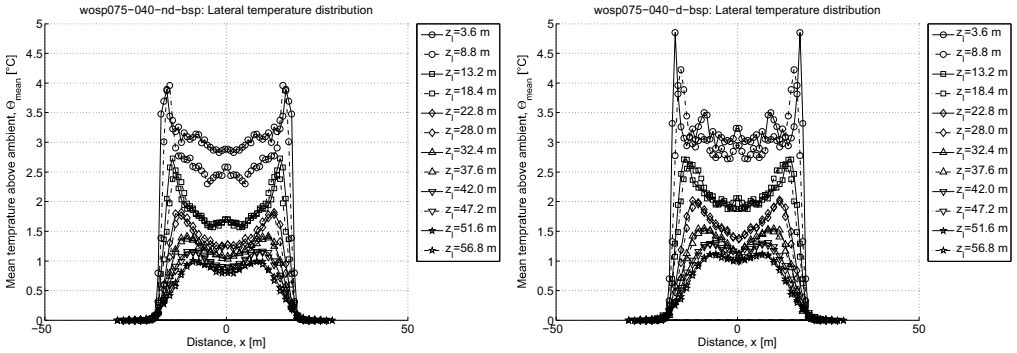

(e) WOSP075-040-ND-BSP. (f) WOSP075-040-D-BSP.

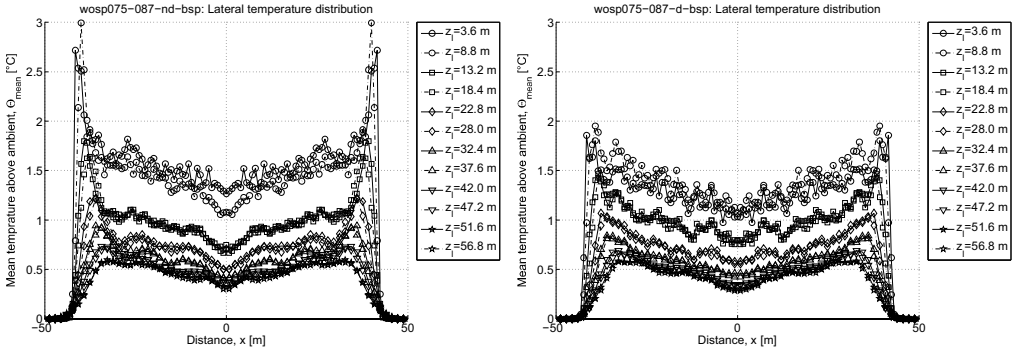

(g) WOSP075-087-ND-BSP. (h) WOSP075-087-D-BSP.

Figure J.1 *WOSP075-XXX-XX-BSP: Lateral mean temperature distributions.*

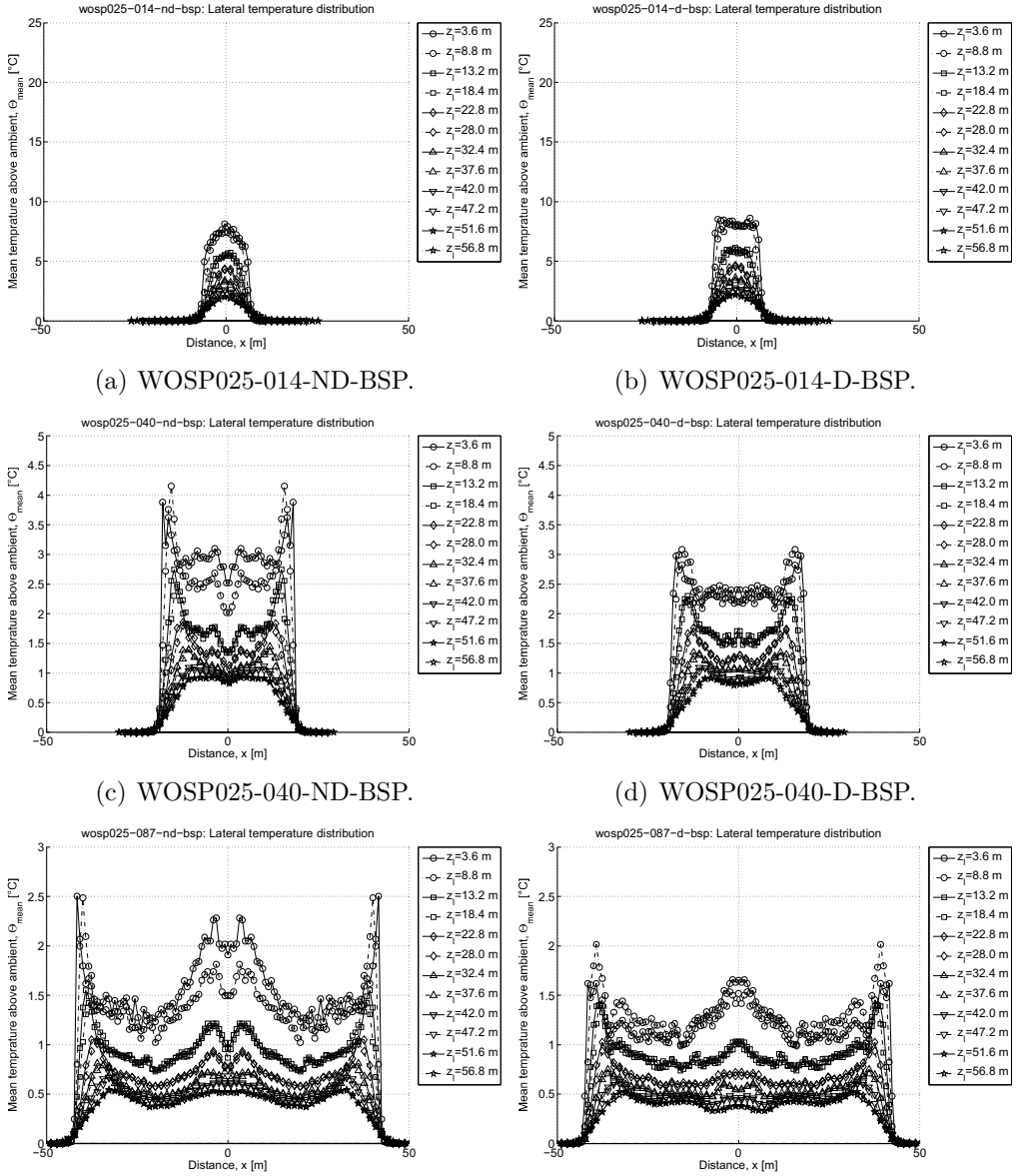

(a) WOSP025-014-ND-BSP.

(b) WOSP025-014-D-BSP.

(c) WOSP025-040-ND-BSP.

(d) WOSP025-040-D-BSP.

(e) WOSP025-087-ND-BSP.

(f) WOSP025-087-D-BSP.

Figure J.2 *WOSP025-XXX-XX-BSP: Lateral mean temperature distributions.*

Appendix K

Lateral Temperature Distribution in WOSP

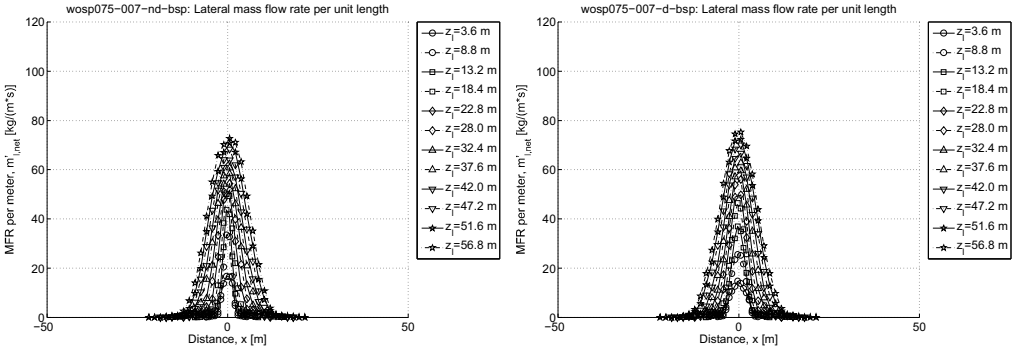

(a) WOSP075-007-ND-BSP. (b) WOSP075-007-D-BSP.

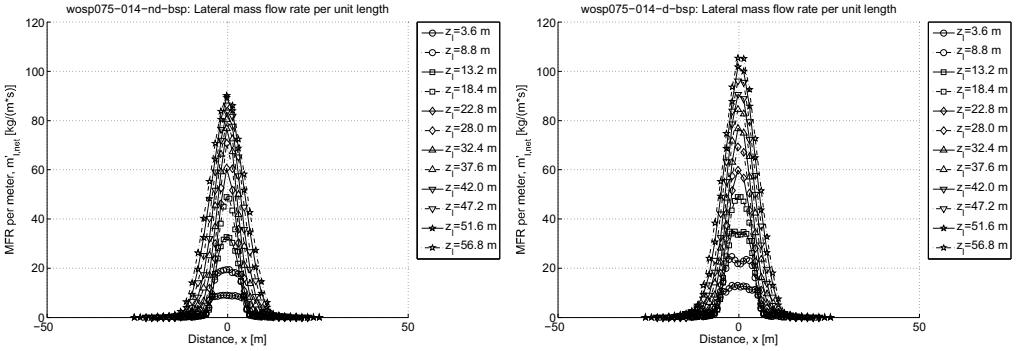

(c) WOSP075-014-ND-BSP. (d) WOSP075-014-D-BSP.

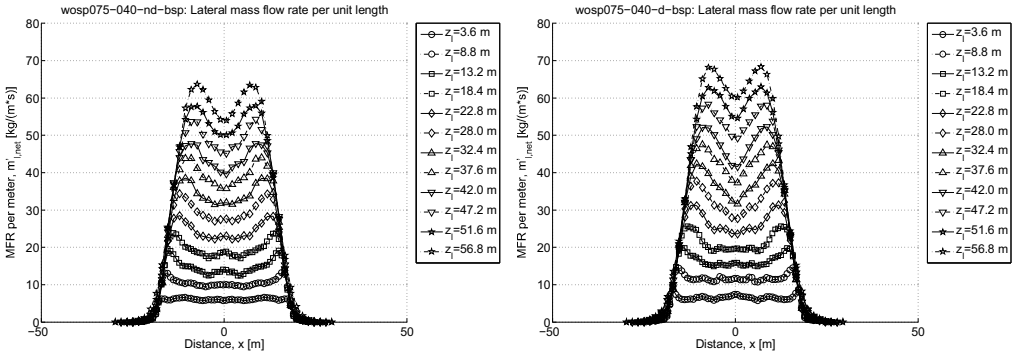

(e) WOSP075-040-ND-BSP. (f) WOSP075-040-D-BSP.

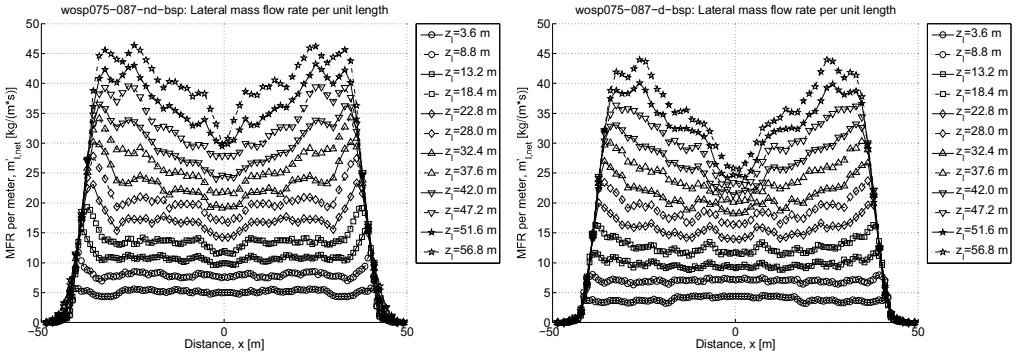

(g) WOSP075-087-ND-BSP. (h) WOSP075-087-D-BSP.

Figure K.1 *WOSP075-XXX-XX-BSP: Lateral mass flow rate distributions.*

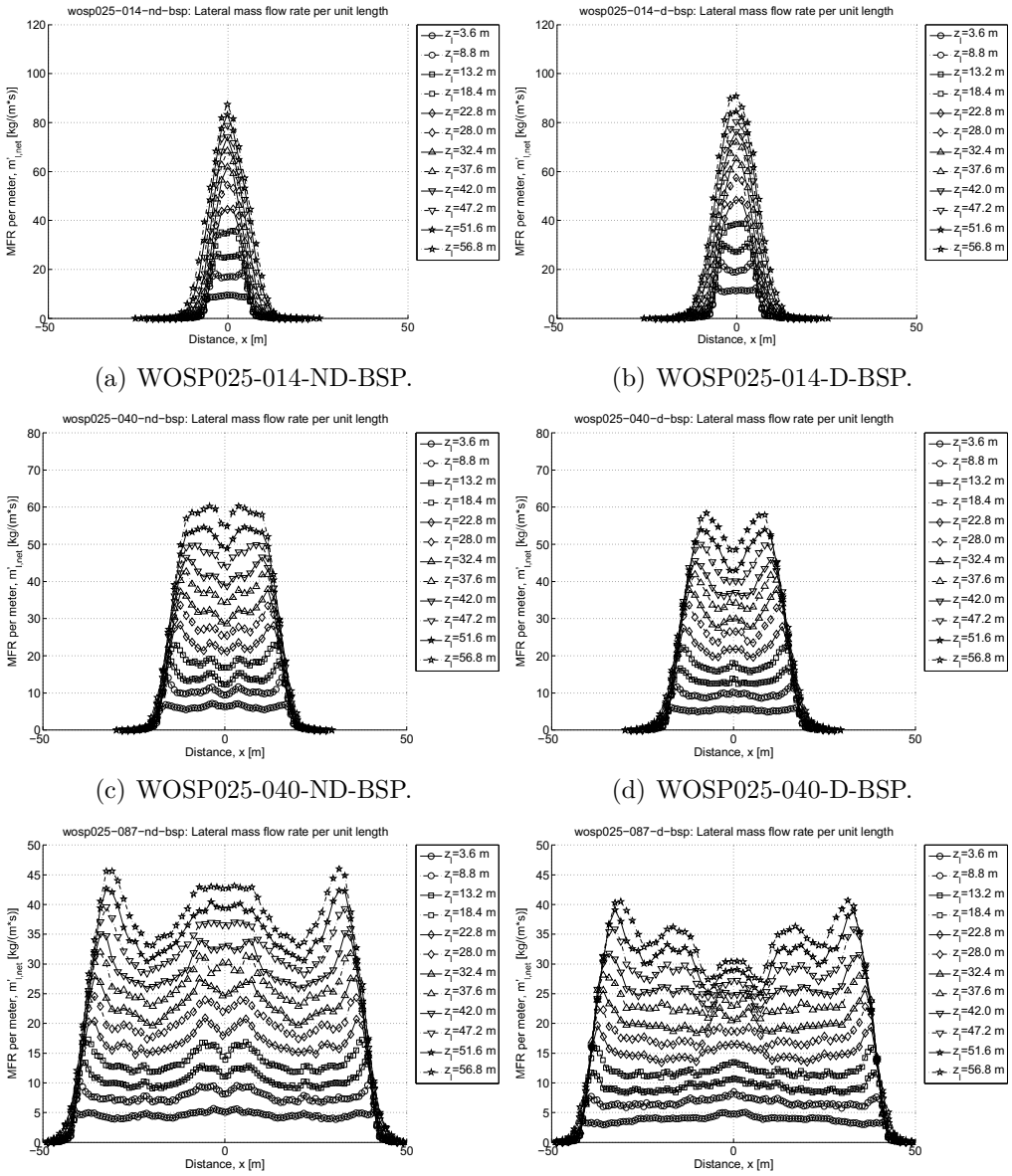

(a) WOSP025-014-ND-BSP.

(b) WOSP025-014-D-BSP.

(c) WOSP025-040-ND-BSP.

(d) WOSP025-040-D-BSP.

(e) WOSP025-087-ND-BSP.

(f) WOSP025-087-D-BSP.

Figure K.2 *WOSP025-XXX-XX-BSP: Lateral mass flow rate distributions.*

Appendix L

Cross-sectional Temperature Distribution in WOSP

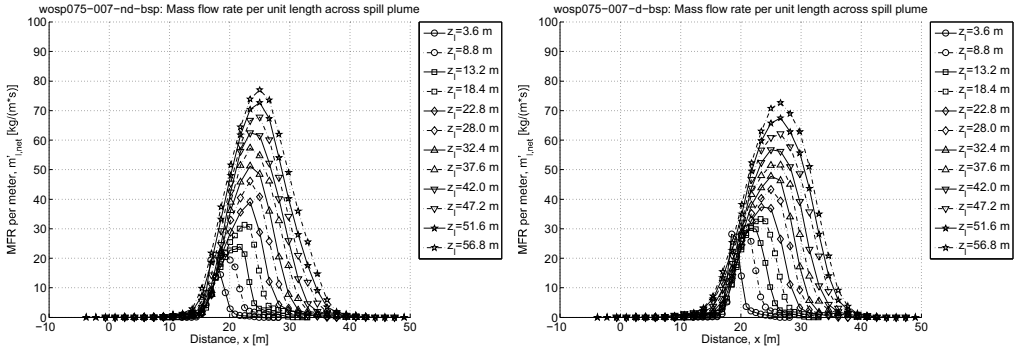

(a) WOSP075-007-ND-BSP. (b) WOSP075-007-D-BSP.

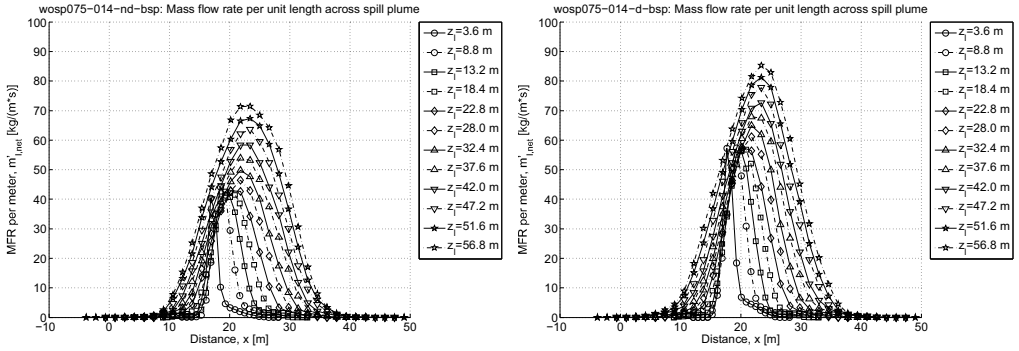

(c) WOSP075-014-ND-BSP. (d) WOSP075-014-D-BSP.

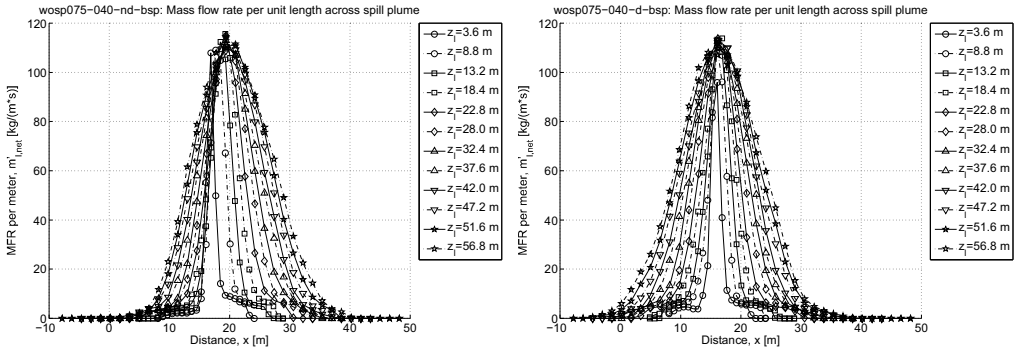

(e) WOSP075-040-ND-BSP. (f) WOSP075-040-D-BSP.

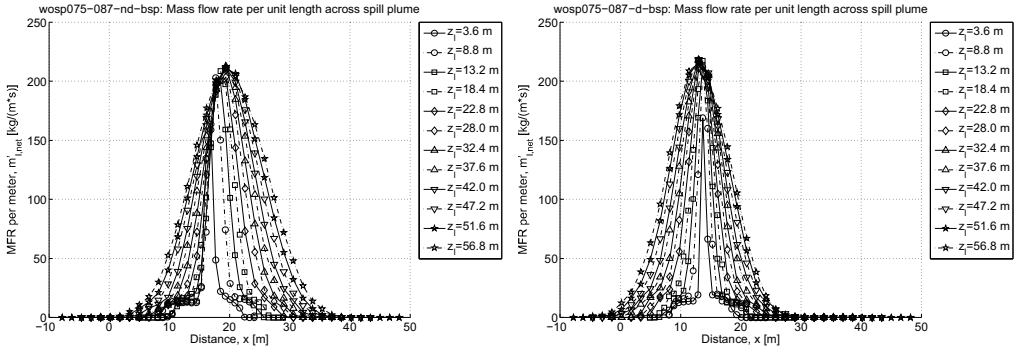

(g) WOSP075-087-ND-BSP. (h) WOSP075-087-D-BSP.

Figure L.1 *WOSP075-XXX-XX-BSP: Cross-sectional mass flow rate distributions.*

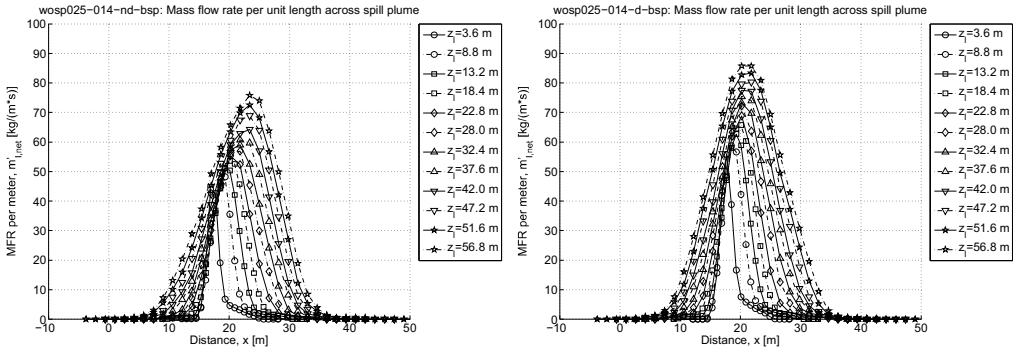

(a) WOSP025-014-ND-BSP. (b) WOSP025-014-D-BSP.

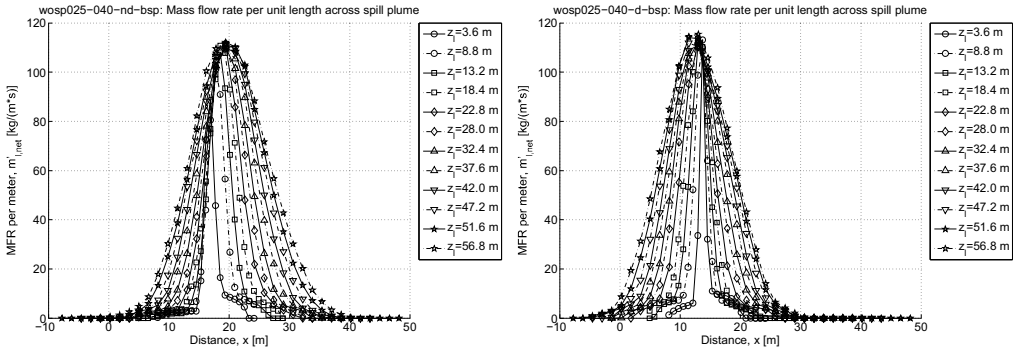

(c) WOSP025-040-ND-BSP. (d) WOSP025-040-D-BSP.

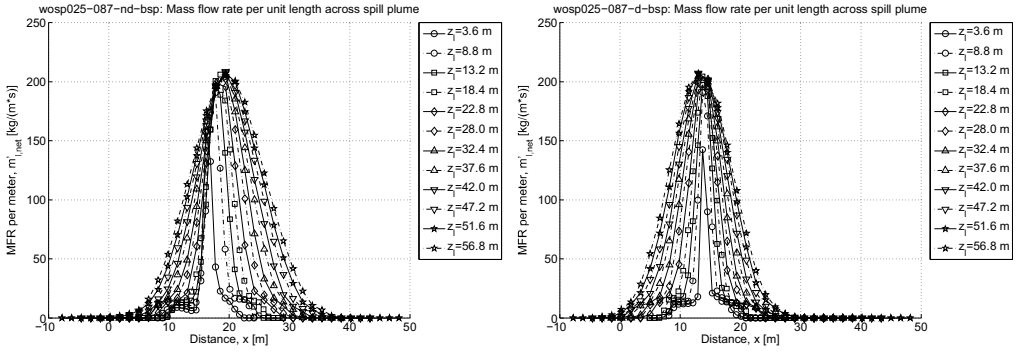

(e) WOSP025-087-ND-BSP. (f) WOSP025-087-D-BSP.

Figure L.2 *WOSP025-XXX-XX-BSP: Cross-sectional mass flow rate distributions.*